# PERCHED WATER IN FRACTURED, WELDED TUFF: MECHANISMS OF FORMATION AND CHARACTERISTICS OF RECHARGE

by

Elizabeth Gail Woodhouse

---

A Dissertation Submitted to the Faculty of the

DEPARTMENT OF HYDROLOGY AND WATER RESOURCES

In Partial Fulfillment of the Requirements
For the Degree of

DOCTOR OF PHILOSOPHY

In the Graduate College

THE UNIVERSITY OF ARIZONA

1997

THE UNIVERSITY OF ARIZONA ®
GRADUATE COLLEGE

As members of the Final Examination Committee, we certify that we have read the dissertation prepared by Elizabeth Gail Woodhouse

entitled Perched Water in Fractured, Welded Tuff: Mechanisms of Formation and Characteristics of Recharge

and recommend that it be accepted as fulfilling the dissertation requirement for the Degree of Doctor of Philosophy

R L Bassett 3/24/97
Randy L. Bassett Date

12/10/96
William J. Shuttleworth Date

Simon Ince
Simon Ince Date

Dec 10, 1996
Joaquin Ruiz Date

Virginia Colten-Bradley Dec. 10 1996
Virginia Colten-Bradley Date

Final approval and acceptance of this dissertation is contingent upon the candidate's submission of the final copy of the dissertation to the Graduate College.

I hereby certify that I have read this dissertation prepared under my direction and recommend that it be accepted as fulfilling the dissertation requirement.

R L Bassett 3/24/97
Dissertation Director Date
Randy L. Bassett

## STATEMENT BY AUTHOR

This dissertation has been submitted in partial fulfillment of requirements for an advanced degree at The University of Arizona and is deposited in the University Library to be made available to borrowers under the rules of the Library.

Brief quotations from this dissertation are allowable without special permission, provided that accurate acknowledgment of source is made. Requests for permission for extended quotation from or reproduction of this manuscript in whole or in part may be granted by the head of the major department or the Dean of the Graduate College when in his or her judgment the proposed use of the material is in the interests of scholarship. In all other instances, however, permission must be obtained from the author.

SIGNED: Elizabeth T Wood

## ACKNOWLEDGMENTS

Numerous people contributed to the production of this dissertation. Above all, Dr. Randy Bassett convinced me not to leave the department with this project, and has consistently provided a wealth of suggestions, advice, thoughts, and the hard-to-answer questions that really made me think. Dr. Jim Shuttleworth lent strong support on the micrometeorological aspects of the project. Dr. Ginny Colten-Bradley made several forays out here from Washington to help with the geologic interpretations. Dr. Joaquin Ruiz and Dr. Simon Ince also contributed valuable help, comments, and questions.

Dr. Tom Nicholson of the Nuclear Regulatory Commission has provided continued undying enthusiasm and strong support for the Apache Leap project for as long as he has been associated with it; his efforts were critical to keeping this project moving ahead.

Dr. Kathy Marsaglia of the University of Texas at El Paso gave generously of her time, microscope, and home, and greatly increased my understanding of what the thin-sections were showing me. Dr. Shlomo P. Neuman helped greatly with the aquifer test analysis.

Alex Paul, Chief Mine Geologist at BHP's Shaft 9 mine in Superior, provided access to core samples and maps, and donated his time to helping me.

The field work would not have been possible without the technical help and labor from Dick Thompson, and before him, Charles Lhorstorfer. The additional labor from Mike Geddis, Dave Stephens and Walter Illman (who also helped with aquifer test interpretation) made possible projects I could not have attempted on my own. Dick also was responsible for all the flume data that were collected for this project.

Dr. John Guilbert, professor emeritus from the Geosciences Department, told me about the process he developed for crossed-nichols thin-section photocopying; Al Yadao of Reproduction, Inc. was most willing to work with me until we got it just right. Dan Braithwaite also assisted in imaging the thin sections to make porosity estimates.

Dr. Don Post of the Department of Soil and Water Sciences provided soil and rock albedo and soil texture data to use to calibrate the BATS model. Dr. Dave Hendricks of that department performed the x-ray diffraction analyses.

Jim Leenhoutz provided the photographs of the thin-section blocks that first revealed to me the nature of the porosity changes that are occurring.

Edwin Welles and Tade Orr wrote and assisted in writing most of the programs used to process the Bowen ratio data. Helene Unland, Luis Bastidas, and Jean Morrill gave generously of their time working with me to understand, debug, and run the BATS program that nearly pushed me over the edge.

Finally, my family and friends who have become my Tucson family are not to be overlooked; their support throughout all the ups and downs of my tenure here has been invaluable. Among this group, Howard Grahn was especially important as a friend, a sounding board for my ideas, and as my editor for some of the tricky parts. He also made sure I had fun once in a while.

A most sincere thank you to all.

# DEDICATION

This dissertation is dedicated to those who kept on believing in me, even during the times I stopped believing in myself. I would not have completed this project without them.

## TABLE OF CONTENTS

TABLE OF CONTENTS--Continued

TABLE OF CONTENTS--Continued

TABLE OF CONTENTS--Continued

TABLE OF CONTENTS--Continued

# LIST OF FIGURES

LIST OF FIGURES--Continued

LIST OF FIGURES--Continued

LIST OF FIGURES--Continued

LIST OF FIGURES--Continued

# LIST OF TABLES

# ABSTRACT

Perched water zones have been identified in the fractured, welded tuff in the semi-arid to arid environments of Yucca Mountain, Nevada and near Superior, Arizona. An understanding of the formation of such zones is necessary in order to predict where future perched water might form at Yucca Mountain, the proposed site of a high-level nuclear waste repository. The formation or growth of a perched zone above a repository is one factor of the factors to be considered in the risk assessment of the Yucca Mountain site.

The Apache Leap Research Site (ALRS) near Superior, Arizona is a natural analog to the Yucca Mountain site in terms of geology, hydrology, and climate. Perched water has been identified over an area of at least 16 km$^2$ in the Apache Leap Tuff, a mid-Miocene fractured, welded ash-flow tuff. A primary goal of this investigation was to characterize the physical and hydrologic properties of the tuff in the region above and including the perched zone, and to evaluate those characteristics to develop a model for a perching mechanism in the tuff. A second goal was to determine what fraction of water entering a watershed reaches the subsurface, to potentially recharge the perched zone.

The Apache Leap Tuff has been subject to considerable devitrification and vapor phase crystallization, which dominate the character of the rock. With depth to the perched zone, pumice fragments become increasingly flattened and segregated; the pumice fragments are the primary locations of porosity in the rock, therefore porosity also becomes greatly reduced with depth, to the extent that the rock matrix is virtually impermeable at the perched water zone. Fractures are the primary pathways by which water moves through the rock; fracture hydraulic conductivity values were determined to

be nine orders of magnitude greater than measured matrix hydraulic conductivity at the perched zone. An increase in fracture filling by silica mineralization beneath the perched zone reduces the secondary permeability, enhancing the formation of perched water. Thus, the primary mechanisms for the formation of the perched zone include fracture flow bringing water into the subsurface, combined with extremely low matrix hydraulic conductivity at depth, and reduced secondary permeability by filled fractures and lower fracture density.

Water budgets were calculated for two years in a 51.4-ha watershed. Direct measurements were made of precipitation and runoff; evapotranspiration was both directly measured, and modeled based on measurement of a number of weather parameters. Infiltration was calculated as the residual of precipitation after runoff and evapotranspiration were removed. Infiltration was determined to be less than 10% of the annual water budget; evapotranspiration removes on the order of 90% of precipitation on an annual basis.

# CHAPTER 1
# INTRODUCTION

Yucca Mountain in southwestern Nevada is being investigated by the U.S. Department of Energy (DOE) as a potential site for a high-level nuclear waste repository. The site was chosen in part because it has a thick unsaturated section of welded and zeolitized tuff, on the order of several hundred meters. This unsaturated zone should impede a significant flux of water from the land surface down to a deeply-buried repository, and retard transport from the repository to the zone of permanent saturation several hundred meters below, thus minimizing the likelihood of corrosion or spent fuel dissolution problems if any release of radionuclides were to occur from the repository. Before the repository can be licensed, however, the DOE must demonstrate that the repository will remain inaccessible to the environment for at least 10,000 years (EPA, 1985). Therefore, a detailed understanding of the complex hydrologic regimes present in such a geologic, hydrologic, and climatologic setting as Yucca Mountain is necessary.

While Yucca Mountain is characterized by a thick unsaturated zone, locally saturated water conditions may also occur, due to heterogeneities in the geologic material and/or to intense meteorological events on a short time scale, or climatic changes on a larger scale. If such a perched water body formed near the repository, it would have the potential to either flood the repository, or to provide a more rapid pathway of radionuclide transport away from it to the accessible environment. Therefore, an understanding of the mechanisms of formation of such perched zones is necessary to properly evaluate the suitability of the site for high level waste disposal.

The Apache Leap Research Site (ALRS) near Superior, Arizona is composed of fractured welded tuff with climatic and topographic conditions similar to Yucca Mountain, making it a highly suitable natural analog for an independent characterization of hydrological processes in such material. Investigations have been ongoing at ALRS to test some of the methods, assumptions, and results of the work at Yucca Mountain. The primary focus of this investigation concerns the formation of, and recharge to, perched water zones in fractured, welded tuff.

This research was funded by the U.S. Nuclear Regulatory Commission (NRC) under contracts NRC-04-90-51 and NRC-04-95-041.

## 1.1 Focus of Research

Perched water zones have been identified in fractured, welded tuff in the arid environments of both Yucca Mountain and the ALRS. The mechanisms of the formation of, and recharge to, these perched zones are not well understood. Three questions served to focus this research. First, what are the physical and hydrological characteristics of the tuff, including the pathway(s) by which water moves through the tuff? Second, can variations in some of these characteristics and properties be correlated to the location of the perched water zone? Third, what fraction of precipitation is available to recharge and/or maintain the perched zone? These questions will be addressed in the following chapters.

## 1.2 Approach

One goal of this research was to gain an understanding of the mechanisms which caused the formation of the perched zone in the Apache Leap Tuff. The hypothesis tested was that a correlation exists between the physical and hydrological characteristics of the tuff and the location of the perched zone. In order to evaluate such a correlation, a thorough characterization of the tuff in the region including the perched zone was necessary. The location of the perched zone was established by drilling; physical characteristics which were examined for potential correlation include: mineralogy and alteration characteristics, density, moisture content, hydraulic conductivity, geochemistry, geophysical response, and the degrees of fracturing, weathering, welding and devitrification. These characteristics were examined through analyses of hand specimens, thin sections, x-ray diffraction results, scanning electron microscope techniques, aquifer tests, and correlation with the work of other researchers; the characterization is presented in Chapter 2.

The hydrologic response of the aquifer was examined by conducting aquifer and slug tests, described in Chapter 3. The hypothesis to be tested under this portion of the investigation was that fracture flow dominates in this system. The response of the aquifer to pumping or the addition of a slug was analyzed and compared to models for fracture-dominated flow systems. The results of this analysis revealed the primary pathways for fluid flow through the tuff.

The physical and hydrological characteristics of the tuff, described in Chapters 2 and 3, were then evaluated against potential models for the formation of the perched water zone in Chapter 4. This evaluation allowed a combination model for the perching mechanism at the ALRS to be developed.

Finally, the third goal of this research was to determine what fraction of precipitation is available for recharge to the perched water zone. A water budget was used to determine the fraction of precipitation that is infiltration, or the quantity of water potentially available to recharge the perched zone. The evapotranspiration component of the water budget was measured directly, using a Bowen ratio energy balance (BREB) system, and indirectly, using a biosphere-atmosphere transfer scheme (BATS) model. This portion of the investigation is discussed in Chapter 5.

The major conclusions of this research are presented in Chapter 6.

## 1.3 Description of the Study Area

The field location for this investigation is the Apache Leap Research Site (ALRS) near Superior, Arizona (Fig. 1.1), 160 km north of Tucson. The site was chosen for its climatologic, hydrologic, and geologic similarity to Yucca Mountain, and its proximity to Tucson. In this investigation, a 51.4-ha watershed (Fig. 1.2) within the ALRS was instrumented and sampled to study the perched water zone beneath it.

### 1.3.1 Physiography

Apache Leap is a distinctive escarpment rising 500 m above the adjacent Superior basin. The upper section of the escarpment and the plateau extending back from it are composed of the Apache Leap Tuff. The surface of the deposit is highly irregular, the result of erosion, weathering, and faulting. The watershed under investigation contains 133 m vertical relief, and is characterized by steep promontories and rock cliffs surrounding a more gently-sloping drainage channel approximately 1.2 km long. The upper 1/3 of the watershed faces northeast; the central section drains east, and the lower

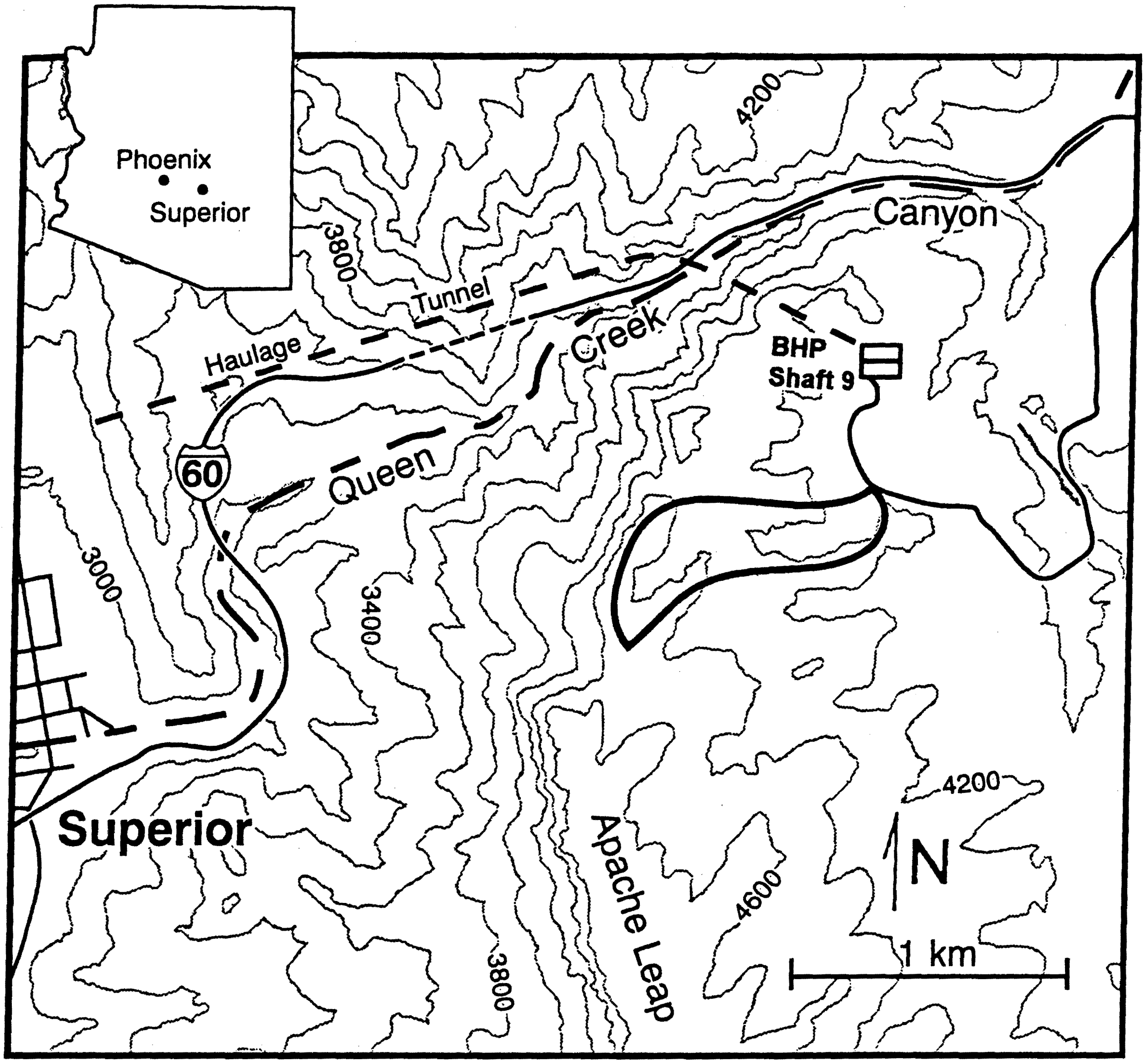

Figure 1.1 Location of the Apache Leap Research Site.

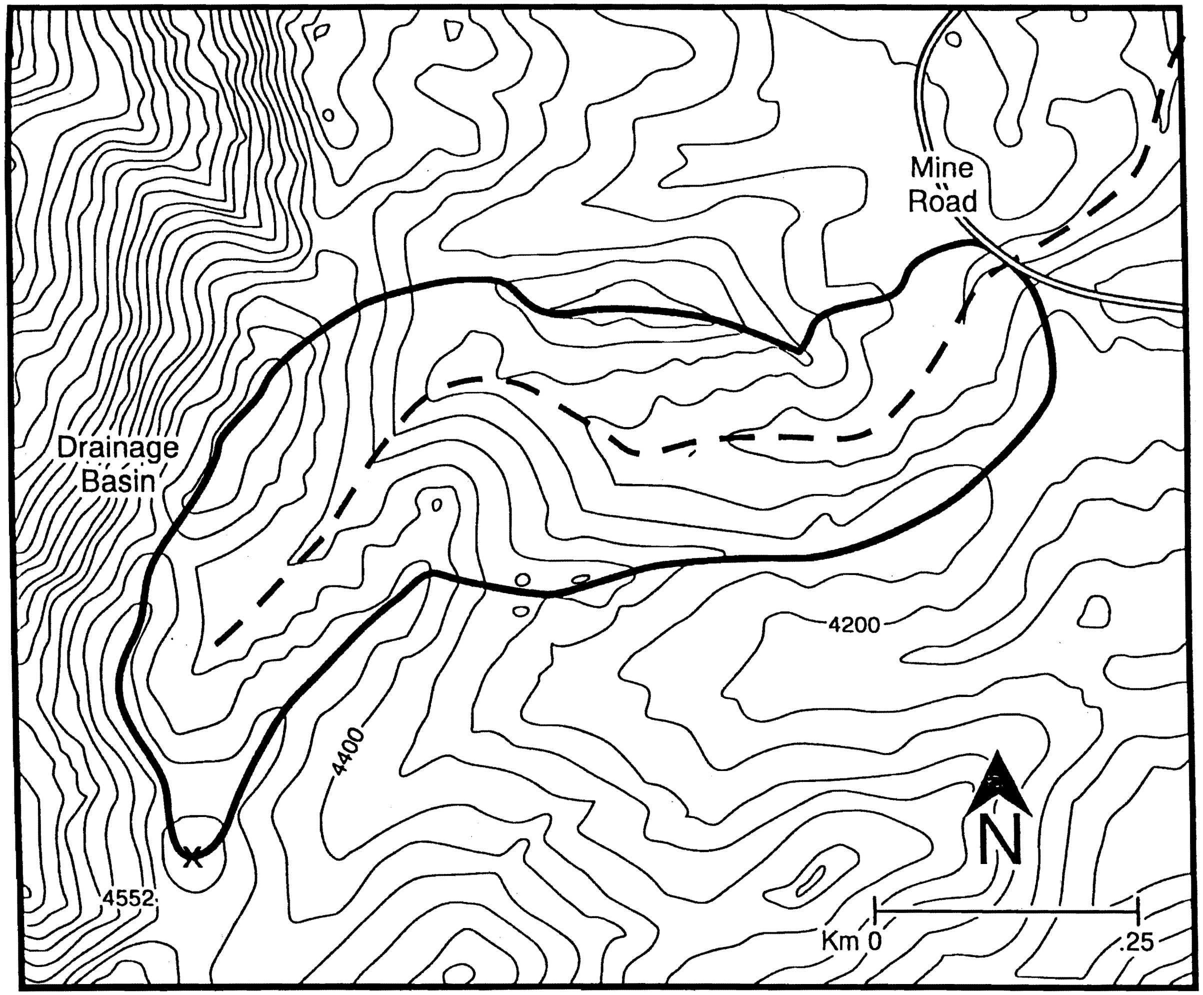

Figure 1.2 Detail of the watershed under investigation at the Apache Leap Research Site.

1/4 curves back to a northeastern exposure. The surface of the watershed consists of approximately 50% exposed fractured rock, with the remainder covered by a mixture of thin, sandy soil, and vegetation consisting primarily of manzanita, scrub oak, juniper, and cacti.

The ALRS is in a region of semi-arid climate, receiving an average of 389 mm of precipitation per year, some of which was snow, over a 2-year study period. Precipitation in the area generally occurs as brief, intense monsoon-type storms in the mid- to late summer months, and as more widespread, less intense, frontal-type storms in the late winter months. Spring and fall are typically relatively dry. Average summer temperatures during the period of investigation ranged from a high of 34°C to a low of 22°C; average winter temperatures ranged from a high of 13°C to a low of 4°C.

### 1.3.2 Regional Geology

#### *1.3.2.1 Geologic History*

The Apache Leap Tuff is a mid-Miocene ash-flow tuff of approximate age 20 my. The tuff was deposited on Pennsylvanian Naco Limestone and isolated deposits of early Tertiary Whitetail Conglomerate. The surface was considerably eroded and faulted, and had high topographic relief prior to the deposition of the tuff. Local rhyolitic lava flows and plugs immediately preceded the more widespread dacitic ash flow tuff, which smoothed out some of the irregular topography. The deposit covered at least 1000 km$^2$, perhaps as much as 3900 km$^2$ (Peterson, 1961). Subsequent to deposition, and perhaps starting before the deposit was completely cool, north- to northwest trending faulting and eastward tilting of the region continued from pre-deposition time. In addition, the region underwent subsidence, and the Gila Conglomerate was deposited in the lower valleys and basins of the tuff. Finally, regional uplift resulted in development of the present drainage pattern and topography (Hammer and Peterson, 1968). The present deposit has a maximum exposed thickness of 600 m at the escarpment, an average thickness of about 150 m, and covers about 260 km$^2$. In general, the tuff is thickest near the center of the deposit and thins towards the edges, and to the northeast.

Peterson (1961) concluded that the Apache Leap Tuff represents a single cooling unit composed of many (several tens) flows deposited in rapid succession. Identification of individual flows in such a tuff deposit is extremely difficult, and under the clearest circumstances, may be as subtle as a millimeters-thick layer of ash that settled on the top for a brief time before the next flow came along (Peterson, personal communication). This ash layer would typically be incorporated into the next flow, but its existence could affect the movement of water in the cooled unit.

#### *1.3.2.2 Zones of the Tuff*

Peterson (1961) divided the tuff into five stratigraphic units based on differences in the groundmass. From the bottom, the five units are the basal tuff, vitrophyre, brown zone, gray zone, and white zone. The three upper zones are distinguished on the basis of the color of their fresh surface; color is a convenient distinction for field mapping, but does not represent individual flows (Peterson, personal communication).

The basal tuff is a nonwelded, poorly- to moderately-indurated tuff. It is white to light gray and averages 4-7 m thick, but is often covered by talus and not visible in outcrop. The contact with the vitrophyre above occurs over a range of less than one to ten m, and is characterized by the appearance of streaks of black glass in the upper portion of the basal tuff (Peterson, 1961).

The vitrophyre is a hard, densely welded porphyritic glass, averaging 2-8 m in thickness. Its weathered surface is dark gray to dark brown, but the fresh surface is glassy black, mottled with phenocrysts and lithic fragments. In places, the vitrophyre contains spherical nodules which are more resistant to weathering than the matrix containing them, but which have hollow, weathered out centers. The nodules average about 10 cm in diameter, but may be up to 1 m across. They are composed of phenocrysts in a brown, aphanitic groundmass similar to the overlying brown unit, and according to Peterson (1961), may have formed during the devitrification of the glass. The contact between the vitrophyre and the brown unit is relatively abrupt, occurring over just a few meters (Peterson, 1961).

The brown unit is a densely welded, highly resistant tuff composed of phenocrysts in an aphanitic, partly glassy, brownish-orange matrix. Its weathered surface is lighter brown to grayish brown, similar to the units above it, making differentiation between them difficult. The unit contains on average about 10% lithic fragments, a higher abundance than the units above it. In addition, in most places the brown unit exhibits a foliated texture, the result of compressed volcanic particles, including pumice fragments. The thickness of this zone is highly variable, ranging from about 7 to 70 m thick. Its upper boundary with the gray unit is extremely gradational; the actual delineation of the contact is subjective in most places (Peterson, 1961).

The gray unit is generally the thickest zone of the tuff, extending more than 350 m in some areas. It is firmly welded, with phenocrysts in a pinkish gray aphanitic to cryptocrystalline matrix streaked with white to light gray flattened pumice nodules. The weathered surface is not clearly distinguishable from the units above and below. The outcrop pattern of the gray unit is controlled by vertical joints, which are in turn cut by horizontal joints which run generally parallel to the foliation. The contact with the white unit above is also highly gradational, occurring over perhaps 100 m in places, and again is highly subjective (Peterson, 1961). The perched water zone under investigation occurs in this unit.

The white unit contains phenocrysts in a light pinkish-gray to white aphanitic matrix. The fresh surface is soft and nonresistant, but the weathered surface is hard and appears similar to the units below it. In some outcrops, the white unit exhibits a pock-marked surface where pumice nodules have been weathered out; in other areas, the pumice remains. No perceptible foliation is seen in the white unit; the pumice fragments are only slightly flattened to euhedral, and the unit appears massive. The white unit is cut by the same vertical joints as the gray unit below, but the horizontal component of the fractures is not as well developed, due to the lack of foliation. As this is the uppermost unit, much of the original thickness has been eroded; at present, the average thickness of this unit is about 100 m, with a maximum thickness of about 245 m (Peterson, 1961). The white zone is present in the upper sections of the boreholes at ALRS.

Superimposed on the stratigraphic units are cooling-related zones of welding, devitrification, and vapor phase crystallization, which have obscured the original textures of the deposit in all but the lower part (Peterson, 1961). Figure 1.3 shows the relationship

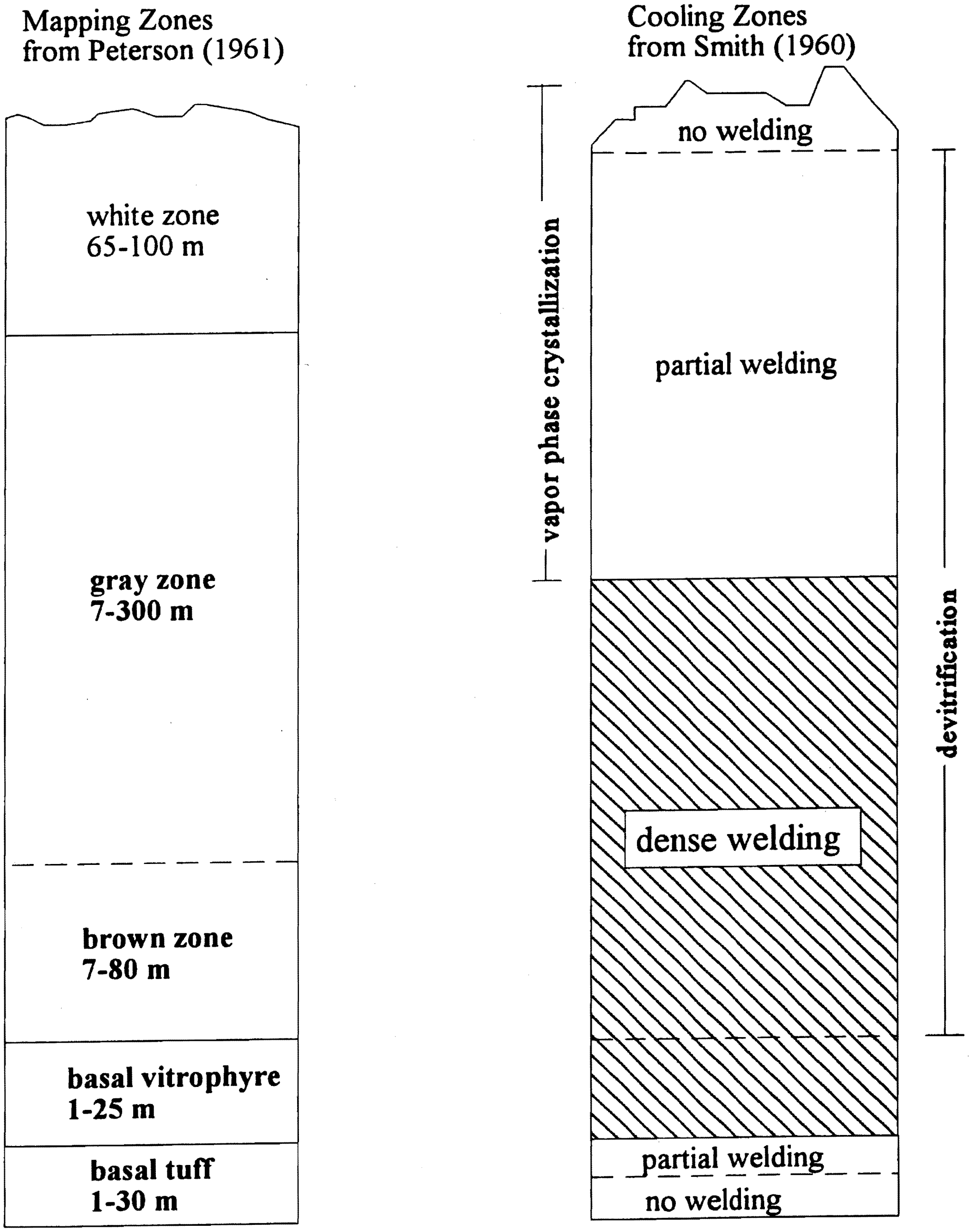

Figure 1.3 Relationship between Peterson's (1961) mapping units and cooling units in the Apache Leap Tuff.

between Peterson's mapping units and the cooling units. The basal tuff is nonwelded, and the vitrophyre, brown zone, and lower portion of the gray zone are highly welded. The degree of welding decreases upwards in the gray zone and into the white zone, and the uppermost portion of the white zone is nonwelded. Devitrification is first evident in the middle of the brown zone, and increases upwards to the surface. Vapor phase crystallization begins in the lower part of the gray zone and also increases to the surface.

#### *1.3.2.3 Structure*

The tuff was deposited as a sheet on a surface of considerable relief. As a result, the dip of the deposit ranges from horizontal to 30° or greater (Peterson, 1961). Peterson (1961) was able to map faults with significant offset, identified by different stratigraphic zones or different degrees of pumice nodule flattening. Most of the large faults he mapped had a north-south orientation, with the west side downdropped.

Vertical or near-vertical joints dissect the tuff, generally with spacing of 1.6 m to 5 m, but ranging from a few centimeters to more than 13 m apart. Thornburg (1990) identified three separate fracture sets: 1) with strike ENE and azimuth of 67° to 77°; 2) with strike N and azimuth of 2° to 19°; and 3) with strike NW and azimuth of 136° to 145°. Peterson (1961) suggested that they were of tectonic origin rather than simple cooling cracks because of their continuity over 100 m to more than 1 km, however, Thornburg (1990) associated the first set with flexing around the pre-existing topography. The timing of the joints may have been during cooling, but their orientation was probably affected by regional tectonic stresses. The second of Thornburg's (1990) fracture sets are of the same strike as the steep cliffs which comprise the Apache "Leap".

#### *1.3.2.4 Mineralogy*

According to Peterson (1961), the entire thickness of the tuff has relatively uniform mineralogy and chemical composition, supporting its origin as a single magma source. The proportion of phenocrysts to matrix remains fairly constant at 35-45% throughout the entire depth; lithic fragments are somewhat more abundant near the bottom of the section, in the vitrophyre and lower brown unit, but overall make up only 1-2% of the tuff. The phenocrysts are predominantly plagioclase, with lesser amounts of quartz, biotite, sanidine, and magnetite, and occasional hornblende. Pumice fragments comprise as much as 25% of the tuff in the white unit, but are virtually absent in the deeper units. The matrix consists dominantly of cryptocrystalline cristobalite and plagioclase throughout the entire thickness. The tuff is compositionally a quartz latite, but if classified according to phenocryst type, it is a dacite, as it is commonly called (Peterson, 1961).

### 1.3.3 Regional Hydrology

#### *1.3.3.1 Surface Water*

Surface water leaves the tuff by ephemeral flow off the plateau. Most drainage from the ALRS and surrounding area runs generally northeastward in a series of shallow, roughly parallel drainages that eventually lead to Queen Creek, which flows south and west near the west end of the site. Small amounts of runoff are captured in stock ponds on the surface of the tuff. Devil's Canyon, about 6 km east of Superior, flows south and drains much of the Apache Leap Tuff area east of ALRS . Both Queen Creek and Devil's

Canyon are ephemeral streams which in places have cut deep canyons into the tuff and, near the southern edge, through to the underlying Paleozoic limestones. A few springs in both drainages maintain isolated pools or moist areas perennially except during severe drought.

#### *1.3.3.2 Ground Water*

According to the Arizona Department of Water Resources (1990), groundwater may exist in small, closed, isolated basins in the tuff, with local water tables as close as 2.5 m below the surface. Pumping and precipitation events cause great fluctuations of the water levels in these shallow perched aquifers, however, making them unreliable as water sources, especially in dry years (Bassett et al., 1994).

Figure 1.4, from Bassett et al. (1994), shows the uppermost occurrence of a widespread saturated zone covering at least a 16-km$^2$ area of Apache Leap Tuff, including the ALRS. This figure was prepared from the drilling logs of exploration boreholes of mining companies, other miscellaneous wells, and from the locations of springs, although in general, hydrologic data were not collected during drilling, and records are incomplete. In several boreholes, however, unsaturated conditions were observed at lower depths, therefore the surface created by contouring these elevations suggests a regional perched water zone with a gradient to the south, ultimately discharging into Devil's Canyon.

Perched water beneath ALRS did drain into Queen Creek at one time, however. BHP Copper Company operates a mine near the site (Shaft #9; see Figure 1.1), and in 1972 began pumping water out of the mine to enable access to their workings. At that time, two springs which previously discharged into Queen Creek dried up, suggesting

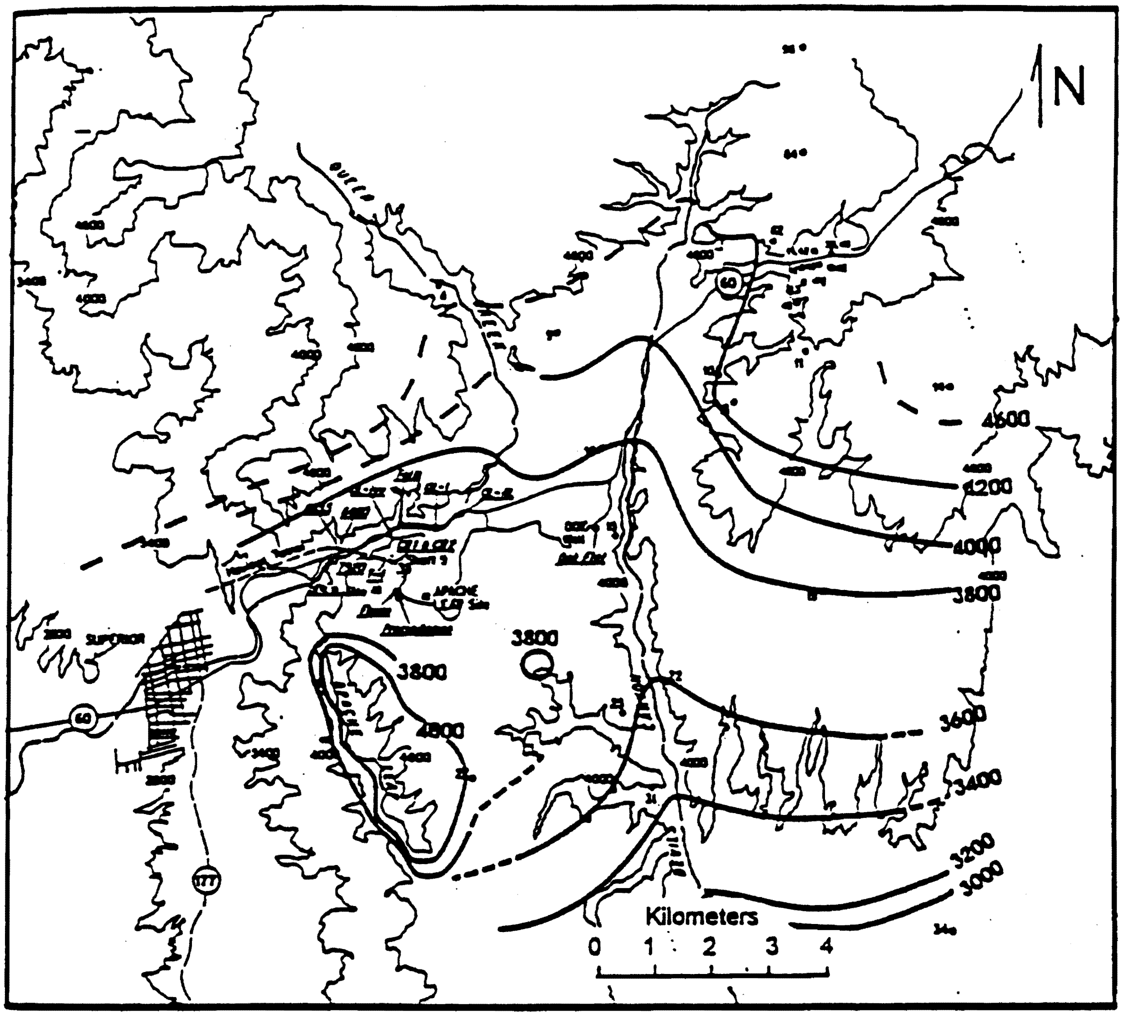

Figure 1.4 Surface of the uppermost perched water in the Apache Leap region (from Bassett et al., 1994).

partial or total aquifer dewatering (Bassett et al., 1994).

The depth of the regional (non-perched) water table is not well-documented, but is generally considered to be well below the base of the Apache Leap Tuff, based on mine exploration records.

### 1.3.4 Vegetation

Approximately 50% of the surface of ALRS is covered by vegetation. The dominant plant types are manzanita and scrub oak; sawtooth sotol, agave, bear grass, and mountain mahogany are very common as well. Also present in this semi-arid, upper Sonoran desert location are juniper, yucca, pinyon, catclaw, mistletoe, grease bush, and various cacti, primarily prickly pear and cholla (Davidson, 1995).

# CHAPTER 2

# PHYSICAL AND HYDROLOGIC CHARACTERIZATION OF THE APACHE LEAP TUFF IN THE REGION INCLUDING THE PERCHED WATER ZONE

## 2.1 Introduction

In order to determine which mechanisms might be responsible for the formation of perched water in the Apache Leap Tuff, a thorough understanding of the physical and hydrologic properties of the tuff was first required. Sources of information for such a characterization included the previous detailed geologic analysis of the entire deposit by Peterson (1961), which served as a baseline for the detailed study of specific units in this investigation. Additional information was obtained from recent or in-progress investigations by others at the ALRS. New information was obtained from two boreholes which were installed at the ALRS watershed: a deep slant borehole (DSB), which extends 201 m down at an approximate 45° angle, and a vertical observation borehole (VOB), which is collared upgradient and 15 m from the top of the DSB, and extends down to 170 m. Figure 2.1 shows the location of these boreholes; both were terminated just below the uppermost perched water zone as described in Section 1.3.3.2. The core from the DSB was collected and preserved for analyses for several different investigations, including this one. Additional, select sections of core were available for observation from an exploratory borehole identified as MB10-A, which was drilled through the entire section of tuff by BHP Copper, Inc.; its location is also shown on Figure 2.1. Finally, core information was also available from the vertical Oak Flats borehole, which was drilled about 3 km from the ALRS (Figure 2.1) by the U.S.G.S., and extends to a depth of 522 m.

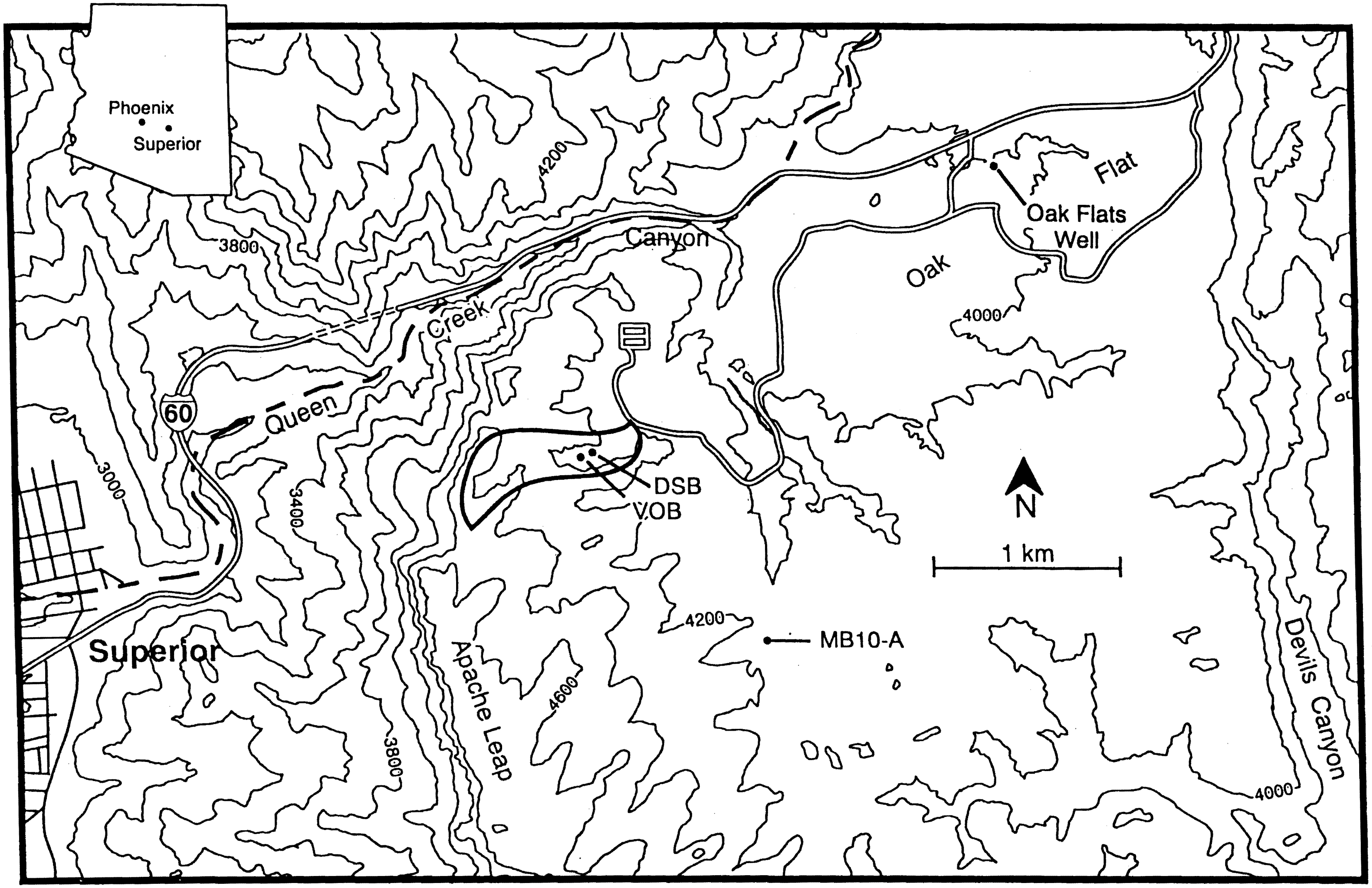

Figure 2.1 Location of boreholes at the Apache Leap Research Site.

## 2.2 Objective

The objective of the research in this chapter was to compile all existing and new information on the zones of the Apache Leap Tuff that contain or may affect the perched water zone. Those zones include Peterson's (1961) white unit, which covers the surface of the deposit, and the gray unit beneath it, which contains the perched water zone. Information on both the physical and hydrologic properties of the tuff will be used to evaluate potential models for perching mechanisms in Chapter 4.

## 2.3 Previous Work

### 2.3.1 Characteristics of Tuff Deposits

Discussions and descriptions of the origin, identification, petrography, and zonation of ash-flow tuffs by Smith (1960) and Ross and Smith (1961) provided the greatest source of background information for this investigation. Photographs of textures and characteristics of tuff deposits around the world in those publications aided in the understanding and description of the Apache Leap Tuff. Enlows' (1955) work on the welded tuffs of Chiricahua National Monument in Arizona described pumice alteration very similar to that which has occurred in the Apache Leap Tuff, and which distinguishes these deposits from many others. As discussed previously, Peterson (1961) provided a detailed geologic background of the entire section of the Apache Leap Tuff; and the discussion by Roberts and Peterson (1961) enabled differences between welded ash tuffs and welded crystal tuffs to be determined. The significance of compaction in creating textures that were observed in the tuff was supported by the work of Ragan and Sheridan

(1972) , who studied the Bishop Tuff in California. Information regarding devitrification products, textures, and replacement phenomena in ash flow tuffs was provided by Anderson (1969), Tarshis (1973), Wise et al. (1973), and Carr (1981).

### 2.3.2 Alteration Characteristics of Tuff

Alteration characteristics of the Apache Leap Tuff were investigated with regards to their potential effect on the physical or hydrologic properties of the tuff. In order to recognize and understand the factors which influence alteration, the alteration characteristics of a number of different Tertiary tuff deposits around the world was researched. The results of that investigation enabled a typical alteration sequence to be developed, controlled primarily by pore water chemistry and reaction chemistry. Typical alteration begins with the dissolution of glass and silicates and the precipitation of clay minerals, especially smectite, often as rims around the existing minerals. This hydration reaction increases the pH and salinity of the pore waters, especially in more restricted systems where the solutes are not carried away. Increased alkalinity and salinity favors the precipitation of zeolites, most commonly clinoptilolite. Zeolite formation removes certain cations from solution, changing the pore water chemistry again. If sufficient heat is present, either by deep burial or the presence of geothermal fluids, dehydration may occur, transforming alkaline zeolites into analcime, and possibly altering smectite into a mixed-layer illite-smectite.

While a general alteration sequence can be described, the environment of deposition, the original composition of the deposit, the temperature of fluids, and the permeability of the rock will dictate the ultimate paragenetic sequence. Tuffs that were deposited in lacustrine environments (Ratterman and Surdam, 1981; Altaner and Grim, 1990; De Pablo-Galan, 1990) had a source of circulating water and, especially in closed lakes, cations to react with the tuffaceous minerals. Available water could increase the rate of hydration and the production of zeolites. Altaner and Grim (1990) determined that where saline water was not available, only clay minerals formed, with no zeolites.

Altaner and Grim (1990) also noted the significance of the original composition of the tuff to its alteration products. Bentonite units formed from dacitic ash deposits, whereas clinoptilolite zeolites formed from more rhyolitic, siliceous ash. De Pablo-Galan (1990) found that an originally rhyodacitic deposit altered to a glassy tuff where it was deposited on dry land, and to a bentonitic unit where it was deposited in water. Dacitic ash deposited in water altered to massive bentonite beds (Altaner and Grim, 1990), whereas dacitic ash deposited on land was leached into a noncrystalline aluminosiicate material (De Pablo-Galan, 1990).

The presence of high-temperature fluids may allow alteration to proceed to a greater extent, according to the work of Moncure et al. (1981), Tsolis-Katagas and Katagas (1989), Bish (1989) and Altaner and Grim (1990), resulting in the formation of analcime. However, a lack of analcime, in spite of the presence of geothermal fluids, was attributed to low alkalinity of the pore fluid, based on low pHs measured in the geothermal waters (Tsolis-Katagas and Katagas, 1989).

Finally, permeability was found to influence the alteration characteristics of tuffaceous rocks. Ahn et al. (1988) noted that clays derived from more permeable volcanigenic sediments were altered to a greater extent than those from low-permeability sediments. Levy and O'Neil (1989) recognized that most of the zeolitized units at Yucca Mountain are generally more permeable, nonwelded tuffs, but they discovered a concentration of hydrous (zeolitic) minerals in the transition zone between the densely welded, devitrified tuff and the underlying vitrophyre, especially associated along the borders of devitrified fractures, where fluids may have been more abundant.

### 2.3.3 ALRS Investigations

Isotopic analyses of $^{14}C$ and $^{3}H$ were performed by Davidson (1995) and Bassett et al. (1994), and contributed to the hydrologic characterization of the Apache Leap Tuff. Hardin (1996) measured porosity, saturation content, and saturated hydraulic conductivities of core from the DSB, which provided information on the physical and hydrologic properties of the tuff. Geochemical investigations using surface water, perched water and pore water from the DSB were made by Davidson (1995), who used the geochemical model NETPATH (Plummer et al., 1991) to model the evolution of the perched zone to evaluate the importance of fracture flow to the hydrologic system. The geophysical analyses by Hardin and Bassett (1995) from both the DSB and the VOB provided further data on the hydrologic and physical systems. The specific contributions of each of these investigations to the characterization of the Apache Leap Tuff, including chemical and geophysical data, are detailed in Section 2.5.

## 2.4 Data Collection Methods

### 2.4.1 DSB and Additional Core Analyses

The DSB was advanced with a surface trace of N55°E, at approximately 45° from the vertical plane. The orientation was chosen to maximize the intersection of the borehole with fractures that dip to the west at approximately 5° from vertical and strike nearly due north (Davidson, 1995). Continuous core was collected from the borehole and preserved for subsequent in situ pore water measurements, as described by Davidson (1995). Total core recovery was 95%. In this investigation, core from the DSB was described and quantified, primarily in terms of fracture abundance, orientation, coating material, and degree of sealing. Other characteristics that were noted include overall apparent degree of alteration, abundance of vugs and slickensides, and approximate degree of pumice flattening. The core was analyzed in 3-m (10-ft) intervals, and the quantities of various features were measured for each interval. In 16 of the 66 intervals that were measured, 75% to 95% of the core was missing, due partly to poor recovery but predominantly to the use of the core by previous workers which destroyed its original properties. 50% of the intervals contained 50% or more of the core for that interval. To account for the missing core, the quantitative results were normalized to the amount of core that was available for observation, which was assumed to be representative of the entire section. Table 1 in Appendix C shows the core available for observation for each interval.

Additional Apache Leap Tuff core available for observation was obtained from the Oak Flats borehole. Also, BHP Copper North America allowed the author to inspect 3-m core sections collected at 30-m intervals through the entire Apache Leap Tuff, from an exploratory vertical borehole (MB-10A) located approximately 1 km from the DSB (Figure 2.1), and drilled through a vertical fault zone. Neither the Oak Flats core nor the

BHP core was described in the same detail as the DSB core; they were used for comparison of select intervals.

### 2.4.2 Thin Section Preparation and Analysis

Thin sections were made from 37 core samples covering the entire length of the DSB core, but concentrated along the lower 30 m. The thin sections included samples from intervals described in the geologic log as "rubble zones", samples through large pumice nodules, and samples from above, below, and within the perched water zone. An additional three thin sections were also made from samples of the basal tuff and basal vitrophyre. The thin sections were photocopied under crossed nichols into 8-1/2 x 11-inch reproductions using the slide copier mechanism of a color photocopier, resulting in an image with magnification approximately 8 times. This process allowed the sections to be compared side-by-side to observe trends or changes along the boring.

Eleven additional thin sections were made by vacuum-impregnating, at a pressure of 1.5 mb, 2.5-cm x 3.5-cm blocks of core with blue-dyed epoxy, prior to cutting the thin sections. This work was performed by National Petrographic Service, Inc. of Houston, Texas. Seven of these sections were made from the DSB core, and four were made from the BHP core at depths below the bottom of the DSB. The blue epoxy enabled pore spaces and fractures to be clearly identified under ordinary transmitted light in thin sections, and on the polished block sections. These thin sections were also photocopied under transmitted light, using the color photocopier technique as above. The color images of the thin sections were then scanned into a computer program which could count the number of pixels that contained the color range of the blue epoxy. The fraction of blue pixels relative to the total number of pixels could then be calculated and taken as a rough measure of the porosity of the thin section. This method provides only a relative measure of porosity, as color reproduction in the scanned image was imperfect and selection of the color range was difficult to make so that similar colors in the rock material would be certain to be excluded.

### 2.4.3 X-Ray Diffraction Analysis

X-Ray powder diffraction (XRD) analyses were performed on 25 core samples ranging over the entire length of the DSB. In addition, clay separation and analyses were performed as described in Starkey et al. (1984) on 10 of those samples from the lowest 27 m of the DSB core, including core from both above and below the apparent saturated zone, as defined by the geologic log. (Core from directly within the saturated zone was reserved for isotopic analysis described in Davidson, 1995). The clay sample analyses included treatment with ethylene glycol and heating to 550°C.

### 2.4.4 Scanning Electron Microscope Analysis

Scanning electron microscope (SEM) analyses were performed on several samples from the DSB, especially in the vicinity of the perched water zone. Images were obtained of some fracture-filling clays and partially dissolved quartz grains, as well as of the more common minerals and textures observed in the tuff.

### 2.4.5 Aquifer Test Performance and Analysis

Both a pumping test and a slug test were performed on the DSB, as described in detail in Chapter 3. The aquifer was pumped for 18.8 hours; the VOB was equipped as an observation well, but no response was ever recorded. A slug of water was added to the

DSB and the response was again observed only in the DSB. The pumping data and the slug test data were analyzed by three different methods each, for comparison purposes, as described in Chapter 3.

## 2.5 Results and Discussion

### 2.5.1 Physical Properties of the Tuff

### *2.5.1.1 Lithology*

A brief description of the entire section of the Apache Leap Tuff, as described by Peterson (1961), was given in Chapter 1 (Section 1.3.2.2), but in this investigation, efforts were focused on the white and gray units. The white unit is a very light, mottled, brownish-pink color, and is speckled with oxidized micas and weathered iron-oxide minerals. The most noticeable macroscopic feature in the white unit is the randomly oriented, relatively equidimensional pumice fragments (Figure 2.2). In contrast, the gray unit is darker, and contains pumice fragments which have been distinctly flattened, imparting a visible fabric to the rock (Figure 2.3). In both units, the pumice fragments are frequently miarolitic, or coarsely crystalline and vuggy. The transition from white to gray units occurs gradually, over approximately 10 m.

The cut surfaces of the DSB core that were vacuum-impregnated with blue epoxy illustrate the macroscopic textural changes that occur in the gray unit with depth to the perched water zone. Figure 2.4a shows the gray unit at a depth of 36 m, and Figure 2.4b is the core at 148 m. The blue color represents epoxy-filled pore spaces. The core at 36 m appears relatively uniformly heterogeneous, with white pumice fragments and some

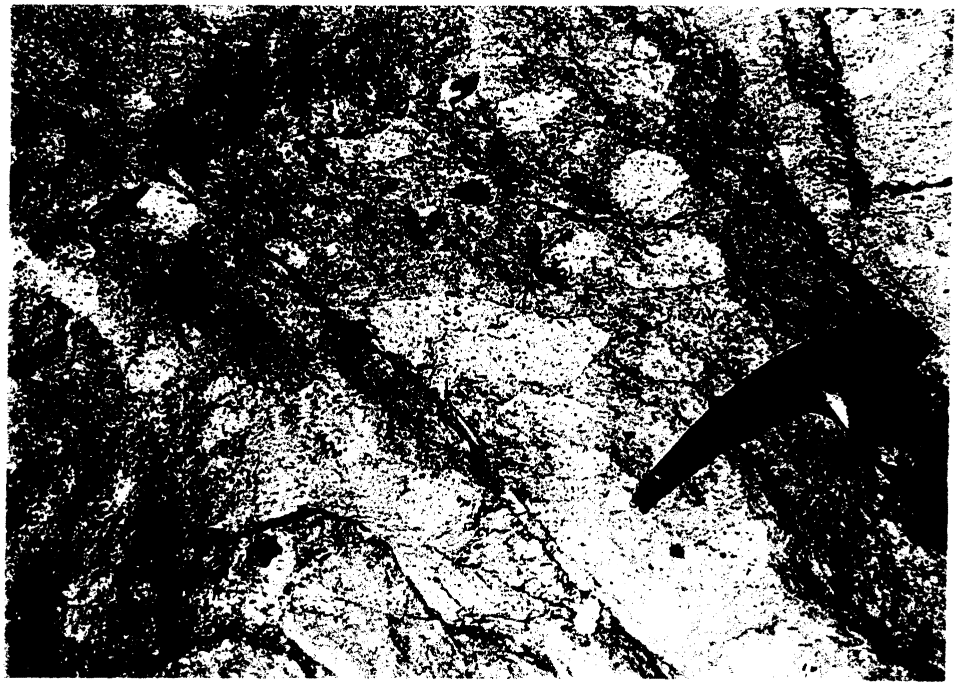

Figure 2.2 Outcrop of white unit at the Apache Leap Research Site

Figure 2.3 Outcrop of the gray unit at the Apache Leap Research Site

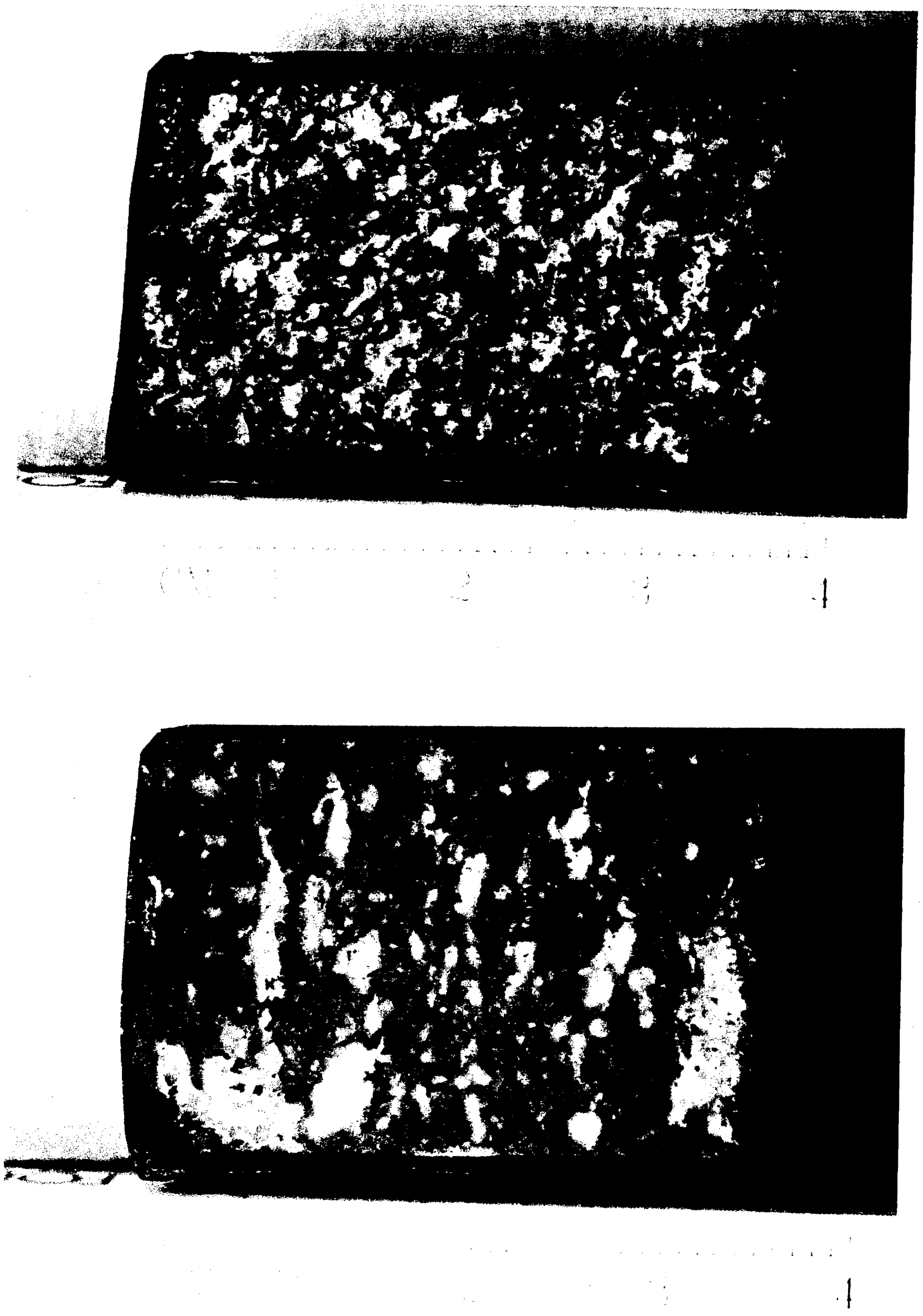

Figure 2.4 Epoxy-impregnated cut sections of DSB core from (top) 36 m with top of core to the upper-left corner, and (bottom) 148 m with top of core to the left side

larger clear-white quartz and gray feldspar grains scattered randomly throughout the pinkish-brown matrix. A faint linearity is seen running diagonally from the lower left to upper right sides of the photograph. The porosity occurs in regions generally associated with the pumice fragments, but is scattered throughout the rock. In contrast, the core from 148 m shows much more discrete regions of white pumice and comparatively pumice-free matrix-plus-phenocrysts; the orientation has become more distinct, with the top at the left side of the photograph. Porosity is significantly reduced, and is only observed in a few of the larger pumice fragments. Compaction during cooling is likely to have caused the reduction in porosity that is seen, as supported by the work of Ragan and Sheridan (1972), who determined that the dominant mechanism for producing the alignment of textural components seen in welded tuffs of Bishop, California was compaction. Furthermore, Smith (1960) stated that the transition towards increasingly more complete welding is primarily due to compaction, and consists of a progressive loss of pore space.

#### *2.5.1.2 Petrography*

Much of the petrography of the white and gray units has been affected by the processes of devitrification and vapor phase crystallization. Devitrification is described by Ross and Smith (1961) as a replacement of the original glass shards by a cryptocrystalline intergrowth of, usually, cristobalite and feldspar. The new minerals form within the boundaries of the glass shards or massive glass. Vapor phase crystallization, in contrast, is the formation of crystals, often of tridymite and feldspar, in open spaces under the influence of a vapor phase, and consequently the crystals tend to be larger. According to

Ross and Smith (1961) devitrification is more likely to occur in regions of densely packed glass shards or completely compacted pumice fragments; ion diffusion occurs over short distances, but vapor-phase transfer does not occur, even though the glass may contain volatiles in solution. Where pumice fragments have not completely collapsed, or vesicles remain, vapor-phase transfer of materials occurs and the crystals fill in the pore spaces. Ross and Smith (1961) noted that more rarely, biotite, amphiboles, and zeolites may also form from vapor-phase crystallization. Both devitrification and vapor phase crystallization can obscure primary textures such as degree of welding, which is typically determined according to the degree of compaction and deformation of the glass shard components; if the glass has been devitrified, classification of degree of welding becomes difficult.

The partial degree of welding in the white zone could only be inferred by Peterson (1961), because devitrification and vapor-phase crystallization have essentially obliterated all of the original groundmass texture. Peterson (1961) determined that the induration of the white zone was likely to be more the result of vapor-phase crystallization rather than significant welding, considering that compaction, which is a primary cause of welding, would be minimal at the top of the deposit. According to Peterson (1961), relict textural features such as pumice fragments can occasionally be seen in this zone, however in this investigation, the white unit was not extensively studied and no such textures were observed.

The degree of welding in the gray zone is also indistinct, primarily because of devitrification. However, Peterson (1961) determined that the lower part of the gray unit is likely to be densely welded, based on the degree of compaction of the pumice fragments

Ross and Smith (1961) devitrification is more likely to occur in regions of densely packed glass shards or completely compacted pumice fragments; ion diffusion occurs over short distances, but vapor-phase transfer does not occur, even though the glass may contain volatiles in solution. Where pumice fragments have not completely collapsed, or vesicles remain, vapor-phase transfer of materials occurs and the crystals fill in the pore spaces. Ross and Smith (1961) noted that more rarely, biotite, amphiboles, and zeolites may also form from vapor-phase crystallization. Both devitrification and vapor phase crystallization can obscure primary textures such as degree of welding, which is typically determined according to the degree of compaction and deformation of the glass shard components; if the glass has been devitrified, classification of degree of welding becomes difficult.

The partial degree of welding in the white zone could only be inferred by Peterson (1961), because devitrification and vapor-phase crystallization have essentially obliterated all of the original groundmass texture. Peterson (1961) determined that the induration of the white zone was likely to be more the result of vapor-phase crystallization rather than significant welding, considering that compaction, which is a primary cause of welding, would be minimal at the top of the deposit. According to Peterson (1961), relict textural features such as pumice fragments can occasionally be seen in this zone, however in this investigation, the white unit was not extensively studied and no such textures were observed.

The degree of welding in the gray zone is also indistinct, primarily because of devitrification. However, Peterson (1961) determined that the lower part of the gray unit is likely to be densely welded, based on the degree of compaction of the pumice fragments and its location within the thick single cooling zone; the degree of welding decreases upwards. Evidence of vapor phase crystallization can be found in the upper part of the gray unit, especially in the form of zeolites, which were identified as being particularly abundant in the sample from 79 m depth, and appear to be filling in existing cavities (Figure 2.5). Thin sections from the gray zone show streaky, discontinuous bands of alternating dusty-brown and light-colored matrix that appear to flow around the phenocrysts in what is called eutaxitic texture, the result of nearly complete deformation of the shards (Figure 2.6). Occasional pumice fragments can also be found that show remnants of their original "woody" texture (Figure 2.7), but have been stretched and are now incorporated into the eutaxitic texture. In some locations, devitrified glass shards were observed, in which a fine-grained intergrowth of cristobalite and sanidine feldspar appeared in an axiolitic (radial) pattern. Photographs of representative thin sections from the entire depth of the DSB, as well as from the basal tuff and basal vitrophyre, are included in Appendix A.

#### *2.5.1.3 Mineralogy*

An extensive mineralogical investigation of the entire thickness of the Apache Leap Tuff was made by Peterson (1961). Table 2.1 shows the results of his whole-rock chemical analyses of different sections of the tuff. Peterson noted remarkable consistency in the nature, distribution, and appearance of the phenocrysts throughout most of the unit. The phenocrysts generally comprise 35-45% of the rock, with plagioclase the most abundant, followed by quartz, biotite, sanidine, and magnetite (Table 2.2). Small amounts of hornblende are present in some areas, as are sphene, apatite, and zircon. The relative

Figure 2.5 Zeolite filling cavity at 79 m vertical depth from the DSB core (photographed in plane-polarized light at 40X magnification).

Figure 2.6 Eutaxitic texture observed at a vertical depth of 151 m in the DSB core (photographed in plane-polarized light at 5X magnification).

Figure 2.7 Remnants of a pumice fragment seen at a vertical depth of 156 m in the DSB core (photographed in plane-polarized light at 10X magnification).

| | **Basal Tuff** | **Vitrophyre** | **Brown Unit** | **Gray Unit** | **White Unit** |
|---|---|---|---|---|---|
| $SiO_2$ | 66.4 | 67.8 | 67.7 | 68.0 | 68.7 |
| $Al_2O_3$ | 14.4 | 15.3 | 16.3 | 16.5 | 16.7 |
| $Fe_2O_3$ | 2.1 | 2.1 | 2.5 | 2.6 | 2.7 |
| FeO | 0.34 | 0.77 | 0.13 | 0.12 | 0.1 |
| MgO | 0.80 | 0.72 | 0.76 | 0.52 | 0.38 |
| CaO | 2.3 | 2.3 | 2.5 | 2.4 | 2.2 |
| $Na_2O$ | 1.8 | 4.0 | 4.1 | 4.2 | 4.2 |
| $K_2O$ | 4.3 | 3.6 | 3.6 | 3.5 | 3.6 |
| $H_2O^-$ | 7.1 | 2.3 | 1.8 | 1.8 | 1.4 |
| $H_2O^+$ | na | na | na | na | na |
| $TiO_2$ | 0.41 | 0.46 | 0.43 | 0.40 | 0.40 |
| $CO_2$ | 0.05 | 0.05 | 0.05 | 0.05 | 0.50 |
| $P_2O_5$ | 0.10 | 0.14 | 0.16 | 0.14 | 0.15 |
| MnO | 0.09 | 0.09 | 0.08 | 0.08 | 0.08 |
| TOTAL | 100.2 | 99.6 | 100.1 | 100.3 | 101.1 |

Table 2.1 Whole-rock chemical analysis of specimens from each subunit of the Apache Leap Tuff (after Peterson, 1961, as presented in Bassett et al., 1994). Concentration units in mg/L; n a= not analyzed.

abundances of each kind of phenocrysts vary only slightly between locations, and the pumice fragments also contain a similar assemblage of phenocrysts in approximately the same proportion (Peterson, 1961). The phenocrysts typically average between 0.5 and 1 mm in diameter. The relatively high proportion of phenocrysts (greater than 25%) places the unit into Roberts and Peterson's (1961) category of a welded crystal tuff, as opposed to a welded ash tuff. According to Roberts and Peterson (1961), this type of tuff results

| | Basal Tuff | Vitrophyre | Brown Unit | Gray Unit | White Unit |
|---|---|---|---|---|---|
| % total phenocrysts | 36.5 | 38.8 | 36.8 | 42.7 | 41.0 |
| % phenocryst composition | | | | | |
| plagioclase | 73.9 | 71.2 | 73.7 | 71.4 | 67.1 |
| sanidine | 2.4 | 2.1 | 2.2 | 3.5 | 7.0 |
| quartz | 8.9 | 9.2 | 9.9 | 11.9 | 14.1 |
| biotite | 8.7 | 10.4 | 8.9 | 9.0 | 6.2 |
| magnetite | 3.0 | 3.4 | 4.3 | 2.9 | 3.4 |
| hornblende | 2.5 | 3.4 | 0.9 | 0.7 | 1.8 |
| TOTAL (%) | 99.4 | 99.7 | 99.9 | 99.4 | 99.6 |

Table 2.2 Mineralogical composition of phenocrysts of subunits of the Apache Leap Tuff (after Peterson, 1961, and Bassett et al., 1994).

from a long period of crystallization in the magma chamber prior to eruption, and a moderate volatile content in the eruption, resulting in less fragmentation of the material as it erupted, thereby forming relatively larger particles.

Lithic fragments are also present in the tuff, and on average comprise 2 to 4% of the rock volume (Peterson, 1961). Most fragments in the white and gray units range from 0.5 to 2 cm across, although occasionally fragments up to 6 cm were observed during the analysis of the DSB core. The inclusions are dominantly rhyolite, probably derived from earlier rocks; diabase, quartzite, limestone, and granitic rocks were also identified.

The white unit contains a cryptocrystalline groundmass of scattered spherulites and masses of randomly crystallized material (Figure 2.8). According to the XRD analyses performed by Peterson (1961) and verified by analyses performed as part of this

Figure 2.8 Cryptocrystalline groundmass of the white unit, from vertical depth of 24 m in the DSB core (photographed under plane-polarized light at 5X magnification).

investigation (Appendix B), the composition of the groundmass is mostly cristobalite and sanidine feldspar. Occasionally, cristobalite, quartz, and rarely tridymite crystals are large enough to be identified under the microscope (Peterson, 1961). Pumice fragments were difficult to distinguish from the rest of the matrix in the sections observed in this study, but could sometimes be discerned by their lack of brownish, hematitic (Peterson, (1961), Anderson, (1969)) dust coloration that is present in much of the matrix.

The gray zone has a cryptocrystalline groundmass composed primarily of cristobalite and K-feldspar (most likely sanidine), with lesser amounts of quartz and plagioclase, according to Peterson's (1961) XRD analyses and confirmed by the analyses of this investigation (Appendix B). The matrix was observed in this analysis to be nearly opaque in many locations, due to a high hematitic dust content.

#### *2.5.1.4 Fracture Characteristics*

The results of the fracture quantification of the DSB core are shown in Figure 2.9; additional logging information is contained in Appendix C. The figure shows a clear trend of increasing fracture abundance with depth (shown as length along the borehole), including an increase in the number of filled and sealed fractures, and of slickensides. This trend is attributed to the fact that a fault zone was probably intersected by the boring in the region from 174 to 180 m along the DSB (135-139 m vertically) : high fracture density, poor core recovery, abundant slickensides, and the geophysical response (Hardin and Bassett, 1995) all suggest the presence of a fault. A 40-cm thick interval at about 154 m depth, below the perched water zone, was observed to appear much less altered and fractured than any of the core above it. The cut outer surface of the core was smoother

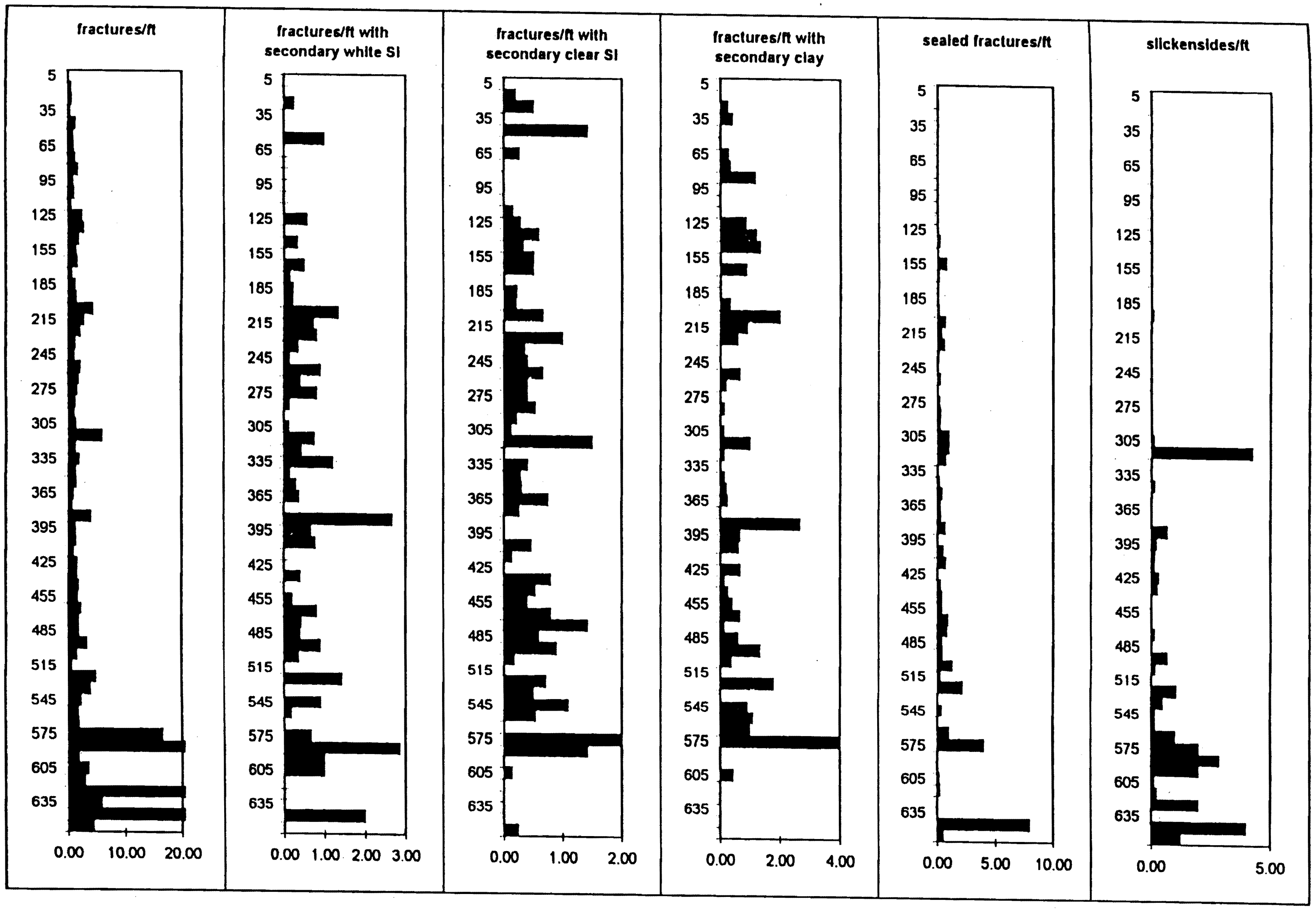

Figure 2.9 Quantification of fracture characteristics in the DSB core (note: units in feet along length of DSB)

and less pitted than elsewhere; the field notes indicated that "progress [was] extremely slow" through this interval, and that the drill bit became worn smooth and required replacement sooner than anticipated. The characteristics of the core below this interval were more typical of the unfaulted portions of the gray unit above.

Core samples were only saved in 3-m sections at 30-m intervals from the BHP core MB-10A, so the data were not continuous. However, an increase in fracture abundance to about the 200-m interval (650-660 ft) was observed based on the intervals available for inspection (Figure 2.10). The 200-m interval appeared highly altered as well as highly fractured; much fluid loss occurred in this region during drilling (BHP, personal communication). Below this interval, the core became much less fractured, and fractures were more often sealed with silica minerals. At 290 m, the core became densely welded with a few thin sealed fractures, and overall was quite massive. The BHP log of this borehole, with additional notes by the author, is included in Appendix D.

The Oak Flats core log (Sample Management Facility, 1990) indicated that mineralization occurred on roughly one-half of the moderate- to high-angle fractures. Iron oxides and clays were observed from the surface down to about 183 m; silica minerals in the fractures were most abundant in the intervals 122-128 m and 360-372 m, calcite appeared sporadically in the interval 381-442 m, and zeolites were tentatively identified in the upper 30 m and from 510 to 522 m. Four highly fractured zones were noted in the upper 172 m; two fracture zones were noted from 367 to 428 m, and a partially vitric zone was noted at 416-437 m. Characteristics of the Oak Flats core based on the Sample Management Facility (1990) drilling log are illustrated in Figure 2.11. Hardin (1996)

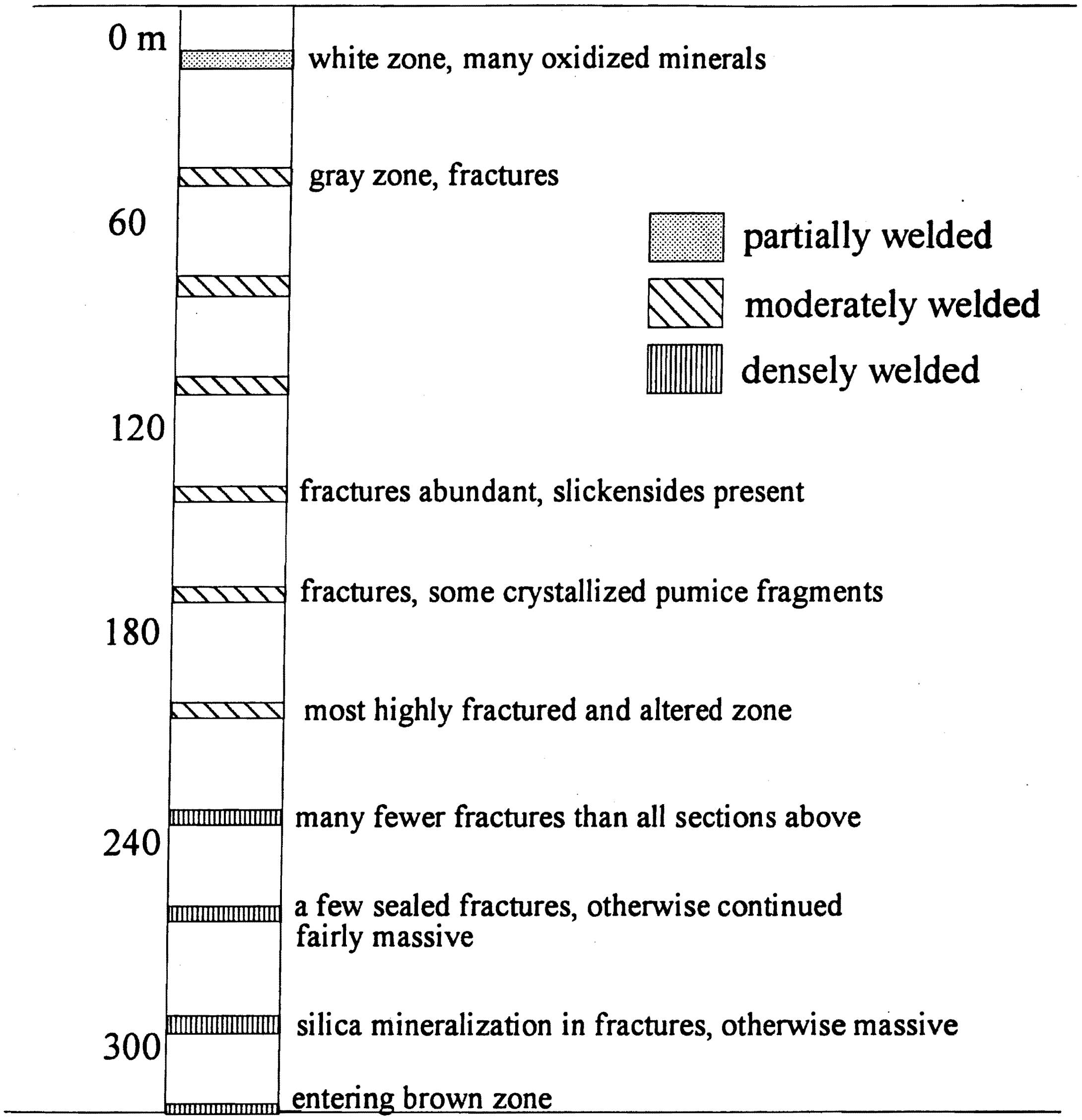

Figure 2.10 Schematic diagram of the characteristics of the MB-10A core, based on BHP drilling log (Appendix D) and observations of 3-m sections.

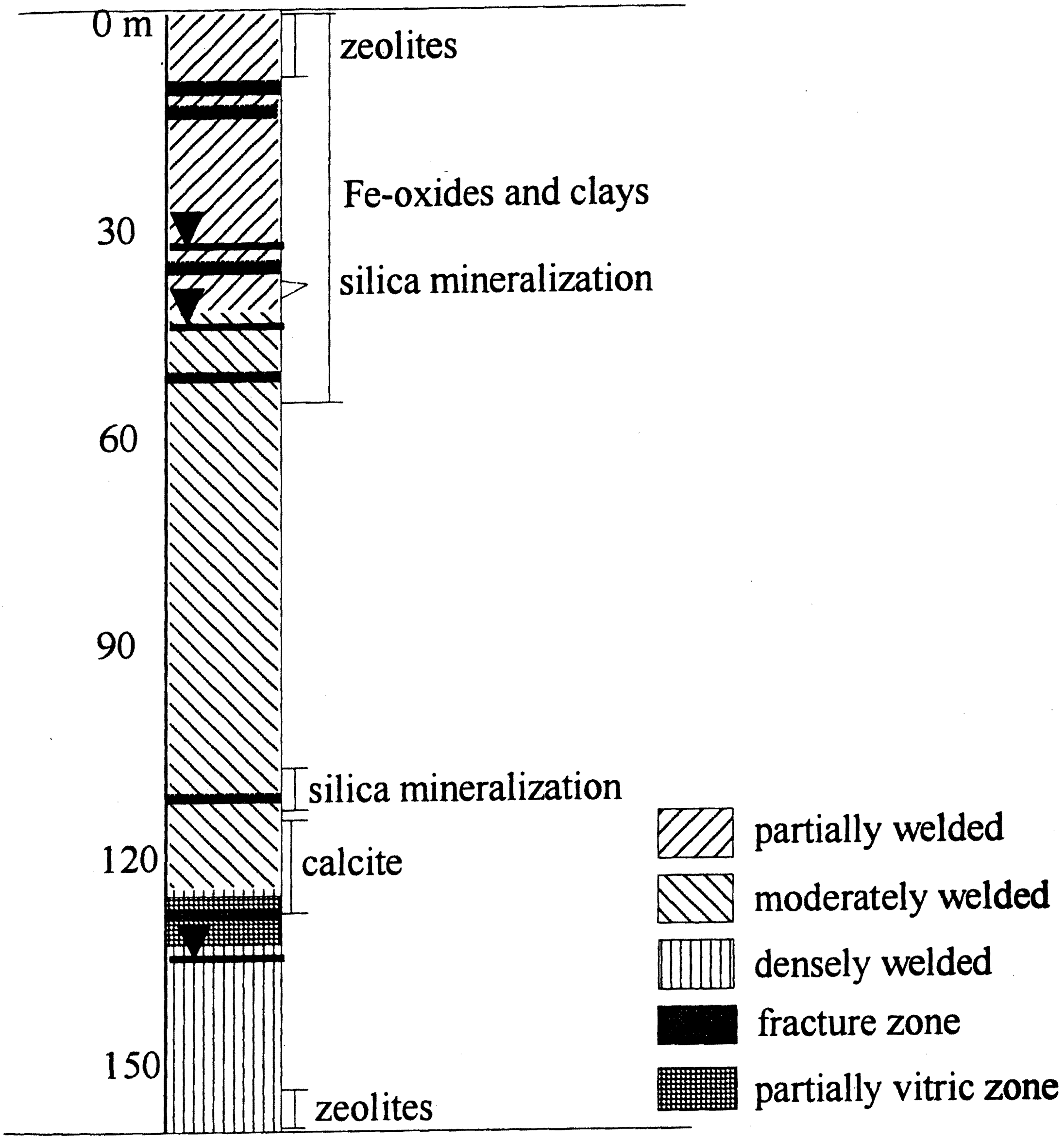

Figure 2.11 Schematic diagram of the characteristics of the Oak Flats core, based on drilling log from Sample Management Facility (1990).

inspected portions of the Oak Flats core and noted many fractures in the lower part of the gray unit that appeared to be extensively sealed with a silica precipitate.

### *2.5.1.5 Alteration Characteristics*

The most striking macroscopic alteration feature of the Apache Leap Tuff is the white, devitrified pumice fragments (Figure 2.3). Welding and compaction *without* devitrification would cause the pumice fragments to darken and, under strongly welded conditions, to become glassy and obsidian-like (Ross and Smith, 1961). The pumice fragments would create a dark, streaky foliation in contrast to the lighter matrix of crystals. However, according to Smith (1960), in a very thick (he estimated greater than 600 m) deposit, welding would occur extremely rapidly, and, if the flow was even moderately gas-rich, gas would be entrapped throughout much of the deposit. Pumice fragments typically act as loci for the entrapped gas under such conditions. Crystallization of these pumice fragments creates a streaky, *light*-colored foliation, with a miarolitic texture. Smith (1960) used the Rhyolite Canyon Formation of Chiricahua National Monument originally described by Enlows (1955) as an example of this type of texture. The photographs of the Rhyolite Canyon Formation in Smith (1960), look remarkably similar to the Apache Leap Tuff.

On the microscopic scale, while nearly all of the matrix has been devitrified, the biotite grains were noted by Peterson (1961) to be the only phenocrysts to exhibit significant alteration, aside from fracturing; he noted that the degree of alteration in the biotite increases upwards from the gray zone into the white zone, where grains become distorted and frayed at the edges, and contain chlorite and inclusions of oxides. Hardin

(1996) noted significant oxidation effects on magnetite and ilmenite in the upper 20 m of the tuff, as reflected in dramatically (> 30 times) reduced magnetic susceptibilities of those minerals in that zone, compared to deeper regions. In this study, most of the phenocrysts were observed to have broken faces, and many are fractured, but those features are evidence of the pyroclastic deposition of the rock, rather than alteration.

The XRD analysis of the clay fraction of the tuff indicated that smectite is present in some quantity through the perched zone, and is the primary component of the clay fraction (Table 2.3). A small quantity of unspecified feldspar, and traces of biotite, kaolinite, and quartz were also identified in the clay-size fraction. The size of the XRD

| depth | smectite | mica | kaolinite | quartz | feldspar |
|---|---|---|---|---|---|
| 140.2 | 5[a] | 1 | 1 | 1 | 2 |
| 141.8 | 4-5 | 1 | 1 | 1 | 2 |
| 143.7 | 4-5 | 1 | 1 | 1 | 2 |
| 144.7 | 4-5 | 1 | 1 | 1 | 1 |
| 145.4 | 4-5 | 1 | 1 | 1 | 2 |
| 146.3 | 4-5 | 1 | 1 | 1 | 2 |
| 153.3 | 5 | 1 | 1 | 1 | 2 |
| 154.0 | 5 | 1 | 1 | 1 | 2 |
| 154.4 | 4-5 | 1 | 1 | 1 | 2-3 |
| 154.5 | 5 | 1 | 1 | 1 | 2 |

[a] 5=dominant, 4=large quantity, 3=moderate quantity, 2=small quantity, 1=trace.

Table 2.3 Results of XRD analysis of clay-sized fraction (< 2μm) separated from tuff samples.

clay minerals do not change significantly with depth. Clay was observed to be somewhat more abundant in samples from fractured or faulted zones which were more prevalent deeper in the section, however. When observed in thin section, smectite most typically filled small fractures through grains and occasionally continuing into the matrix, and rarely, lined more significant fractures, such as the one shown in Figure 2.12 from a depth of 138 m. With the SEM, smectite was observed in some regions between grains (Figure 2.13 from 148 m), but overall, it was not abundant. The smectite is likely to be a product of the dissolution and devitrification of the glass rather than weathering of feldspar phenocrysts, as the feldspar grains show minimal evidence of chemical alteration.

Thin fractures completely filled with silica minerals, most likely cristobalite, were observed in many samples from the gray unit, and were most abundant towards the bottom of the DSB (Figure 2.14 from 143 m depth). Larger fractures filled with silica were observed at a depth of 290 m in the core from MB-10a (Figure 2.15); in addition, Hardin (1996) noted many sub-vertical fractures in the lower part of the gray unit in the Oak Flats core to be extensively sealed with silica mineralization. Wise et al. (1973) determined from their SEM investigation of altered rhyolitic tuff that the dissolution of volcanic glass resulted in a reprecipitation reaction forming smectite and cristobalite; they therefore concluded that excess silica must be produced from the devitrification of the tuff; this silica would be available to fill fractures. In addition to excess silica production from the devitrification process, chemical weathering of the silica-rich tuff would also produce fluids with high silica concentrations.

When all of the alteration characteristics are considered together, the Apache Leap

Figure 2.12 Clay-lined fracture from a vertical depth of 138 m, DSB core (photographed under crossed nichols at 10X magnification)

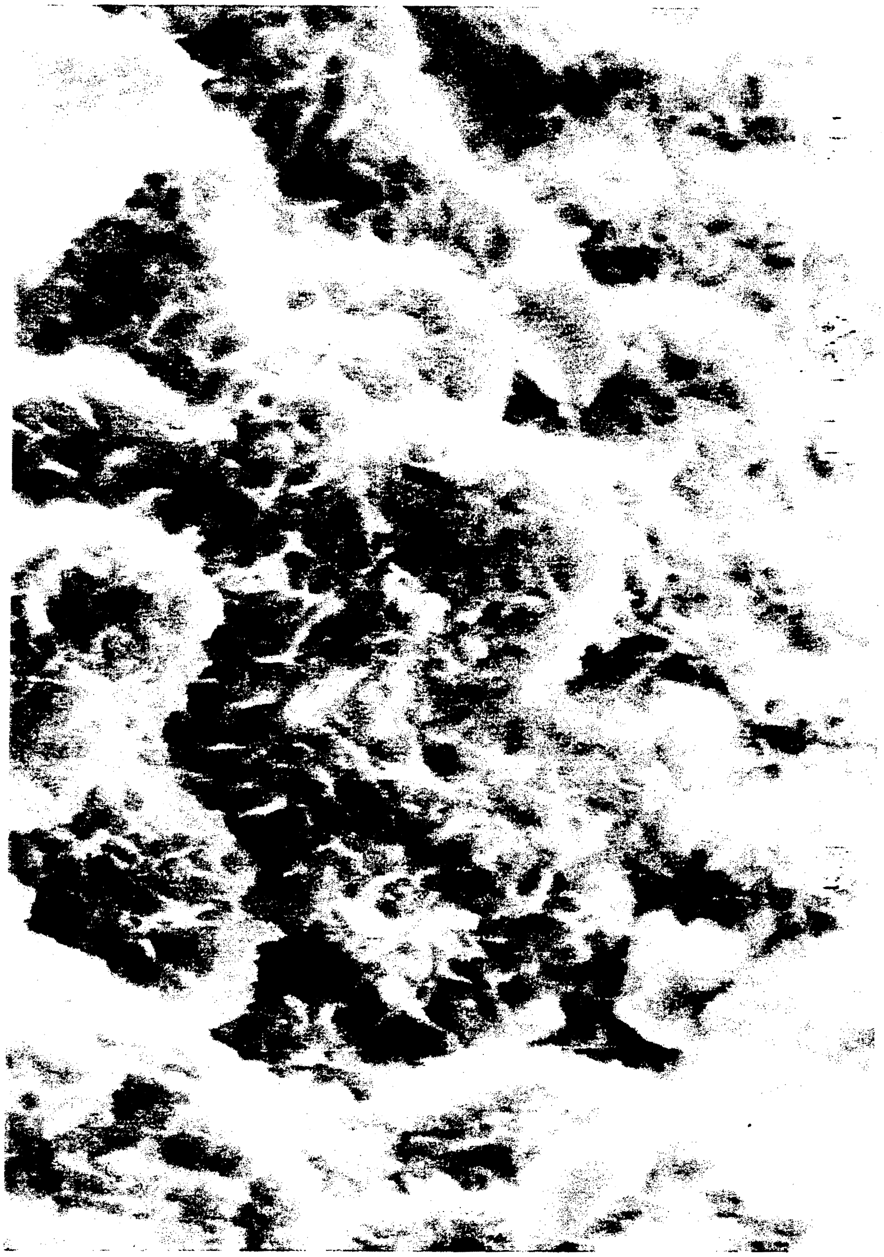

Figure 2.13 Scanning Electron Microscope image of smectite clays at 148 m vertical depth, DSB core (photographed at 2.5Kx magnification).

Figure 2.14 Silica-mineralized fractures at a vertical depth of 143 m, DSB core (photographed under crossed nichols at 10X magnification).

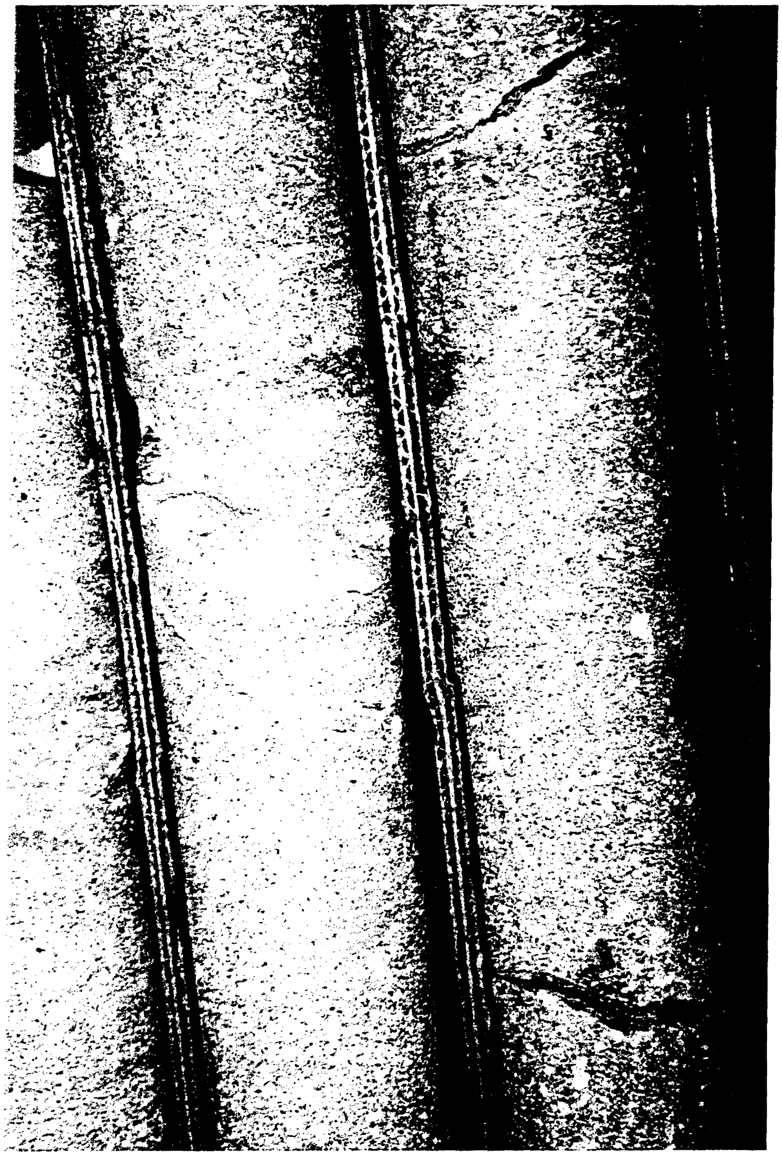

Figure 2.15 Silica-filled fractures from a depth of 290 m in core from MB-10a.

Tuff in the vicinity of the perched water zone appears to have been most altered by the processes of devitrification and vapor phase crystallization. The original composition and depositional environment of the tuff was similar to the dacite La Zorra Formation studied by De Pablo-Galan (1990), and, not surprisingly, the cryptocrystalline devitrified groundmass of the Apache Leap Tuff observed by SEM appears quite similar to that described and photographed by De Pablo-Galan. If the Apache Leap Tuff followed "typical" alteration patterns, smectite should have been found concentrated as rims around altered glass shards or phenocrysts. Instead, smectite was only rarely observed to form such rims, and more typically, it filled in microfractures or lined small pore spaces. This observation suggests that devitrification may have occurred rapidly, reducing the permeability of the matrix to the extent that hydrating waters were not able to effectively penetrate the matrix. Tsolis-Katagas and Katagas (1989) described a phenomenon in which the formation of early authigenic silicates sealed the open spaces and fractures in Santorini Volcanics, greatly reducing the movement of water and vapor in the system and limiting the amount of alteration that could occur. The silicate-sealed fractures observed in the deeper portions of the Apache Leap Tuff could be evidence of a similar process. Without a significant source of salts, clinoptilolite production would be predicted to be minimal (Altaner and Grim, 1990), and, in fact, in the section of the Apache Leap Tuff studied in greatest detail, zeolites (tentatively identified as clinoptilolite) were present only as isolated products of vapor-phase crystallization, rather than as smectite alteration products. To summarize, the alteration of the Apache Leap Tuff in the region of the perched water zone appears to have been primarily controlled by its original composition and depositional environment, its thickness, and its low permeability.

A description of the paragenetic sequence of the Apache Leap Tuff summarizes the various types of alteration that have impacted the deposit. Starting with an originally undulating terrestrial surface, the approximately several tens of individual, silica-rich flows were deposited in rapid succession over the existing topography. These flows cooled as a single unit over a long time, due to the extreme thickness of the deposit. During this long cooling process, devitrification and vapor phase crystallization occurred along with welding, reducing the matrix permeability significantly. Cooling fractures, as well as tectonically-induced fractures formed at this time also, and tectonic fractures continued to develop after cooling was complete, during periods of regional uplift. The fractures allowed access of meteoric waters into the tuff during and following cooling. This water reacted with the tuff, becoming silica-saturated, and subsequently completely filling much of the deeper fractures. At present, meteoric waters continue to move into the tuff through the fractures.

#### *2.5.1.6 Porosity/Permeability Characterization*

Hardin (1996) measured matrix hydraulic conductivity at discrete intervals along the DSB. His results (Table 2.4) show that matrix hydraulic conductivity declines sharply with depth to values as low as 0.001 mm/yr in the region of the perched water zone. Below a depth of 20 to 30 m from the surface, hydraulic conductivity drops from on the order of 10 to 140 mm/yr down to 2 mm/yr or less, suggesting that below this depth, recharge must move primarily through fractures, as the matrix is virtually impermeable.

Hardin and Bassett (1995) measured bulk density, volumetric moisture content,

| depth (m) | no. samples | $K_{sat}$ (mm/yr) | depth (m) | no. samples | $K_{sat}$ (mm/yr) |
|---|---|---|---|---|---|
| 5.32 | 4 | 28.3 | 63.4 | 5 | 0.15 |
| 9.8 | 7 | 135.3 | 116.7 | 5 | 0.09 |
| 12.5 | 2 | 124.0 | 148.7 | 1 | 0.006 |
| 16.7 | 4 | 9.3 | 149.2 | 1 | 0.001 |
| 33.0 | 5 | 2.0 | | | |

Table 2.4. Average matrix saturated hydraulic conductivity values obtained by Hardin (1996) from DSB core.

porosity, and apparent saturation of sections of core from the DSB. Their results are shown in Figures 2.16-2.18. The trend of the wet bulk density values reflects the transition between the less densely welded, upper white unit, and the lower gray unit. Values for the white unit ranged from 2.2 to 2.4 g/cm$^3$ with depth, whereas the gray unit was a more consistent 2.4 to 2.5 g/cm$^3$. Volumetric moisture content measurements showed an increased moisture content in the upper 61 m of the section, which would correspond to higher porosity. Deeper in the section, below 91 m, the scatter of the data increases, suggesting a change in formation conditions (Hardin and Bassett, 1995). Porosity and apparent initial saturation measurements were made for the gray unit only; the porosity of that unit varies from 5 to 8%, and nearly all the core had an initial saturation of at least 80%, with some sections appearing to be completely saturated.

The blue-dyed thin sections make visible the changes in porosity with depth. Figure 2.19 shows the white zone at a depth of 23 m. Pore spaces are shown scattered thoroughly throughout the matrix, implying considerable connectivity between them. In the section from 36 m, from the upper part of the gray zone, the pattern of porosity has

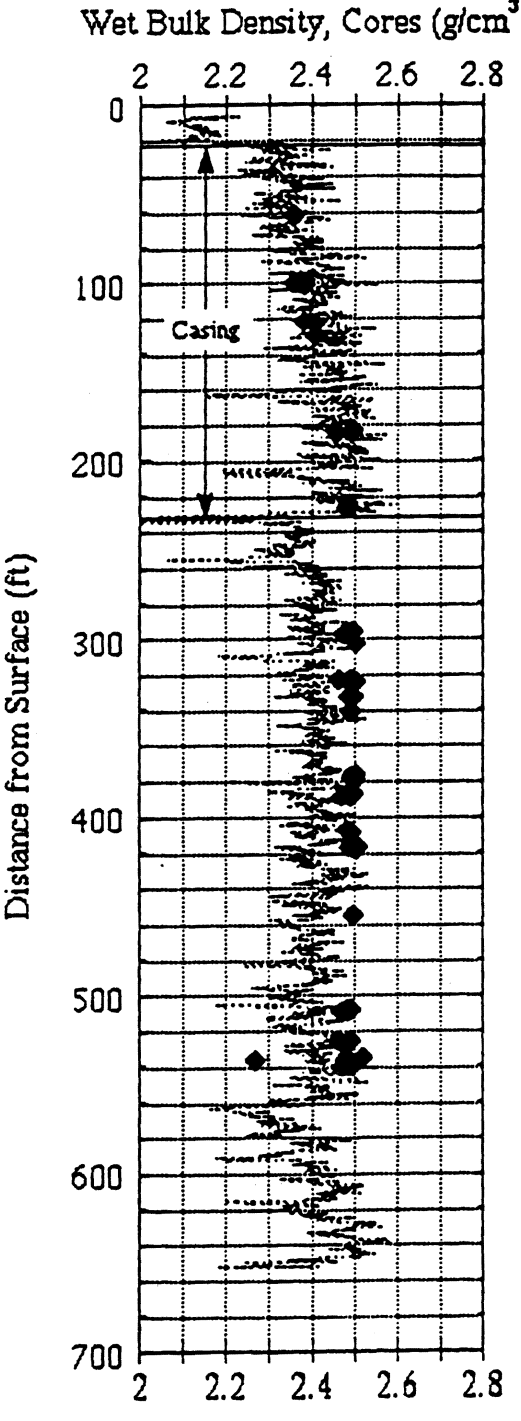

Figure 2.16 Density log and wet bulk density for selected **samples from the DSB core,** from Hardin, 1996 (note vertical axis is depth in units of feet).

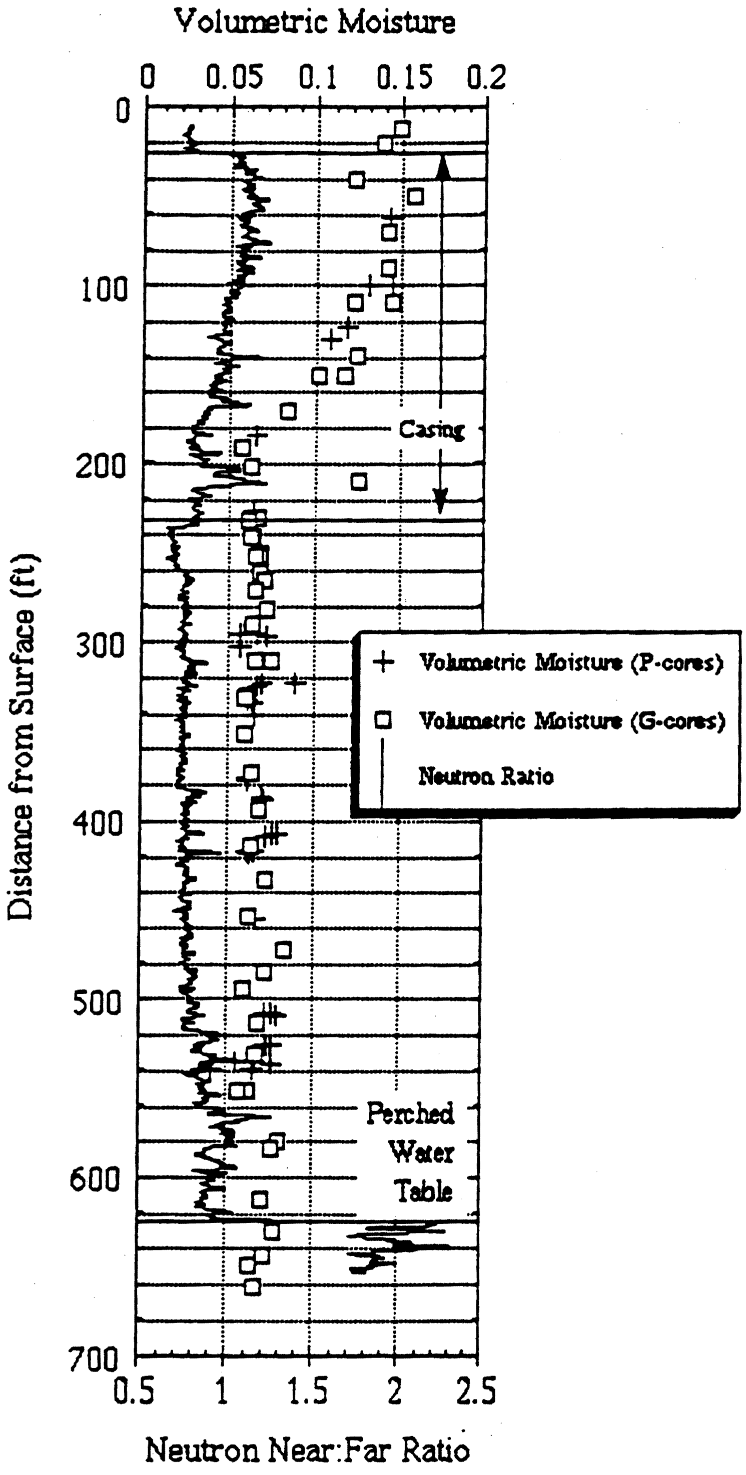

Figure 2.17 Volumetric moisture content for selected samples from the DSB core, plotted with the uncalibrated near:far neutron count ratio log, from Hardin, 1996 (note vertical axis is depth in units of feet).

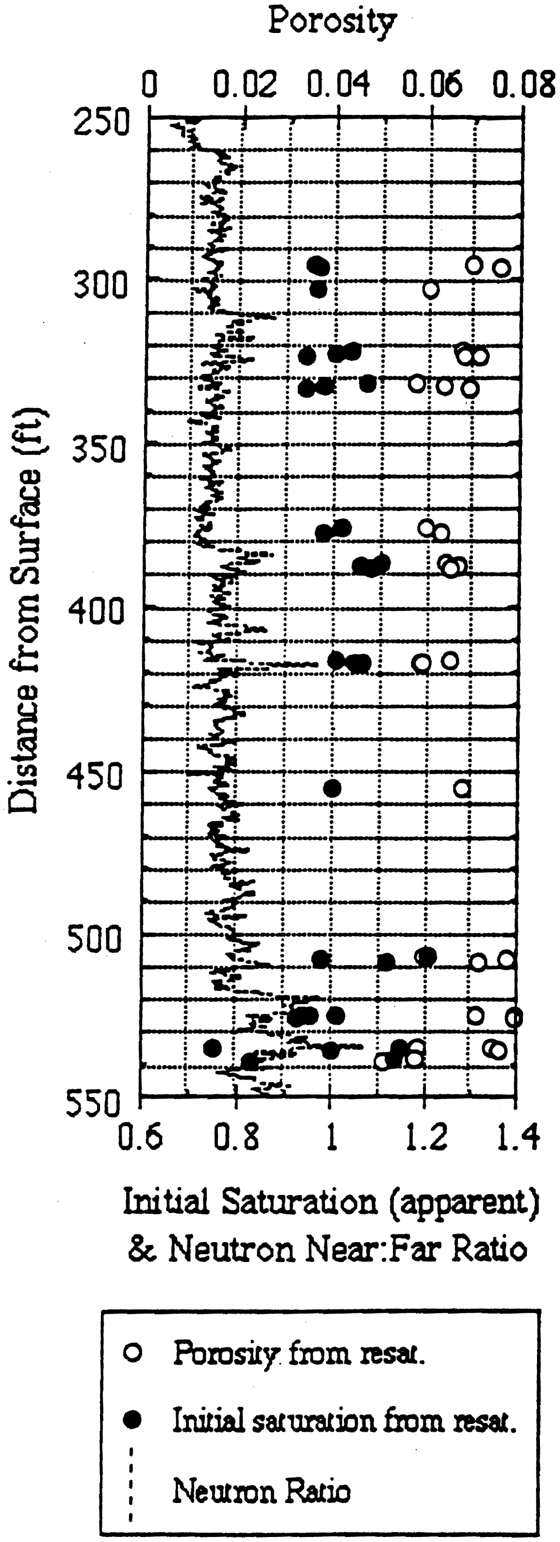

Figure 2.18 Porosity and apparent saturation of selected samples of DSB core, plotted with the neutron log, from Hardin, 1996 (note vertical axis is depth in units of feet).

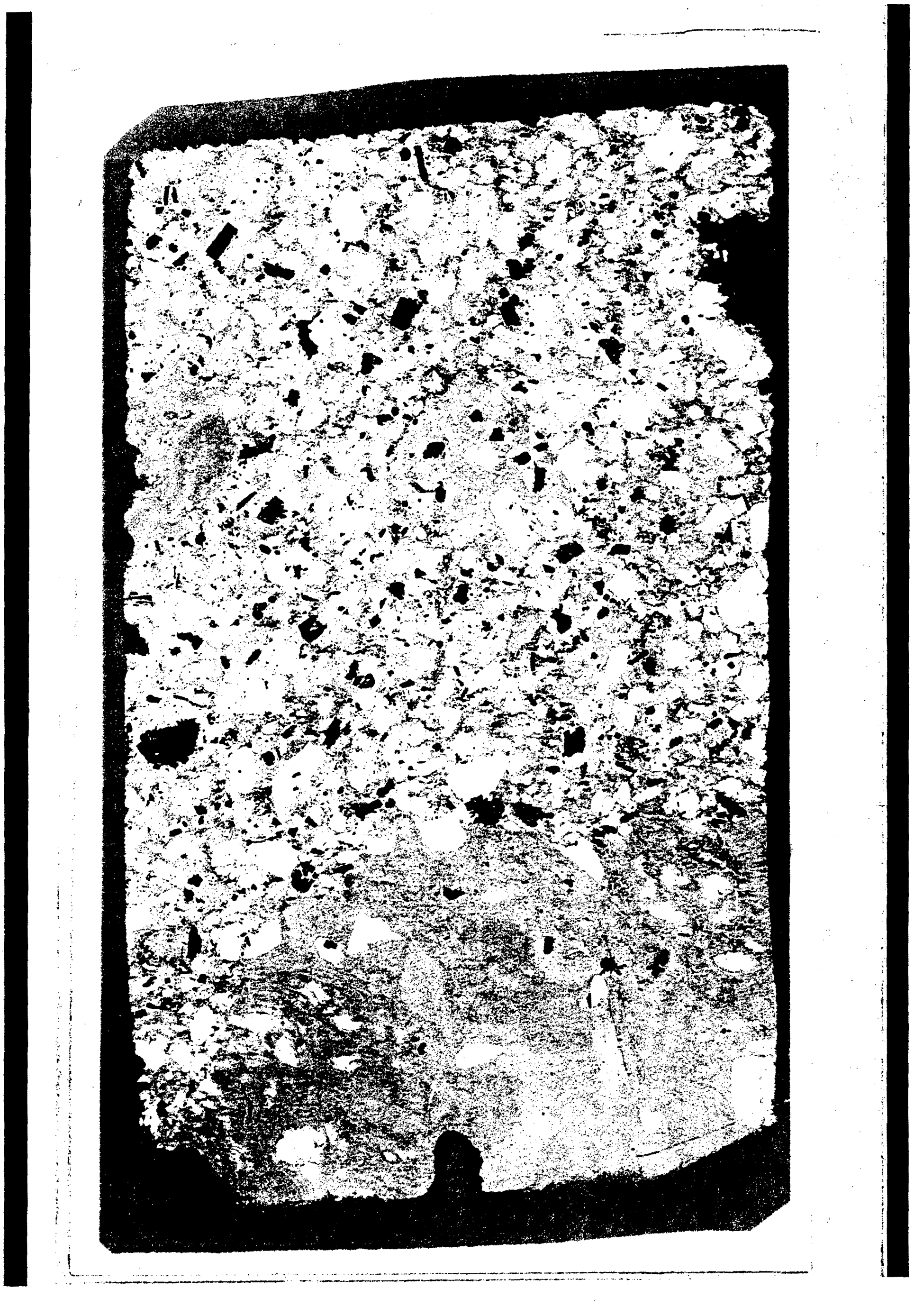

Figure 2.19 Epoxy-impregnated thin section from 23 m vertical depth, DSB core (magnification 4.4X)

changed considerably (Figure 2.20). Porosity is concentrated primarily in small but discrete regions generally associated with pumice fragments; it also is observed in small fractures in the phenocrysts. Small, isolated regions showing no apparent porosity are observed at this depth. In Figure 2.21, from a depth of 142 m, the major porosity regions correlate with the location of pumice fragments, and the matrix shows a developed eutaxitic texture indicative of compression having nearly eliminated pore spaces in those regions. At 148 m depth, in the perched water zone, Figure 2.22 shows even further reduction in the porosity and large impermeable regions. The pumice-related porosity zones correlate to the thin white regions shown in the macroscopic view of this core in Figure 2.4b.

The pixel scan of these thin sections indicated a 36% reduction in porosity between the white unit and the upper gray unit sections (from 8.8% to 3.2%). Further reductions occurred in the gray unit: the pixel-calculated porosity at 142 m was 2.5%, and at the perched water zone it was 1.1%, for an overall reduction through the gray unit of 34%. As discussed previously, this method did not produce actual porosity measurements, but does provide information regarding relative change in porosity through the section.

### 2.5.2 Hydrologic Properties of the Tuff

#### *2.5.2.1 Isotopic Analysis*

Davidson (1995) compared $^{14}$C activities from water sampled directly from the perched aquifer, and from pore waters from core within that saturated zone, and concluded that perhaps as much as half of the water in the aquifer beneath the DSB may

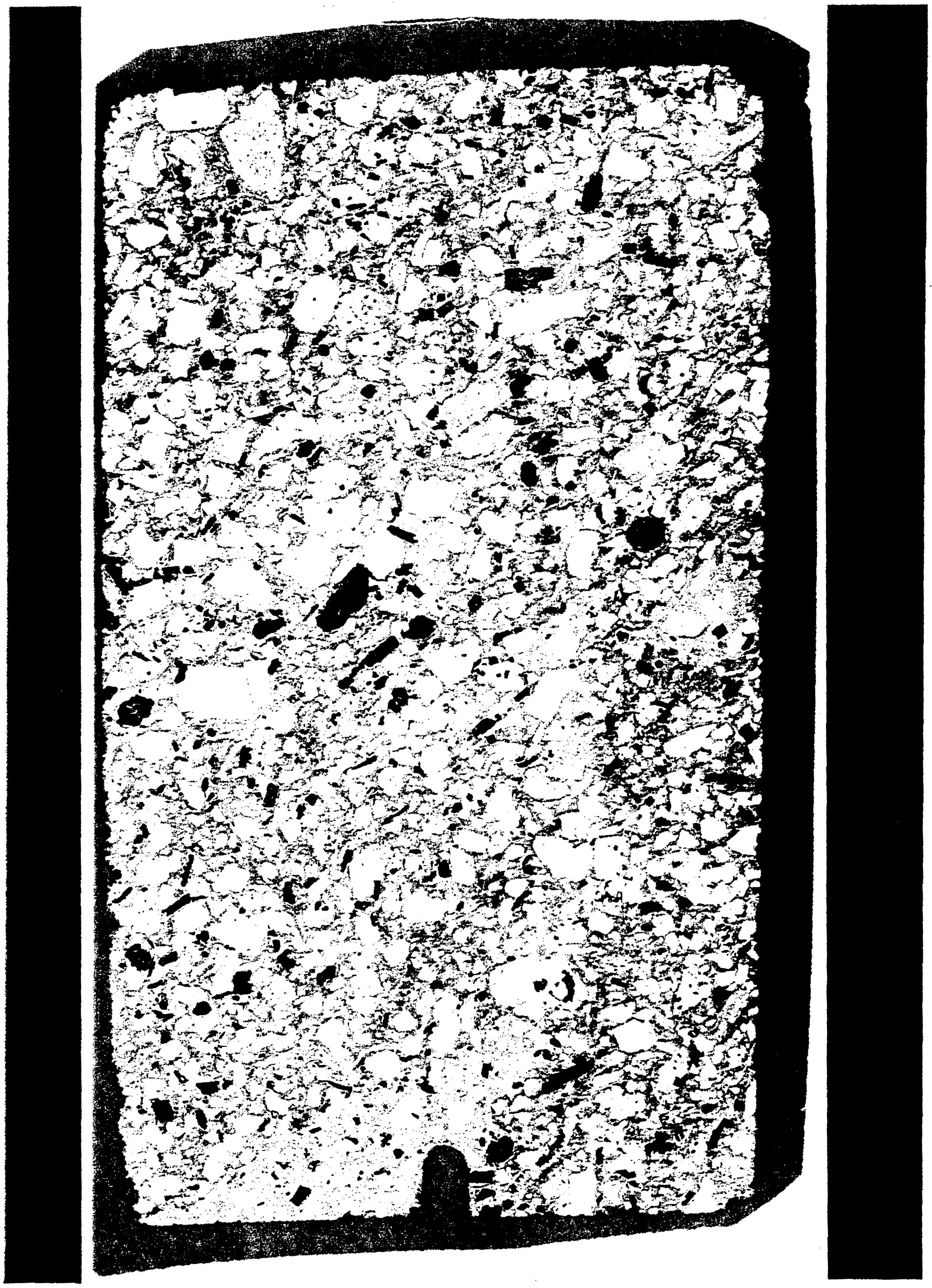

Figure 2.20 Epoxy-impregnated thin section from 36 m vertical depth, DSB core (magnification 4.4X)

Figure 2.21 Epoxy-impregnated thin section from 142 m vertical depth, DSB core (magnification 4.4X).

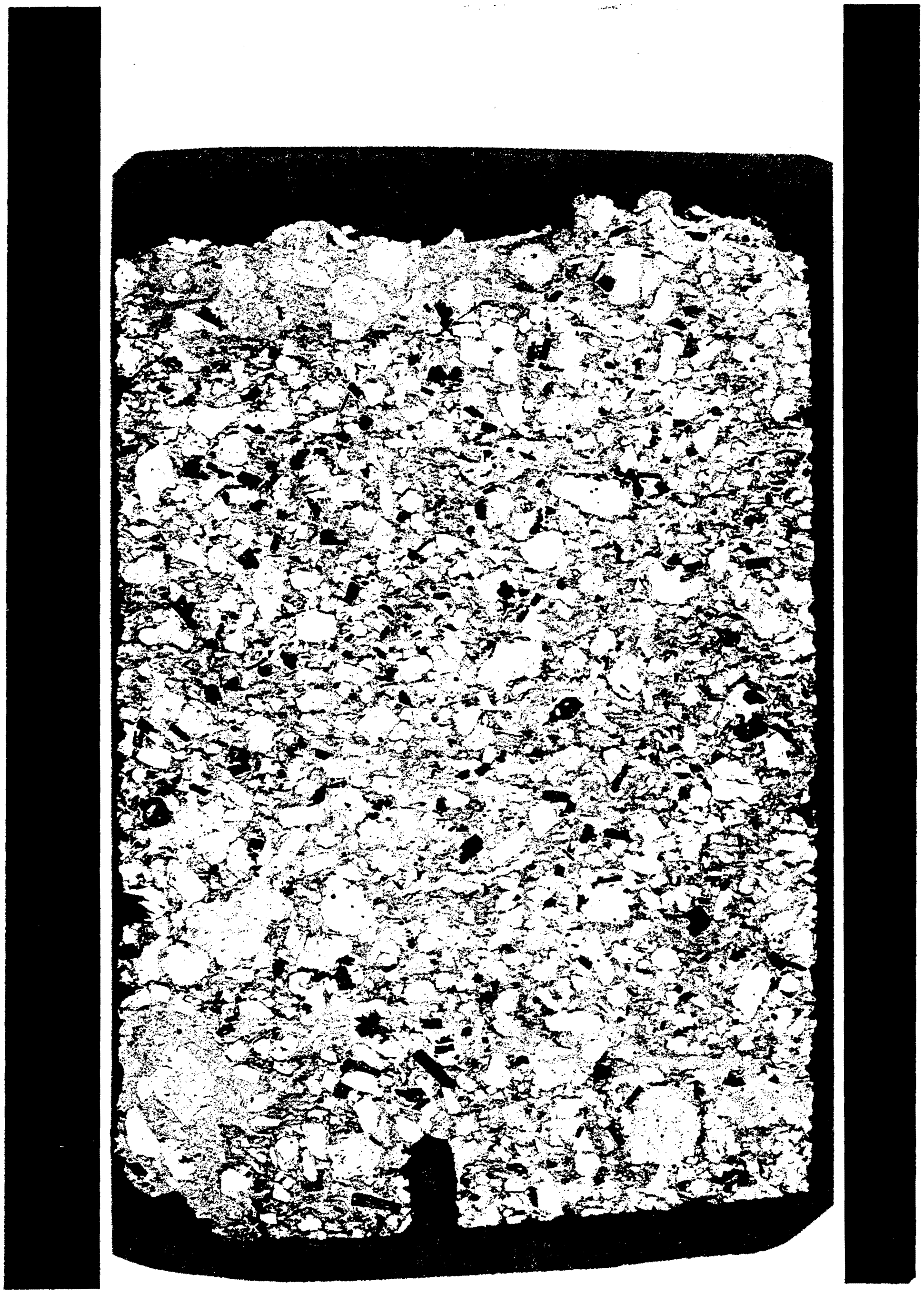

Figure 2.22 Epoxy-impregnated thin section from 148 m vertical depth, DSB core (magnification 4.4X).

be derived from nearby fractures. He found that the $^{14}C$ activity of the pore water was much higher than from the aquifer, and proposed that water from fractures may enter a mixing zone, resulting in a localized region of higher $^{14}C$ activity, whereas the pumped perched zone water represents more of an average over a larger area. $^{14}C$ activities obtained from pore water within the saturated zone and from within 5 m above it are quite similar, suggesting the perched water zone may have been higher in the past.

Davidson's (1995) isotopic work also suggested that the primary source of pore water in the matrix is imbibition from fractures. The fractures flow only ephemerally, but near-saturation of the rock matrix adjacent to flowing fractures suggests that imbibition may be limited in those fractures, such that water is forced to flow deeper through fractures until it encounters less saturated matrix. Thus, water entering the matrix from a fracture is mixed with water from previous flows.

#### *2.5.2.2 Geochemical Analysis*

Davidson (1995) used geochemical data from surface water runoff and DSB pore waters, combined with additional analyses in Bassett et al. (1994), to model the perched aquifer water. Table 2.5 shows the chemical composition of pore water from the saturated zone, and average chemical compositions of pumped perched water and surface water that were used for the modeling. The solutions from several NETPATH models indicate that the aquifer water is composed dominantly of surface water runoff, with only a small (less than 2%) contribution of pore water that has reacted with the rock matrix (Table 2.6). The model results suggest that older aquifer water moving into the mixing zone beneath the DSB is largely derived from fracture recharge.

| | pore water from 152.8 m | pumped perched water | surface water |
|---|---|---|---|
| pH | 7.5 | 7.3 | 5.9 |
| $HCO_3^-$ | 121.5 | 120.9 | 2.8 |
| $SO_4^{-2}$ | 34.1 | 1.9 | 18.0 |
| $NO_3^{-2}$ | 23.5 | 1.1 | BD |
| $PO_4^{-3}$ | <0.5 | BD | BD |
| $Cl^-$ | 46.0 | 4.2 | 2.3 |
| $Na^+$ | 47.7 | 21.9 | 3.7 |
| $K^+$ | 18.0 | 0.9 | 1.3 |
| $Ca^{+2}$ | 35.9 | 20.2 | 5.0 |
| $Mg^{+2}$ | 7.1 | 3.7 | 1.4 |
| $SiO_2$ | 43.0 | 53.0 | 32.3 |
| TDS | 377 | 228 | 67 |

Table 2.5 Chemical composition of pore water from the saturated zone, pumped perched water (average of 3 samples), and surface water (average of 6 samples). Concentrations are in mg/L; BD = below detection limit. (Reproduced from Davidson, 1995).

### *2.5.2.3 Geophysical Analysis*

Hardin and Bassett (1995) collected nuclear, electrical induction, and borehole television logs from the DSB and electrical induction logs from the VOB. Figure 2.23 shows neutron, density, and resistivity logs from the DSB, which show distinct responses at small features which are likely to be high-moisture fractures. Many of these features could be correlated to fractures observed on the borehole television log. The broadness of some of the peaks suggests the movement of water in the fractures, and the correlation of moisture conditions in the rock matrix to fracture flow (Hardin and Bassett, 1995).

The resistivity logs show a trend of decreasing resistivity with depth in the DSB.

| | | | |
|---|---|---|---|
| avg. surface runoff | 98.2% | 98.2% | 98.1% |
| pore water from 15.6 m | 1.8% | 1.8% | 1.8% |
| evaporate | 1.45x | 1.45x | 1.43x |
| plagioclase ($An_{32}$) | +0.975 | +0.975 | +0.889 |
| biotite | +0.532 | +0.044 | |
| hornblende | | | +0.029 |
| $CO_2$ | +1.881 | +1.881 | +1.880 |
| chlorite | -0.260 | | |
| smectite | | -0.207 | -0.073 |
| illite | -0.927 | | |
| $SiO_2$ | | -1.737 | -2.076 |

Table 2.6 Example NETPATH (Plummer et al., 1991) solutions for the geochemical evolution of perched aquifer water beginning with average surface runoff and a pore water from 15.6 m. Positive and negative signs indicate mmol/L dissolved or precipitated, respectively (reproduced from Davidson, 1995).

This trend was attributed to increasing moisture content, as it corresponded to a similar trend on the neutron log (Hardin and Bassett, 1995). However, measurements of DSB core porosity, saturation, and pore fluid resistivity combined could not account for the observed range of resistivity; Hardin and Bassett proposed that a lithology change, such as secondary mineralization, could be responsible for the lower resistivity in the deeper portion of the borehole. The borehole television video did appear to show greater alteration in that section; furthermore, core recovery was significantly reduced over the interval. A similar resistivity response was not observed in the VOB (Figure 2.24); while the resistivity did show a gradually decreasing trend with depth, the magnitude was not as great as in the DSB, suggesting an absence of apparent secondary alteration. Hardin and

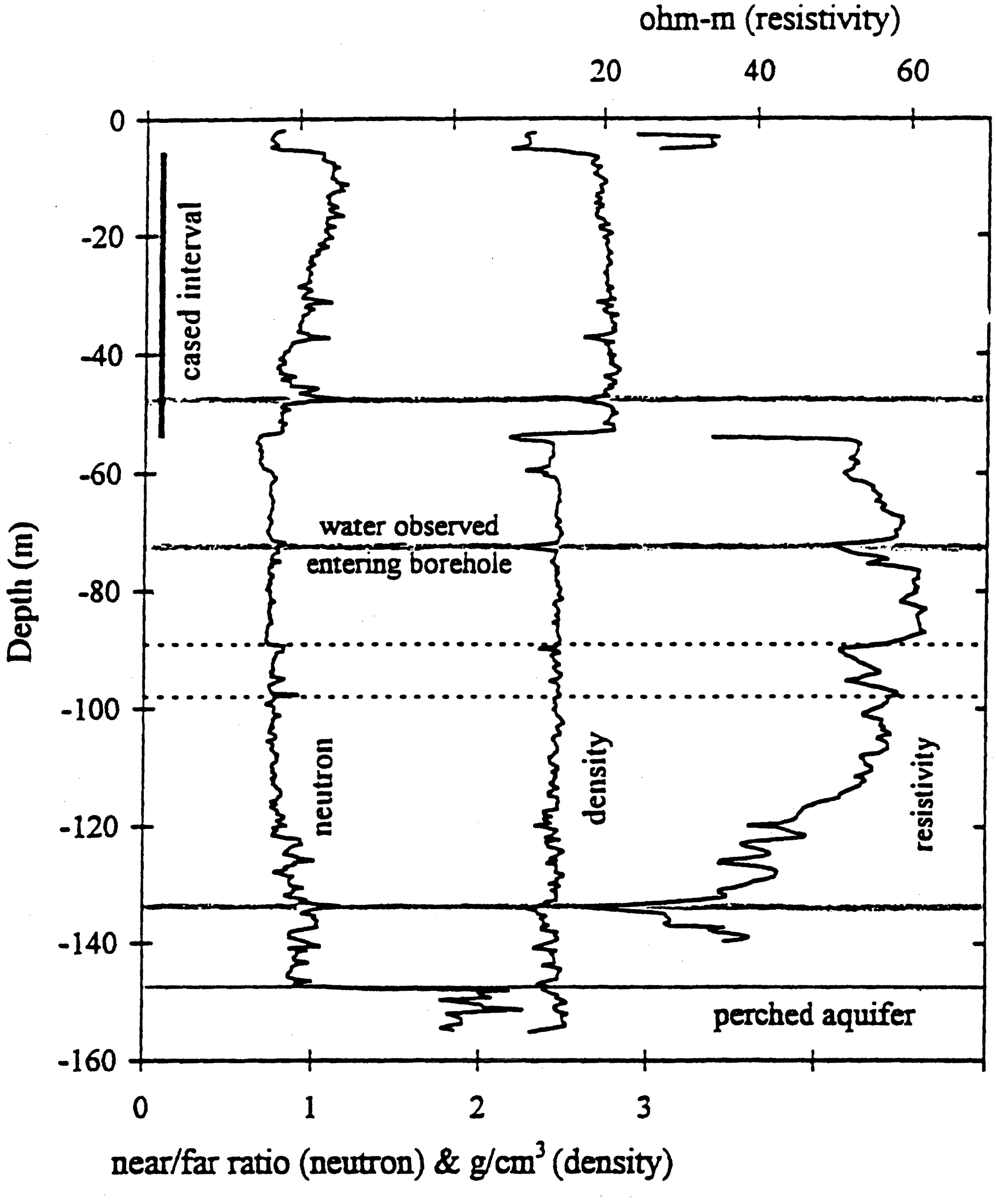

Figure 2.23 Neutron, density, and resistivity logs from the DSB. Horizontal lines drawn where water-bearing fractures were suspected based on video and geophysical logs; dashed lines drawn in regions of moisture indicated by geophysical evidence (geophysical data from Hardin and Bassett, 1995, as presented in Davidson, 1995)

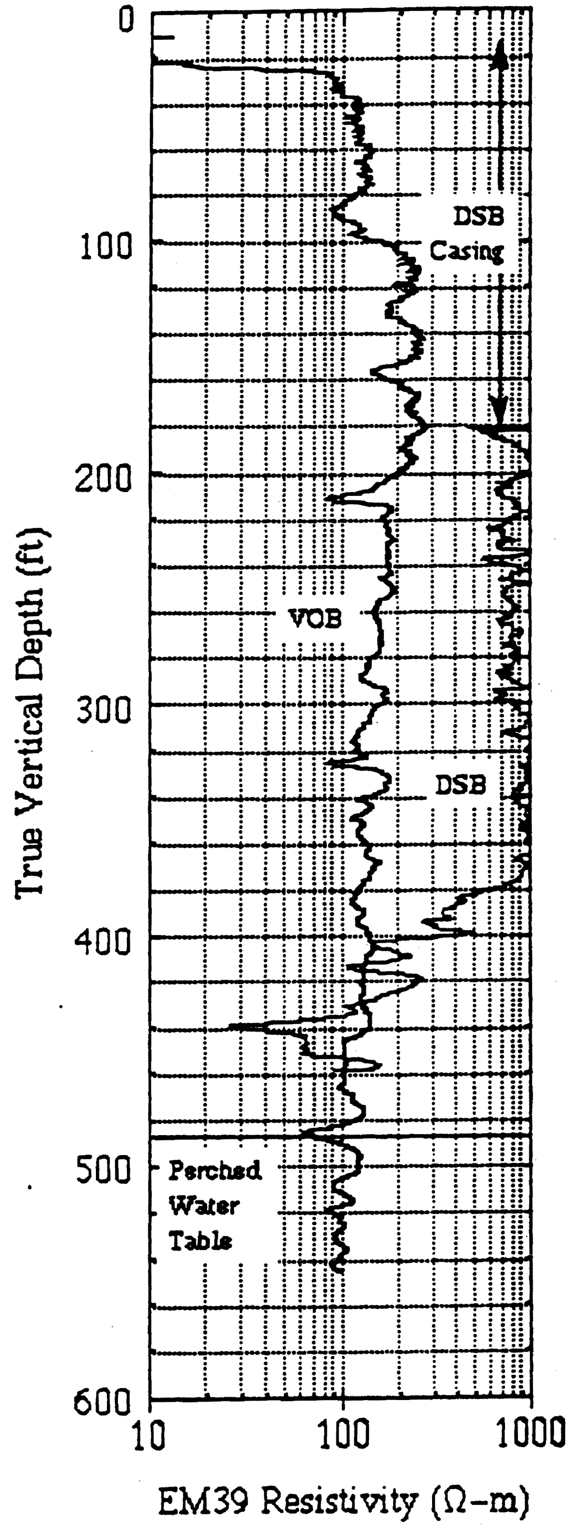

Figure 2.24 Comparison of resistivity logs for the VOB and the DSB, from Hardin 1996 (note vertical axis is depth in units of feet).

Bassett (1995) proposed that the DSB may intersect a discontinuous structural feature, such as a fault or major fracture zone above the perched water zone, that the VOB did not.

In 1995, COLOG logged sections of the VOB using their Borehole Image Processing System (BIPS). This system produces an image of the borehole that is similar to a video image, but enables identifications to be made of specific fracture locations and orientations in the borehole. The VOB was logged over the depth intervals of 21 m to 34 m, 55 m to 91 m, and 140 m to 166 m (approximately 5 m above the bottom of the borehole), at which point the water became too cloudy with suspended particles to permit further imaging. The borehole contains about 21 m of standing water; in the portion of the deepest interval that was logged, twelve distinct fractures were observed. In the uppermost logged section, a distinct fracture was observed at 30 m.

#### *2.5.2.4 Aquifer Test Analysis*

The results of the analyses of the aquifer and slug tests are discussed in detail in Chapter 3; the conclusions are summarized here briefly. The results show that the Apache Leap perched aquifer is more accurately portrayed by a discrete fracture model than by a dual porosity system, which indicates that the matrix hydraulic conductivity is so much less than the fracture hydraulic conductivity that it is insignificant to the system. The fracture hydraulic conductivity was calculated to be nine orders of magnitude greater than the matrix hydraulic conductivity as measured by Hardin (1996). These results indicate that the ALRS perched aquifer system is fracture-dominated.

## 2.6 Conclusions

The upper 200 m of the Apache Leap Tuff at the ALRS is characterized as a densely to partially welded tuff that has been substantially altered by devitrification and vapor phase crystallization. Both the white and gray units are distinguished in outcrop by distinctive, light-colored pumice fragments which become progressively flattened with depth. In thin section, the degree of welding has been nearly obliterated by alteration processes, resulting in a eutaxitic, flowing-type texture, especially prevalent near the bottom of the section that was studied. Phenocrysts comprise 35-34% of the rock and are dominantly plagioclase, with lesser amounts of quartz, biotite, sanidine, and magnetite. Lithic fragments comprise about 2-4% of the rock, and pumice fragments comprise roughly 25% of the rock and contain approximately the same proportion and type of phenocrysts as the matrix. The matrix consists predominantly of cryptocrystalline cristobalite and feldspar, although some pumice fragments have been filled by vapor phase crystallization and may contain tridymite or zeolites.

The 200-m section that was studied is cut by many high-angle fractures, as well as by fractures parallel to the depositional surface of the rock. Fractures appear to become more abundant towards the bottom of the section, but the presence of a fault near the bottom of the borehole may influence those results. Below the 200 m depth, fractures appear to become both rarer and more frequently filled by silica mineralization.

The primary alteration feature is the devitrified matrix and pumice fragments. Below the white zone, the phenocrysts do not exhibit evidence of secondary alteration. Smectite is present in relatively small amounts throughout the interval, frequently filling microfractures in phenocrysts or lining small pores. Silica minerals completely fill small fractures seen near the bottom of the study section, and may be byproducts of the devitrification process.

The porosity of the rock appears to be strongly correlated to the pumice fragments. With depth, the pumice fragments become increasingly more flattened, and more isolated from the rest of the groundmass. Blue epoxy-impregnated thin sections clearly illustrate that porosity is associated with these pumice fragments, and therefore also decreases with depth and becomes less connected.

Analyses of the hydrologic properties of the tuff indicate that fracture flow is the dominant mechanism for water to move through the tuff, especially below about 30 m, when matrix hydraulic conductivity becomes extremely low. Geochemical and isotopic investigations support a relatively direct transport of surface waters down to the perched aquifer; fractures identified by various geophysical methods correlate to locations of excess moisture and flowing water.

# CHAPTER 3
# AQUIFER TESTS AND ANALYSES

## 3.1 Hypothesis

As discussed in the preceding chapter, isotopic, geochemical, and geophysical data collected by Davidson (1995), Hardin and Bassett (1995), and Bassett et al. (1994) support fracture flow as the dominant mechanism for recharge to the perched zone. Therefore, the goal of this portion of the investigation was to test the aquifer to determine that the response of a well in the Apache Leap Tuff to pumping is also characteristic of a fracture flow-dominated system. Furthermore, measurements of aquifer parameters such as transmissivity and hydraulic conductivity should reflect fracture flow, and be much higher than comparable measurements made on unfractured core segments (such as by Hardin, 1996).

## 3.2 Methods

### 3.2.1 Borehole Drilling and Development

In December 1994, the vertical observation borehole (VOB) was advanced using an air-rotary drilling method. The total depth of the borehole is 170.7 m. Static water level has been fairly constant (within a few centimeters) since the borehole was drilled, at about 149 m below the surface, 21.7 m above the bottom of the hole. Because of the drilling method, in which air was forced into the borehole under high pressure, reliable first recordings of perched water could not be obtained; however drilling notes record an observation of moisture in the cuttings at 20 m from the surface, and more substantial wetness at 158 m, 164 m, and 168 m. At 170 m, the cuttings had dried out, and the drilling ceased shortly thereafter. While no standing water was observed in the hole at the cessation of drilling, within 18 hours, the water had risen to 148 m below the surface. The borehole was not developed.

In September 1995, COLOG logged two sections of the VOB using their Borehole Image Processing System (BIPS). The product of this work shows specific locations and orientations of fractures in the vertical borehole (Figure 3.1) which are likely to be major pathways for water traveling to the perched zone. In the interval from 157-165.7 m, twelve individual fractures intersecting the borehole were identified. In addition, a 7-m thick zone of water containing abundant suspended clay-sized material, too opaque to penetrate with the BIPS, was seen at the bottom of the hole.

Transport of various equipment into and out of the hole revealed that a considerable amount of rock dust may have been pushed into the fractures and formation. The dust turned into mud and ran down the borehole wall when the fractures flowed. This observation, combined with the identification of the high suspended-load zone identified by the BIPS, lead to efforts to develop the well. First, the well was bailed several times to remove as much material as possible. In addition, the well was pumped at the maximum capacity of the pump, to complete drawdown, more than one dozen times, with complete recovery between times. The water noticeably cleared up during these efforts, although some cloudiness remained.

### 3.2.2 Aquifer pumping test

In March, 1996, both an aquifer pumping test and a slug test were conducted in

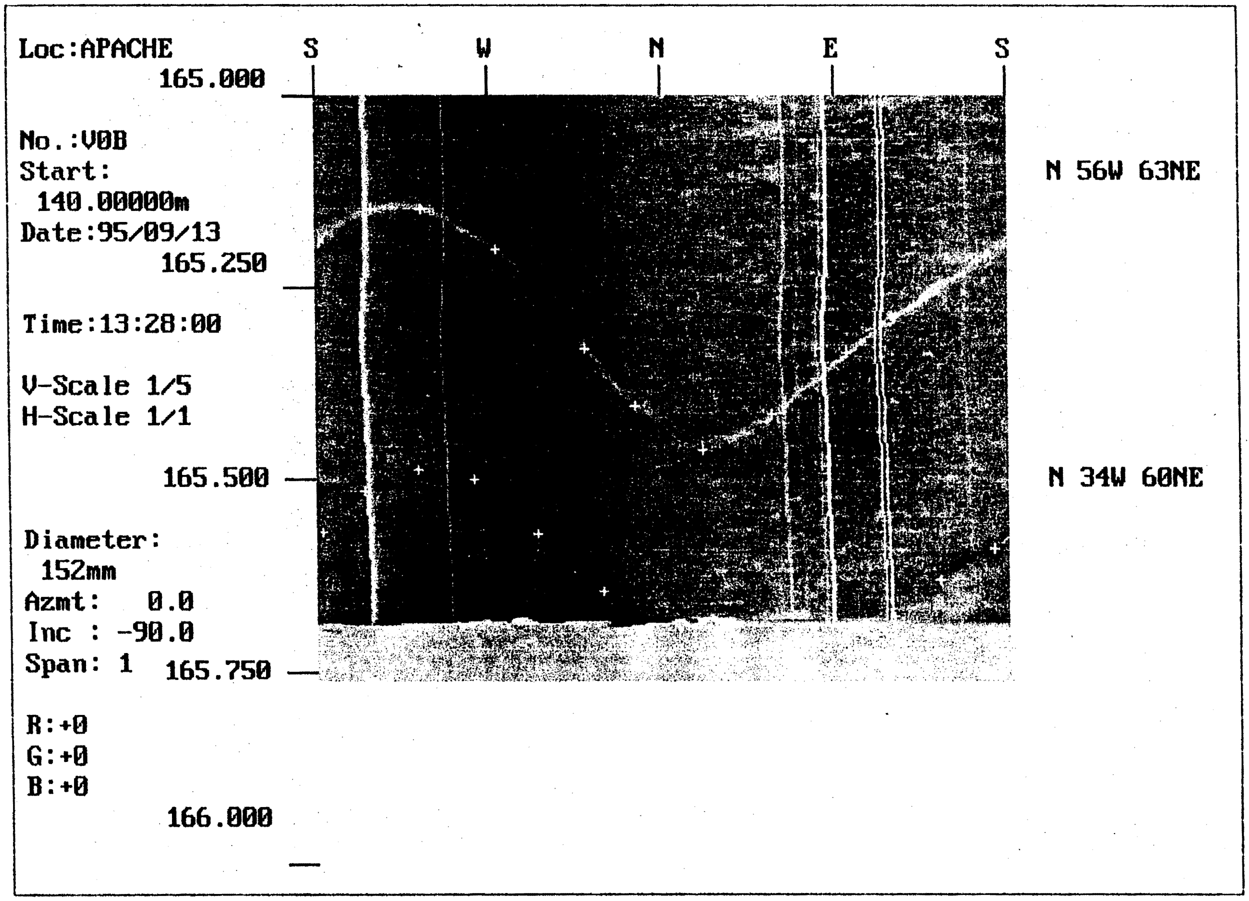

Figure 3.1 Image of fracture at 165 m depth in the VOB, provided by COLOG's BIPS

the VOB to measure the hydrologic response in the well in the zone which included the fracture shown in Figure 3.1. The setup for the 18.8-hour aquifer test is shown in Figure 3.2. A 1-horsepower, 10-cm diameter, submersible domestic pump was placed above the 7-m interval that had shown high amounts of suspended material, to avoid the possibility of clogging. A 50-psi absolute pressure transducer sensitive to 0.03 m was placed 1.5 m above the pump intake to measure drawdown and recovery. Therefore, at the start of the test, 12.5 m of head was above the transducer. A second transducer was installed in the deep slant borehole, which, at the depth of the static water level, is approximately 150 m horizontally away from the vertical borehole. No response was ever recorded in the deep slant borehole. The discharged water was routed by hose to a location approximately 160 m downgradient of the wellheads, and downgradient of any vertical fractures that could potentially recharge into the deep slant borehole.

Initially, the vertical borehole was pumped at the maximum capacity of the pump; at a pumping rate of about 13 L/min, the water level would drop to just above the transducer in approximately 35 minutes; complete recovery took about 2 hours. This pumping rate was too high to see any other than well storage effects, but was useful for well development. A three-hour test was run at 4.5 L/min, and showed a distinct change in drawdown rate after 48 min; however, the water level was dropping too far at that rate to continue the test. The 18.8-hour (1127-min) test was run at a discharge rate of 3.56 L/min. The discharge rate was monitored visually with a flowmeter installed in the discharge plumbing, which was calibrated using a 1-L graduated cylinder and stopwatch. Flow was adjusted manually using a diaphragm valve installed downstream of the

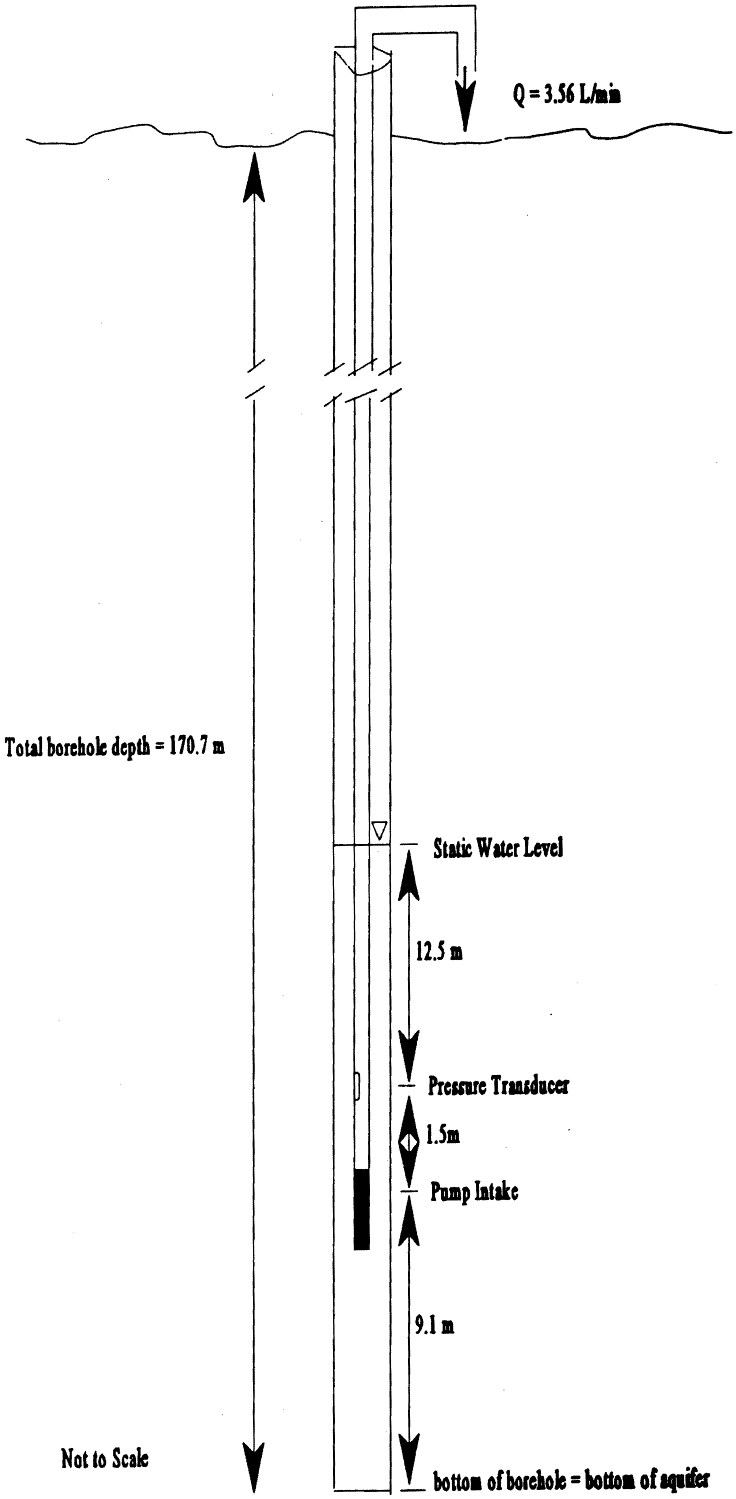

Figure 3.2 Schematic diagram of aquifer test setup.

flowmeter. Flow was monitored frequently, but not continually, and was adjusted as deemed necessary. Following numerous slight adjustments during the first 10 min of the test, flow adjustments were made at 19, 32, 78, 104, 182, 460, 472, 742, and 997 minutes into the test.

### 3.2.3 Slug test

Approximately 1500 L of the water pumped from the VOB during the aquifer test was saved in a tank. This water was then poured as a slug down the well at a later time. The actual time required for all of the water to enter the well was about 30 min, resulting in a maximum rise in the borehole of 47.2 m above static water level. The discharge pipeline and cables for the aquifer test remained in the well during this test, therefore, the measured head was not made up entirely of water. After 23 hours (1379 min), recovery was more than 98% complete.

## 3.3 Results

### 3.3.1 Pumping Test Analyses

Gringarten (1982), Sauveplane (1984), and Milne-Home (1988) summarized the numerous models available for interpretation and analysis of pumping tests in fractured rock aquifers. The models fall into three major categories: the discrete fracture models such as those developed by Gringarten and Witherspoon (1972), the dual (or more) porosity models stemming from the work of Barenblatt et al. (1960), and the single continuum models in which the cubic law of fluid flow is used to derive an equivalent porous medium hydraulic conductivity (Snow, 1969). Increasingly more complex models have been developed for specific systems within those categories. Discrete fracture models generally separate fractures into vertical or horizontal categories of various geometric organizations; flow may be radial, linear, or a combination of both, and the nature of the aquifer may vary through a range of isotropic-homogeneous to anisotropic-heterogeneous states, depending on the model (Milne-Home, 1988); matrix flow is insignificant. In dual porosity models, the rock matrix and the fractures are treated as two separate hydrologic systems that interact; the system can be further broken down into a three-part system if, for example, distinctly defined fracture sets can be identified. In these models, the geometry of the fracture network may be random, spherical, or orthogonal, the aquifer may be confined or unconfined, and block drainage may be unsteady or quasi-steady (Milne-Home, 1988). The single continuum models require parameters from a representative elementary volume (REV) that represents the distribution of void spaces and the solid matrix within it. Fractures are usually incorporated by including anisotropy in the model (Gringarten, 1982). The Apache Leap system could conceptually be fit to a variety of fracture-flow models; in order to apply an analytical solution using the limited amount of data that were available, however, the use of the more complex models could not be justified. Therefore, two relatively simple models, a discrete fracture system and dual porosity system, were used to analyze the ALRS data. In addition, for comparison, the recovery data were analyzed using a porous-media model.

Figures 3.3a and 3.3b show the results of the pumping test, plotted on semi-log (a) and log-log (b) scales. Some of the flow adjustments that were made during the test, such as those at 78, 182, 460-472, and 742 minutes, may have been significant enough to

[illegible]

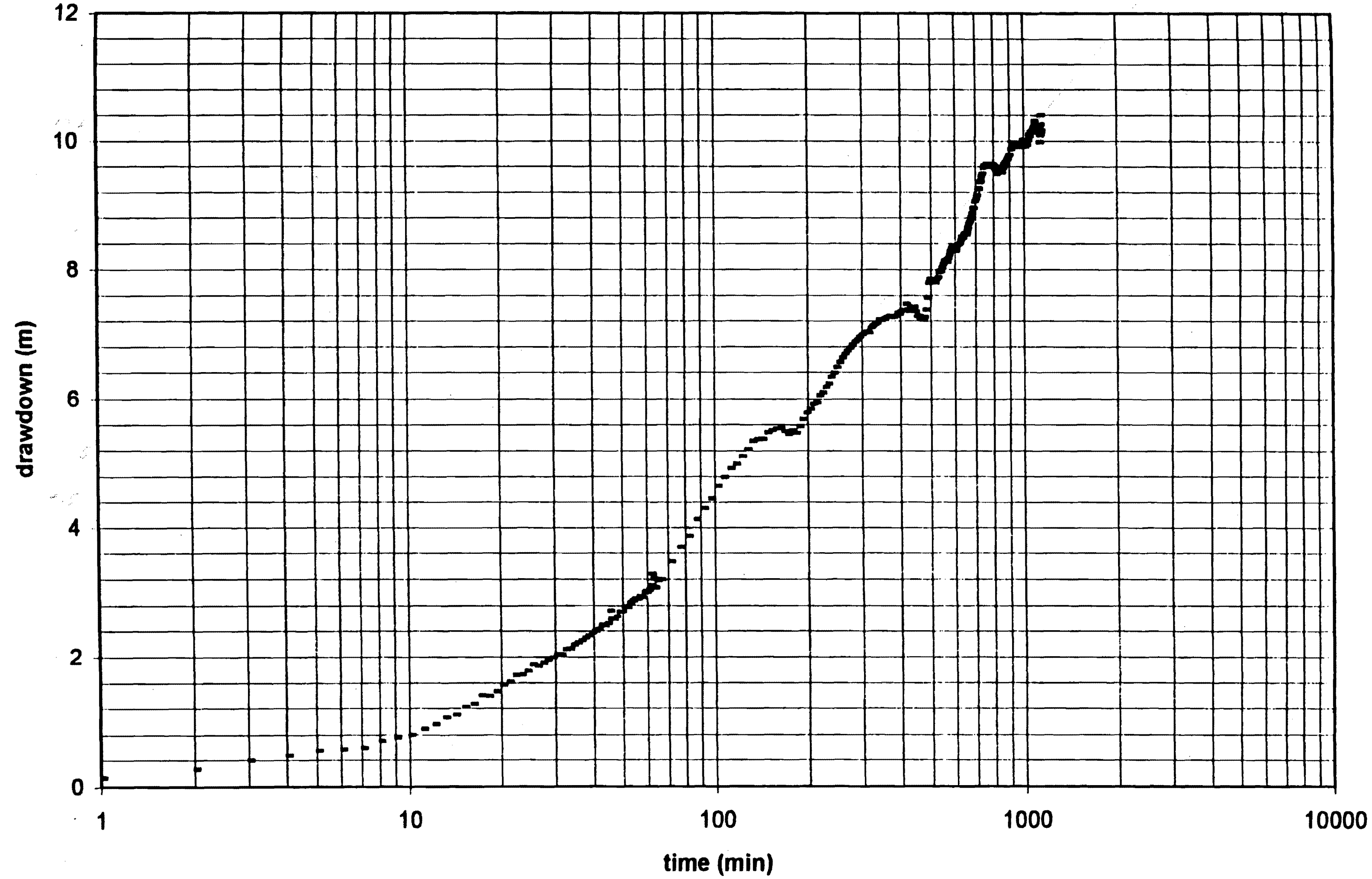

Figure 3.3a Semi-log drawdown plot of 18.8-hour aquifer test performed in the VOB.

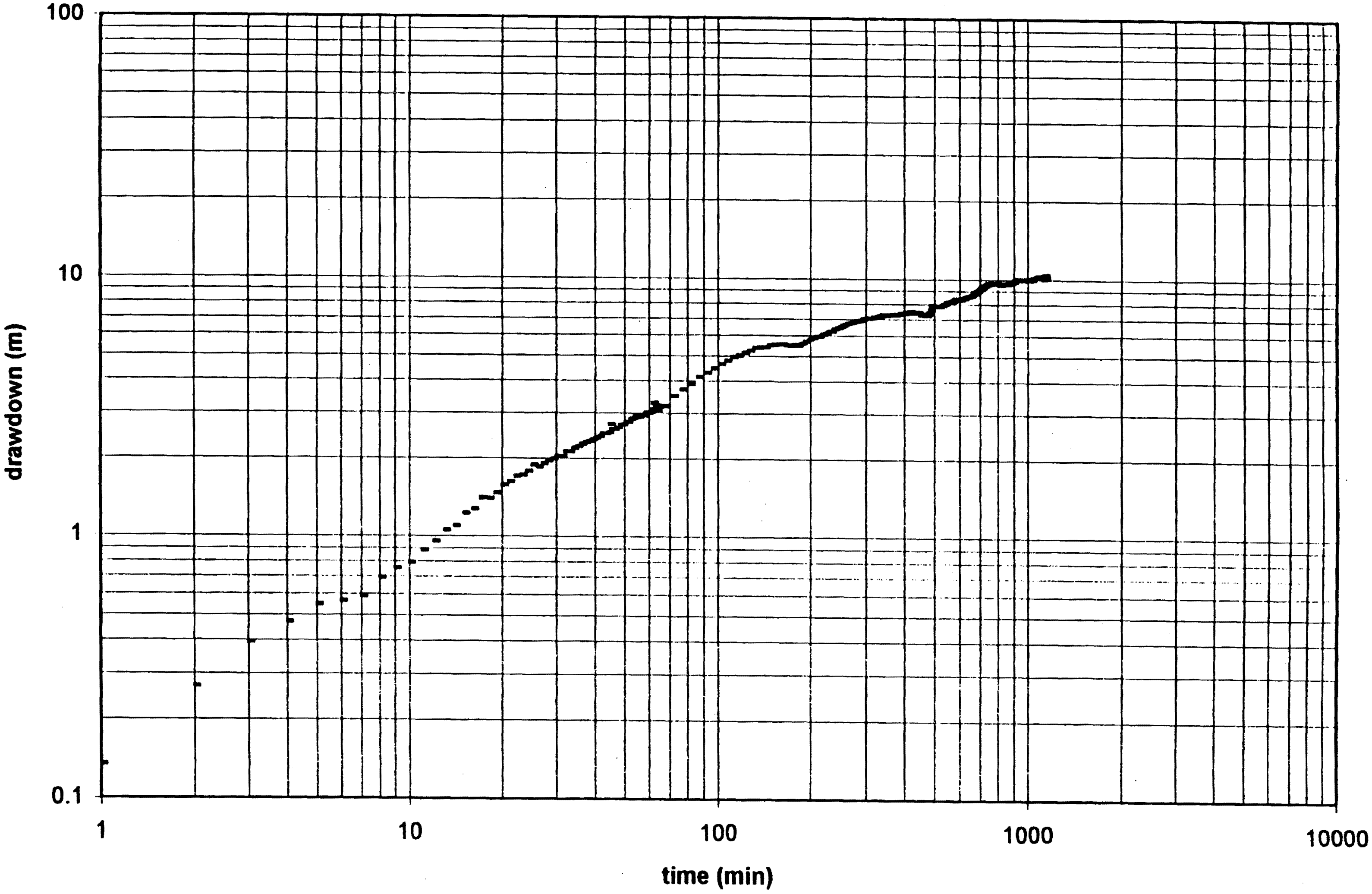

Figure 3.3b Log-log drawdown plot of 18.8-hour aquifer test performed in the VOB

affect the drawdown curve at those times, but do not affect the overall trend of the curve.

### *3.3.1.1 Discrete fracture model*

The pumping test data were first fit to a type curve derived from Gringarten and Ramey's (1973) method of using an appropriate Green's function to solve unsteady flow problems. The analytical expression that was used represents the aquifer system as an infinite, horizontal, homogeneous slab (or short cylinder) of thickness b and hydraulic conductivity $k_m$. This slab is completely penetrated by a well. A single, horizontal, symmetrical fracture (or fracture zone) of radius $x_f$ and hydraulic permeability $k_f$ is centered at the well and within the slab. Figure 3.4, modified from Gringerten and Ramey (1974) shows a cross-section of this idealized model. The matrix region may include fractures that are not as significant to fluid flow as the primary fracture or fracture zone. This discrete fracture model was chosen as the one likely to most closely fit the conditions known to exist in the ALRS system, due to the geophysical data and BIPS images which showed increased fracture abundance in the perched zone.

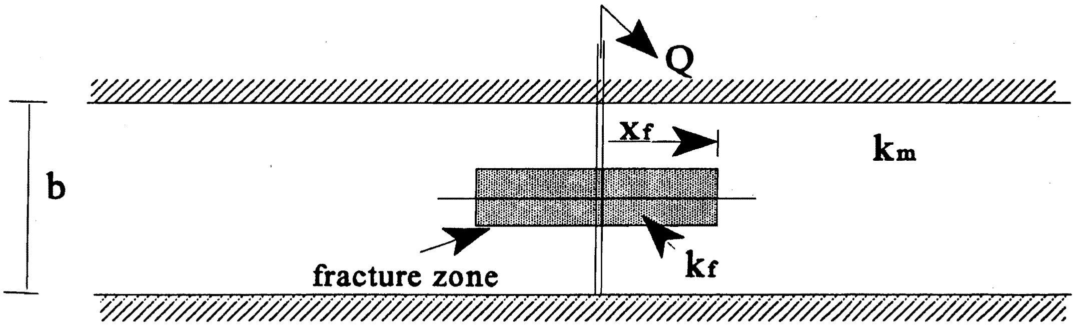

Figure 3.4. Cross-section of horizontal fracture model, modified from Gringarten and Ramey (1974).

The following equations were applied:

$$s_D(t_D) = \frac{4\pi b \sqrt{k_f\, k_m}}{Q}\, s(t) \qquad (3.1)$$

$$t_D = \frac{k_f\, t}{S_{sm}\, x_f^2} \qquad (3.2)$$

$$s_D(t_D) = 2\pi\sqrt{t_D}\; erf\left(\frac{1}{2\sqrt{t_D}}\right) + E_1\left(\frac{1}{4t_D}\right) \qquad (3.3)$$

$$E_1(u) = \int_u^\infty \frac{e_{-y}}{y}\, dy, \quad where \quad u = \frac{1}{4t_D} \qquad (3.3a)$$

where: $s_D$ = dimensionless drawdown

$t_D$ = dimensionless time

b = aquifer thickness

$k_f$ = hydraulic conductivity of the fracture

$k_m$ = hydraulic conductivity of the matrix

Q = pumping rate

s(t) = drawdown at time t

$S_{sm}$ = specific storage of the matrix

$x_f$ = thickness of the fracture

erf = error function, obtained from Abramowitz and Stegun, (1967)

$E_1(u)$ =Theis model, obtained from Abramowitz and Stegun, (1967)

Figure 3.5 shows the type curve obtained from the Gringarten and Ramey (1973) method, with the pumping test data superimposed over the best-fit location. The drawdown portion of the type curve was generated from Equation 3.3 to plot $s_D$ versus $t_D$. Then, a recharge well was superimposed to obtain recovery curves from:

$$s(t) = \frac{Q}{4\pi b\sqrt{k_f\, k_m}} \left[s_D(t_D) - s_D(t_D^{\prime})\right] \tag{3.4}$$

$$s_D(t_D^{\prime}) = 0 \quad for \quad t \le t_s \tag{3.5}$$

$$t_D^{\prime} = \frac{k_f\,(t - t_s)}{S_{sm}\; x_f^2}; \qquad t_s = shutin\ time\ (end\ of\ pumping) \tag{3.6}$$

Recovery type curves were obtained by plotting $s_D(t_D)$ - $s_D(t_D')$ versus $t_D$ on the same graph as the drawdown curve, for various shutin times.

The fit of the data onto the type curve is fair, and improves with increasing pumping time into the test. The deviations due to flow adjustment affect discrete time intervals but do not invalidate the observed trend. At times where the drawdown data more closely approximated the type curve, the recovery data was a poor match, and vice versa. The pumping data were used to match the type curve.

From a match point on the type curve, an effective transmissivity was calculated

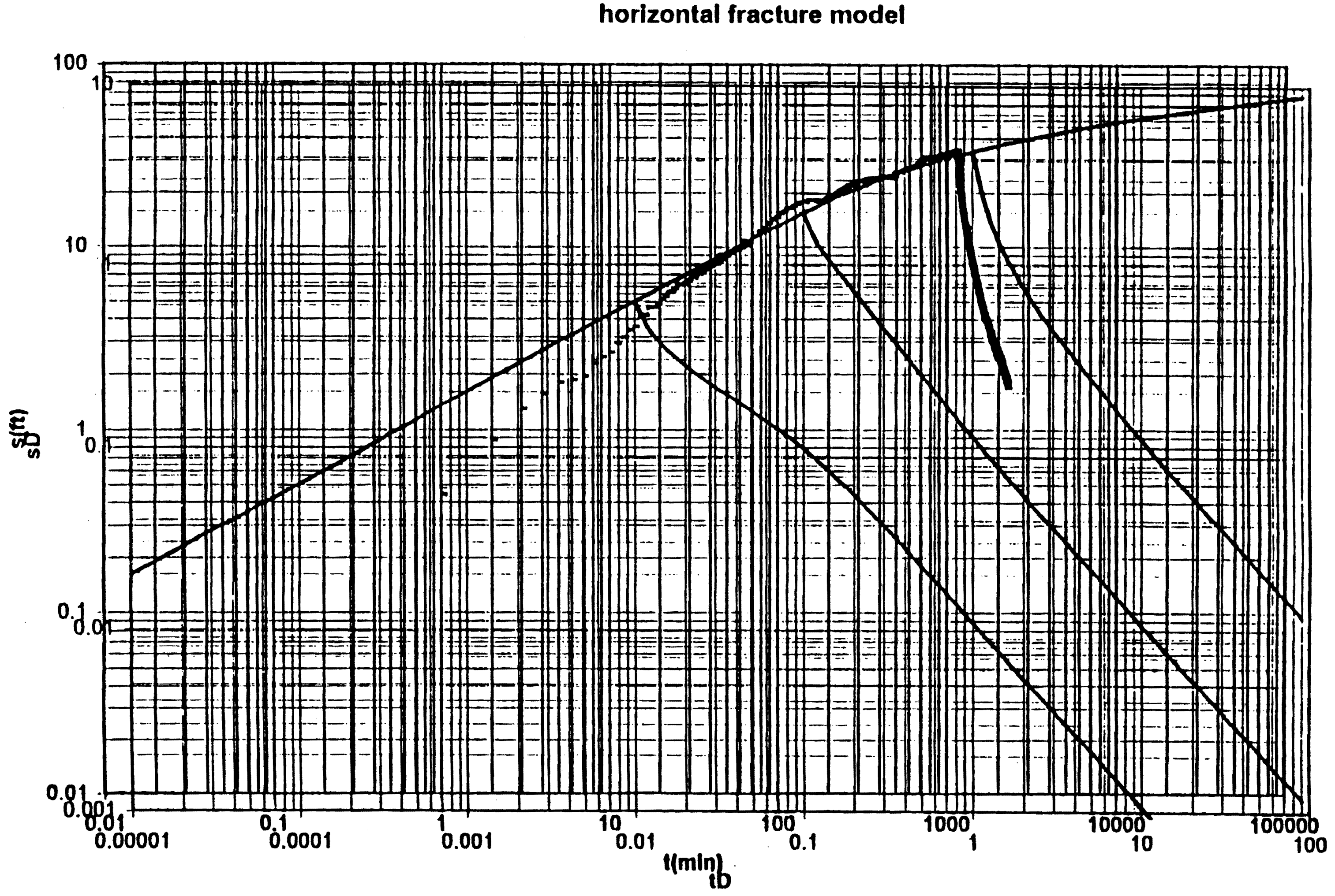

Figure 3.5 Type drawdown and recovery curves (solid lines) from Gringarten and Ramey (1973) model, with VOB 18-hour aquifer test data superimposed.

from Equation 3.1 of 0.161 $m^2$/day. A fracture hydraulic conductivity was then obtained from approximations of aquifer thickness and matrix hydraulic conductivity, using the same equation. The aquifer region was estimated to be 21 m thick, based on the height of the water in the borehole. The matrix hydraulic conductivity was estimated to be 2.47 x $10^{-7}$ m/day, based on measurements of the Apache Leap Tuff by Hardin (1996). These values of aquifer thickness and matrix hydraulic conductivity produced an estimated fracture hydraulic conductivity of 238 m/day, clearly supporting the significance of fracture flow in this system.

#### *3.3.1.2 Double porosity model*

Kruseman and de Ridder (1990) presented several methods for analyzing pumping test data based on the double-porosity model that was originally developed by Barenblatt et al. (1960). Double-porosity models assume that the natural system is composed of two separate media: the rock matrix, and the fractures that divide the matrix. The rock matrix is characterized by having primary porosity and low hydraulic conductivity, while the fractures have low storage capacity and high permeability. No variation in head is assumed to exist in the matrix, such that interporosity flow is in a pseudo-steady state; fracture flow towards the well is assumed to be radial, and in unsteady state (Kruseman and de Ridder, 1990).

One of the dual-porosity models presented by Kruseman and de Ridder (1990) was that originally developed by Warren and Root (1963) for a pumped well. To demonstrate this model, Kruseman and de Ridder used time-drawdown data from a test conducted on Well UE25b1 as part of the assessment of the hydrologic properties of Yucca Mountain (the data were originally published by Moench, 1984). The successful application of this model to a deep (470 m), unconfined aquifer in the fractured, variably welded ash flow tuffs of Yucca Mountain bode well for its application to the ALRS data.

To apply Warren and Root's (1963) dual-porosity model, Kruseman and de Ridder (1990) created a semi-log plot of drawdown (s) versus time, which, for a true dual-porosity system, is predicted to reveal two parallel straight lines (with approximately equal slope) connected by a transitional curve (Figure 3.6). The early-time straight line data represent flow to the well derived solely from the fractures; the straight line may be obscured by storage effects in the well and in the fractures intersecting the well. The late-time straight line is assumed to represent flow to the well from both the fractures and the matrix, and is comparable to the response of an unconsolidated homogeneous isotropic aquifer with a transmissivity equal to the fracture transmissivity, and a storativity equal to the arithmetic sum of the storativities of the fractures and the aquifer matrix (Kruseman and de Ridder, 1990).

When Kruseman and de Ridder applied the data of Moench (1984), the semi-log plot did not show the early-time straight line, due to storage effects (Figure 3.7). However, they were able to obtain a straight line from the late-time data, and calculated a fracture transmissivity of 333 $m^2$/day (Kruseman and de Ridder, 1990). The late-time data did not begin to form a straight line until approximately 1000 minutes into the more than 4000-minute test.

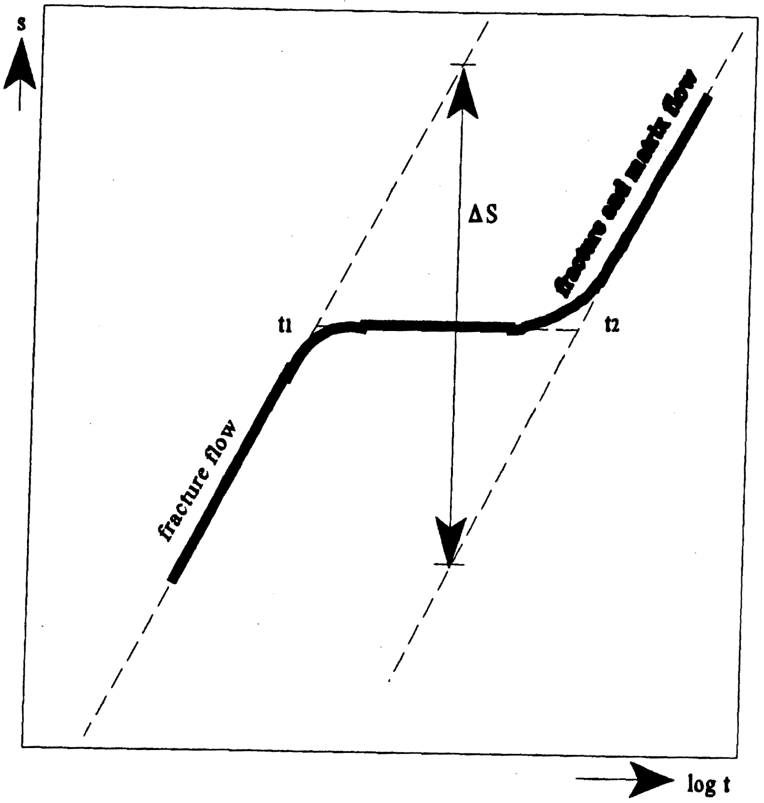

Figure 3.6 Predicted semi-log drawdown vs. time plot for a pumping test in a dual-porosity system (modified from Kruseman and de Ridder, 1990).

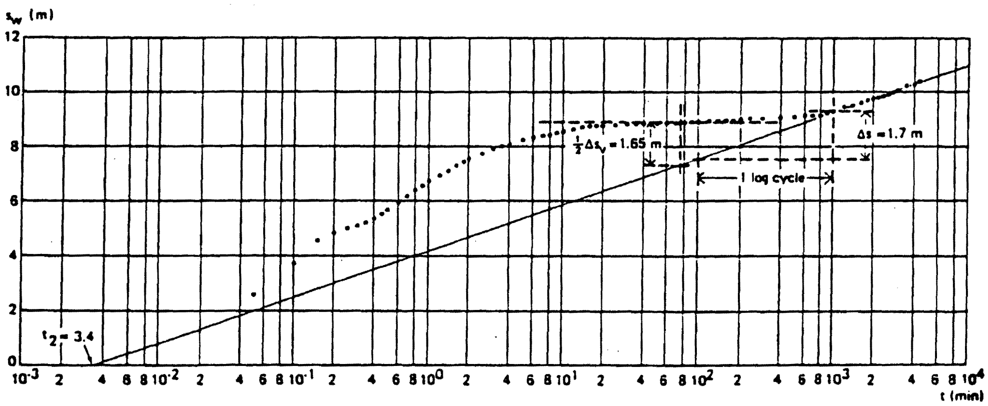

Figure 3.7 Semi-log plot of Moench's (1984) data from a dual-porosity system, as analyzed by Kruseman and de Ridder (1990).

The semi-log plot of the ALRS data (Figure 3.3) does not show either early- or late-time straight-line behavior, therefore, the application of this method to the ALRS system was not possible. The fact that the Yucca Mountain data did not begin to exhibit late-time straight-line behavior until 1000 minutes into the test suggests that perhaps the ALRS test was not carried out for a long enough time period to use this method. Alternatively, the Apache Leap system may not be a dual-porosity system, due to the extremely low matrix permeability, in which case attempts to use this model would be inappropriate.

### *3.3.1.3 Recovery data method*

For comparison to the results of the discrete horizontal fracture model, the effective transmissivity of the perched aquifer was calculated using the Theis recovery method. According to Kruseman and de Ridder (1990), this method is valid for confined aquifers, but can be applied to unconfined aquifers using the later-time data, when a straight line is more likely to be achieved on a semi-log plot of residual drawdown versus time since the start of pumping relative to time since the cessation of pumping (t/t'). The equation used to calculated transmissivity from the straight line plot is developed from Theis (1935):

$$\Delta s' = \frac{2.30Q}{4\pi KD} \tag{3.7}$$

where: $\Delta s'$ = residual drawdown difference per log cycle of t/t'

Q = rate of recharge = rate of discharge ($m^3$/day)

KD= aquifer transmissivity ($m^2$/day)

Figure 3.8 shows the ALRS recovery data semi-log plot. From this graph, a transmissivity of 0.18 $m^2$/day was calculated, which represents an effective transmissivity for the combined matrix material and fractures. The value is similar to the effective transmissivity calculated with the Gringarten and Ramey (1973) model, 0.161 $m^2$/day.

### 3.3.2 Slug Test Analyses

Numerous models are available for the analysis of slug test data, including many models designed for very specific types of systems, as summarized by Sageev (1986). The results of the pumping test analyses showed that both the discrete fracture model and the porous-media recovery method produced similar calculations of effective transmissivity, therefore, the analyses of the slug test data were also designed to test models of different types of systems. First, two simple porous-media methods of slug test analysis were applied to the ALRS data, and then a more complex model designed for a fractured system was used for comparison.

#### *3.3.2.1 Cooper et al. (1967) method*

Cooper et al. (1967) derived a solution for a slug test in a fully-penetrating large-diameter well in a confined, unsteady-state aquifer that is homogeneous, isotropic, and of uniform thickness over the area influenced by the slug test.

According to Cooper et al. (1967), a slug of volume V instantaneously injected into a well of diameter $2r_c$ will cause an instantaneous change of hydraulic head in the well:

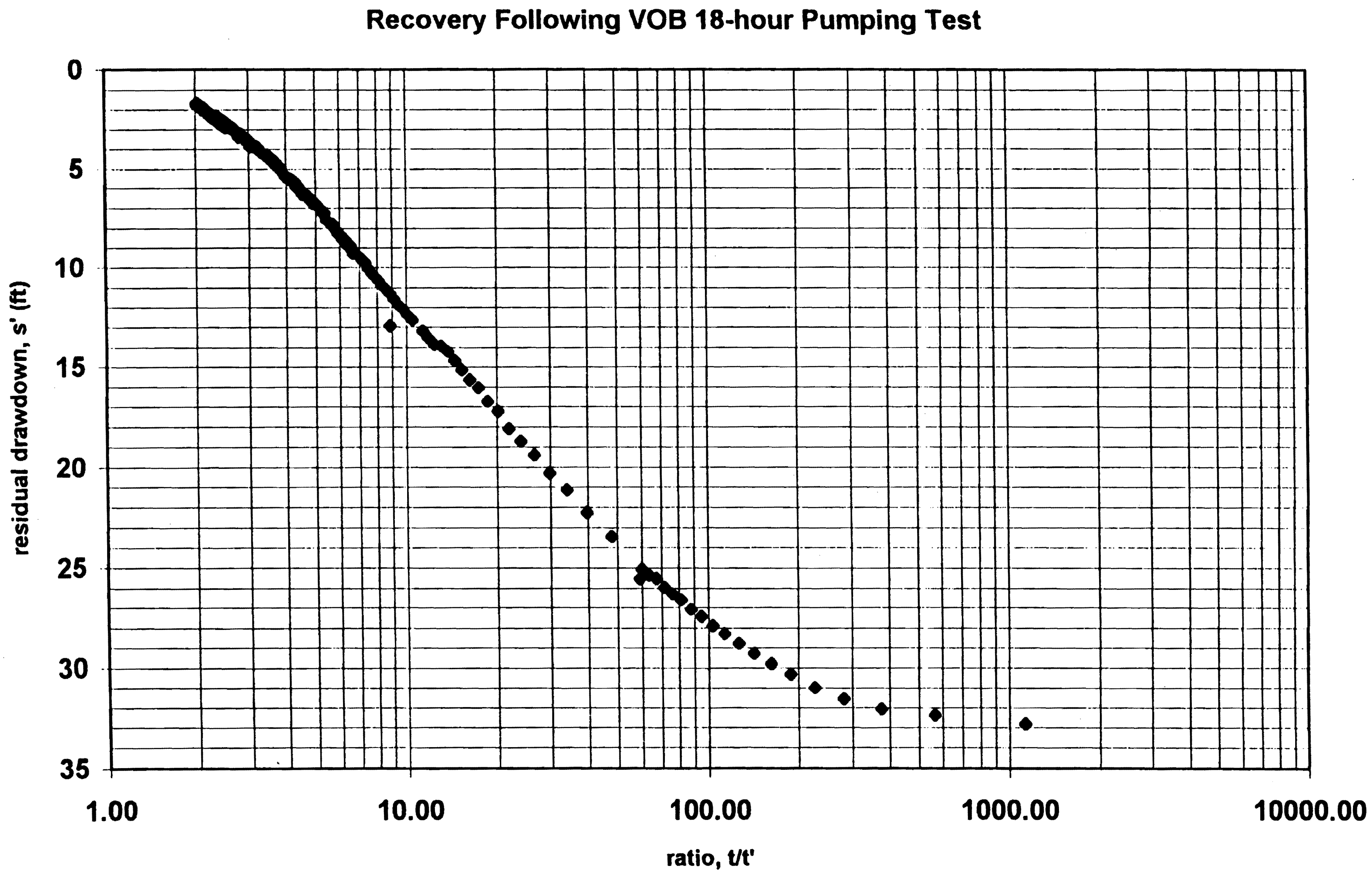

Figure 3.8 Semi-log plot of recovery data from 18.8-hour aquifer test in the VOB.

$$h_o = \frac{V}{\pi r_c^2} \tag{3.8}$$

Once the slug has been added, the recovery of the head to its initial head is described by:

$$\frac{h_t}{h_o} = F(\alpha, \beta) \tag{3.9}$$

where:

$$\alpha = \frac{r_{ew}^2 S}{r_c^2} \tag{3.10}$$

$$\beta = \frac{KDt}{r_c^2} \tag{3.11}$$

and: S = storativity of the formation

K = hydraulic conductivity of the formation

D = aquifer thickness

$h_o$ = instantaneous change of head in the well at time $t_o = 0$

$h_t$ = head in the well at time $t > t_o$

$r_c$ = radius of well where head is changing

$r_{ew}$= effective radius of the open part of the well

Cooper et al. (1967) then defined the function $F(\alpha,\beta)$, which was used to generate a series of type curves drawn as a semi-log plot of $F(\alpha,\beta)$ versus $\beta$ for a range of values of $\alpha$. A semi-log plot of the slug test data in the form of $h_t/h_0$ versus t is then superimposed over the type curves to locate a match. From this match, Equation 3.11 is used to calculate a value of transmissivity equal to the aquifer thickness times hydraulic conductivity, and Equation 3.10 is used to calculate a value of storativity. Because the type curves are very similar in shape, especially for the smallest values of $\alpha$, the error in the storativity calculation is as large as the error in $\alpha$; however, the error in transmissivity will still be small. According to Papadopulos et al. (1973), for $\alpha < 10^{-5}$, an error of two orders of magnitude in $\alpha$ will result in an error of less than 30% in the calculation of transmissivity.

Figure 3.9 shows the Cooper et al. (1967) type curves with the ALRS slug test data fit to $\alpha = 10^{-10}$. In the uncased, rock-lined borehole of the VOB, $r_c$ was assumed to equal $r_{ew}$, so that the formation storativity $S = 10^{-10}$. From this curve fit, an aquifer transmissivity of 0.167 m$^2$/day was calculated, which was similar to those values obtained from the pumping test analyses of the discrete fracture model and the Theis recovery method.

### *3.3.2.3 Bouwer-Rice (1976) method*

Bouwer and Rice (1976) developed a method, based on Theim's (1906) equation for well discharge, to measure aquifer parameters from the rate of flow into a well in an unconfined, steady-state aquifer after the sudden removal or addition of a slug of water. Hydraulic conductivity, K, in the vicinity of the well can be calculated from:

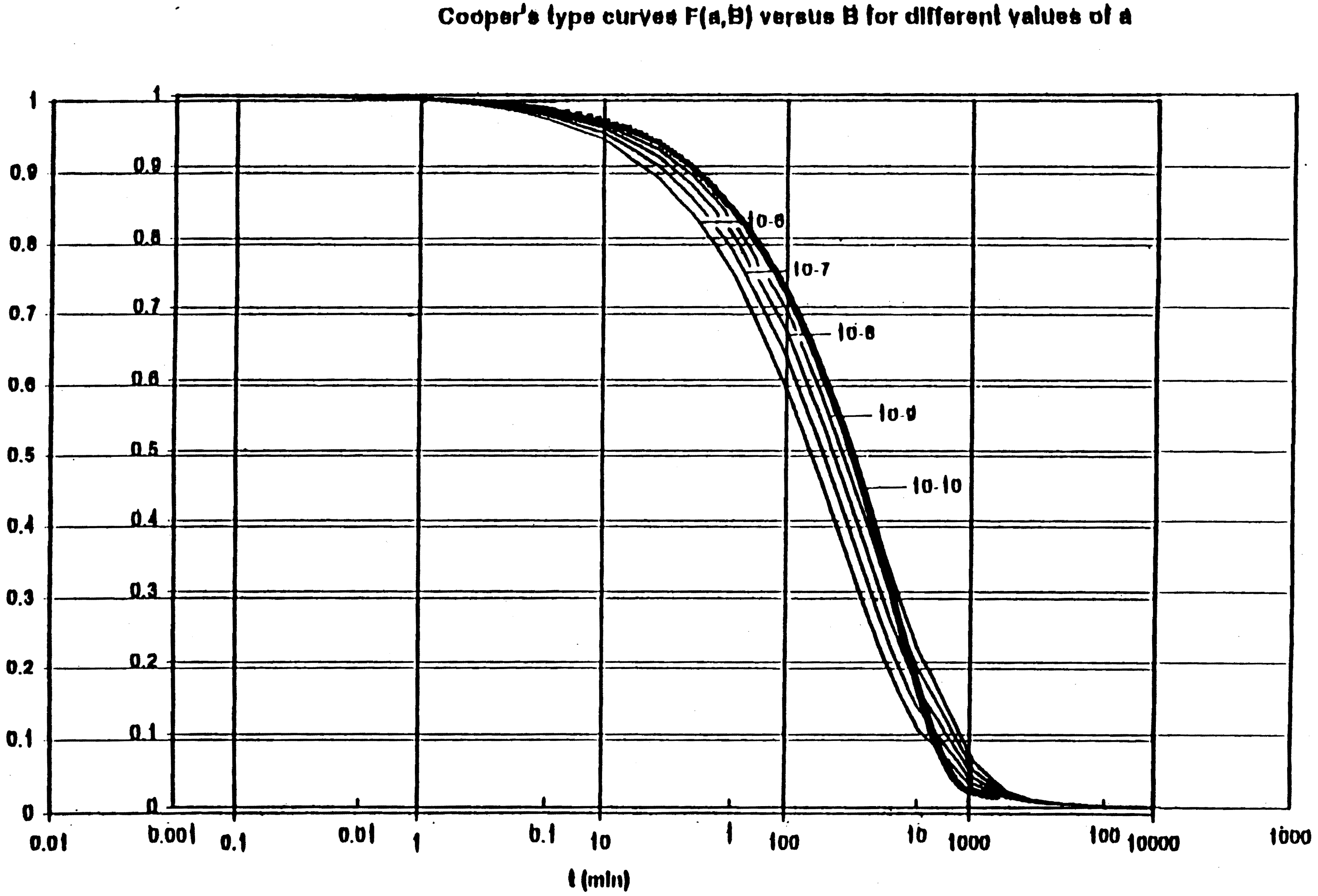

Figure 3.9 Cooper's (1967) type curves with data from the VOB (heavy line) fit to $\alpha = 10^{-10}$

$$K = \frac{r_c^{\,2}\ln(R_e/r_w)}{2d}\ \frac{1}{t}\ \ln\frac{h_o}{h_t} \tag{3.12}$$

where: $r_c$=radius of the well where head is falling

$r_w$=horizontal distance from center of well to undisturbed aquifer

$R_e$=radial distance over which the difference in head, $h_o$, is dissipated in the flow system of the aquifer

d =length of the open section of the well

$h_o$=head in the well at time $t_o = 0$,

$h_t$=head in the well at time $t > t_o$

Bouwer and Rice used a resistance network analog to determine values of $R_e$ for different values of $r_w$, d, and aquifer thickness, b, for fully penetrating wells, and developed an empirical equation:

$$\ln\frac{R_e}{r_w} = \sqrt{\frac{1.1}{\ln(b/r_w)} + \frac{C}{d/r_w}} \tag{3.13}$$

where C is a dimensionless parameter that is a function of $d/r_w$, and is obtained from a curve provided in Bouwer and Rice (1976).

As the values of K, $r_c$, $r_w$, $R_e$, and d in Equation 3.12 are constants, the expression $(1/t)\ \ln(h_o/h_t)$ is also a constant. Therefore, a semi-log plot of drawdown versus time should form a straight line that can be used to evaluate $(1/t)\ \ln(h_o/h_t)$ to solve Equation

3.12 for K. Transmissivity is then obtained by multiplying by the aquifer thickness.

Figure 3.10 shows the semi-log plot of the ALRS slug test data. A straight line was drawn through the early-time data in order to intersect $h_o$. When Equation 3.12 was applied, an effective aquifer transmissivity of 0.057 $m^2$/day was calculated, somewhat lower than the values obtained from Cooper et al.'s (1967) method and the pumping test analyses.

### *3.3.2.3 Linear/Radial flow model*

Finally, the slug test data were modeled to a linear/radial flow model developed by Karasaki et al. (1988). This model was developed on the theory that when flow near the well is restricted to be entirely within those fractures near and intersecting the well, the flow near the well is primarily linear. Further away from the well, the number and interconnection of the fractures is significant enough that flow becomes radial. Thus, the system is described by an inner region of linear flow with unique characteristics and properties, surrounded by an outer region of radial flow that can [illegible] porous medium. The outer region is similar to Cooper et al.'s (1976) system.

The reader is referred to Karasaki et al. (1988) for complete development of the solutions to this two-system model. Type curves for the model were generated iteratively from estimates of the radius of the inner region, and the ratios of the diffusivities, transmissivities, and storativities of the inner to the outer regions, which were calculated from the following equations:

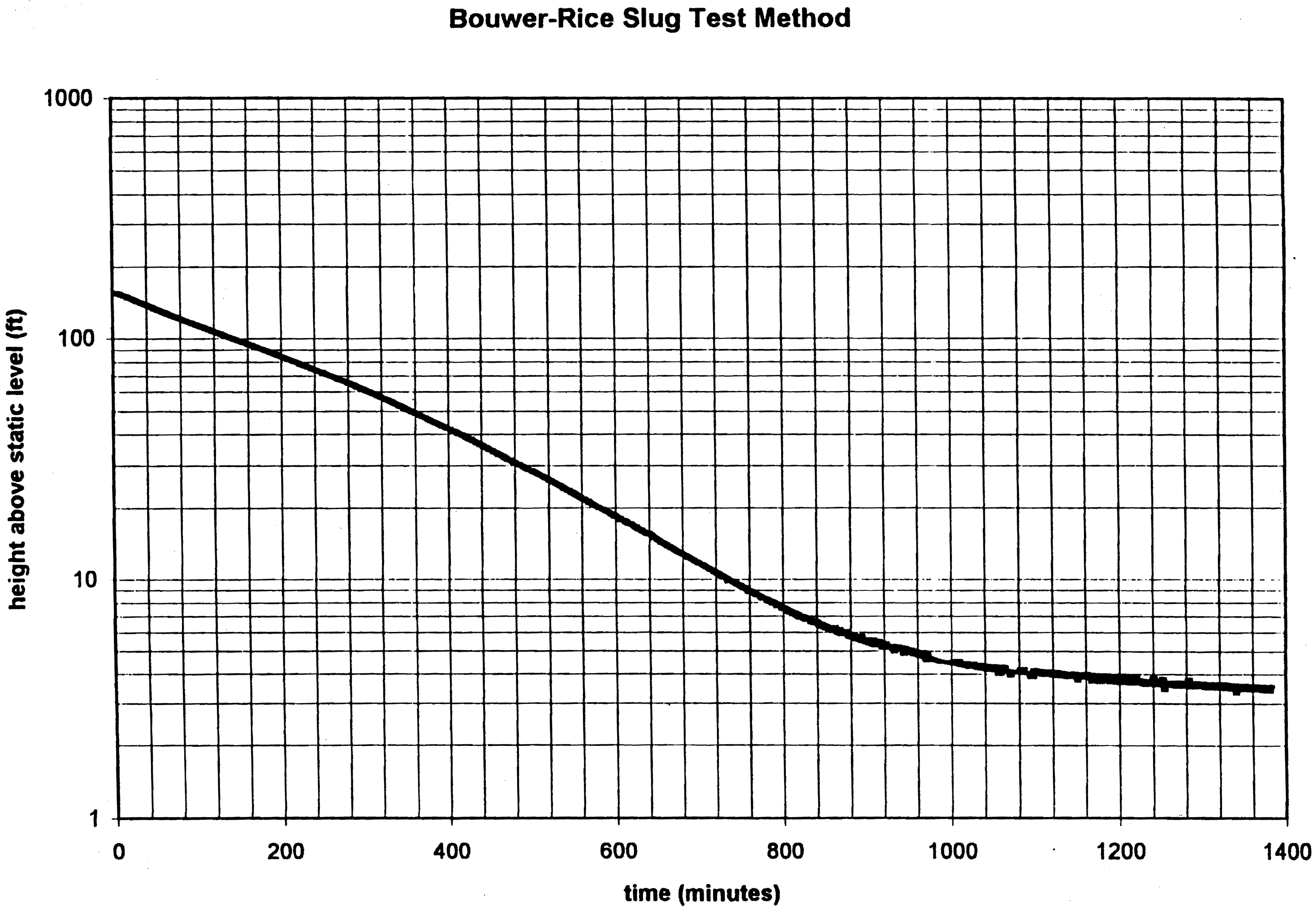

Figure 3.10 Semi-log plot of slug test data from the VOB for Bouwer-Rice (1976) application

$$r_c = \frac{r_w}{r_f} \tag{3.14}$$

$$\alpha_c = \frac{\alpha_1}{\alpha_2} = \frac{T_1/S_1}{T_2/S_2} \tag{3.15}$$

$$\beta = \frac{nk_1b}{2\pi r_f k_2} \tag{3.16}$$

$$\omega = (2\pi r_f^2/C_w)S_2, \quad where\ C_w = \pi r_a^{\ 2} \tag{3.17}$$

where: $r_c$ = ratio of wellbore radius to inner region radius

$\alpha_c$ = dimensionless hydraulic diffusivity

$\beta$ = dimensionless transmissivity

$\omega$ = storage ratio of the formation to the well

$C_w$ = well storage

and: $r_w$ = well bore radius

$r_f$ = radius of the inner region

T = transmissivity

subscript 1 refers to inner region

subscript 2 refers to outer region

S = storativity

n = number of fractures intersecting the well

k = hydraulic conductivity

b = fracture aperture

$r_a$ = casing radius

Due to the large number of parameters required to be known or estimated for the model, values calculated from the models used above, including fracture and effective hydraulic conductivities and transmissivities, were used to calculate initial estimates for $\alpha_c$, $\beta$, and $\omega$.

Figure 3.11 shows the ALRS slug test data fit to a type curve in which $r_c = 0.005$, $\alpha_c = 10$, $\beta = 1000$, and $\omega = 1 \times 10^{-5}$. In the iterative process of fitting the data to a type curve, the storage ratio ($\omega$) was found to have by far the most significant effect on curve shape (Figure 3.12). Using Equation 3.17, values of $\omega = 1 \times 10^{-5}$ and $r_f = 15$ m (corresponding to $r_c = 0.005$) produced an outer-zone storativity of $1.25 \times 10^{-10}$, which is nearly equal to the value of $1 \times 10^{-10}$ obtained from the Cooper et al. (1967) type curves in Section 3.3.2.1. The value of $r_c$ was varied over 5 orders of magnitude, such that the radius of the inner region ranged from 0.15 m to 1500 m, which resulted in virtually no change in either the shape or placement of the type curves (Figure 3.13). Varying the dimensionless transmissivity, $\beta$, resulted in some shifting of the curves over the range of 1 to $1 \times 10^5$ (Figure 3.14). The curves for $\beta = 10$, 100, and $1 \times 10^3$ were nearly identical, and matched the ALRS data better than those for 1, $1 \times 10^4$, or $1 \times 10^5$. An initial estimate of $\beta$ was made using Equation 3.15 with the values of 12 fractures of 0.002 m aperture (based on the COLOG imaging), a 15-m inner zone radius, and fracture and effective hydraulic conductivities ($k_1$ and $k_2$) based on the values obtained from the Gringarten and

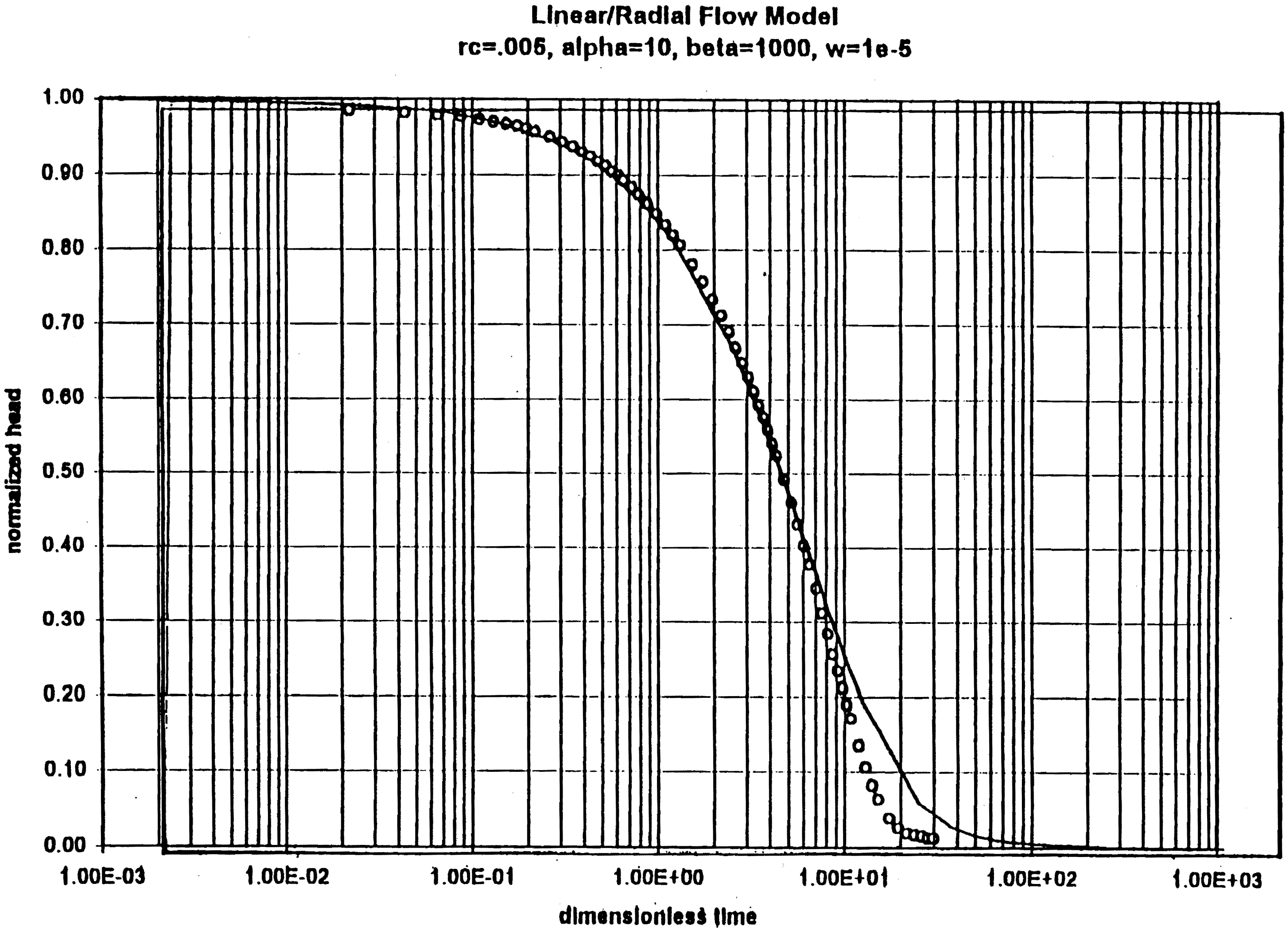

Figure 3.11 Linear/radial flow model type curve (solid line) with VOB slug test data fit

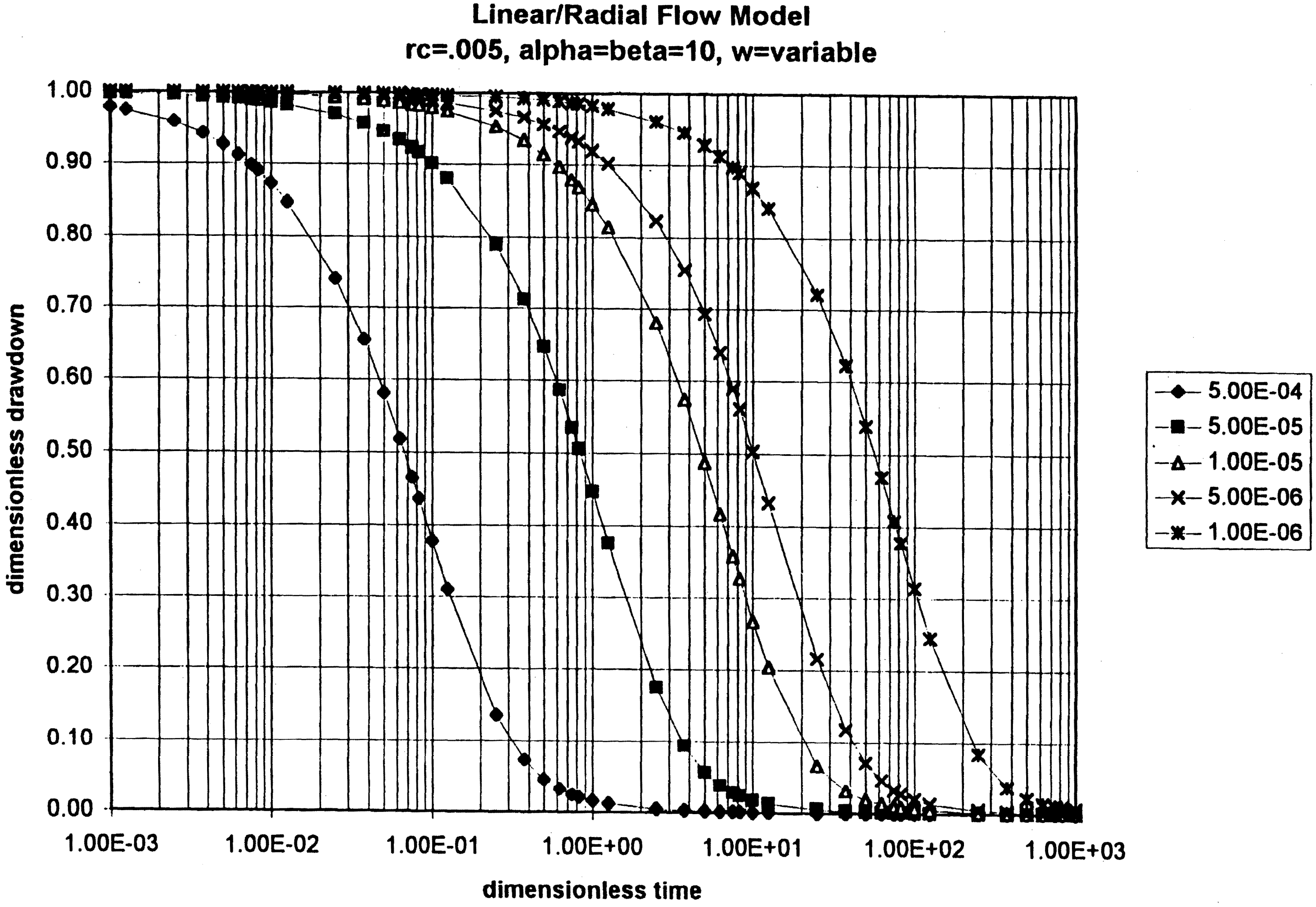

Figure 3.12 Variations due to change in storage ratio on linear/radial flow model type curves

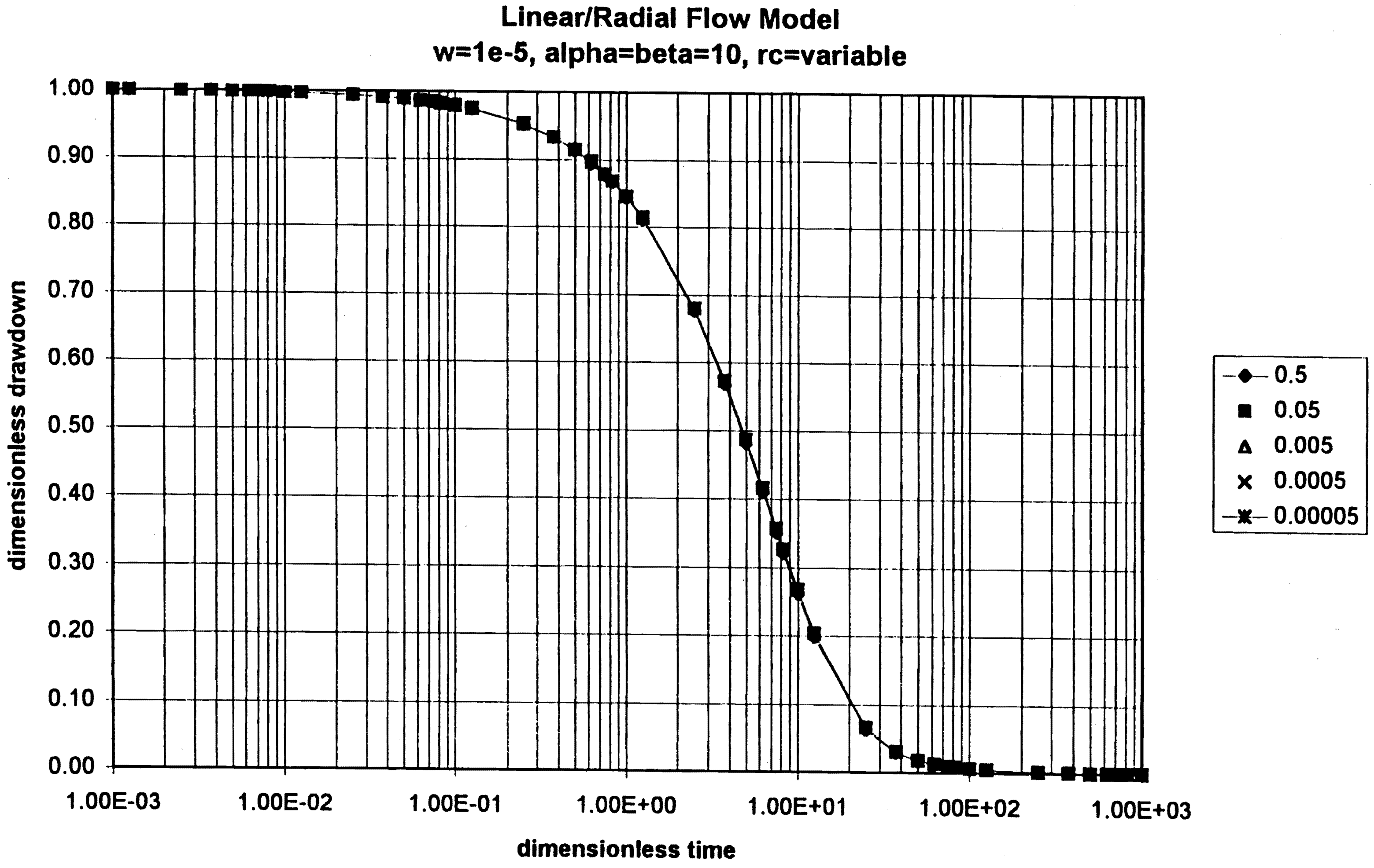

Figure 3.13 Variations due to radius of inner region ($r_c$) in linear/radial flow model type curves

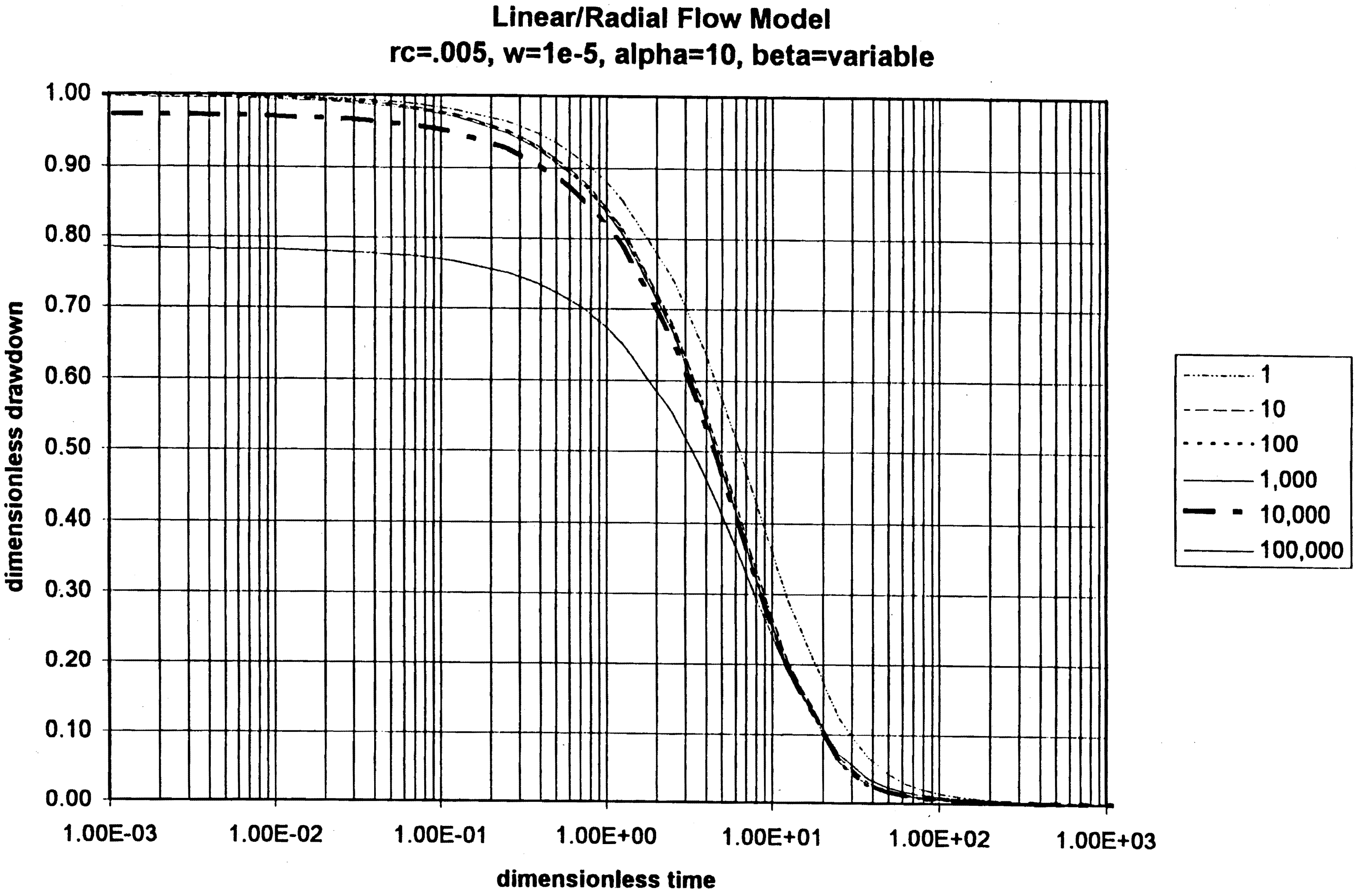

Figure 3.14 Variations due to dimensionless transmissivity (β) in linear/radial flow model type curves

Ramey model (Section 3.3.1.1). The estimated value of $\beta$ was 1.11 x $10^3$, which supports the curve-match value of 1 x $10^3$. Finally, variations in the value of $\alpha_c$ produced identical curves for the range 10 to 1 x $10^4$, all of which matched the ALRS data; $\alpha_c = 1$ produced a slightly shifted curve with a poorer fit (Figure 3.15).

The parameters that generated the best-fitting curve support the results of previous models of both the pumping test data (Sections 3.3.1.1 and 3.3.1.3) and the slug test data (Section 3.3.2.1). Furthermore, the ability of this flow model, which combines linear, near-well flow with radial, distant flow, to match the ALRS data quite closely suggests that it is a representative model for the ALRS system.

## 3.4 Discussion

Of the two types of fractured-rock aquifer models that were used to analyze the pumping data, only the discrete fracture model provided a reasonable fit. In fact, the fit of the discrete fracture model was predicted by the slope of the data on a log-log plot (Figure 3.3b), according to Gringarten (1982), who associated a unit slope of one-half with a high-conductivity fracture dominating the system. The fact that the semi-log plot of the data did not exhibit dual-porosity behavior suggests that the effective porosity of the matrix is so many orders of magnitude less than that of the fractures that it is not significant (Milne-Home, 1988).

The lack of a very close fit between the pumping data and the horizontal fracture model may be the result of two types of factors affecting the data: inaccuracies due to the mechanical setup and collection of data, and differences between the model assumptions

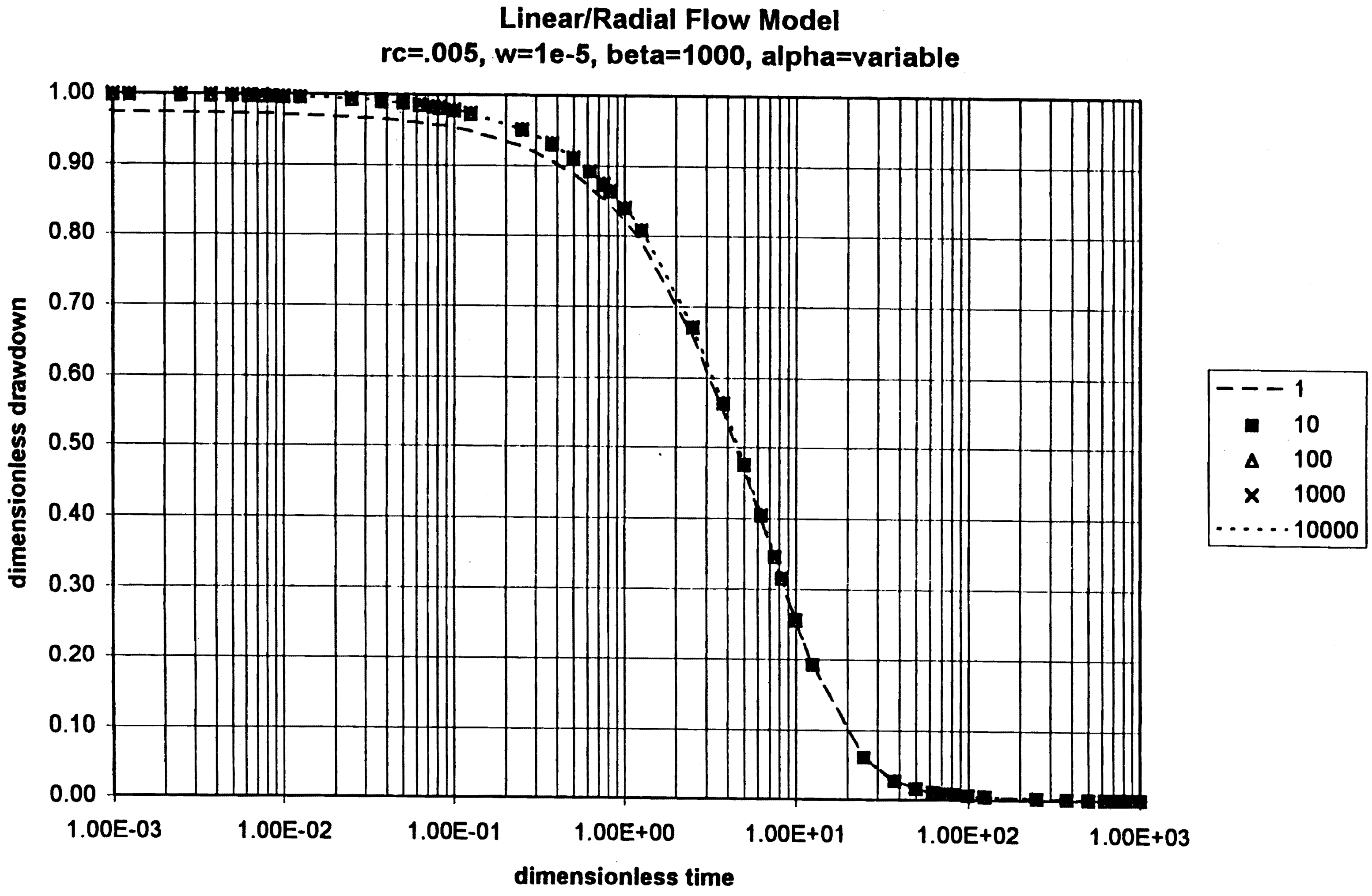

Figure 3.15 Variations due to changes in dimensionless diffusivity (α) in linear/radial flow model type curves

and the natural system. The mechanical setup was discussed earlier in this chapter. The test was limited by the capabilities of the pump that was available, and the degree of well development that was possible. Differences between the model and the natural system are likely to exist. The use of an analytical solution such as the Gringarten and Ramey (1973) model incorporates certain assumptions which may not reflect the conditions of the natural system. Deviations in the natural system from the model could include a greater contribution to flow from fractures in the matrix, the fact that several fractures, rather than one single one, make up the fracture system; or aberrations in the aquifer such that it does not closely meet the assumed boundary conditions. The pumping test resulted in drawdown of 48% of the head in the borehole; while the data showed no clear indication of a boundary effect, such as a sharp steepening of the drawdown curve indicative of a diminished water supply, it seems likely that such a significant proportional reduction in head would exert some influence on the drawdown behavior. In spite of such potential errors in the approach, the reasonable fit between the data and type curve does support the theory that fracture flow is dominant in the system, even if it is not as precisely defined as the model.

Analysis of slug test data dictates an awareness that slug tests reflect the hydraulic parameters of a limited area near the well (Papadopulos et al., 1973), and suffer from problems of nonunique solutions more than other well tests (Karasaki, 1987). Karasaki et al. (1988) recommend that slug test analyses use as much existing borehole and geologic information as possible prior to developing a conceptual model, as was done in this investigation.

The work of Karasaki (1987) and Karasaki et al. (1988) focussed on the interpretation of slug test data from fractured rock aquifers, including the linear/radial model used for analysis of ALRS data. Karasaki's (1987) attempt to model slug test data from fractured tuff aquifers at Yucca Mountain using the Cooper et al. (1967) method resulted in no satisfactory match to the type curves; the Yucca Mountain curves as a group dropped more steeply than all of the Cooper et al. curves at late times (Karasaki, 1987). Karasaki attributed this phenomenon to conditions in the natural system which are not accounted for in the Cooper et al. model: fracture flow, non-radial flow, outer boundary effects, and non-Darcy flow. All of these conditions are likely to exist at ALRS as well; the ALRS slug test curve also dropped more steeply than the Cooper et al. curves at late times. In addition to deviations in the natural system from the model assumptions, poor matches to analytical slug test solutions in the case of the ALRS data may also result from the manner in which the slug test was conducted, as described previously.

Table 3.1 summarizes the results of the various analyses that were performed on the aquifer and slug test data. The effective transmissivities obtained from the horizontal fracture model, the recovery test, the Cooper et al. model, and the linear/radial flow model fell into the range of 0.16-0.18 $m^2$/day, translating to effective hydraulic conductivity of 7.6 x $10^{-3}$ to 8.6 x $10^{-3}$ m/day. Hydraulic conductivity of the matrix in the region of the perched water, estimated from the measurements of Hardin (1996), is on the order of 2 x $10^{-7}$ m/day; fracture hydraulic conductivity based on that figure is on the order of 2 x $10^2$ m/day. The nine orders of magnitude between fracture and matrix hydraulic conductivity is strong evidence of a fracture-dominated system. Even if the estimate of effective

| Test type | Model | Conditions | $T_{eff}$ (m$^2$/day) | Notes |
|---|---|---|---|---|
| pumping | Gringarten-Ramey (1973) | discrete fracture | 0.161 | poor recovery match |
| pumping | Warren-Root (1963) | dual porosity | not available | no straight line formed |
| recovery | Theis (1935) | confined/unconfined, porous | 0.18 | homogeneous, isotrop. assumpts. |
| slug | Cooper et al. (1967) | confined; unsteady-state | 0.167 | less close match for late times |
| slug | Bouwer-Rice (1976) | unconfined, steady-state | 0.057 | system may not be steady-state |
| slug | Karasaki (1988) | linear/radial flow | 0.17 | based on values from other models |

Table 3.1 Comparison of aquifer test results for various models

hydraulic conductivity is used for comparison, that value is still on the order of 350 times greater than the matrix hydraulic conductivity.

## 3.5 Conclusions

Modeling efforts of the pump test and slug test data indicate an effective aquifer transmissivity on the order of 0.16 to 0.18 m$^2$/day. Perhaps more important than the calculation of effective transmissivity, however, is the fact that these results show that the Apache Leap system is more accurately portrayed by a discrete fracture model than by a dual-porosity model, due to the extremely low permeability of the matrix compared to that of the fractures. Estimated fracture hydraulic conductivity is nine orders of magnitude greater than estimated matrix hydraulic conductivity, demonstrating that the Apache Leap perched aquifer is a fracture-dominated system. These figures are supported by the linear/radial flow model of the slug test data.

The estimates of aquifer transmissivity and fracture and matrix hydraulic conductivities were based on the limited amount of data that were available, and on the best fit of the data to the models; "best" was not, in all cases, terribly close. In addition to possible inaccuracies of the data due to the mechanical setup and data collection processes, deviations of the natural system from the various assumptions of the models could have further affected the outcome of the tests. Regardless of the uncertainties of the specific values that were calculated, however, the system was shown to exhibit behavior characteristic of a fracture-dominated system, which was the goal of this portion of the investigation.

# CHAPTER 4

# MECHANISMS FOR THE FORMATION OF PERCHED WATER IN THE APACHE LEAP TUFF

## 4.1 The Occurrence of Perched Water Zones in Tuff

### 4.1.1 Apache Leap

A perched water zone in the Apache Leap Tuff was identified 152 m below the surface in the deep slant borehole (DSB) (Figure 4.1; also refer to Figure 2.1). The zone is 110 meters below the approximate boundary between the white and gray stratigraphic units, and exists entirely in the gray unit. Perched water was also identified 149 m below the surface in the vertical observation borehole (VOB), collared 15 m upgradient from the top of the DSB (Figures 4.1 and 2.1). At the depth of the perched water, the VOB is a lateral distance of approximately 150 m from the DSB.

At Oak Flats (refer to Figure 2.1), perched water zones were identified at 110, 148, and 448 m below the surface (Figure 4.1). The geologic log from the Oak Flats core (Sample Management Facility, 1990) does not differentiate the stratigraphic units. The surface of the Apache Leap Tuff in the vicinity of Oak Flats was determined by Peterson (1961) to be one of the stratigraphically highest sections of the tuff remaining; although the surface elevation of Oak Flats is approximately 65 m lower than that of the DSB and VOB, the Oak Flats surface may well be stratigraphically higher, due to the undulating original surface on which the tuff was deposited.

As discussed in the Introduction (Section 1.3.3.2), Bassett et al. (1994) used borehole records of first appearances of water, together with spring elevations to generate

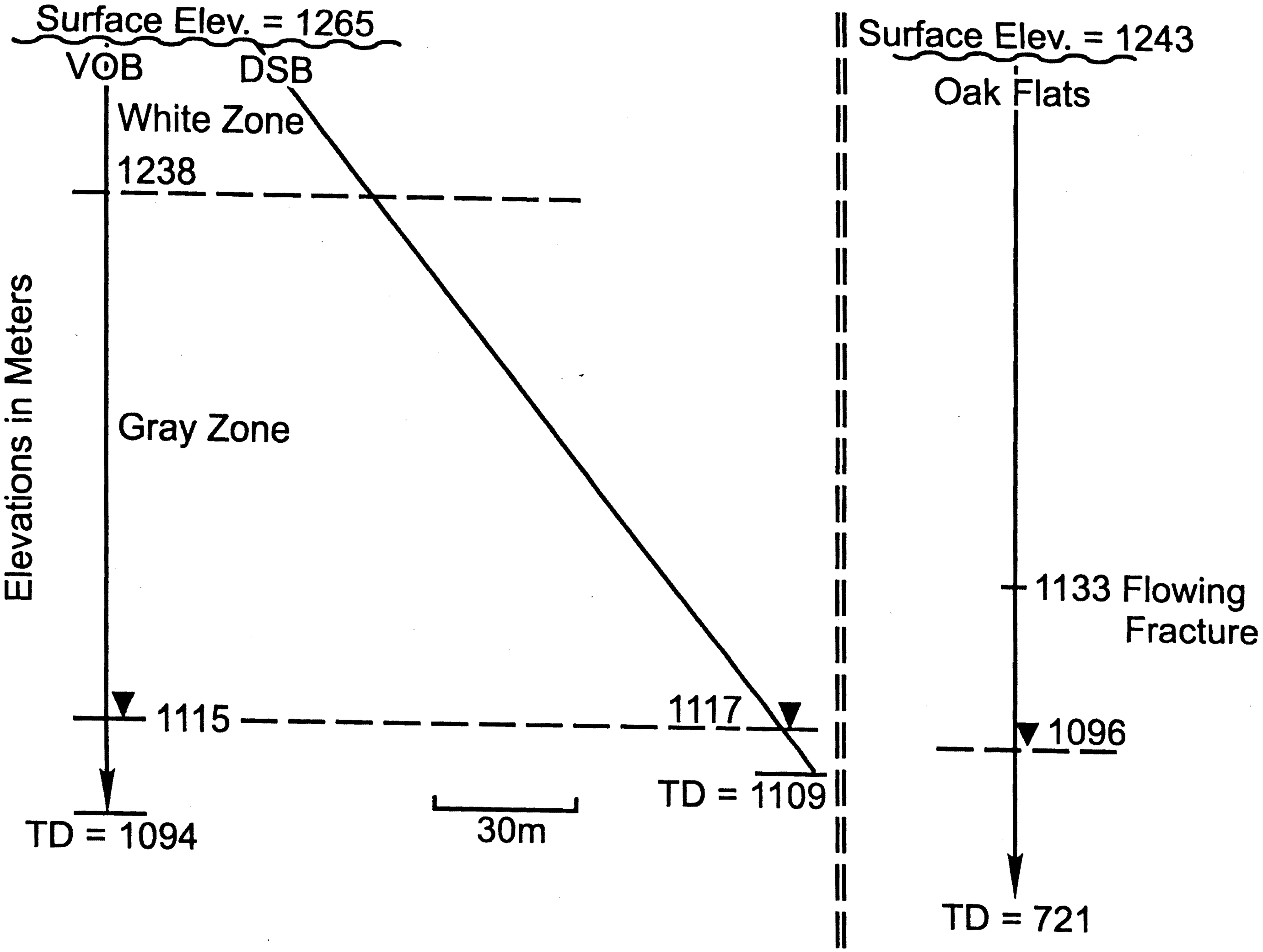

Figure 4.1 Schematic cross-section showing relation of boreholes and perched water.

Figure 1.4, which shows a surface representing the elevation of the uppermost perched zone over an area of approximately 16 km$^2$. While this figure indicates that perched water is prevalent across the region, determination of whether the mapped surface represents one continuous, or numerous discrete, perched zones could not be made without additional data.

### 4.1.2 Yucca Mountain

At Yucca Mountain, perched water zones have been encountered in several different stratigraphic or structural locations, in several different tuff units. According to Wu et al. (1996), perched water locations include: just below a zone of fractured rock, above the basal vitrophyre, below the contact of bedded tuff with partially welded pyroclastic flow, and in association with a major fault. Perched water has been found both above and below the basal vitrophyre unit (in separate borings), and in a visibly silicified zone in bedded tuff (Joe Rousseau, personal communication). None of the identified perched zones at Apache Leap have been associated with the vitrophyre (most borings have not penetrated that far), nor have visible low-permeability zones been identified, implying that a variety of settings may lead to the occurrence of perched water in tuff. Part of the licensing requirements for a repository at Yucca Mountain will be the answer to the question of where water becomes perched in tuff, and if the location can be predicted; clearly, an effort needs to be made to correlate these perched zones to some identifiable features.

## 4.2 Hypothesis

The goal of this portion of the research was to gain an understanding of the origin of the perched water zone in the Apache Leap tuff. The hypothesis to be tested was that the physical and hydrological characteristics of the tuff can be correlated to the location of the perched zone. Such a correlation would reveal the mechanisms which caused the perched zone to form. The perched zone was identified as a region where water flowed freely into the borehole, in sufficient quantity such that it could be pumped continuously at some relatively constant, if low, rate. Information used to study the characteristics of the perched zone included the data presented in Chapters 2 and 3: isotopic and geochemical properties of the waters in and above the perched water zone; measured hydrologic parameters of the perched zone; geophysical and measured parameters of the tuff; megascopic and microscopic observations of the tuff, including mineralogical, alteration, and structural features; and the lateral and vertical extent of perched water in the region.

## 4.3 Previous Work

Perched water zones are relatively common in the volcanic rocks of Hawaii, and generally occur in more highly permeable lava flows overlying less permeable ash and tuff (Davis and Yamanaga (1966), Takasaki (1971) and Souza (1983)). In the Mahantango Creek watershed in Pennsylvania, perched water occurs in a zone of rock fracturing which is underlain by less fractured sedimentary rocks (Urban, 1977). Perched aquifers occur in the Inner Basin of the San Francisco Volcano in northern Arizona, and are also the result of more permeable volcanic flows over denser, less fractured units (Montgomery and

DeWitt, 1974). In the Lower Henry's Fork region of eastern Idaho, perched water occurs 3in basalt lying above siliceous volcanic rocks (Crosthwaite et al., 1970). At Yucca Mountain, Scott et al. (1983) evaluated the geologic setting and rock physical properties, and proposed that local perched water tables could exist above relatively unfractured, nonwelded, highly porous but relatively nontransmissive zeolitized tuffs underlying highly fractured, densely welded, relatively nonporous but highly transmissive ash-flow tuffs. Later, Flint et al. (1993) used rock properties and climate models to determine that the most likely location for perched water to form in the Yucca Mountain proposed repository rock unit is above the basal vitrophyre, due to its extremely low porosity.

## 4.4 Possible Mechanisms for Perching

The simplest definition of a perched water body is that it is unconfined groundwater separated from a deeper, more regional body of groundwater by an unsaturated zone (Driscoll, 1986). Freeze and Cherry (1979) state the generally accepted concept that a layer of lower-permeability material can lead to the formation of a perched lens above it. The lower-permeability layer, or region, could conceivably be created by stratigraphic, structural, volcanic, or alteration processes. Fractured rocks increase the complexity of mechanisms for perching; such mechanisms are not commonly described. Potential mechanisms that could cause perched water to form at ALRS are introduced below, and illustrated in Figure 4.2.

### 4.4.1 Individual Flow Model (Figure 4.2a)

The Apache Leap Tuff consists of numerous individual flows which were

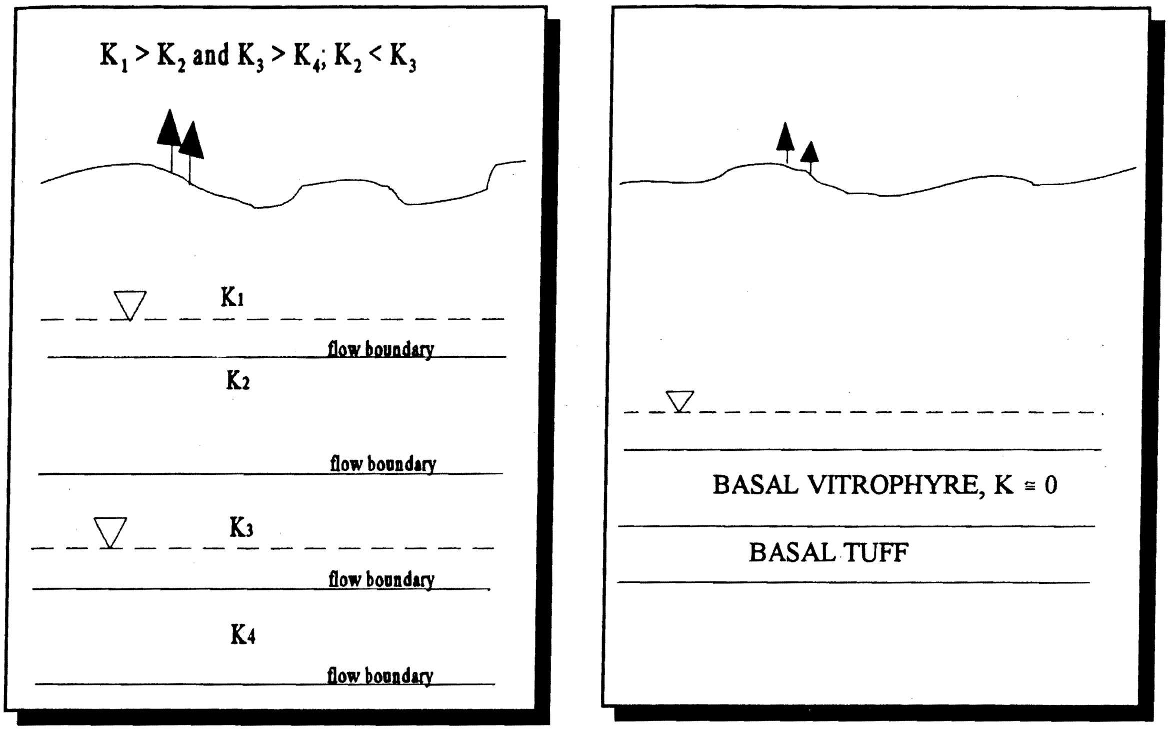

a. Individual flow model

b. Cooling zone model

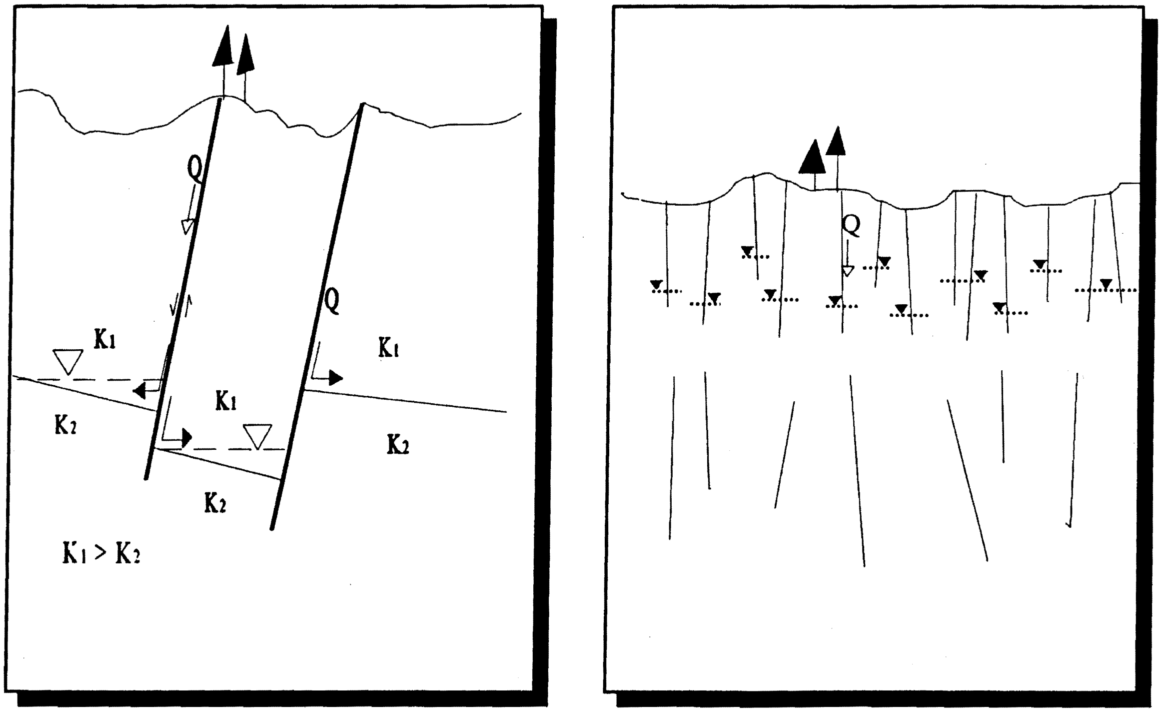

c. Faulting model

d. Fracture set model

Figure 4.2a-d Potential perching mechanisms.

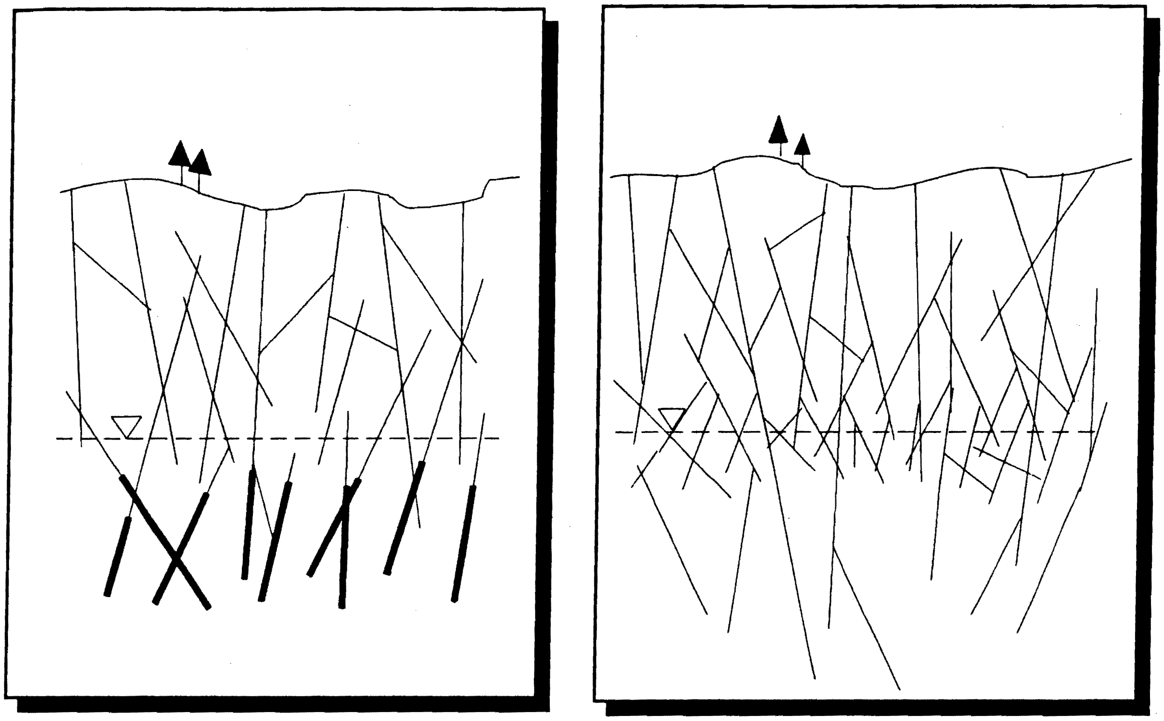

e. Fracture fill model

f. Fracture density model

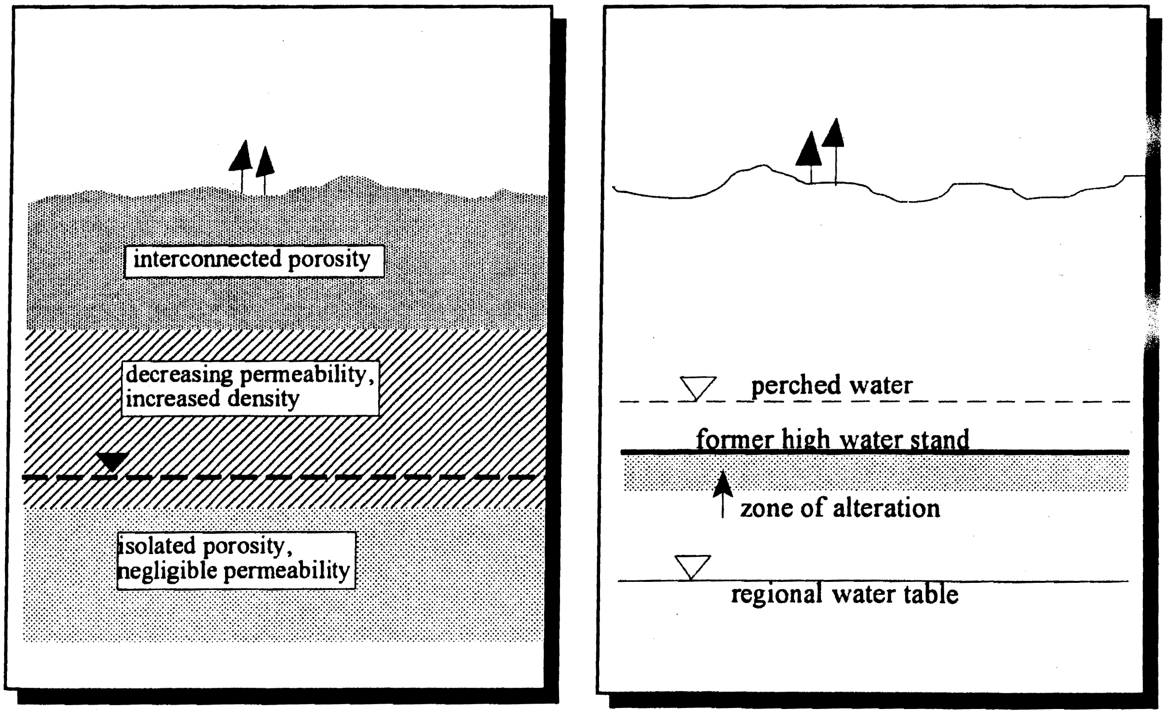

g. Matrix properties model

h. Weathering/chemical alteration model

Figure 4.2e-h Potential perching mechanisms, continued.

deposited in rapid succession and then cooled as a single unit (Peterson, 1961). Slight variations in the composition of flows, or enough time for slight cooling between flows, could potentially create a permeability contrast sufficient to create perched water. This model would be similar to the perched conditions that occur between individual volcanic units in Kilauea (Davis and Yamanaga, 1966). While individual flows have not been identified at Apache Leap, several separate perched zones were noted in the Oak Flats boring log, suggesting that conditions causing perched water may occur at different depths.

### 4.4.2 Cooling Zone Model (Figure 4.2b)

In a single cooling unit such as the Apache Leap Tuff, the typical cooling zones of a tuff deposit, as originally described by Ross and Smith (1961), are superimposed over the individual flows taken as a whole. Zones of vitrification or dense welding which characteristically form in the lower section of the unit would be expected to have very low permeability, and could therefore create a perched water zone. Perched water has, in fact, been found to form above the vitrophyre at Yucca Mountain (Wu et al., 1996).

### 4.4.3 Faulting Model (Figure 4.2c)

A third possible model for the formation of a perched zone at the ALRS arises from the fact that the region experienced significant faulting during and since the emplacement of the tuff (Peterson, 1961). The activity of faulting could have created channels or preferential flowpaths that would allow water to move quickly down through the formation. This model is a variation of the individual flow model, as heterogeneities in the vertical permeability are necessary, together with the faults, to create perched water "traps". Turner and Bagtzoglou (1995) proposed a version of this model as a mechanism for perched water formation at Yucca Mountain. This model could give rise to isolated basins separated by fault blocks, which may occur at Apache Leap.

### 4.4.4 Fracture Set Model (Figure 4.2d)

Perched water zones could also result from the existence of fracture sets which are not continuous (Wu et al., 1996). Fractures which carry water down from the surface could terminate at a similar depth and not be continuous with a different fracture set beneath them. Perched water could therefore collect at the base of the upper fracture set, as a series of disconnected, smaller perched zones (Figure 4.2d).

### 4.4.5 Fracture Fill Model (Figure 4.2e)

An increase in the degree of filling of fractures at depth could reduce the effective permeability of the tuff such that perched water could form. Water movement through the fractures from the surface would become reduced as fracture openings became restricted or blocked. This model would not require any change in the fracture network, but would require material to fill the fractures.

### 4.4.6 Fracture Density Model (Figure 4.2f)

The perched zone could be created by a change in the density of fractures. Burger and Scofield (1994) found that relative fracture density has a strong influence on the accumulation of perched water at Yucca Mountain. A relatively high fracture density in the upper portions of the tuff at Apache Leap could allow water to move down relatively rapidly. If a lower fracture density region was then reached, it would serve as a reduced permeability zone which could then cause perched water to form.

### 4.4.7 Matrix Property Model (Figure 4.2g)

A change in the matrix properties of the tuff, such as in the arrangement, size, or abundance of phenocrysts, pumice fragments, and/or lithic fragments; or in the devitrification and vapor phase crystallization effects on the matrix, could affect the degree to which pore spaces are connected. Pumice fragments may be flattened at depth, and either devitrified or completely vitrified, either of which could influence the movement of water through the rock. A decrease in the effective permeability caused by such changes could result in perched water.

### 4.4.8 Weathering/Chemical Alteration Model (Figure 4.2h)

In the final model, the perched water table could have been created by a former high stand of the regional water table. Water saturating the formation could have created a chemically altered zone, such that the product of feldspar weathering created a clay-rich, reduced permeability zone sufficient to cause perching.

The perched zone at the ALRS is likely to be the result of one or a combination of the above models. In this portion of the research, existing and new data were compiled and compared, with the objective of eliminating some of the models and confirming the validity of others.

## 4.5 Evaluation of Models Against the Data

### 4.5.1 Individual Flow Model

The boundary between individual flows as a mechanism for perching at the ALRS does not appear to be a likely model, primarily because no flow boundaries were identified after further investigation, and the zonation characteristics of the entire unit are typical of one single cooling unit. A boundary between flows would be likely to be characterized by a break in porosity or density trends with depth (Peterson, 1961), or perhaps by a thin clay layer that formed from ash deposited at the surface of a flow subsequent to burial (Peterson, pers. comm.). While 100% continuous core through and below the perched water zone was not available for inspection, the lithologic, petrographic, and mineralogical data that were available did not support this model for perching.

### 4.5.2 Cooling Zone Model

The cooling zone model has been shown to be a mechanism for perching at Yucca Mountain above the basal vitrophyre (Wu et al., 1996). The perched zone beneath the ALRS is clearly well above the vitrophyre, and above the zone of densest welding. However, it does occur in the transition region between moderately to densely welded tuff. The hydraulic conductivity measurements by Hardin (1996), which show a decrease to nearly impermeable matrix conditions in the perched water region, suggest that the increase in degree of welding may have been a factor in the formation of the perched water zone at that location. Thus, the cooling zone model may be a valid model, alone or in combination with other models, at Apache Leap.

### 4.5.3 Faulting Model

Numerous large-offset, nearly-vertical faults have been mapped over the surface of Apache Leap by Peterson (1968), and many faults with smaller offsets are presumed to exist in the region, but are difficult to identify in the field because the characteristics of the tuff change only gradually with depth (Peterson, 1961). The geophysical results by Hardin and Bassett (1995) suggest that the lower portion of the DSB intercepted a fault zone that the VOB did not. The fault zone model calls for preferential flow along the fault zone which would allow large quantities of water to reach the subsurface. The DSB core analysis did show an increase in the amount of fracture filling and sealing in the DSB fault zone that could help produce a hydrologic trap, however that zone is above the perched water zone. The VOB did not show similar characteristics in terms of a fault zone, according to the geophysical investigation (Hardin and Bassett, 1995), yet the perched zone is present, suggesting that while faulting may aid in transporting water to the subsurface, faulting alone is not the mechanism for perching at the ALRS.

### 4.5.4 Fracture Set Model

Fractures have been demonstrated to be the primary pathway by which water is recharging the perched zone, as shown by the isotopic and geochemical results of Davidson (1995), the geophysical results of Hardin and Bassett (1995), and the results of the aquifer test analyses. Pervasive fracture sets have been mapped at the surface by Thornburg (1990), and the DSB core analysis showed an abundant, and increasing, number of fractures throughout the length of the borehole, as was also seen in the borehole video logs and the COLOG images from the VOB. Attempts to project major fractures intercepting the DSB at depth up to the surface have not resulted in a positive identification of the fractures at the surface (Stephens, personal communication), but that fact does not mean that the fractures are not connected. In order for this model to be viable, the fracture set that is recharging the perched water zone from the surface would have to be shown to terminate below the perched zone, and the evidence for that is inconclusive. Furthermore, the apparent regional expanse (Figure 1.4) of the perched water suggests that the system is not composed of individual, small perched zones. Thus, this model is neither accepted nor rejected based on the available information.

### 4.5.5 Fracture Fill Model

This model calls for an increase in filled fractures beneath the perched water table. The thin-section analysis revealed an increase in the appearance of thin, silica-filled fractures in the lower 17 m of the DSB. The macroscopic inspection of BHP's borehole MB10-A revealed an increase in filled fractures below 200 m, most noticeably at 290 m. The Oak Flats core log indicated increased silica mineralization in a region between the two uppermost perched zones, at 122-128 m depth, and again much deeper at 360-372 m. Also, Hardin (1996) observed an increase in macroscopic silica-mineralized fractures in the lower portion of the Oak Flats borehole. As discussed in the previous section, the hydrologic data strongly support fracture flow as the primary means by which water moves through the unsaturated zone to the perched water zone. The physical evidence suggests that an increase in filled fractures may be a mechanism to reduce permeability once the water reaches the perched zone.

### 4.5.6 Fracture Density Model

Evaluation of this model is similar to that of the fracture set model. The hydrologic data indicate that fractures are a contributing mechanism for the formation of the perched zone, and the physical data, including borehole geophysics, the borehole imagery, and the DSB and MB10-A core analyses, suggest that fracture density increases with depth to approximately the perched zone; this trend could be due to faulting, however. To unequivocally accept this model, additional fracture density information is needed from further beneath the perched zone than the DSB and VOB extend. However, data from the Oak Flats core (Hardin, 1996) and BHP boring MB-10A do show a reduction in fracture density at depths below the perched zone, lending support for this model.

### 4.5.7 Matrix Property Model

In this model, changes in the properties of the matrix are responsible for the reduced permeability zone that causes perched water to form. The data showed considerable support for this model. First, the lithologic data showed that porosity is correlated to the crystallized pumice fragments, which become increasingly flattened, more discrete, and less connected with depth. The petrographic data supported that finding on a microscopic scale, as the epoxy-impregnated thin sections showed increasingly larger regions of virtually no permeability with depth, especially in the region of the perched water zone. Analysis of the alteration characteristics further explained the association of porosity with the pumice fragments: the pumice served as loci for entrapped gasses and were subsequently crystallized, often by vapor phase crystallization, which could leave small amounts of pore space remaining. Hardin's (1996) matrix hydraulic conductivity measurements showed a reduction to nearly impermeable conditions in the perched zone region, which was supported by the increased density and reduced porosity measurements in that region by Hardin and Bassett (1995). The isotopic and geochemical data from Davidson (1995) indicate that matrix water constitutes only a small fraction of the water in the perched zone. Finally, the aquifer test analyses showed that matrix flow in the perched zone is insignificant compared to the magnitude of fracture flow that occurs. Thus, the data overwhelmingly support changes in matrix properties as a mechanism responsible for causing perched water at Apache Leap.

### 4.5.8 Weathering/ Chemical Alteration Model

This model calls for a previous high stand of water to have accelerated chemical weathering such that significant production of clays and related minerals created a low permeability zone. The physical evidence refutes this model for two reasons. First, none of the lithologic, petrographic, or mineralogic investigations identified evidence of such chemical weathering in or beneath the perched zone. The XRD analyses showed no change in clay abundance, which was already relatively low, in that region, nor were any weathering-related changes in mineralogy or texture, such as concentrations of iron hydroxides, aluminum hydroxides, weathered phenocrysts, or residual oxyhydroxides of iron and aluminum observed in thin section. Porosity reduction in the tuff was shown in the epoxy-impregnated thin sections to occur gradually. Second, if the tuff was susceptible to increased chemical weathering, such weathering would have been likely to have been observed in the region above the present perched water table, at the former level it maintained before the BHP mine began extensive pumping 24 years ago. Hardin and Bassett (1995) and Davidson (1995) observed some evidence of increased alteration in that region of the DSB, but such evidence could also easily be attributed to a fault zone which crossed the borehole at that depth. Therefore, this model does not seem to be a valid mechanism for perching water at Apache Leap.

## 4.6 A Model for Apache Leap

Table 4.1 summarizes the evaluation of the physical and hydrologic characteristics of the tuff against the potential perching models. Two mechanisms are clearly shown to influence the formation of the perched zone at Apache Leap. First, fracture flow appears to be responsible for the transport of water from the surface to the perched zone, as indicated by the isotopic, geochemical, geophysical, and aquifer test data. Second, very low matrix porosity and permeability is responsible for the lack of, or severely reduced, transport of water through the perched zone, as indicated by the lithologic and

| | indiv. flow | cooling zone | faulting | fracture set | fracture fill | fracture density | matrix property | weath./ alter'n |
|---|---|---|---|---|---|---|---|---|
| lithology | x | x | | | | | 3 | x |
| petrography | x | 1 | | | 2 | | 3 | x |
| mineralogy | x | | | | | | | x |
| fracture char. | | | 1 | 1 | 2 | 2 | | |
| alteration char | | | x | | 2 | | 3 | x |
| porosity/ perm. | x | 1 | | | | | 3 | |
| isotopes | | | | 0-1 | 0-2 | 0-2 | 3 | |
| geochem | | | | 0-1 | 0-2 | 0-2 | 3 | |
| geophysics | | | 1 | 0-1 | 0-2 | 0-2 | | |
| aquifer test | | | | 0-1 | 0-2 | 0-2 | 3 | |

Table 4.1 Evaluation of Apache Leap Tuff physical and hydrologic characteristics against perching models. x = data refutes model; 0 = data indeterminate; 1 = data may support model; 2 = data support model; 3 = data strongly support model.

petrographic data, alteration characteristics, and porosity and permeability data. Thus, the matrix property model is accepted, and one or a combination of the fracture models must be accepted as well. Both the fracture fill model and the fracture density model are supported by data from the deeper boreholes. The petrographic data and fracture characteristics from the bottom of the DSB, and from Oak Flats and MB-10a indicate an increase in fracture filling by silica minerals below the perched zone, and a decrease in fracture density, as well. The silica mineralization is likely to have been more prevalent in the deeper part of the tuff because of prolonged higher temperatures favoring silica dissolution and subsequent reprecipitation.

A combination model is therefore proposed to explain the formation of the perched water table at the ALRS. Figures 4.3 and 4.4 illustrate two versions of such a model; both feature changes in the matrix property with depth, fractures as the primary recharge mechanism, and filled fractures beneath the perched water zone. Figure 4.3 illustrates a possible model for the region that includes the DSB, showing a fault intercepting the borehole, and the increased fracture density associated with it. The model must be applicable to a larger area than just the location of the DSB and VOB, however, as perched water has been identified over at least a 16 km$^2$ area of Apache Leap Tuff (Figure 1.4). Figure 4.4 presents a more generic model for the entire region. The mechanisms that have been proposed would appear to fit a regional model. Peterson (1961) documented the consistency of petrology, mineralogy, and fracture pattern of the unit over much of the entire Apache Leap deposit, and showed that the deposit is a single cooling unit. This information suggests that the matrix properties would in turn be likely to be

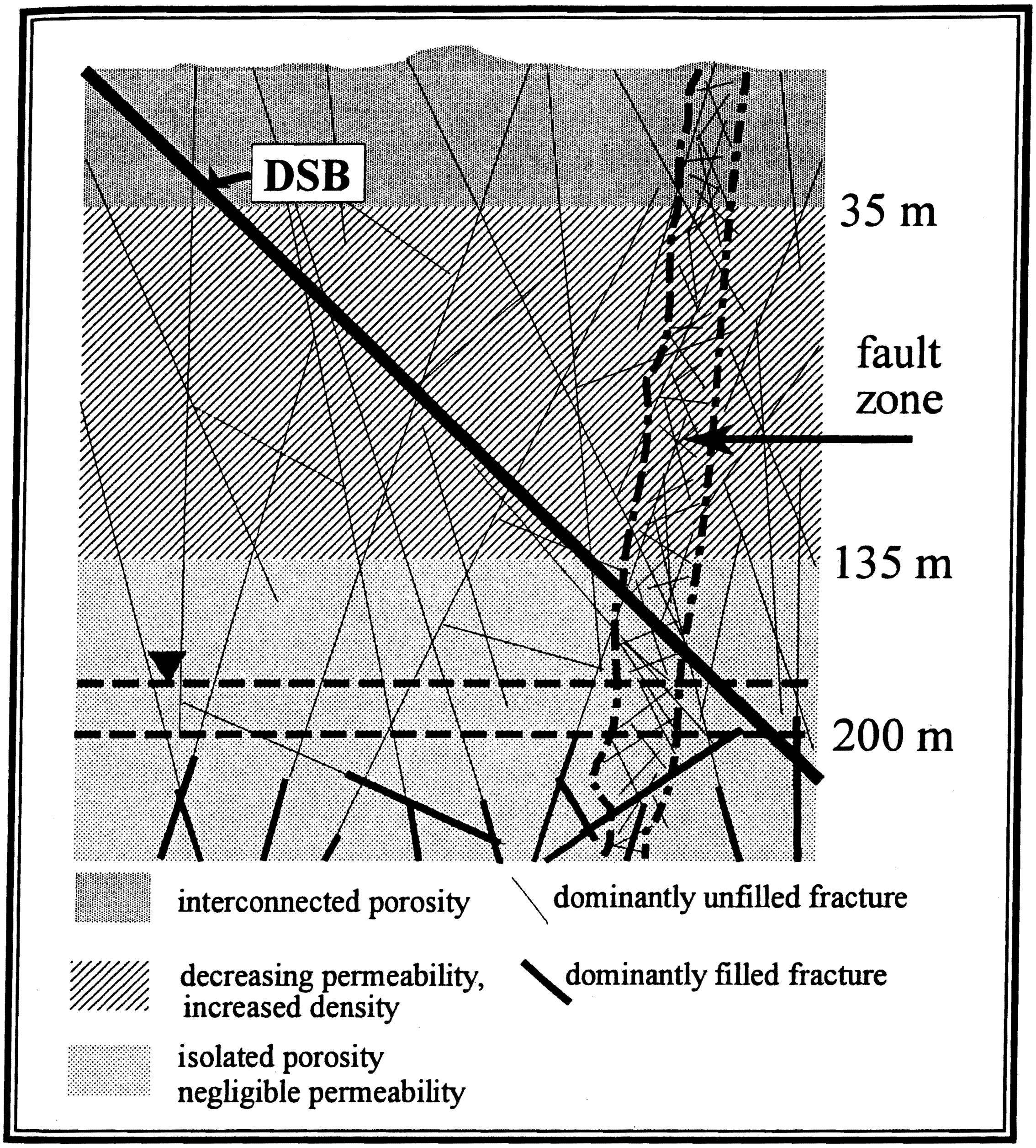

Figure 4.3 Combination model for perched water in the vicinity of the DSB at ALRS.

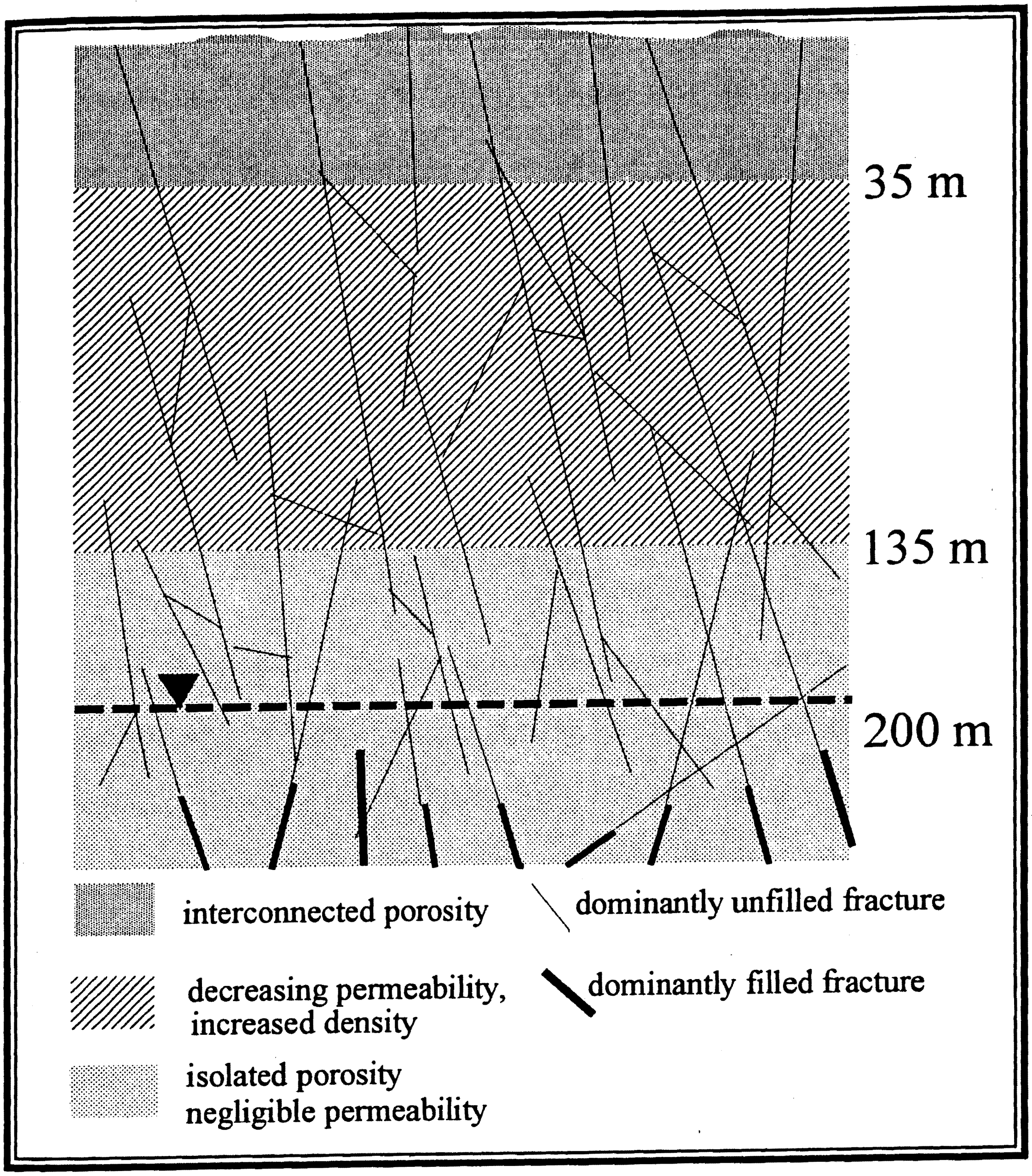

Figure 4.4 Generalized combination model for perched water over the ALRS region

consistent over the region. Furthermore, the zone of greatest welding and heat would also be expected to be continuous over approximately the same depth, allowing for topographic variations, such that fracture filling would occur in a similar pattern over the region. Thus, the proposed combination model appears to fit for the Apache Leap region as well as the ALRS in particular.

## 4.7 Discussion

The combination model for the formation of the perched water zone at Apache Leap fits the conditions of the uppermost perched zone, but may not necessarily explain the formation of deeper perched zones at Apache Leap, or of any of the perched zones at Yucca Mountain. This research has shown that many different factors can or might influence the movement of water through fractured, welded tuff. Both matrix properties and fracture characteristics appear to exert strong influence on fluid flow, and should be considered when evaluating locations for the potential formation of perched zones.

One of the primary issues of concern at Yucca Mountain is that a perched zone could form above or near a repository, and potentially either flood the repository, or expedite the transport of radionuclides away from the repository to the accessible environment. One characteristic of the rock that must be present is enough space for a significant amount of water to collect such that it would flow. If the rock has such low porosity that it can only contain a small amount of water, even if it is fully saturated, then a "perched water" zone in such a location should not be a concern. Therefore, a feature that creates additional reservoir rock could be of great importance in low permeability tuff. Such a feature could exist in a region of shattered tuff broken up by faults or fractures, creating void space sufficient to collect and hold quantities of water to enable flow to occur.

## 4.8 Conclusions

The evaluation of the physical and hydrologic characteristics of the Apache Leap Tuff against eight potential models of perching mechanisms resulted in the elimination of some of the models, and the acceptance of others into a combination model that fits the conditions of Apache Leap. Matrix properties and fracture characteristics were determined to be the most significant factors contributing to the formation of the perched zone. The porosity in the matrix is generally associated with pumice fragments; the pumice fragments become more flattened and isolated with depth, such that both porosity and permeability are reduced to very low values in the perched water region. Fracture flow is the primary mechanism by which water is transported from the surface to the perched zone, and an increase in the amount of fractures that are filled, typically by silica mineralization, beneath the perched zone suggests a reduction in the secondary permeability at the perched zone as well. Other factors which could contribute to perched zone formation include a reduction in fracture density or disconnected fracture sets; Oak Flats and MB-10A data offer support for a fracture density reduction with depth. Perching models calling for weathering and chemical alteration by a former high stand of water, or for permeability changes between individual flow units, were found not to be supported by any of the data.

While the combination model that has been described fits the data collected from Apache Leap, it is not the only combination of mechanisms that could cause perched water to form in fractured, welded tuff. This portion of the research has shown that numerous factors must be considered, ranging from microscopic to megascopic in scale, in order to assess where such zones could form.

# CHAPTER 5
# INFILTRATION MEASUREMENTS FROM THE WATER BUDGET

## 5.1 Introduction

A major goal of this research was to determine what fraction of precipitation is available for recharge to the perched water zone. In the previous two chapters, fractures were identified as the primary pathway by which water reaches the perched zone. If the fractures act as direct pathways, a significant portion of water might be expected to enter the subsurface. However, in arid to semiarid environments, as much as 95% of precipitation has been shown to be lost by evapotranspiration (Harshbarger et al., 1966), suggesting only a small proportion of water infiltrates to the subsurface. Thus, the objective of this portion of the research was to determine the significance of fractures to infiltration in the environment of Apache Leap.

## 5.2 Hypothesis

In a water budget for a basin, the amount of water entering a basin that does not exit by runoff is stored near the surface in puddles and in the soil and fractures. From the storage locations, water proceeds either to evaporate and be used by plants for evapotranspiration, or to infiltrate through the soil, fractures, and rock matrix. The conditions of saturation prior to a storm will determine how much water runs off, and how much goes to storage. In an arid environment such as at ALRS, most of the storage component is expected to evaporate, rather than slowly infiltrate. However, the fractures in the tuff could serve as direct conduits for water movement into the subsurface, allowing a greater fraction of the total water budget to enter the subsurface. Thus, the hypothesis to be tested is that fractures increase the transport of water into the subsurface over the amount that typically infiltrates in a semi-arid to arid environment.

## 5.3 Water Budget Approach to Measurement of Infiltration

Infiltration can be measured directly with such instruments as infiltrometers or lysimeters, which are placed directly on the surface and measure the amount of water that passes through the interface to the subsurface over time. These methods generate values for the single point at which the measurement is made; in order to obtain a meaningful estimation of infiltration at ALRS, a seemingly infinite number of such measurements would have to be made to account for all the variations in surface cover, vegetation, fracture density, soil depth, slope and aspect at the site. An alternative to the direct measurement approach is to use the components of the water budget to calculate infiltration. The water budget is determined on a watershed-size scale, which therefore averages conditions over a large area. The ALRS watershed used for this study was shown in Figure 1-2.

In a water budget, precipitation (P) into an watershed is balanced by runoff (R), evapotranspiration (E), and infiltration (I):

$$P = R + E + I \tag{5.1}$$

This budget assumes no net groundwater flow into or out of the basin, and no change in surface water storage over time. These assumptions were considered to be valid for the ALRS watershed. Precipitation can be directly measured with recording rain gages, and runoff can be directly measured with recording flumes. Evapotranspiration can measured by both direct and indirect means, so that infiltration is the only unknown in the equation.

### 5.3.1 Direct Evapotranspiration Measurement with an Energy Balance

Evapotranspiration can be measured directly through the use of an energy budget. In the energy budget, net incoming solar radiation, $R_n$, is balanced by energy used to heat the air (sensible heat flux, H), energy to heat the soil and rocks (soil heat flux, G), and energy used to evaporate water from the ground and vegetation (latent heat flux, $L_e$). Evaporation from an area over time can be determined by:

$$E = L_e / \lambda \tag{5.2}$$

where $\lambda$= latent heat of vaporization.

The latent heat flux can be calculated directly from measurements of a temperature and relative humidity gradient between two elevations, soil temperatures and temperature changes, and net radiation, using the Bowen ratio energy balance (BREB) method. The theory behind the BREB method is explained fully in Appendix E, and is summarized here. The Bowen ratio ($\beta$) is the ratio of the sensible heat flux to the latent heat flux:

$$\beta = H / L_e \tag{5.3}$$

It can be calculated by multiplying a constant to the ratio of a temperature gradient to a vapor pressure gradient, where the gradients are the difference between measurements from two elevations:

$$\beta = c\,(T_2 - T_1) / (e_2 - e_1) \tag{5.4}$$

where c is the psychrometric constant, T is temperature, and e is vapor pressure. Subscripts 1 and 2 refer to elevations. The Bowen ratio is related to the latent heat flux by:

$$L_e = (R_n - G)/(1 + \beta) \qquad (5.5)$$

Net radiation and the soil heat flux can be obtained from field measurements, as can the temperature and vapor pressure gradients. Because the BREB method uses values from meteorological sensors, the fluxes obtained are representative of the conditions upgradient from the recording location, thus they represent an average over an area.

The BREB system was originally developed for use over crops, and is typically deployed in relatively flat, vegetated regions for short durations (one day to one month) (Bingham et al., 1987; Dugas et al., 1991; Cellier and Olioso, 1993); its success as a long-term method for providing evapotranspiration data in natural settings had not been rigorously tested at the start of this investigation. The instrumentation required to measure the fluxes for the BREB method is sensitive to weather extremes, and requires regular maintenance and recalibration.

### 5.3.2 Indirect Measurement of Evapotranspiration Using a Biosphere-Atmosphere Transfer Scheme (BATS) Model

Evapotranspiration values can be modeled using the field-measured parameters of temperature, relative humidity, vapor pressure, total incoming and net radiation, wind speed, and precipitation. The advantage of this approach over direct measurement methods such as the BREB is that the data needed for modeling are collected relatively easily and reliably over long periods of time and from remote locations.

Soil-vegetation-atmosphere transfer schemes (SVATS) are one-dimensional submodels that have been developed to describe the interactions between the soil, vegetation, and atmosphere. SVATS models are generally used to provide input for larger- scale global change models (GCMs), however, the flux information that they provide can stand alone. One of the more commonly used SVATS is the Biosphere-Atmosphere Transfer Scheme (BATS) model developed by Dickinson et al. (1993), which is the model used in this investigation.

The BATS model uses the field parameters listed above to calculate a wide variety of fluxes and measurements, including evapotranspiration. In addition to the field data, the model is further keyed to a particular site by a separate list of soil and vegetation input parameters specific to the site. These parameters include soil texture, albedo, initial moisture content, and long-term average temperature; and fractional vegetation cover, and vegetation transpiration and root zone characteristics. The BATS model does allow the option of choosing default soil and vegetation settings for a semi-arid climate; these default parameters represent average conditions for all such climates world-wide, and therefore are likely to depart from specific site characteristics for at least some parameters. Therefore, this option was not used for the ALRS data. Once the data and site parameters are input, the model can be calibrated with additional field-measured data, such as either directly-measured evapotranspiration or runoff data.

## 5.4 Previous Work

Gay (1985, 1993) advocated the use of the energy balance method for determining catchment-scale water balances. According to Gay, the energy balance is preferable over direct measurements by lysimeters because the lysimeter method is costly, transport of the instruments is difficult, and lysimeters represent specific point measurements that are not necessarily representative of the surroundings in a natural setting. Amiro and Wuschke (1987) used the energy balance method in a boreal forest drainage basin containing regions of both bare rock/jack pine forest upland and aspen willow forest lowland. Their results agreed well with precipitation minus runoff measurements for the basin, allowing the remainder to be attributed to infiltration or spring discharge, depending on the season. Vogt and Jaeger (1990) and Culf et al. (1993) also used the energy balance method to estimate the water budget in a pine forest and a patterned woodland/bare soil setting, respectively. In both cases, surface cover was highly variable, making representative measurements of direct infiltration difficult.

An energy balance can be determined for an area by several different methods; the BREB system described previously, and the eddy correlation system are two of the more commonly used methods, due to their reported accuracy. The BREB method has been successfully employed for measuring evapotranspiration over crops (Bingham et al., 1987; Dugas et al., 1991; Cellier and Olioso, 1993), which represent flat, homogeneous surfaces. Several authors have successfully used the method over forests, however, where more turbulent conditions are expected (McNeil and Shuttleworth, 1975; Spittlehouse and Black, 1979 and 1980; Shuttleworth et al., 1988). Several studies compared the results from the BREB method to eddy correlation measurements (Spittlehouse and Black, 1979 and 1980; and Dugas et al., 1991), and found the results comparable. Wilson et al. (1992) presented the results of several studies comparing the BREB method to eddy correlation, hand-held porometer, and remote sensing methods in the arid natural desert environment of Owens Valley, California. They concluded that on a daily basis, all of the systems tested could adequately describe water loss from the site, although on an hourly basis noticeable variation occurred. The tests were performed over a 4-day period in June; the authors concluded that averaging values over an even longer period, such as monthly, would further reduce the variations between methods.

Previous efforts to employ a water balance to quantify water infiltration at ALRS were made by Rasmussen and Evans (1993). They instrumented two smaller watersheds adjacent to the one used in this investigation, and employed three different methods to evaluate the rainfall-runoff relationship. Their methods included annual total rainfall minus runoff calculations, the USDA curve number method for individual storms, and a mass balance for four major storms. The instrumentation in the watersheds included one common recording rain gage, and flumes at the outlet of each watershed. Evaporative losses were estimated from pan evaporation data obtained at a location 150 km to the south of ALRS. The results of the investigation for each method were not comparable between methods, and indicated the complexity of the infiltration process for fractured rock.

Unland et al. (in review) compared the BREB, eddy correlation, and sigma-T methods for measuring energy fluxes at the surface, and used such measurements to calibrate and evaluate the energy fluxes produced by the BATS model. Their field site was in the semi-arid Sonoran Desert just west of Tucson, Arizona, about 160 km from the ALRS, at a slightly lower elevation than the ALRS. Comparison of the fluxes produced by direct measurements showed acceptable agreement among all three methods when data were available; the authors reported substantial problems associated with the field collection of data by all methods, including the BREB system. The BATS model was shown to reasonably accurately describe the energy fluxes that were observed; the accuracy was improved by careful tailoring of the model using the site-specific vegetation and soil parameters.

## 5.5 Data Collection

### 5.5.1. Precipitation

Precipitation measurements were obtained from two recording rain gages placed at ground level, one at a centrally-located micrometeorological station (described below), and one at the top of the watershed. The gages recorded tenths of millimeters of precipitation by a mechanism that tips to one side, sending an electronic pulse to the datalogger, every time 0.1 mm is collected. They were calibrated by adjusting the tipping mechanism. According to the manufacturer, the gages had an accuracy of 1% at rainfall rates of 50 mm/hr or less. In addition to the recording rain gages, thirteen plastic, wedge-shaped, nonrecording gages were placed throughout the watershed in a variety of settings, to monitor spatial variability of rainfall. These gages were read during regular site visits, which were generally not immediately after each rain event.

### 5.5.2. Runoff

Runoff out of the watershed was recorded by two H-L flumes installed at the watershed drainage outlet. A large flume was used to record discharges greater than 0.01 $m^3/s$, and a small flume downstream of the larger one was used to record discharges up to

0.01 $m^3/s$. Overlap of the range which the flumes were capable of measuring existed, however. The flumes were each equipped with a 2.5 psi gage-type vibrating wire pressure transducer which was sensitive to a 2 mm change in head, translating to a discharge sensitivity of 2.55 L/s for flows greater than 4 L/s. Flows of less than 4 L/s were not readily distinguishable from random transducer fluctuations. Both of the transducers were connected to dataloggers for long-term data recording.

### 5.5.3. Evapotranspiration

To acquire the necessary measurements for the BREB calculations and the BATS modeling, an automatically recording micrometeorological station was set up in the watershed in the fall of 1993. The specific location for installing the station was chosen in an attempt to represent the average conditions in an area that exhibits mostly extremes. The weather station was situated approximately midway both crosswise and lengthwise in the watershed, but slightly closer to the bottom for access purposes. The area immediately surrounding the station contains both bare rock, sandy soil, and vegetation, so a mixed cover is monitored. A 6-m high tower was installed to place the instruments above the local vegetation, but not so high as to be above the local climatic conditions.

An "off-the-shelf" Bowen ratio system manufactured by Campbell Scientific, Inc. (CSI) was set up at the micrometeorological station in the watershed, shown in Figure 5.1. All of the sensors were wired to a CSI CR-10 datalogger mounted on the tower, which also held other weather monitoring instruments, including two 1.5-m long "arms" extending out parallel to the ground and holding some of the sensors. The datalogger was kept in a weatherproof box which also contained the dew point hygrometer used to

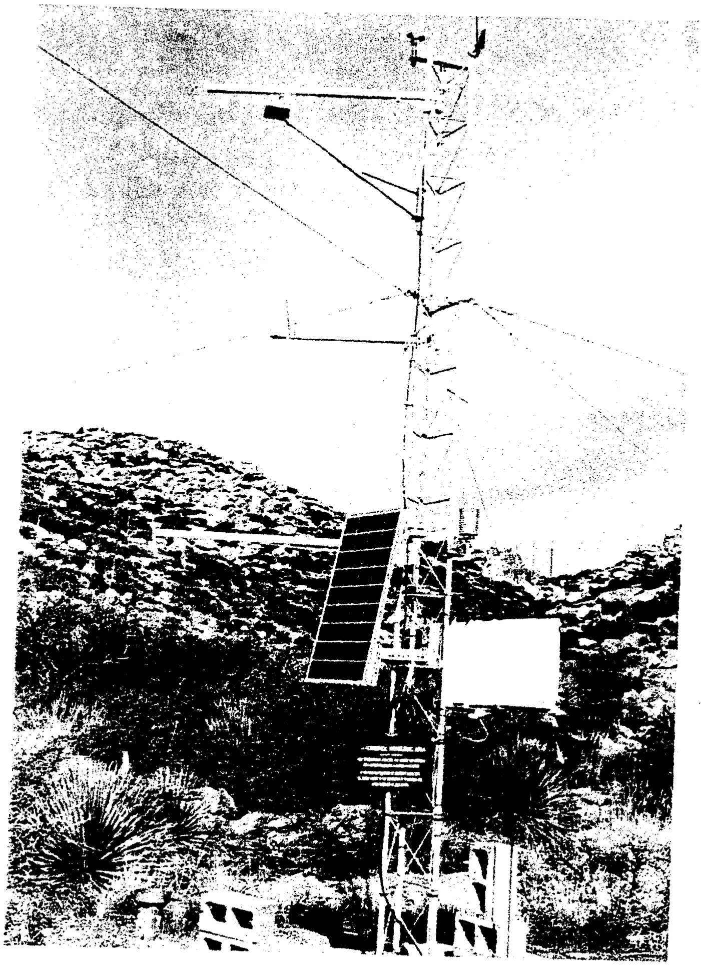

Figure 5.1 Micrometeorological station set up in the ALRS watershed

measure the vapor pressure gradient. The datalogger and hygrometer were powered by a single deep cycle marine battery which was recharged by a 51-watt solar panel. Measurements were made in intervals of 1 or 10 seconds, and 20-minute averages were recorded until January, 1996, when the BREB system was shut down due to perpetual mechanical problems.

The temperature gradient for the BREB system was measured every second by 75-µm diameter chromel-constantine thermocouples located at the end of each arm. The arms were 4 m apart vertically. Each thermocouple had two parallel junctions to minimize loss of data. The differential voltage created by the difference in temperature between the two arms was measured by the datalogger; the resolution of the datalogger was 0.006°C.

The vapor pressure gradient was measured through the difference in relative humidity between the two arms. Filtered air-intake ports were located midway out the arms, and a pump ducted the air to 2-liter buffering containers. The air from the different heights was ducted alternately to a common dew point sensor, minimizing instrument error. The air was buffered in temporary storage to minimize any possible impact of the fact that the two heights were sampled at slightly different times. Air was ducted from a given arm for two minutes, during which time measurements were made every second, before switching to the other arm. Thirty seconds were allowed to elapse immediately following the switch to allow complete exchange of air. The average values for each arm were then recorded at the end of every 20 minutes.

The dew point humidity sensor consisted of a small mirror with an electronic cooler and thermometer over which the sample was drawn, together with a light source and light detector capable of measuring the amount of light reflected by the mirror. The air was cooled as it passed over the mirror, causing the mirror to mist over when the temperature became cool enough to saturate the air in contact with the mirror, thereby altering its reflectivity. When this occurred, the thermometer recorded the dew point. This process was repeated to give a time series of samples of dew point temperatures. The vapor pressure was calculated from the dew point at a given temperature through well-established empirical functions. The measured dew point could be affected (usually raised) by dust that provides nucleation sites on the mirror; for this reason, the air was carefully filtered at the intake point, and the mirror was periodically cleaned. Slight contamination of the mirror should still have provided good data, however, because both upper and lower measurements were made on the same mirror, and only the absolute difference was of interest.

Net incoming solar radiation was measured by a net radiometer mounted on a separate pole away from the main tower, to minimize interference from tower instruments and components. The net radiometer was placed over an area of mixed ground cover, including bare rock, soil, and vegetation, to record an average value. Previous studies made at the weather station described in Unland et al. (in review) showed that one net radiometer mounted somewhat higher over mixed cover gives essentially the same value as separate net radiometers close to the ground, one over vegetation and one over bare ground, assuming 40 to 70% bare ground.

Soil heat flux was measured by a combination of two soil heat flux plates and four parallel thermocouples. The soil heat flux plates were buried 8 cm below the surface, one beneath a bush, and one under bare soil. The soil thermocouples were located above the plates at 6 cm and 2 cm depth, and were wired together to yield an average temperature in the soil above the heat flux plates. The heat flux at the surface was calculated by adding the heat flux at depth to the energy stored in the layer above the plates. To calculate the energy stored, the change in soil temperature over the averaging period was multiplied by the soil heat capacity. The soil heat capacity is a function of the soil bulk density, the specific heat of dry soil, the soil water content, and the specific heat of water. The bulk density and water content are not only site-specific, but vary according to site conditions. Therefore, soil samples were collected from the site under different moisture conditions to be used for the calculations; at each time, several samples were collected; an average value was used for the calculations.

Several additional instruments were installed on the micrometeorological tower as part of the collection of a complete set of weather data, and to provide input for the BATS model. All instruments were tied into the common CR10 datalogger. Additional measurements included wind direction and wind speed, and the standard deviation of each; total incoming solar radiation, and temperature and relative humidity independent of the Bowen ratio system. All measurements were made every 10 seconds, and an average was recorded every 20 minutes until January, 1996, when the averaging time was increased to hourly.

The datalogger program used to operate the micrometeorological station is included in Appendix F.

### 5.5.4 Calibration and maintenance

All of the sensors tied into the micrometeorological tower arrived calibrated by the manufacturer, and frequent calibration of all but the Bowen ratio hygrometer was not required. The temperature and vapor pressure measurements from the BREB system were compared to data from the combination temperature/relative humidity probe also mounted on the tower to evaluate data quality from the BREB system, however, and the net radiometer measurements were compared to pyranometer measurements for comparable (though lower magnitude) signals. As recommended by the manufacturers, the net radiometer, pyranometer, temperature/relative humidity probe, soil heat flux plates, and soil temperature thermocouple were returned to their manufacturers for recalibration approximately 19 months into the study, during the summer of 1995. The tipping bucket rain gages were field-calibrated annually. The BREB system required maintenance on a frequent basis, therefore a 2-week site visit/maintenance schedule was established. At that time, data were downloaded, the mirror was cleaned and recalibrated, all sensors and wiring were checked, and the nonrecording rain gages were emptied if necessary.

Periodic repair or replacement of some of the sensors was required due to environmental damage. On two occasions, the net radiometer dome was damaged by hail or birds and was replaced; on two other occasions, one BREB air thermocouple junction was broken, but each time the unit was replaced before any data were lost. Once, a rodent chewed through the wire of a recording rain gage. The tubing of the BREB air-intake system developed obvious leaks after long-term exposure to ultraviolet light and was replaced after about 16 months. Unland et al. (in review) suggested that breakdown of the tubing may be responsible for substantial amounts of poor-quality data before such leaks are obvious.

The BREB system's chilled mirror hygrometer proved to be the most troublesome component of the entire data-collection system, an observation also noted by Unland et al. (in review). The mirror was designed for operation in relatively moist environments, when the dew point is above freezing. The normal operating range of the mirror at ALRS was therefore frequently exceeded during dry, relatively cool weather, a condition which often caused the cooling pump to fail to switch off after the dew point was reached, resulting in buildup of ice on the mirror surface. If this condition persisted, the entire hygrometer became packed with ice. Either this condition or other undetermined factors would result in the surface of the mirror becoming scratched or pitted, resulting in poor quality data. Persistent cycles of freezing also strained the heat pump, so that it was subject to failure and, along with the mirror, required replacement. An additional problem source of poor-quality data resulted from a sticking solenoid valve used to switch the air flow between the two arms. Numerous site visits were typically required to determine the source of the problem and the proper means to repair or replace the faulty parts; in addition, much time was lost sending parts back to the manufacturer for repair or replacement. As a result of all of these factors, the quantity of reasonably reliable data from the BREB system was minimal.

## 5.6 Data Manipulation and Analyses

### 5.6.1 Precipitation Data

The recording rain gages collected data regarding rainfall intensity, hourly totals, and daily totals. For the purpose of calculating a water budget, only the total rainfall over a given time period was required. In general, the average of the total rainfall from both of the recording locations was used to calculate the water budget. However, occasional malfunctions of one or the other gage, such as due to a broken wire or a stuck tipping mechanism, dictated using only the amount from the working one. Furthermore, during intense rainfall, the normal operating conditions of the recording gages were exceeded, and they had a tendency to "spike", and record rainfall amounts that were at least an order of magnitude beyond what could have been reasonable. At these times, the nonrecording gages provided estimates of the approximate rainfall (see Appendix G); thus, all recorded data were compared against the averages of the nonrecording gages for a check of "reasonable-ness". As a result, the daily precipitation values that were used were derived from a combination of straight arithmetic averaging between the two gages, and subjective adjustment based on the nonrecording gages when warranted. This rainfall amount was then multiplied by the surface area of the basin to obtain a quantity of rainfall for the basin for a given period of time.

### 5.6.2. Runoff Data

The head in the flume was converted to flow rate according to established relationships for the specific types of flumes as defined in Brakensiek et al. (1979). Field calibration measurements of head vs. discharge were made to confirm and slightly modify the established relationships, in order to develop functional relationships for each of the two flumes. The total runoff for a specified period of time, or storm, was determined by using a Riemann sum technique. Discharge rates of less than 4 L/s were not detectable by the pressure transducers measuring the head.

### 5.6.3. Evapotranspiration Data

#### *5.6.3.1 Energy Flux Calculations*

Prior to calculation of energy fluxes, the dew point temperatures recorded from the BREB system were converted into relative humidity values and compared against the independently measured relative humidity probe values. This exercise served to identify all the periods of poor-quality data collection from the BREB system. When a time period was identified during which the BREB numbers correlated reasonably well to the independent probe measurements, then the energy fluxes were calculated for that period. A series of computer programs were written to process the BREB data into fluxes (Appendix H). These calculations are described in detail in Appendix I. The data used are presented in graphical form in Appendix J; actual values are saved on tape.

#### *5.6.3.2 BATS Model Parameters and Calibration*

The version of the BATS model that was used is designed to accept one year of data, in a specified interval such as every 20 minutes or one hour, and "recycle", or process, it for as many years as the user specifies, until the fluxes reach some steady state. Two separate years of data were run, using a 20-minute data set from March 1994-March 1995, and an hourly data set from March 1995-March 1996. The 20-minute data parameters of total incoming solar radiation, net radiation, wind speed, air temperature, relative humidity, and vapor pressure were in general obtained directly from the instruments with no additional manipulation (temperature, vapor pressure, and relative humidity were taken from the combination probe, not from the BREB system); precipitation values were averaged and analyzed as described previously. Occassional short periods of missing data, covering just a few time periods, were replaced by interpolating the values before and after the missing data; longer time periods, such as days or rarely a week, were replaced by repeating the parameters from the preceding and following days.

The hourly data set was compiled the same way as the 20-minute set, except that then, hourly averages were calculated. During the months in 1996, however, only hourly averages had been recorded on the datalogger.

Total incoming solar radiation measurements were not available for a 2-month period during the summer of 1995, when the instrument was being recalibrated by the manufacturer. (Replacement sensors were available for all the other sensors during this recalibration period.) In order to supply this data, theoretical total incoming solar radiation, assuming clear skies, was calculated based on the latitude and particular days of the year, which would describe the angle of the earth relative to the sun during that time. The theoretical radiation was then compared to the previous summer's measurements (summer of 1994), and scaled to approximate the conditions that occurred at the site.

#### *5.6.3.3 Potential Evapotranspiration Calculation and Comparison*

The 1994-1995 data set was also used to calculate potential evapotranspiration using daily averages of data from the micrometeorological data, to compare values against the modeled evapotranspiration. Potential evapotranspiration is the amount of evapotranspiration that could occur, given the weather conditions, provided the water was available. It provides a means of determining the driving forces behind evapotranspiration.

The Penman potential evaporation is a calculation of the amount of water that would be evaporated per unit area, per time, from an idealized free water surface under the weather conditions that occurred at the site. The equation used to calculate the Penman potential evaporation is given in Appendix K. Net radiation, average wind speed, vapor pressure deficit, and an estimate of energy advected to a water body were used as input parameters. To make the calculation, the net radiation from the weather station was corrected for the albedo of a free water surface (0.08) by adding to the net radiation the incoming solar radiation multiplied by the difference of the albedo between "crop" and water (0.23-0.08). This resulted in a slightly higher value for net radiation, which would be expected over water. Net radiation was also converted into units of mm water per day. Average wind speed from the weather station, which records the speed at a height of 6 m, was adjusted for a height of 2 m, assuming a logarithmic profile. The vapor pressure deficit was determined from the saturated vapor pressure calculated for the average daily temperature. The energy advected to a water body was assumed to be zero because no data existed regarding the rates or temperatures of inflow or outflow, as no water body actually exists at the site. Other parameters used in the calculation included atmospheric pressure, which was assumed to be a constant value, corrected for the site elevation, and latent heat of vaporization, which was corrected for the air temperature.

Reference crop evaporation is a calculation of the amount of water that would be evaporated per unit area, per time, from an idealized grass crop with a fixed height of 0.12 m, an albedo of 0.23, and a surface resistance of 69 s/m. The equation used to calculate the reference crop evaporation is included in Appendix L. The calculation required net radiation, soil heat flux, wind speed, vapor pressure deficit, air temperature, and the psychrometric constant corrected for wind speed as input parameters. The net radiation was converted to units of mm/d and assumed the same albedo as the site; wind speed at 2 m and the vapor pressure deficit were determined as for the Penman equation; soil heat flux was converted to mm/d and was calculated assuming a constant (average) soil moisture content for the year, a constant soil bulk density and specific heat of dry soil (estimated), and constant atmospheric pressure corrected for the elevation of the site. The latent heat of vaporization was again adjusted for air temperature.

## 5.7 Results

The raw data used for the various calculations of evapotranspiration and evaporation are shown for March 1994-March 1995 in Figure 5.2, and for March 1995-March 1996 in Figure 5.3. In general, the data show the yearly trends of higher temperature and radiation fluxes during the summer months. The three-month period in the summer of 1995 during which incoming solar radiation had to be calculated is evident in Figure 5.3. In the 1994-1995 period, humidity was lowest during the early summer months, and highest in the winter, when wind speeds were also highest, in response to frontal storm systems. In the 1995-1996 period, humidity was greatest in the late summer months, during the summer "monsoon" period. The humidity profile for the winter of

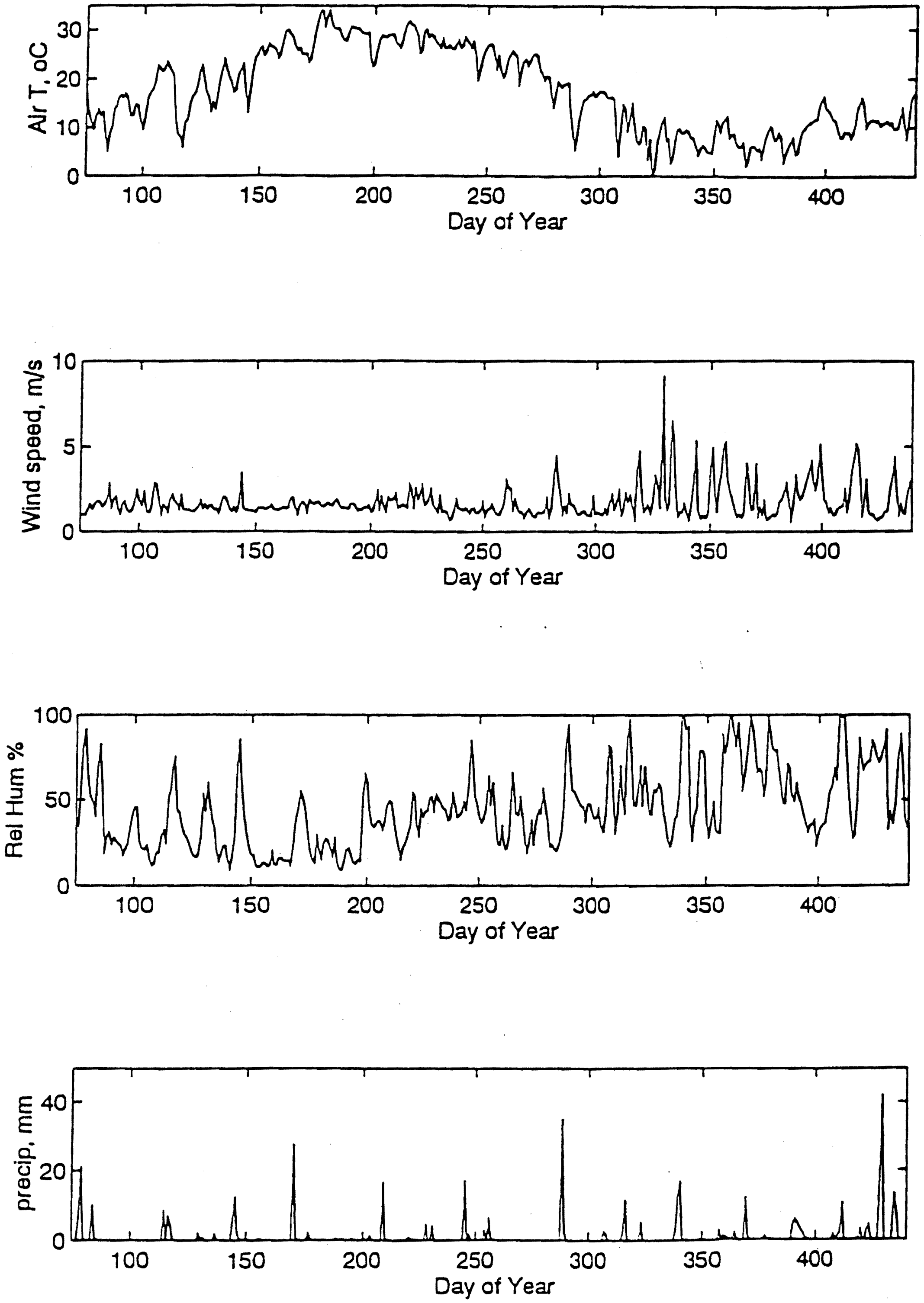

Figure 5.2a Weather data from the ALRS for March 1994 to March 1995

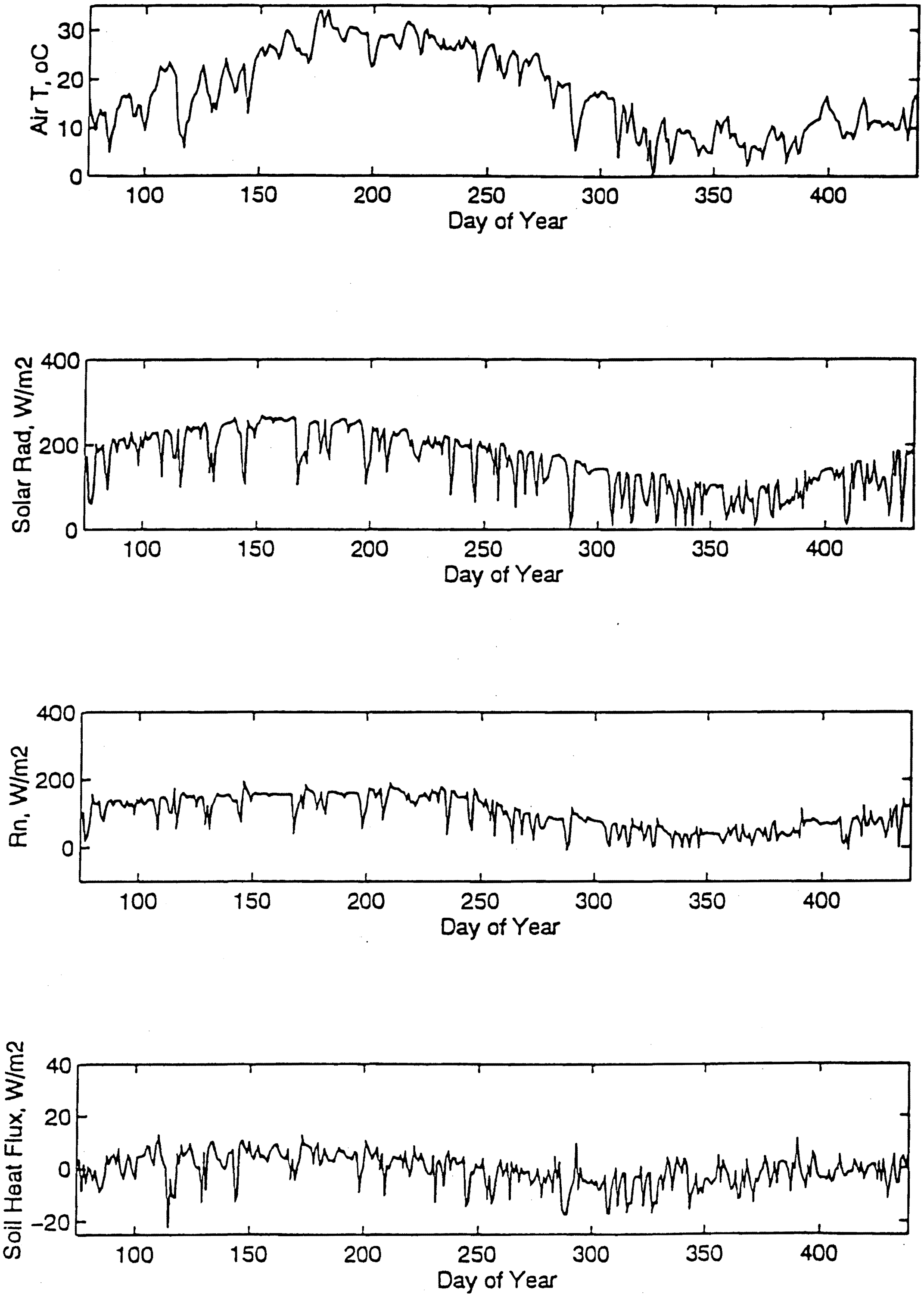

Figure 5.2b Temperature and flux data from the ALRS for March 1994 to March 1995

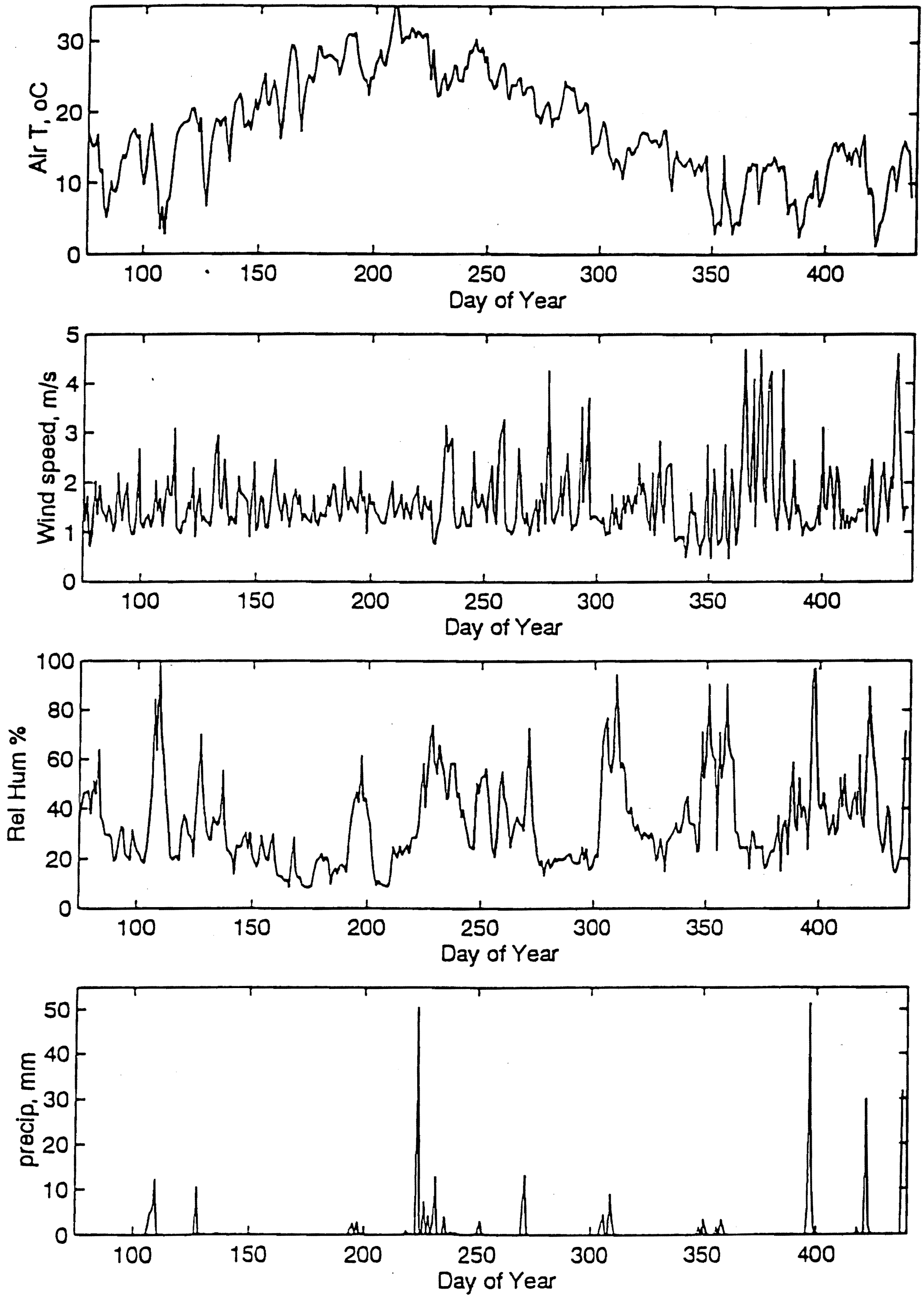

Figure 5.3a Weather data from the ALRS for March 1995 to March 1996

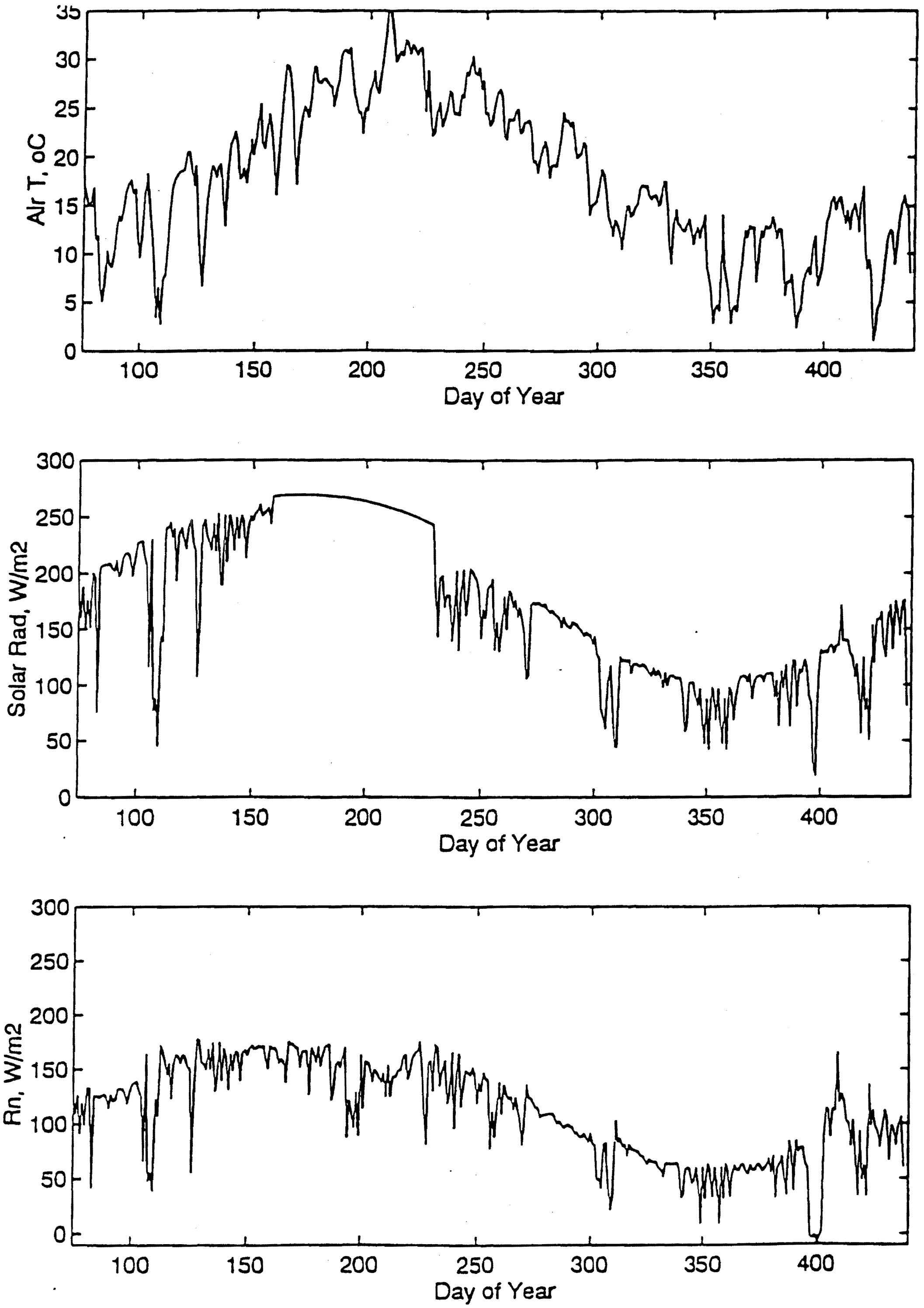

Figure 5.3b Temperature and flux data from the ALRS for March 1995 to March 1996

1995-1996 is atypically low, in response to an unusually dry winter across the entire southwestern U.S. The precipitation record for both years shows a pattern of isolated storms, with neither year showing the typical distribution of intense, high summer rains and more gentle, longer winter rains, with dry periods in between them. The total rainfall for 1994-1995 was 424.2 mm, and for 1995-1996 it was 321.9 mm, again reflecting the exceptionally dry conditions that prevailed over that period.

### 5.7.1 Single Storm

Measured evapotranspiration data and other water budget parameters were used to determine a potential infiltration volume following a winter frontal-type storm which occurred over a five-day period from January 4 to January 7, 1995. Weather measurements made during the storm period are shown in Figure 5.4. The data show that relative humidity and vapor pressure were high, and total incoming and net radiation were low, resulting in lower air temperatures, during precipitation. Wind speed increased after the rain stopped and the sky began to clear. During this period, 16.6 mm precipitation fell over the basin for a total basin rainfall of 8532 $m^3$ , and 7873 $m^3$ of runoff (92% of precipitation) was measured in the flumes. Direct evapotranspiration measurements from the BREB system were not available for this time period (the hydrometer was frozen), however an energy budget constructed during a previous winter frontal storm (for which no runoff data were available), provided an estimate of typical storm period evapotranspiration. Figure 5.5 shows the energy budget that was used; evaporation is not high during conditions of cold, moist air; an average rate of 0.115 mm/day was calculated from the BREB data, for a total quantity of evapotranspiration during this time period of

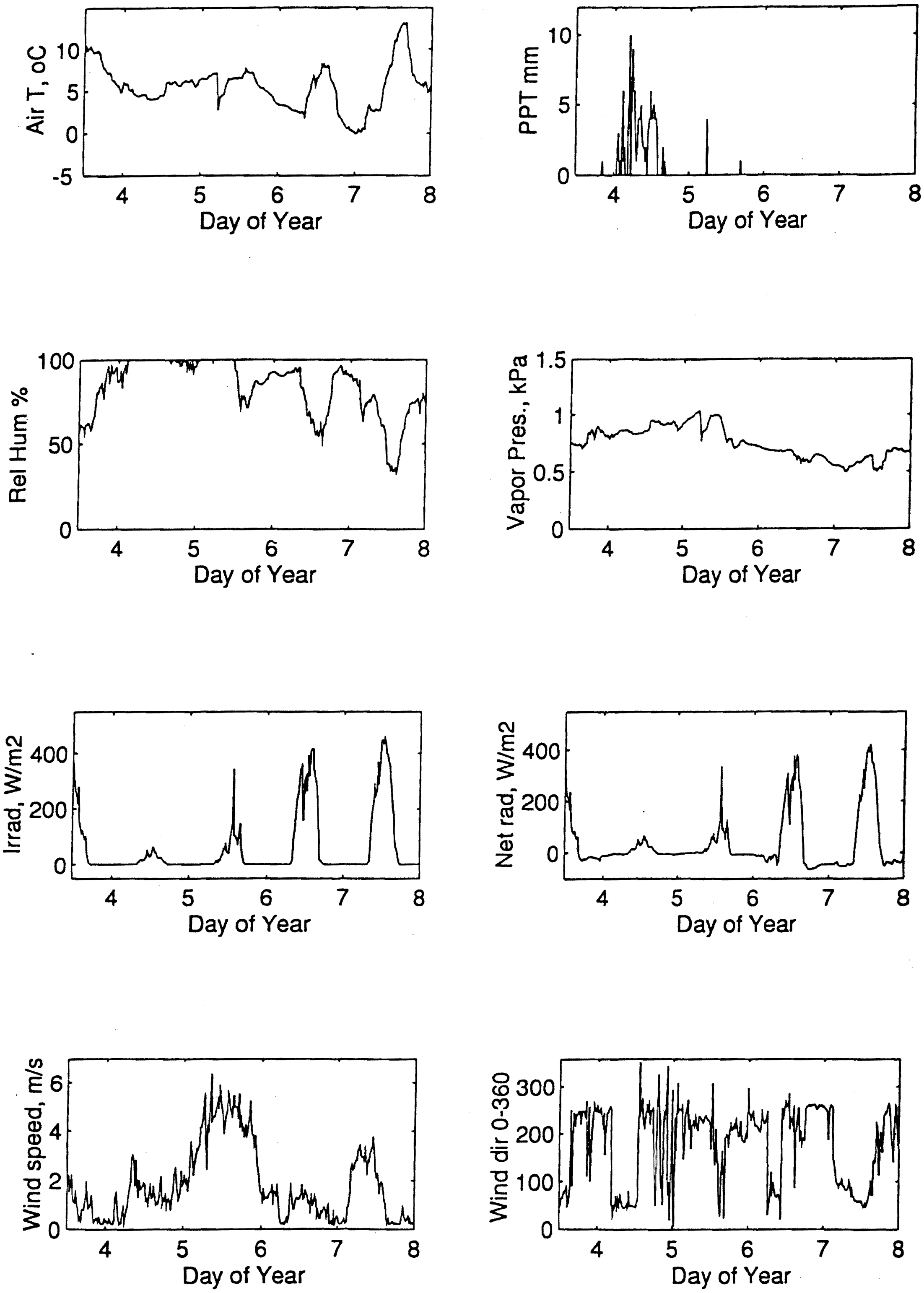

Figure 5.4 Storm weather data from the ALRS for the period January 3-7, 1995

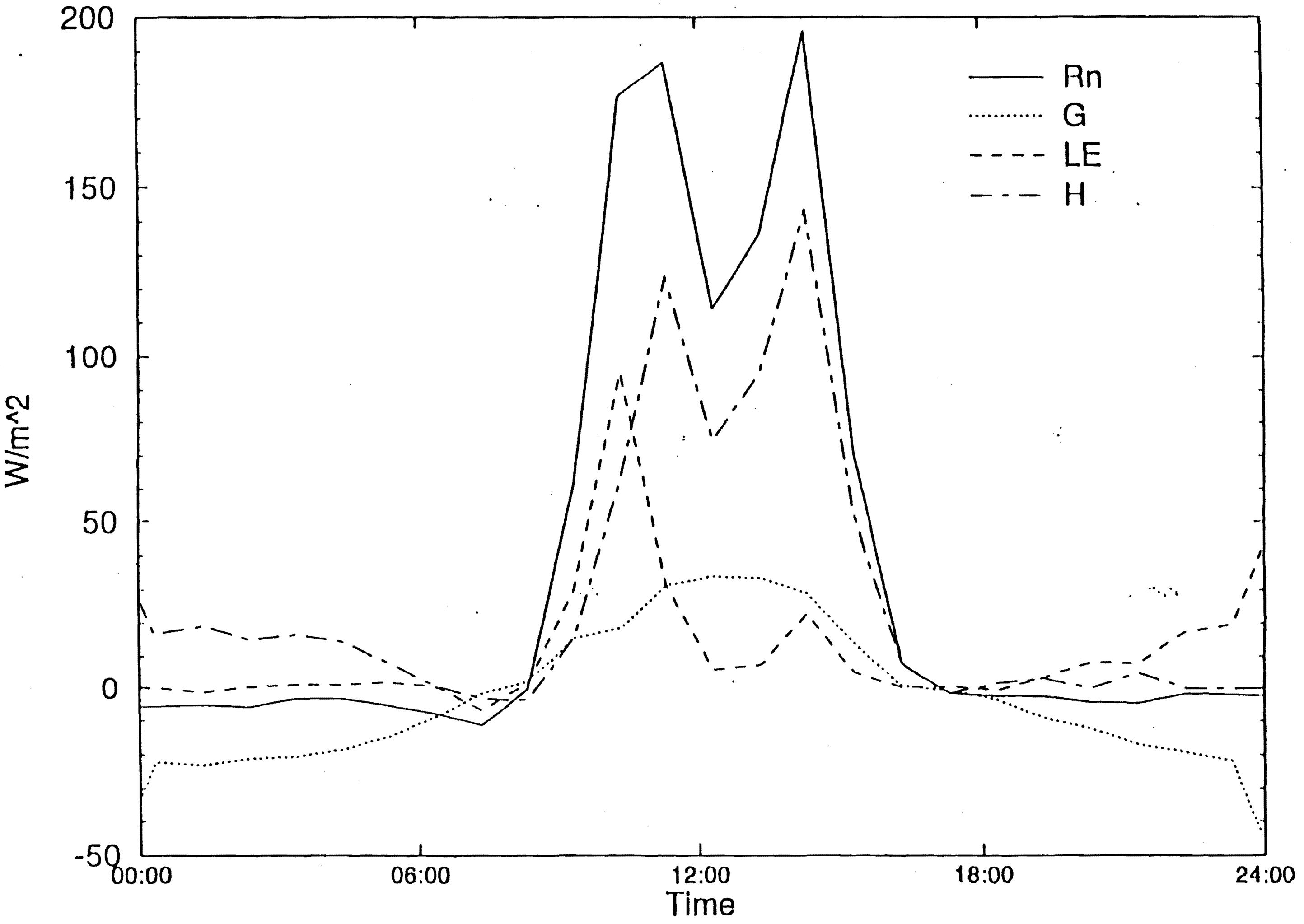

Figure 5.5 Typical energy budget for winter conditions1994-1995

just 177 $m^3$. This volume was then divided into a constant rate over the storm period to construct a water budget, shown in Figure 5.6. The results of the water budget indicate that just 482 $m^3$, or 6% of the precipitation, was available for infiltration. The actual amount of infiltration was probably even less than that, due to further evapotranspiration after the storm. The small fraction of water available for infiltration was not surprising in this situation, as the watershed had received approximately 10 mm rain in the 10-day period preceding this storm, the weather had remained cold and moist during the entire period, the soil and rocks were already saturated, and surface depressions were already full of water.

### 5.7.2 Seasonal Budget

The longest period of frequent rainfall events that occurred during this investigation was from January 1 through March 15, 1995, during which time 147 mm of rain fell. Measured runoff data were available for this period; a depth of 23.7 mm (17% of precipitation) was recorded. BREB evapotranspiration measurements were not available for this period, so the BATS model was used. Measured versus modeled runoff showed a difference of 5%; this difference can be attributed to both mechanical error caused by the flume design, and to assumptions of the BATS model that do not fit the ALRS. Modeled evapotranspiration for the period was 104 mm, or 70% of precipitation. Infiltration calculated according to the measured runoff was 19.8 mm, or 13%. These results suggest that the conditions of winter frontal storms, with relatively low intensities, may enhance infiltration.

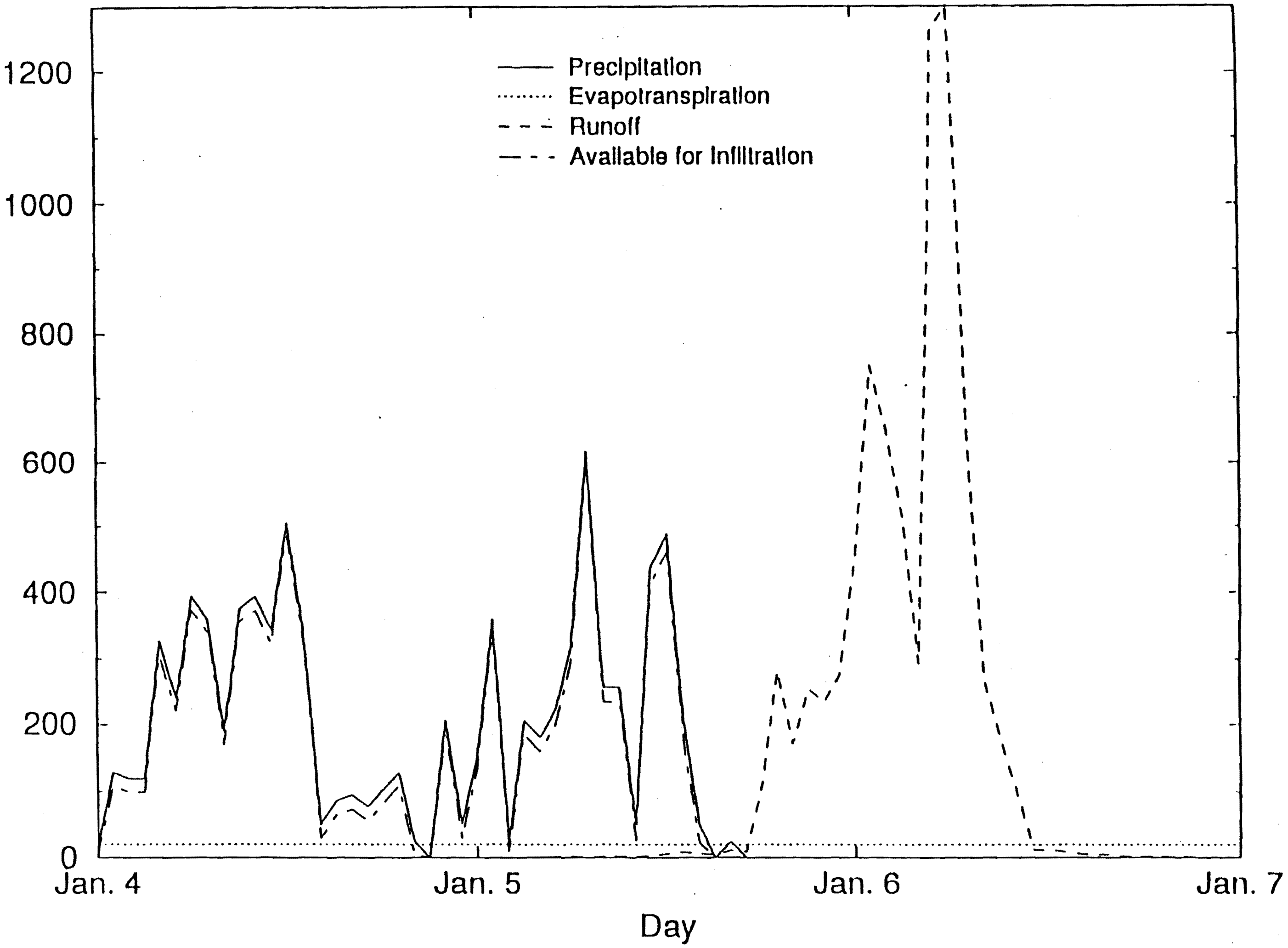

Figure 5.6 Water budget for the January 3-7, 1995 storm at the ALRS

### 5.7.3 Annual Budget

Modeled evapotranspiration was used for calculation of the annual water budgets, as the direct measurements were far too discontinuous to be of use. In the first year of modeling, runoff measurements were not available except for during the final three months. The total rainfall in the watershed during this time was 424 mm; the total evapotranspiration predicted by the model was 379 mm, or 89% of precipitation. Runoff during the final three months was 24 mm (5.6%). As several runoff events had been observed, but not recorded, in the watershed earlier in the year, infiltration is estimated to be about 10 mm, or about 2.5% of the annual precipitation. Had no runoff occurred earlier in the year, infiltration could have been at most 21 mm, or 5.4% of the total precipitation. Figure 5.7 shows the modeled evapotranspiration compared to precipitation for the year: clearly the evapotranspiration rates did not follow a seasonal cycle; rather, peak rates occurred immediately following a precipitation event, and trailed off to nearly zero between events, indicating that evapotranspiration was driven almost entirely by water availability rather than seasonal radiation cycles.

In the second year of modeling, runoff data were collected, but only five measurable runoff-producing events occurred. The BATS model estimated that 95% of the precipitation that fell left the watershed as evapotranspiration. Measured runoff for this period was only 5 mm, or 1.6% of precipitation, leaving just 11 mm, or 3.4% of precipitation, for infiltration. These results seem reasonable, given the overall extreme dryness of the site during this time, and the fact that the two major rainstorms that did occur (in August and February) were short and intense, conditions which would not favor

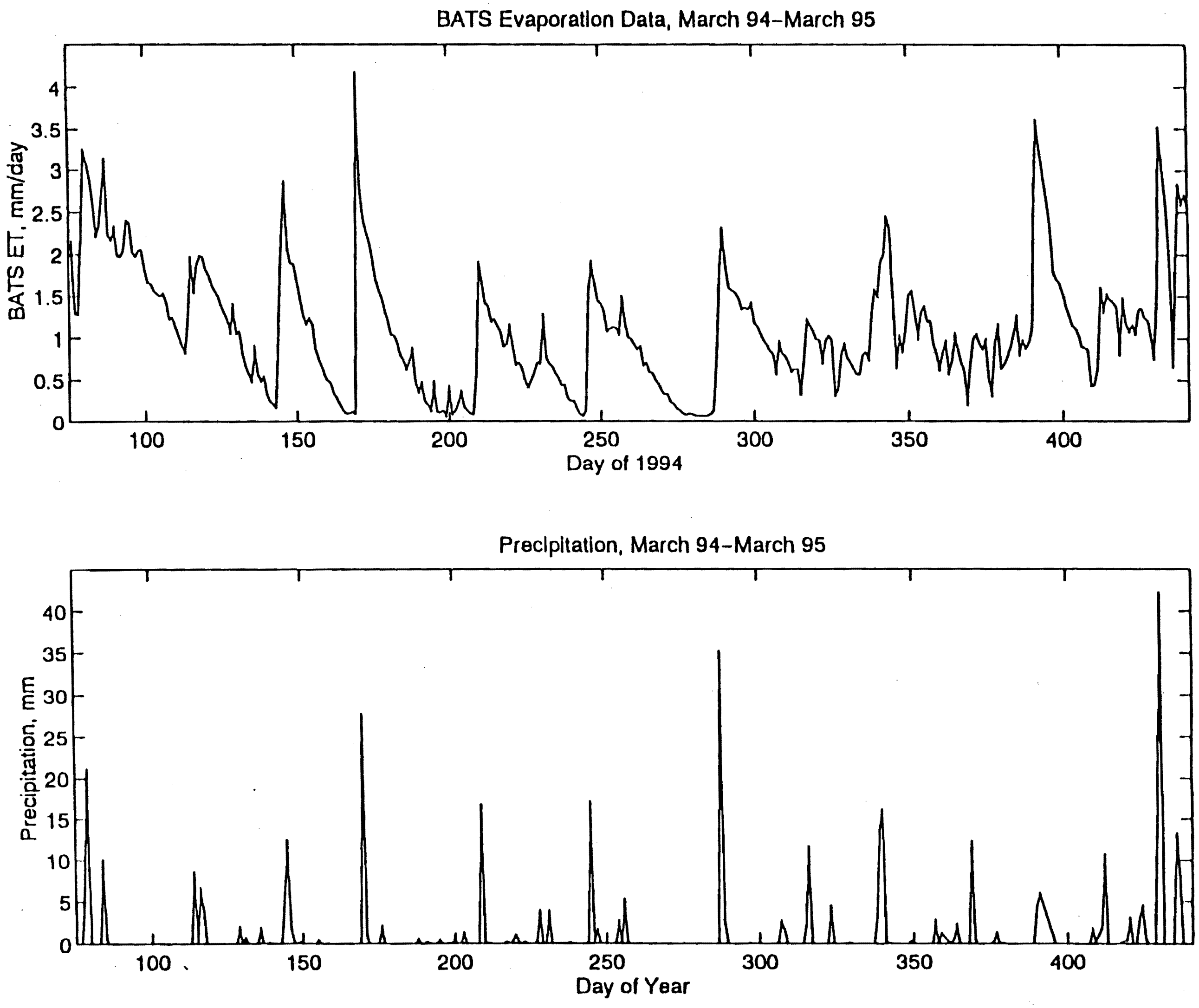

Figure 5.7 BATS modeled evapotranspiration compared to ALRS precipitation, March 1994-March 1995

infiltration. Figure 5.8 shows a comparison of measured precipitation, and modeled evapotranspiration and runoff for the year. Additional runoff events were predicted by the model, which again could be due to either loss of low flows because of mechanical limitations, or to the differences between the BATS assumptions and the site conditions.

### 5.7.4 Potential Evapotranspiration Measurements

Figure 5.9 shows the potential Penman and reference crop evaporation compared to the modeled BATS evapotranspiration for the time period March 1994-March 1995. The two potential evaporation plots are similar, with the Penman evaporation overall slightly higher. The reference crop evaporation appears to show somewhat greater fluctuations of evaporation rate. As expected, the greatest evaporation would occur during the dry summer months, and the least in the wet winter months. The total evaporation for the year calculated by the Penman equation was 1754 mm, and the total evaporation according to the reference crop calculation was 1366 mm. The Penman equation would be expected to yield higher evaporation because it is assuming complete water coverage over the area, whereas the crop evaporation relies heavily on evapotranspiration to remove water, which requires greater energy. In either case, as illustrated by the modeled evapotranspiration, precipitation into the basin is clearly the factor limiting evaporation, as it provided only 1/3 to 1/4 the amount of water that could have potentially evaporated.

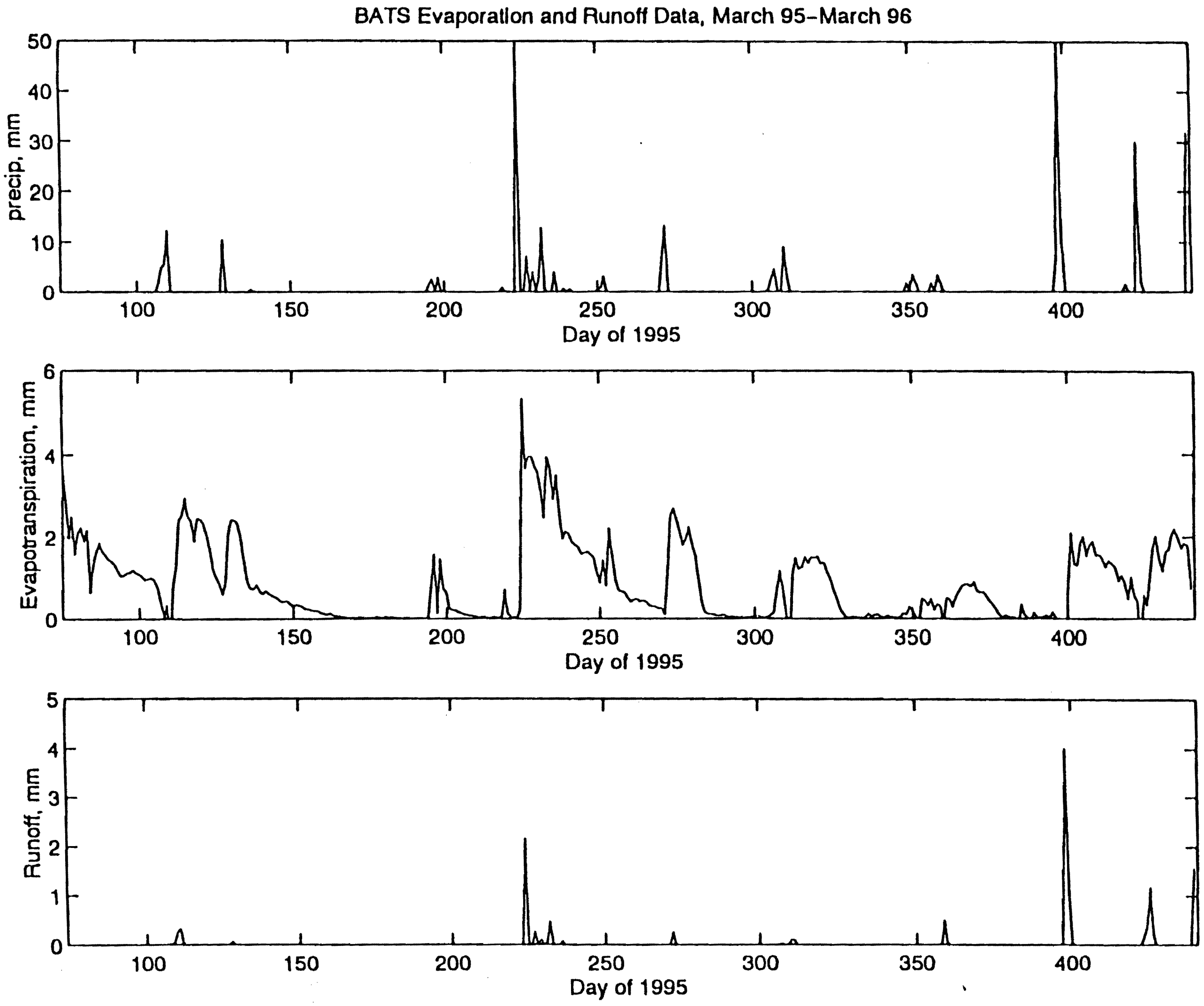

Figure 5.8 BATS modeled evapotranspiration and runoff compared to ALRS precipitation, March 1995-March 1996

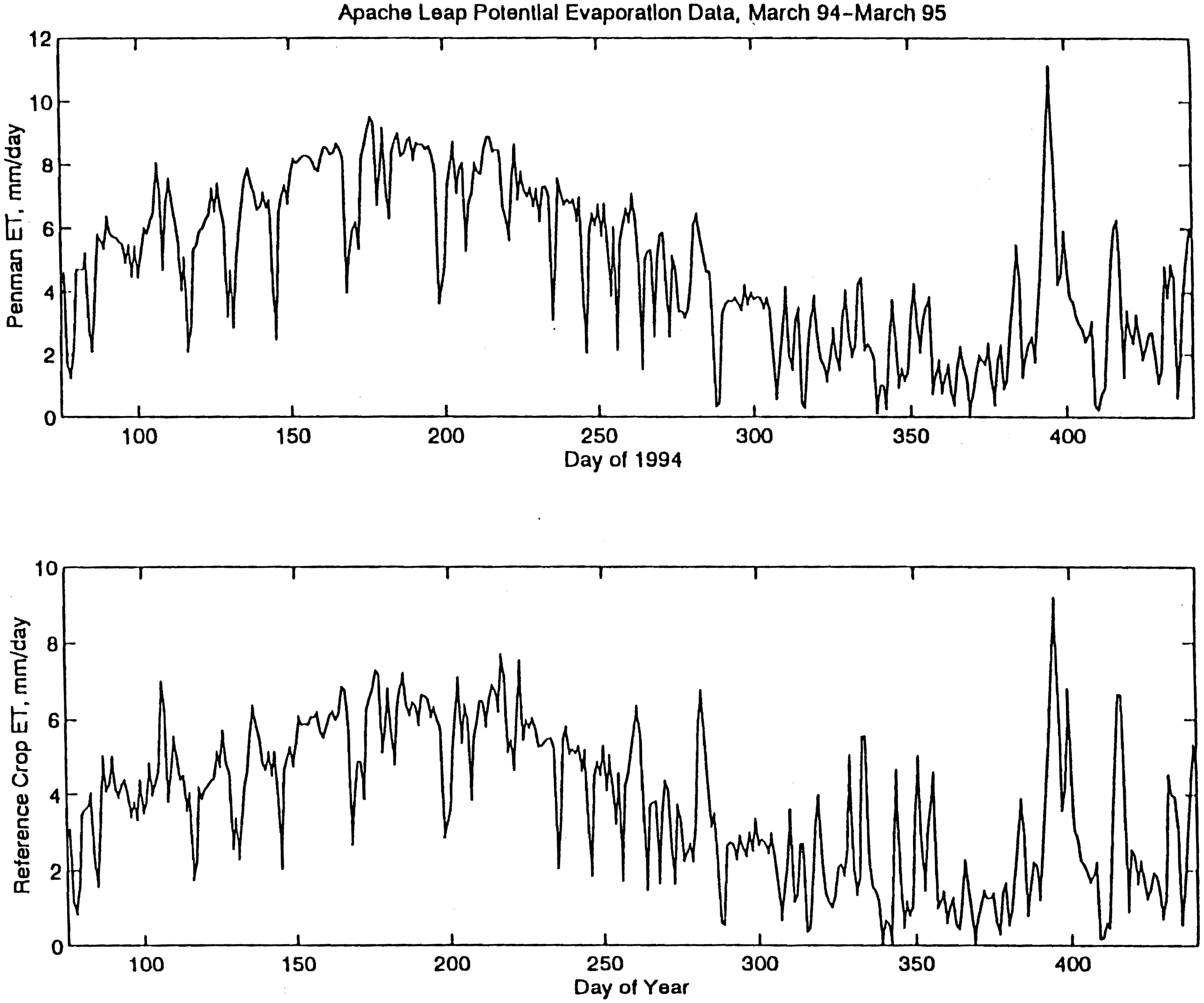

Figure 5.9 Penman potential evapotranspiration and Shuttleworth's reference crop evapotranspiration at ALRS, March 1994-March 1995

## 5.8 Discussion

### 5.8.1 Limitations of the Methods

The limitations of the BREB system in the field have been discussed previously. The system did not prove to be a reliable long-term method for collecting direct evapotranspiration measurements in the environment of the ALRS. The two primary reasons so little "good" data were obtained by this method are 1) nonsuitability of the chilled mirror hygrometer for the site conditions, and 2) the remoteness of the site, which limited the frequency of calibration, maintenance, and repair of the system. However, based on the experiences of Unland et al. (in review), the poor performance of the hygrometer is a factor even when the site is nearby.

The limitations of the BATS model for determining evapotranspiration also are due to some incompatibility with the ALRS site. The BATS model assumes a surface cover of either soil or vegetation (or snow or open water), and makes no provision for a cover of rock, more specifically fractured rock, which makes up the majority of the non-vegetated cover at the ALRS. The BATS model divides up the soil into three layers: a surface zone, a root zone, and a total soil thickness zone. In contrast, the soil cover, where present at ALRS, is very thin, and much of the roots of the vegetation have grown down into the rocks. Thus, while the BATS model is extremely comprehensive and contains rigorously tested physics, its results for the ALRS data can only be taken as estimates, given the discrepancies between model assumptions and site realities.

The precision of the water budget values was further limited by the mechanics of accurately measuring runoff and precipitation. The flume setup was unable to measure flow below a threshold value, and while it was able to record the major storms quite successfully, the quantity of runoff as very low flow that occurred is unknown, and could potentially have been sizeable over the course of a year. Errors in rainfall accuracy were also possible, especially when the high-intensity spikes were recorded and the nonrecording gage data were used. Frequent significant variation between recording rain gage measurements suggested either considerable spatial variation of rainfall, which was documented to a limited extent by the nonrecording rain gages, or inaccuracies in the instruments in spite of recalibration efforts. Spatial variation could be great enough at the ALRS that simply averaging the rainfall from two locations was not an appropriate method for determining total rainfall over the watershed.

The extreme variability in surface cover, slope, aspect, and seasonality at the ALRS adds an uncertainty to the measurements in addition to their mechanical limitations. A single micrometeorological station in such a varied watershed can not realistically collect true average values for the region, even though it does represent data from a greater area than just a single point. This consideration is further reason for placing no more than order-of-magnitude weight on the values of the water budget that were calculated.

### 5.8.2 Implications from Findings

The annual infiltration quantity that was produced from the water budget was used to estimate the amount of time needed to fill the volume of the perched aquifer, or to completely replace the existing water, beneath the watershed. An average infiltration rate of 5 to 10 mm was used, to account for some low runoff volumes that may not have been recorded. The aquifer thickness was assumed to be 21 m beneath the area of the watershed, based on its thickness in the VOB. The effective porosity of the aquifer, representing matrix porosity and fracture spaces, was then estimated to calculate aquifer volume. For an effective porosity of 5%, 105 to 210 years of average annual infiltration would be required to fill the aquifer volume. If the effective porosity is 1%, only 21 to 42 years of infiltration are needed. While the effective porosity of the perched aquifer can at present only be estimated, these calculations provide an estimate of the time frames involved in filling the perched aquifer, under the current climatic conditions.

Evapotranspiration appears to be the significant source of water loss from the ALRS, and would be expected to dominate at Yucca Mountain as well, given its similar climatic characteristics. The results of the water budget calculations suggest that not a significant amount of precipitation enters the subsurface over the long term under the present climatic regime, but more infiltration occurs during prolonged wet periods of storms with relatively low rainfall intensity. A major implication from this observation is that if climatic conditions should change, bringing an increase in frequency and duration of frontal storms, a greater amount of infiltration could occur.

An additional implication from this investigation that direct measurement of evapotranspiration in a highly heterogeneous natural setting can realistically produce only approximate values, with considerable error likely. Attempts to obtain direct measurements of evapotranspiration using similar methods at Yucca Mountain are likely to produce a similar quality of data. While these methods have produced useful estimates of infiltration values, more precise measurements may be required for proper evaluation of

Yucca Mountain for a repository. The use of alternative methods may be warranted for such measurements, perhaps involving expansion of the more traditional point measurement methods to larger regions.

## 5.9 Conclusions

The results of this investigation have shown that only a small percentage of the precipitation entering the watershed is available for infiltration, and that the presence of fractures does not significantly increase the amount of water that reaches the subsurface. Evapotranspiration removes on the order of 90% of the water that enters the watershed; runoff and infiltration together account for only about 10%. In the year for which continuous runoff data were available, runoff was 1.6% of the total budget. The results also showed that more infiltration (13%) occurred during a period of frontal-type storms, which are typically widespread and less intense than monsoon storms, which force rapid runoff to occur. This result suggests that under different climatic conditions, in which frontal storms are more common, a greater amount of precipitation could reach the subsurface. An average annual infiltration rate of 5 to 10 mm would result in a time of 105-210 years necessary for the perched aquifer to be filled, based on a 5% effective porosity of the aquifer; if effective porosity is only 1%, the aquifer could be filled in 21-42 years.

The process of conducting this investigation revealed several challenges associated with the long-term collection of field data in a natural, remote setting. The heterogeneous terrain made collection of representative data difficult. Mechanical problems invalidated most of the BREB data, and caused periodic loss of data from some other instruments. Use of a BATS model entailed certain assumptions which were not necessarily valid for the ALRS. In spite of these obstacles, estimates of infiltration values were possible, and the data set that has been assimilated is of value for comparison to methods of data collection and analysis in other locations, and for use in water transport models.

# CHAPTER 6
# SUMMARY AND CONCLUSIONS

## 6.1 Summary of Results

This investigation produced three major results. First, a detailed description of the physical and hydrologic properties of the upper 200 m section of the Apache Leap Tuff was produced. This description was developed from the compilation of past and ongoing investigations of the Apache Leap Tuff, together with new research. Included in the project was a thorough analysis of aquifer tests performed on the perched water table at the base of the 200-m section under investigation, which provided improved understanding of the hydrologic response of the aquifer. Second, a model for the formation of the perched water table in the Apache Leap Tuff was developed. The physical and hydrologic data were compared against possible perching mechanisms; this process allowed some mechanisms to be rejected and others to be combined to make a model for the site. Third, a water budget for fractured rock in a semi-arid environment was developed and used to estimate infiltration. The budget provided an estimate of the relative proportion of water entering the watershed that reaches the subsurface, potentially to recharge the perched water zone.

### 6.1.1 Characterization of the Apache Leap Tuff

Prior to this investigation, the most complete geologic description of the Apache Leap Tuff was that of Peterson (1961), who addressed the entire thickness and extent of the deposit. A detailed analysis of the upper 200 m was of interest in this investigation because that section contains the perched aquifer, the focus of this research. Geophysical studies (Hardin and Bassett, 1995), isotopic and chemical studies (Bassett et al., 1994, Davidson, 1995), and measurements of specific physical properties (Hardin, in prep) have been made of the upper 200 m, but these data, along with geologic data, had not been compiled to create a detailed description of the physical and hydrologic properties of the tuff, prior to this investigation. Furthermore, this investigation included the first aquifer test on the Apache Leap Tuff, which provided estimates of aquifer parameters.

The upper 200 m of the Apache Leap Tuff is characterized as a densely to partially welded tuff that has been substantially altered by devitrification and vapor phase crystallization. The uppermost, or white, unit is distinguished in outcrop by its relatively euhedral pumice fragments; these fragments become flattened in the lower, or gray, unit, and degree of flattening increases with depth in the gray unit. In thin section, compression and flattening of the entire deposit has resulted in a eutaxitic, or flowing, texture which is progressively more apparent with depth. Both the white and gray units contain 35-45% phenocrysts in a cryptocrystalline matrix composed of cristobalite and feldspar. The phenocrysts are composed of plagioclase, quartz, biotite, sanidine, and magnetite, in order of decreasing abundance, with trace accessory minerals. Approximately 2-4% of the rock is composed of lithic fragments.

Devitrification has altered the original glass of the tuff into the cryptocrystalline cristobalite/feldspar intergrowth, obscuring much of the primary textures. Devitrification is most prevalent in the matrix and pumice fragments; the phenocrysts remain relatively unaltered. Vapor phase crystallization has filled in some of the primary porosity, frequently in the pumice fragments, with tridymite and feldspar; this alteration process increased upward in the section. Devitrification, enhanced with depth by increased heat and compression, and vapor phase crystallization, together appear to have exerted the greatest effect on the porosity characteristics of the tuff. The porosity of the matrix appears to be strongly correlated to alteration of the pumice fragments: as they become increasingly flattened and noncontinuous with depth, so does the porosity become extremely reduced and disconnected. Thin sections and cut rock slabs verify this correlation: porosity was observed to occur primarily in the regions of pumice fragments.

The exposed surface of the Apache Leap Tuff is dissected by fractures of three principal orientations. Quantification of fracture abundance with depth to 200 m revealed no decrease in fracture frequency with depth. Towards the base of the 200-m section under investigation, fractures appeared to be more frequently filled by silica mineralization. Evidence from cores extending deeper into the formation suggests that not only does silica mineralization increase, but fracture abundance may also decrease. Increased silica mineralization is expected deeper in the section, where sustained high temperatures in the deep and central portion of the deposit would favor the dissolution of silica minerals, and subsequent reprecipitation in fractures during cooling.

The hydrologic properties of the Apache Leap Tuff in the region of the perched aquifer are characterized by fracture flow. Geophysical data associates increased moisture with fractures; chemical and isotopic data indicate that most of the water in the perched aquifer is derived from relatively rapid fracture flow from the surface. Aquifer test analyses also confirmed the dominance of fracture flow in the system.

Modeling efforts of a pump test and a slug test resulted in calculation of an effective aquifer transmissivity on the order of 0.17 $m^2$/day. The transmissivity value is based on four different analyses of the data, each of which generated a transmissivity value between 0.16 $m^2$/day and 0.18 $m^2$/day. More significantly, the results of the analyses showed that the Apache Leap fracture system could be fit to the analytical solution of a discrete fracture model, indicating the importance of fracture flow. The estimated fracture hydraulic conductivity, based on measured matrix hydraulic conductivity, is nine orders of magnitude greater than the matrix hydraulic conductivity, rendering matrix flow insignificant.

### 6.1.2 Model for Perched Water in the Apache Leap Tuff

Perched water zones are generally understood to result where a reduction in hydraulic conductivity is sufficient enough to slow water movement to the point that the pore spaces become saturated. However, the mechanics that could create such a hydraulic conductivity contrast, specifically in fractured tuff, had not been addressed prior to this investigation. Thus, the development of a model for perched water in the Apache Leap Tuff represents an advancement in the understanding of several of the mechanisms that could cause the formation of such a zone. The identification of these mechanisms provides information that can be used in the prediction of the location of formation of perched zones elsewhere in similar material.

The evaluation of the physical and hydrologic characteristics of the Apache Leap Tuff against eight potential models of perching mechanisms resulted in the development of a combination model that fits the conditions of Apache Leap. The combination model calls for fracture flow to be the only significant pathway by which water reaches the perched zone. The hydraulic conductivity reduction necessary to cause perching results from both a severe reduction in matrix hydraulic conductivity, the result of compression and crystallization processes occurring over the entire unit, and from an increase in fracture filling by silica minerals beneath the perched zone, reducing secondary permeability.

The combination model not only fits the detailed data obtained from boreholes at Apache Leap, but also can be applied to the regional scale. This application is important, as perched water has been identified over a surface of at least 16 km$^2$. The consistency of the characteristics of the cooling zones over the entire deposit described by Peterson (1961) indicates that mechanisms creating the perched zone, which are predominantly tied to the cooling process, are also likely to be pervasive over a large area.

Several perching models were rejected on the basis of the physical and hydrologic evidence. Permeability contrasts between individual flow units were not supported by mineralogical and petrographic data. A stratigraphic or cooling unit boundary, which has been identified as a perching mechanisms at Yucca Mountain, is not a mechanism at Apache Leap, as the perched zone exists entirely within one such unit. Chemical alteration by a former high stand of water, creating a clay-rich, low-permeability weathered zone, was rejected as a mechanism on the basis of negligible weathering of phenocrysts at all depths, and minor amounts of smectite in no spatial concentrations. Faulting may increase fracture abundance in some locations, but the presence of faults was not consistently correlated to the location of the perched aquifer.

### 6.1.3 Infiltration Measurements from a Water Budget at Apache Leap

This investigation produced order-of-magnitude estimations of all components of the water budget in a remote, highly heterogeneous terrain of fractured rock in a semi-arid environment, a difficult proposition that had not been previously undertaken. Several challenges were faced in the collection of data for infiltration measurements. First, the measurements were desired from a region of highly varied ground cover, slope, and aspect which is unsuitable for direct, point measurements of infiltration. Second, in order to avoid point measurements, micrometeorological measurements were desired, from a region of limited fetch, high relief, and considerable rock cover. Third, in order to try to directly measure evapotranspiration as part of the water budget, state-of-the-art equipment was employed, but the equipment was designed for warmer, humid climates and in accessible locations where it could be monitored frequently, conditions that do not describe the ALRS. Thus, the production of infiltration measurements from this site, while only estimates, provides new data regarding the climatic and hydrologic conditions in such a region. These data can be used in surface or subsurface models as boundary conditions or calibration parameters, to further study the movement of water in fractured rock in semi-arid environments.

The results of the infiltration calculations shows that in spite of numerous fractures intersecting the surface, upwards of 90% of the water entering the watershed (precipitation) leaves as evapotranspiration, on an annual scale. An additional 6% exits the watershed as runoff, leaving only approximately 4% to infiltrate. This amounts to only about 10 mm/year infiltration, a very small quantity. An average annual infiltration rate of a conservative 5 to 10 mm, over the entire watershed, would equal the volume of the perched aquifer in 105-210 years, assuming 5% matrix porosity plus fracture space. For an effective perched aquifer porosity of 1%, only 21-42 years would be required.

The greatest proportion of infiltration appeared to occur during a 3-month long wet season, when 13% of the precipitation that fell over the period was not accounted for by runoff or evapotranspiration. The increased infiltration during this period may be due to the type of storms that occurred: winter-type, frontal storms which have relatively low spatial variability and low intensity. In contrast, the intense summer monsoon-type storms are likely to produce large amounts of water, but in such a short time period that much more of the water runs off. These results indicate that in spite of abundant fractures exposed at the surface, the water budget remains fairly typical for a semi-arid region, with evapotranspiration dominating the balance.

## 6.2 Conclusions and Recommendations

Significant progress was made during the course of this research towards understanding the mechanisms that have created the perched zone at the ALRS, and the mechanisms by which the zone is recharged. A detailed investigation of the physical and hydrologic properties of the Apache Leap Tuff produced a description of the characteristics of the tuff that could be used to evaluate models for perched water. Analysis of these characteristics against potential models enabled a combination model to be developed that would account for the perched zone at Apache Leap. The analysis also allowed several other models to be rejected. Investigation of the hydrologic properties of the tuff revealed that fractures are the primary pathways for water to reach the perched zone from the surface, and the matrix flow is insignificant. Collection of long-term micrometeorological data allowed a water budget to be estimated for the watershed, which indicated that, while infiltration is a minor portion of the total water budget, most infiltration occurs during wet seasons characterized by less intense, widespread, frontal-type storms.

The process of evaluating the characteristics of the tuff against possible perching mechanisms revealed the range of the scale of the parameters, from submicroscopic to macroscopic, that must be analyzed to develop a perching model. The mechanisms that were determined to be critical to the formation of the perched zone at Apache Leap are not necessarily the same mechanisms that would be responsible for perched zones elsewhere; however the evaluation process should follow the same direction in any location.

The Apache Leap perching model could be better defined with additional data, particularly from the region beneath the perched zone. Additional investigations of this area could confirm the abundance of silica-filled fractures, and also add insight regarding fracture density changes or the existence of disconnected fracture sets. Hydraulic conductivity measurements from the region beneath the perched zone should confirm an ever-decreasing permeability with depth.

While the analyses of the aquifer tests, together with geophysical, chemical, and isotopic data, are conclusive evidence of a fracture-dominated flow system, the parameters of the Apache Leap perched aquifer could be more precisely defined with additional testing. Of primary importance to further data collection would be the installation of at least one observation well close enough to the pumping well to be affected by pumping. In addition, a multi-day long pumping test would provide additional insight into aquifer response that was not observed within the limits of the 18-hour test that was performed. However, the value of the additional information gained by further aquifer testing should also be weighed against the objective of such information. In this portion of the investigation, the objective was to confirm the dominance of fracture flow; that objective was met.

While an idealistic objective of this research may have been to obtain precise, accurate, direct measurements of evapotranspiration in order to develop a tightly controlled calculation of infiltration, the difficulties of obtaining such data in a natural, remote, highly heterogeneous setting dictated modification of the objective to order-of-magnitude scale. A single micrometeorological station in a 51.4-ha watershed is not likely to closely represent the conditions of the entire watershed, but the improvement of accuracy with an increased number of such stations is questionable, again because of the scale of heterogeneities of surface cover, fracture abundance, slope, aspect, vegetation, and seasonal change that exists at the site. Direct measurement of evapotranspiration could be improved with a more reliable system, better designed to measure the combination of cool and dry weather that is common at the ALRS. Alternatively, infiltration measurements may be better made by more direct methods such as artificially produced precipitation over a highly controlled area. Improvement in the precision of measurements of the timing and size of infiltration events is an area of research that warrants pursuit, as the quantity of water reaching the subsurface will be significant to the prediction of the formation or growth of perched water zones at Yucca Mountain.

# APPENDIX A
# PHOTOGRAPHS OF REPRESENTATIVE THIN SECTIONS

Notes:
Thin sections are from the DSB core, unless otherwise noted.
Depths are recorded in vertical meters below the surface
Thin sections were photographed under plane-polarized light
Magnification is approximately 1.65X

a. 24 m (white zone)

b. 45 m (upper gray zone)

c. 67 m

d. 79 m (vacuum impregnated with blue epoxy)

i. 146 m

j. 148 m (perched zone)

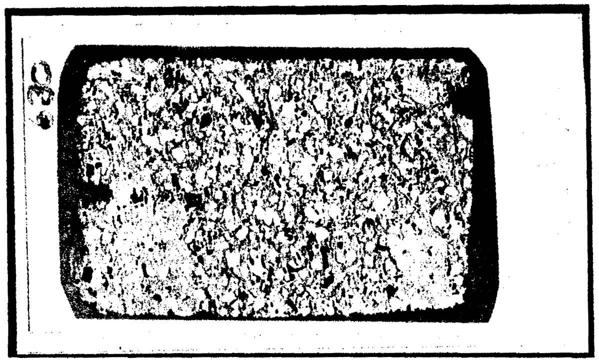

k. 149 m (vacuum impregnated with blue epoxy)

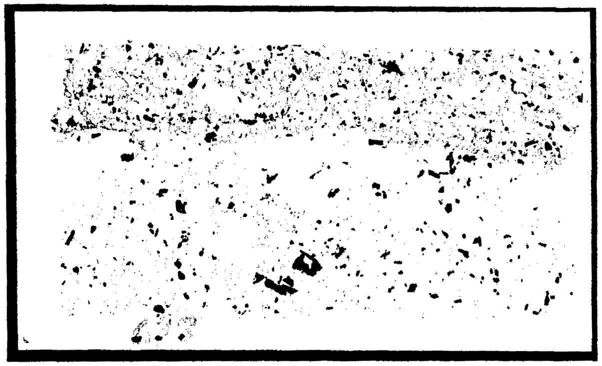

l. 150 m (crossing a vuggy fracture)

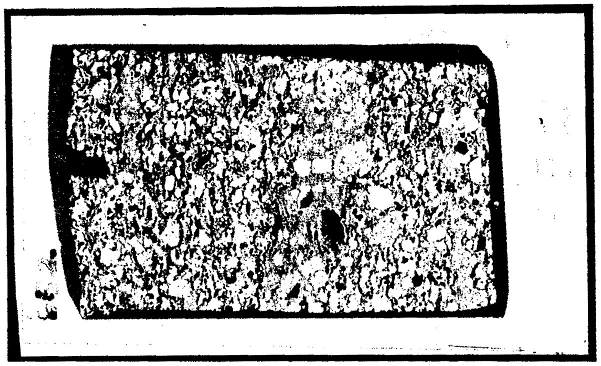

m. 154 m (vacuum impregnated with blue epoxy)

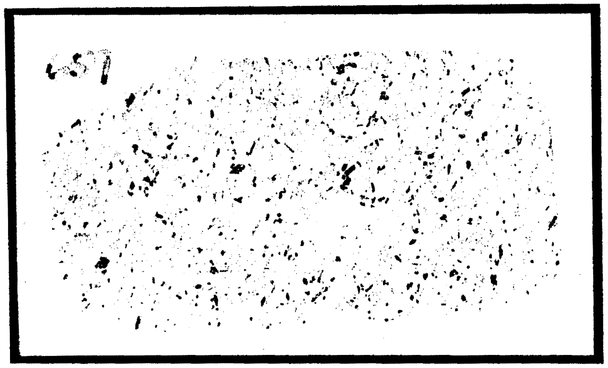

n. 156 m (bottom of DSB; note fractures)

o. basal tuff (from outcrop in Devil's Canyon)

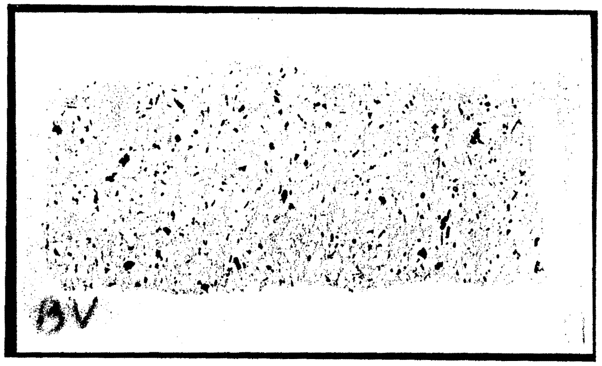

p. basal vitrophyre (from outcrop in Devil's Canyon)

# APPENDIX B
# SAMPLE X-RAY DIFFRACTION PLOTS

a. whole-rock analysis of sample from DSB core, 133 m vertical depth
b. clay separation analysis of sample from DSB core, 146 m vertical depth, Mg-saturated
c. clay separation from 146 m, showing peaks with K-air dried, Mg + ethylene glycol, K + 500°C, and Mg-saturated samples

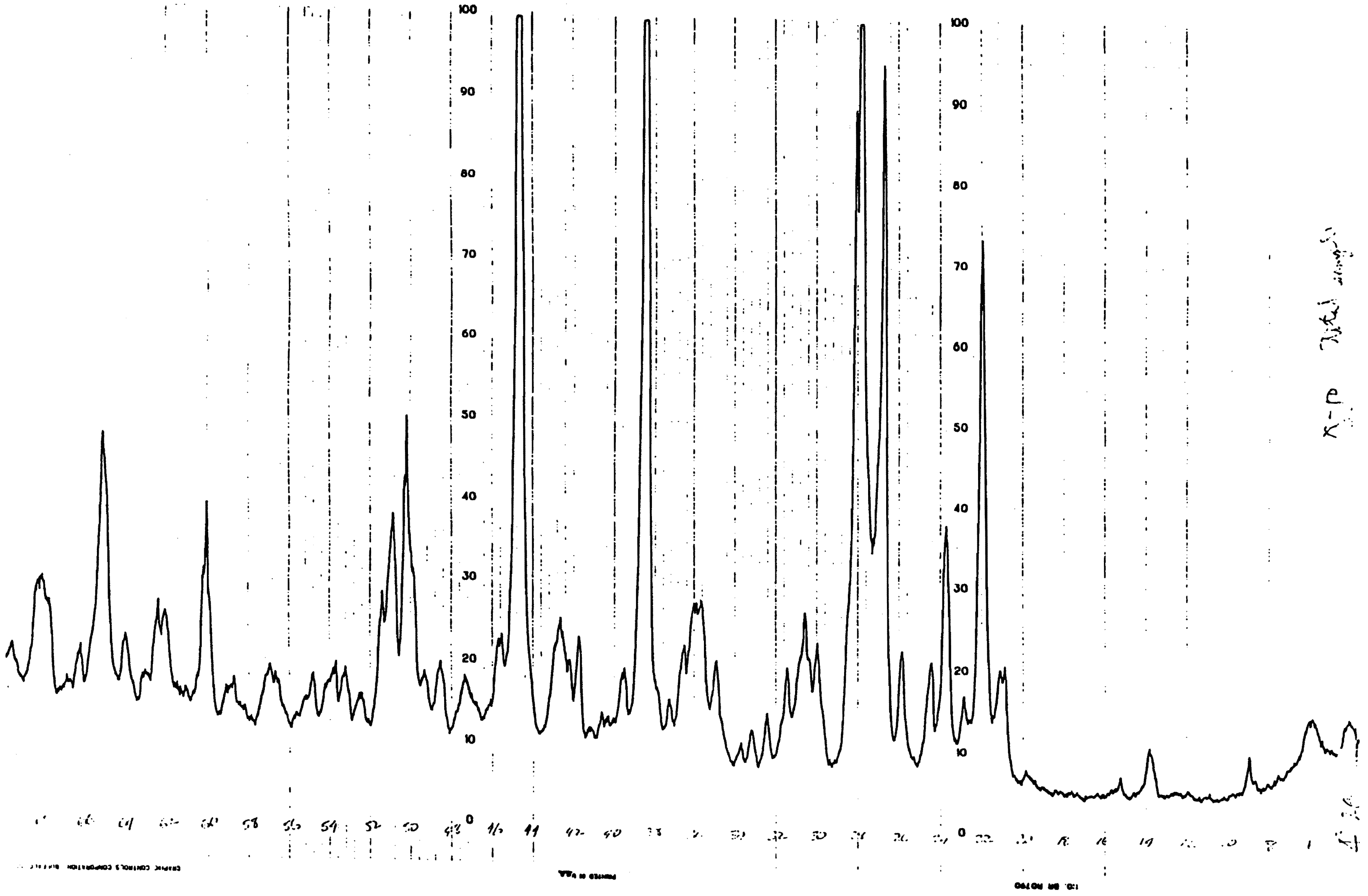

100
90
80
70
60
50
40
30
20
10
0
GRAPHIC CONTROLS CORPORATION BUFFALO
PRINTED IN U.S.A.
NO. BR RO790

a.

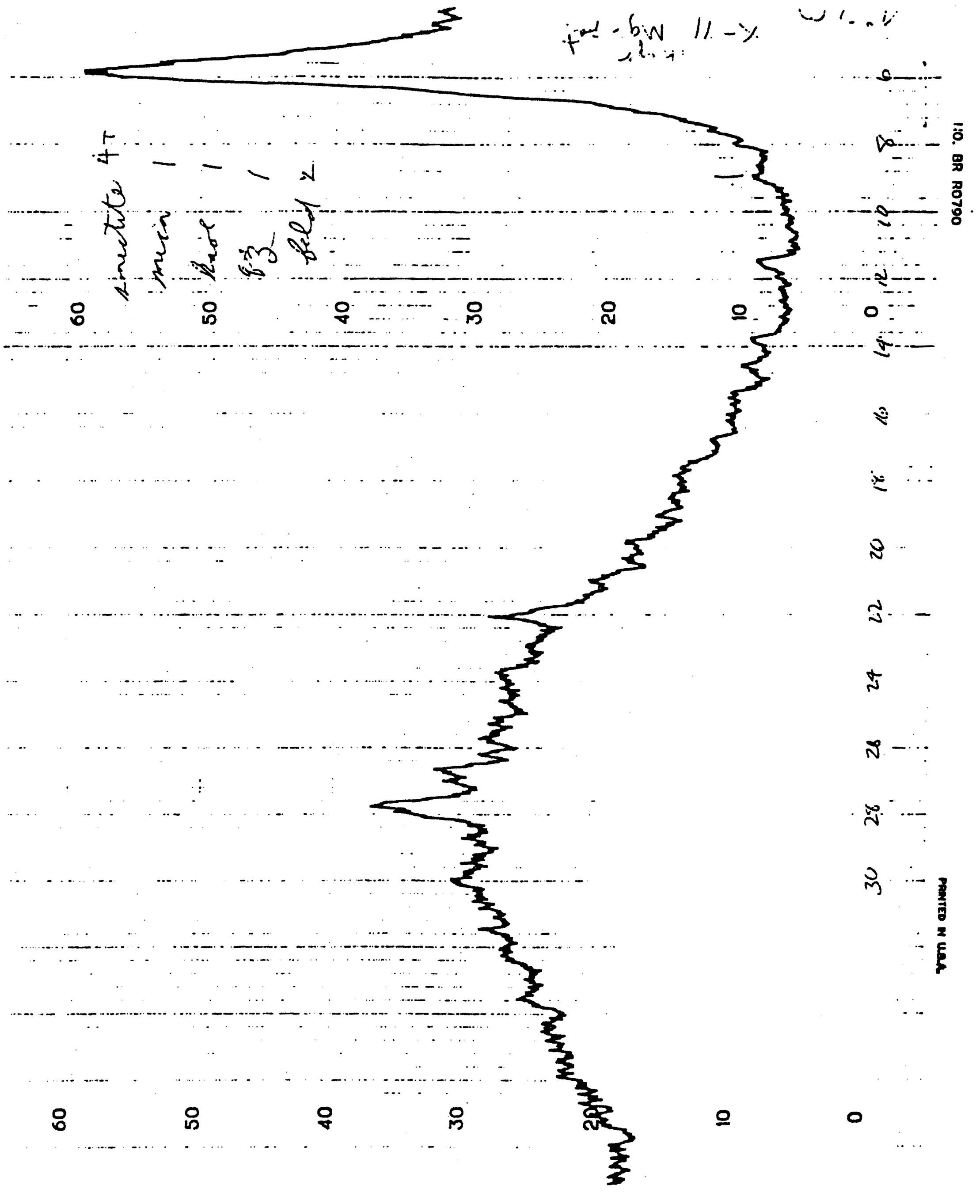
smectite 4T
mica 1
kaol 1
Q3 1
feld 2
X-11 Mg-sat
60
50
40
30
20
10
0
6
8
10
12
14
16
18
20
22
24
26
28
30
NO. BR R0790
PRINTED IN U.S.A.

b.

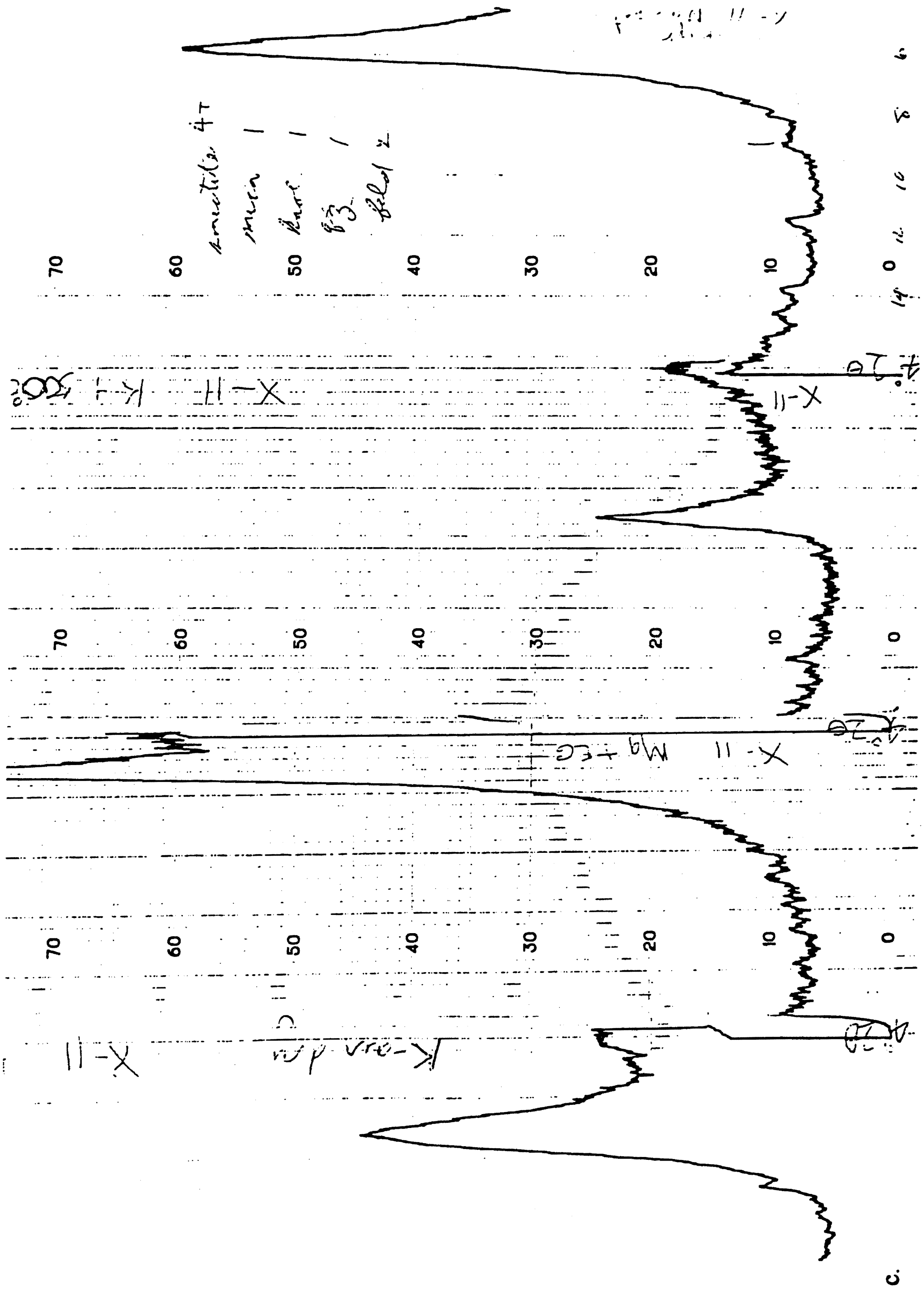
X-11
K-air dry C
4°2θ
X-11 Mg+EG
4°2θ
X-11 K-1 300°
4°2θ
X-11
smectite 4+
mica 1
kaol 1
qtz 1
feldsp 2
0
10
20
30
40
50
60
70

c.

# APPENDIX C

## Notes from the fracture analysis of the Deep Slant Borehole

Note that units are in feet, and depth intervals are in length along the DSB.

## CORE LOG

Hole ID:
Interval: b C D E F G H I J K L M N O P Q R S

| Interval (ft) | missing (ft) | longest length (cm) | rubble interval | fracs/ length | horiz fracs | vert fracs | h fracs sealed | v fracs sealed | h 2ndy white Si | v 2ndy white Si | h 2ndy clear Si | v 2ndy clear Si | h 2ndy yel. zeo | v 2ndy yel zeo | h 2ndy brn soft | v 2ndy brn soft | Other 2nd min | h slicks |
|---|---|---|---|---|---|---|---|---|---|---|---|---|---|---|---|---|---|---|
| 0-10 | 10 | 0 | | | | | | | | | | | | | | | | |
| 10-20 | 5 | 10 | | 3 | 1 | 2 | 0 | 0 | 0 | 0 | 0 | 1 | z | | 0 | 0 | oxm | 0 |
| 20-30 | 6 | 10 | | 3 | 1 | 2 | 0 | 0 | 0 | 1 | 1 | 1 | z | | 1 | 0 | oxm,mn | 0 |
| 30-40 | 7.5 | 61 | 37 | 1 | 1 | 0 | 0 | 0 | 0 | 0 | 0 | 0 | z | | 1 | 0 | mn | 0 |
| 40-50 | 9.3 | 10 | | 1 | 0 | 1 | 0 | 0 | 0 | 0 | 0 | 1 | 0 | | 0 | 0 | | 0 |
| 50-60 | 9 | 14 | 53.4 | 1 | 1 | 0 | 0 | 0 | 1 | 0 | 0 | 0 | z | | 0 | 0 | oxm,fe | 0 |
| 60-70 | 6.3 | 10 | | 4 | 1 | 3 | 0 | 0 | 0 | 0 | 0 | 1 | 0 | | 0 | 1 | oxm,fe | 0 |
| 70-80 | 7 | 33 | | 4 | 1 | 3 | 0 | 0 | 0 | 0 | 0 | 0 | 0 | | 0 | 1 | oxm,fe | 0 |
| 80-90 | 8.3 | 15 | | 3 | 3 | 0 | 0 | 0 | 0 | 0 | 0 | 0 | z | | 2 | 0 | | 0 |
| 90-100 | 9 | 16 | | 1 | 1 | 0 | 0 | 0 | 0 | 0 | 0 | 0 | z | | 0 | 0 | | 0 |
| 100-110 | 7.5 | 18.5 | | 3 | 2 | 1 | 0 | 0 | 0 | 0 | 0 | 0 | z | | 0 | 0 | | 0 |
| 110-120 | 3.5 | 32.5 | | 4 | 3 | 1 | 0 | 0 | 0 | 0 | 1 | 0 | z | | 0 | 0 | mn | 0 |
| 120-130 | 6.5 | 10 | 126-130 | 9 | 7 | 2 | 0 | 0 | 2 | 0 | 1 | 0 | z | | 3 | 0 | mn,fox | 0 |
| 130-140 | 5 | 10 | 131 & 139 | 14 | 12 | 2 | 1 | 0 | 0 | 0 | 3 | 0 | 0 | | 5 | 1 | fox | 0 |
| 140-150 | 7 | 10 | 141.9 | 6 | 4 | 2 | 0 | 0 | 1 | 0 | 1 | 0 | 0 | | 3 | 1 | mn | 0 |
| 150-160 | 6 | 38 | | 6 | 2 | 3 | 2 | 1 | 0 | 0 | 1 | 1 | z | | 0 | 0 | fox | 0 |
| 160-170 | 2 | 45 | | 14 | 5 | 9 | 1 | 0 | 3 | 1 | 1 | 3 | z | | 3 | 4 | fox | 0 |
| 170-180 | 3 | 10 | | 5 | 2 | 3 | 0 | 0 | 0 | 1 | 0 | 0 | 0 | | 0 | 0 | | 0 |
| 180-190 | 5.5 | 10 | | 6 | 5 | 1 | 0 | 0 | 1 | 0 | 1 | 0 | 0 | | 0 | 0 | fox | 0 |
| 190-200 | 0.5 | 34 | | 15 | 11 | 4 | 1 | 0 | 1 | 1 | 1 | 1 | 0 | | 1 | 2 | fox | 0 |
| 200-210 | 5.5 | 20 | 208-210 | 20 | 10 | 10 | 2 | 1 | 4 | 2 | 2 | 1 | 0 | | 4 | 5 | fox | 0 |
| 210-220 | 4.5 | 24 | 210-213 | 16 | 12 | 4 | 2 | 0 | 2 | 2 | 0 | 0 | 0 | | 1 | 4 | fox | 0 |
| 220-230 | 5 | 25 | 228.5 | 11 | 6 | 5 | 3 | 0 | 1 | 3 | 3 | 2 | 0 | | 1 | 2 | bl | 0 |
| 230-240 | 1.5 | 39 | | 11 | 6 | 5 | 1 | 0 | 2 | 1 | 2 | 1 | 0 | | 0 | 0 | bl | 0 |
| 240-250 | 2.5 | 35 | 243 & 246 | 9 | 6 | 3 | 0 | 0 | 1 | 0 | 2 | 1 | 0 | | 0 | 0 | bl,fox | 0 |
| 250-260 | 5.5 | 15 | 256-259 | 10 | 7 | 3 | 0 | 1 | 4 | 0 | 1 | 2 | 0 | | 3 | 0 | fox | 0 |
| 260-270 | 5 | 13 | 261 | 10 | 7 | 3 | 0 | 0 | 1 | 1 | 1 | 1 | 0 | | 0 | 1 | fox | 0 |
| 270-280 | 5 | 37 | | 8 | 8 | 0 | 1 | 0 | 4 | 0 | 2 | 0 | 0 | | 0 | 0 | fox | 0 |
| 280-290 | 2.5 | 40 | | 10 | 5 | 5 | 2 | 0 | 0 | 1 | 3 | 1 | 0 | | 0 | 1 | fox | 0 |
| 290-300 | 5.5 | 16 | | 5 | 4 | 1 | 1 | 0 | 0 | 0 | 1 | 0 | 0 | | 0 | 0 | fox | 0 |
| 300-310 | 2 | 42 | | 11 | 10 | 1 | 8 | 0 | 1 | 0 | 1 | 0 | 0 | 0 | 1 | 0 | | 0 |
| 310-320 | 6 | 22 | 310.5-316 | 24 | 14 | 3 | 1 | 3 | 0 | 3 | 6 | 0 | 0 | 0 | 2 | 2 | | 17 |
| 320-330 | 3 | 49 | | 9 | 9 | 0 | 5 | 0 | 3 | 0 | 0 | 0 | 0 | 0 | 1 | 0 | | 0 |
| 330-340 | 7.5 | 32 | | 5 | 5 | 0 | 0 | 0 | 3 | 0 | 1 | 0 | 0 | 0 | 0 | 0 | | 0 |
| 340-350 | 3 | 59 | | 10 | 8 | 2 | 1 | 0 | 0 | 1 | 2 | 0 | 0 | 1 | 1 | 0 | Fe-ox | 1 |

| | | | | | | | | | | | | | | | | | | |
|---|---|---|---|---|---|---|---|---|---|---|---|---|---|---|---|---|---|---|
| 350-360 | 0 | 59 | | 15 | 5 | 10 | 2 | 2 | 1 | 2 | 1 | 2 | 0 | 0 | 0 | 2 | | 0 |
| 360-370 | 2 | 53 | | 8 | 7 | 1 | 2 | 0 | 2 | 1 | 5 | 1 | 0 | 0 | 1 | 1 | | 0 |
| 370-380 | 2.5 | 78 | | 6 | 6 | 0 | 2 | 0 | 0 | 0 | 2 | 0 | 0 | 0 | 0 | 0 | | 0 |
| 380-390 | 8.5 | 17 | | 6 | 1 | 5 | 1 | 0 | 0 | 4 | 0 | 0 | 0 | 0 | 0 | 4 | | 0 |
| 390-400 | 5.5 | 45 | | 6 | 4 | 2 | 0 | 0 | 1 | 2 | 0 | 0 | 0 | 0 | 1 | 2 | | 1 |
| 400-410 | 3.5 | 62 | | 9 | 6 | 3 | 3 | 0 | 4 | 1 | 3 | 0 | 0 | 0 | 2 | 2 | | 0 |
| 410-420 | 3 | 62 | | 7 | 6 | 1 | 5 | 0 | 0 | 0 | 1 | 0 | 1 | 0 | 0 | 0 | | 1 |
| 420-430 | 4 | 10 | | 10 | 7 | 3 | 0 | 0 | 0 | 0 | 0 | 0 | 3 | 0 | 2 | 2 | | 2 |
| 430-440 | 2.5 | 22 | | 12 | 7 | 3 | 1 | 1 | 2 | 1 | 3 | 3 | 0 | 0 | 1 | 0 | | 0 |
| 440-450 | 2.5 | 57 | 446-446.2 | 15 | 10 | 5 | 2 | 1 | 0 | 0 | 0 | 4 | 1 | 0 | 2 | 0 | | 0 |
| 450-460 | 5 | 41 | 454-455 | 9 | 8 | 1 | 1 | 1 | 1 | 0 | 2 | 0 | 0 | 0 | 2 | 0 | | 0 |
| 460-470 | 2.5 | 18 | | 18 | 12 | 6 | 5 | 2 | 2 | 4 | 2 | 4 | 0 | 0 | 5 | 0 | | 0 |
| 470-480 | 3 | 29 | | 14 | 8 | 6 | 4 | 2 | 0 | 3 | 5 | 5 | 0 | 0 | 1 | 0 | | 0 |
| 480-490 | 5 | 32 | | 10 | 4 | 6 | 2 | 0 | 1 | 1 | 2 | 1 | 0 | 0 | 1 | 2 | Fe Ox. | 0 |
| 490-500 | 5.5 | 21 | | 15 | 5 | 10 | 1 | 1 | 1 | 3 | 1 | 3 | 0 | 0 | 4 | 2 | | 3 |
| 500-510 | 4.5 | 28 | | 9 | 5 | 4 | 0 | 7 | 1 | 1 | 1 | 0 | 0 | 0 | 2 | 0 | | 1 |
| 510-520 | 1 | 64 | | 7 | 4 | 3 | 2 | 0 | 0 | 0 | 0 | 0 | 0 | 0 | 0 | 0 | | 0 |
| 520-530 | 7.2 | 20 | | 14 | 10 | 1 | 5 | 1 | 4 | 0 | 2 | 0 | 0 | 0 | 5 | 0 | | 3 |
| 530-540 | 8 | 15 | 532-539 | 8 | 6 | 2 | 0 | 0 | 0 | 0 | 1 | 0 | 0 | 0 | 0 | 0 | | 0 |
| 540-550 | 4.5 | 23.5 | 545-546 | 13 | 11 | 2 | 1 | 1 | 5 | 0 | 5 | 1 | 0 | 0 | 4 | 1 | | 0 |
| 550-560 | 4.5 | 19 | 555-557 | 10 | 7 | 3 | 0 | 0 | 1 | 0 | 3 | 0 | 0 | 0 | 6 | 0 | | 1 |
| 560-570 | 9 | 16 | 561-570 | 2 | 1 | 1 | 0 | 1 | 0 | 0 | 0 | 0 | 0 | 0 | 0 | 1 | | 0 |
| 570-580 | 8.5 | 12 | 570-580 | 25 | 3 | 7 | 0 | 6 | 0 | 1 | 0 | 3 | 1 | 0 | 0 | 6 | rubber | 0 |
| 580-590 | 9.3 | 7 | 580-590 | 25 | 4 | 4 | | | 1 | 1 | 1 | 0 | 0 | 0 | 0 | 0 | | 2 |
| 590-600 | 9 | 26 | 590-600 | 2 | 2 | | 0 | 0 | 1 | 0 | 0 | 0 | 0 | 0 | 0 | 0 | | 2 |
| 600-610 | 3 | 23 | 601.5; 607 | 25 | 19 | 4 | 1 | 0 | 5 | 2 | 1 | 0 | 0 | 0 | 3 | 0 | | 0 |
| 610-620 | 6 | 15 | 616-620 | 12 | 10 | 4 | 0 | 1 | 0 | 0 | 0 | 0 | 0 | 0 | 0 | 0 | | 0 |
| 620-630 | 9.5 | 12 | 620-630 | 25 | 14 | | | | 0 | 0 | 0 | 0 | 0 | 0 | 0 | 0 | | 0 |
| 630-640 | 8 | 9.5 | 632-635 | 12 | ? | ? | | | 0 | 0 | 0 | | 0 | 0 | 0 | 0 | | 0 |
| 640-650 | 9.5 | 6 | ? | 25 | ? | ? | 3 | 1 | 1 | 0 | 0 | 0 | 0 | 0 | 0 | 0 | | 2 |
| 650-661 | 6 | 14 | | 18 | 13 | 5 | 2 | 0 | 0 | 0 | 1 | 0 | 0 | 0 | 0 | 0 | | 1 |

mn = Mn-oxide (?--black) coating (usu. lines) on fracture surfaces

oxm = copper-colored hexagonal mica scattered throughout

fox = Fe-oxides or oxidized black minerals scattered throughout or on fracture surfaces

T U V W X Y Z AA page AB of ____

| v slicks | lg lith >1.0 | sm lith 0-1.0 | h lith. fract | v lith fract | xeno diam | rel alt | pum flat | Remarks | |
|---|---|---|---|---|---|---|---|---|---|
| | | | | | | | | | |
| | | | | | | | | | 0-10 |
| 0 | 2 | 2 | 0 | 0 | .2-1.5 | 2 | 0.5 | big pum, hard to orient, dries v. slowly | |
| 0 | 0 | 3 | 0 | 0 | .2-3 | 1.5 | 0.5 | some v. soft zen; easy to scratch out | |
| 0 | 0 | 3 | 0 | 0 | .2-2 | 1.8 | 0.5 | same | |
| 0 | 0 | 0 | 0 | 0 | .2-1 | 1.8 | 0.5 | same | |
| 0 | 0 | 3 | 0 | 0 | .2-2 | 1.8 | 0.6 | same | |
| 0 | 3 | 0 | 0 | 0 | .2-3 | 1.5 | 0.8 | v. fracs v.irreg, often like break at zen | |
| 0 | 0 | 4 | 0 | 0 | .2-2 | 1.5 | 0.9 | same | |
| 0 | 1 | 1 | 0 | 0 | .2-1.5 | 1.5 | 1 | a few more eroding zen than above? | |
| 0 | 2 | 3 | 0 | 0 | .2-1.5 | 1.5 | 1 | — | |
| 0 | 2 | 0 | 0 | 0 | .2-1.5 | 1.5 | 1 | hrd to orient; long to dry; alt rings, oxm | 100-110 |
| 0 | 1 | 0 | 0 | 0 | .3-2.5 | 1.5 | 1 | more orientation? oxm | |
| 0 | 1 | 0 | 0 | 0 | .5-.8 | 2 | 1 | h fracs "freckled" w fox | |
| 0 | 3 | 0 | 1 | 0 | .5-2.5 | 2 | 1.3 | 139 v altered/brecchia? fault? | |
| 0 | 1 | 0 | 0 | 0 | .5-1 | 1.8 | 1.4 | — | |
| 0 | 3 | 0 | 2 | 1 | .5-3 | 2 | 1.4 | v lg pumice blobs; longer, less frac'd | |
| 0 | 3 | 0 | 1 | 0 | .5-5 | 1.7 | 1.5 | more brown clay on fracs | |
| 0 | 0 | 3 | 0 | 0 | .5-3.5 | 1.5 | 1.5 | unremarkable | |
| 0 | 0 | 0 | 0 | 0 | .5-1.5 | 1.4 | 1.5 | unremarkable | |
| 1 | 6h2 | 1 | 1 | 0 | .5-4 | 1.4 | 1.5 | — | |
| 0 | 1 | 0 | 1 | 0 | .5-6 | 2 | 1.5 | mn-0x, fox | 200-210 |
| 0 | 0 | 0 | 0 | 0 | .5-6 | 2 | 1.5 | fox, less mn | |
| 0 | 4 | 0 | 0 | 0 | .5-6 | 2.2 | 1.5 | 223 h frac soft white 2nd sampled, mn | |
| 0 | 1 | 5 | 1 | 0 | .5-5 | 2 | 1.5 | fewer fox | |
| 0 | 4 | 1 | 0 | 0 | .5-8 | 2 | 1.5 | 243 rubble vuggy qtz; lg zenoliths | |
| 0 | 0 | 0 | 0 | 0 | .5-4 | 1.8 | 1.4 | no vugs | |
| 0 | 0 | 0 | 0 | 0 | .5-5 | 1.6 | 1.4 | core dirtier but similar to above | |
| 0 | 0 | 0 | 0 | 0 | 1-4 | 1.6 | 1.4 | same | |
| 0 | 5 | 1 | 2 | 0 | 1-4 | 2 | 1.5 | druzy qtz frac; more vugs w fracs | |
| 0 | 1 | 1 | 1 | 0 | 1-4 | 1.8 | 1.5 | fewer vugs again | |
| 1 | 1 | 0 | 4 | 0 | 0.5-4 | 2 | 1.5 | slick @ 300' not planar but fresh | 300-310 |
| 0 | 0 | 1 | 0 | 0 | 0.5-2 | 2.2 | 1.5 | abund. slicks above layered horiz frac | |
| 0 | 1 | 1 | 0 | 0 | 0.5 | 1.8 | 1.5 | --- | |
| 0 | 0 | 0 | 0 | 0 | 0.5 | 1.5 | 1.5 | horiz frac surfaces mostly very irreg. | |
| 0 | 1 | 2 | 0 | 0 | 0.5-3 | 2 | 1.5 | 346.5 sample white soft frac coating | |

| | | | | | | | | | |
|---|---|---|---|---|---|---|---|---|---|
| 0 | 1 | 2 | 0 | 0 | 0.5-5 | 1.8 | 1.5 | more vert fracs than horiz | 350-360 |
| 0 | 4 | 2 | 0 | 0 | 0.5-2 | 2.2 | 1.8 | 4-cm "vug" looks like dissolved rock | |
| 0 | 1 | 0 | 1 | 0 | 0.5-1 | 1.5 | 1.8 | relatively unfractured | |
| 1 | 0 | 9 | 0 | 0 | 0.5-1 | 1.9 | 2 | ~489 looks quite altered | |
| 0 | 1 | 0 | 0 | 0 | 0.5-1 | 2 | 2 | — | |
| 1 | 2 | 1 | 0 | 0 | 1 | 2.2 | 2 | 407 2nd Si extends deep into core | 400-410 |
| 0 | 0 | 1 | 3 | 0 | 0.5-4.5 | 2 | 2 | most alt @ vuggy fracs ~ 412 | |
| 0 | 0 | 0 | 0 | 0 | 0.4-4 | 2 | 2 | big zenolith of granite 4 cm @ 429 | |
| 2 | 0 | 0 | 1 | 0 | 1 | 2 | 2 | slick @ 435.5 v. fresh w/ 2nd Si | |
| 0 | 2 | 3 | 0 | 0 | 0.5-1 | 1.5 | 2 | — | |
| 0 | 0 | 7 | 1 | 1 | 1-2 | 2 | 2 | fewer lithophysae | 450-460 |
| 0 | 4 | 7 | 2 | 1 | 1.2 | 2.2 | 2 | more liths, some v. large, sample | |
| 1 | 2 | 6 | 4 | 0 | 1.2 | 2 | 2 | 478.5 vug fill (zeo?); more filled liths | |
| 0 | 2 | 1 | 2 | 0 | 0.5 | 1.5 | 2 | — | |
| 0 | 1 | 0 | 1 | 1 | 0.5-2 | 2 | 2 | most alt @ 500'; most slicks @ 490' | |
| 0 | 0 | 1 | 0 | 0 | 2 | 2.5 | 2 | 510' sample of brown clay | 500-510 |
| 0 | 1 | 0 | 2 | 1 | 1 | 1 | 2 | core is Fe-stained | |
| 0 | 0 | 1 | | 10 | 1-3 | 3 | 2 | sample @ 521.3 almost brecciated | |
| 1 | 1 | 0 | 0 | 0 | 1 | 1 | 2 | mostly 5-10 cm rubble frags | |
| 1 | 0 | 2 | 0 | 0 | 1 | 2 | 2 | alteration only as fracture coating | |
| 0 | 0 | 0 | 0 | 0 | 1-4 | 2 | 2 | same as above | 550-560 |
| 1 | 0 | 0 | 0 | 0 | 0.2 | 3 | 2 | looks brecciated; hard to orient | 560 |
| 3 | 0 | 1 | 0 | | 1 | 3 | 2 | slicks abund. on frags; looks brecc. | |
| 0 | 0 | 1 | | | 0.5 | 3 | 2 | same, but w/ no brwn 2ndy min | 590 |
| 0 | 0 | 2 | | | 0.5 | 2.5 | 2 | mostly rubble except for 1 pce | |
| 1 | 5 | 0 | 0 | 0 | 1-3 | 2 | 2 | broken, but less slicks & 2ndy min | 600-610 |
| 1 | 3 | 0 | 0 | 0 | 0.3-2 | 1.5 | 2 | rubble | |
| 1 | 0 | 1 | 0 | 0 | 0.5 | 2 | 2 | rubble | |
| 0 | 3 | 0 | 0 | 0 | 0.3 | 2 | 2 | rubble | |
| 0 | 1 | 0 | 3 | 0 | 0.3 | 2 | 2 | v. slight increase in vugs/fracs? | |
| 4 | 0 | 0 | 1 | 0 | 0.3-5 | 1 | 2 | 652-653.3 much smoother, less altere | 650-661 |
| | | | | | | | | 661 sampled for dk red slick mat'l | |

# APPENDIX D
## Core log of MB-10A

Note that depth of the log is recorded in units of feet.

# SUPERIOR DIV.

HOLE No. MB-10A
LEVEL Surface-~~elev 40?0'~~
~~TD 1712.8'~~
bentonite drilling fluid

surface elev 4030'

HOLE SURVEY BY: ______________ $H_2O$ noted around 900' down to base of tuff

| DEPTH | AZ MAG | AZ TRU | MEAS DIP | TRU INCL |
|---|---|---|---|---|
| | | | | |
| | | | | |
| | | | | |
| | | | | |
| | | | | |
| | | | | |

SCALE ______________

NOTES BY SLM

paper filler in mud to restore circulation at ~900'

~~Location N 33°18'53.12~~
~~W 111°2'16.98~~
~~sec 28 Twp 1S Rg 13E~~
Loc. - sec. 6 - begin at dirt road at top of section, go down to intersection of 4040 contour

| DEPTH | COLUMN | COMMENTS | FORMATION | ROCK TYPE | GANGUE | SULFIDES | ALTERATION | | | ASSAYS INTERCEPT | ASSAYS INTERVAL | CU | AG | AU | ZN | PB | INTERCEPT | % RECOVERED | % R.Q.D. |
|---|---|---|---|---|---|---|---|---|---|---|---|---|---|---|---|---|---|---|---|
| 0 | | **0-1,264' – Dacite Tuff**<br>Tg unit. Skeletonized, 10' out of every 100' in upper 1,200'. | | | | | | | | | | | | | | | | | |
| 50–60<br>15-16 | | Compaction foliation in weathered tuff @ ~80° to core.<br>mostly horiz fractures, surfaces w/ abundant black opaque min's<br>white zone<br>Fracs at least every 6'<br>several high ∠ fracs, though, but not vuggy | | | | | | | | | | | | | | | 50–60 | 92 | 24 |
| 150–160<br>46-49 | | Compaction foliation @ 80° to core. Some zeolites in vugs.<br>1 vug filled w/ very hard white qtz-like crystals white xl filling<br>some evidence of slicks on horiz frac w/ sm. amt<br>high ∠ faults w/ abundant orange-yellow filling<br>white-gray fracs 6-18" apart | | | | | | | | | | | | | | | 150–160 | 96 | 56 |
| 250–260<br>76-79 | | Compaction foliation @ 80° to core. Zeolites in vugs.<br>upper gray, fracs 6-18" apart, mostly horiz, but few high ∠<br>double, high ∠ & [illegible] & cemented frac, vuggy<br>no signif alteration area | | | | | | | | | | | | | | | 250–260 | 97 | 59 |
| 350–360<br>107-110 | | Cut by numerous fractures ~ 20° to core.<br>grey fracs 2-10" apart<br>mostly barely sealed fracs at ~30°, also some open high ∠ & ones<br>powdery white-gray frac coating at [illegible] ~10 x/s | | | | | | | | | | | | | | | 350–360 | 98 | 26 |
| 450–460<br>137-140 | | Compaction foliation @ ~80° to core.<br>more fracture at ~20°, few high ∠ ones. Some filled vugs & vuggy fractures<br>highly irreg slick fractures | | | | | | | | | | | | | | | 450–460 | 100 | 42 |
| 550–560<br>168-171 | | Open fractures in dacite @ 10°, 20° from core axis, stand 0.5 to 1.0 cm wide.<br>long filled/vuggy high ∠ frac; open in places, but some very fine white xl & cobwebby-paper? coating | | | | | | | | | | | | | | | 550–560 | 91 | 59 |
| 650–660<br>☆ 175-201 | | A cms-thick clayey shear @ ~20° to core.<br>most highly altered, rubbly box<br>a lot of pasty/clay stuff, & some white xl coatings<br>vert & horiz fracs | | | | | | | | | | | | | | | 650–660 | 78 | 41 |
| 750–760<br>229-232 ☆ | | Core darker, more densely welded than above. Compaction foliation @ ~75°<br>much less fractured, only some horiz ones<br>some faint, thin, non-vuggy sealed fracs | | | | | | | | | | | | | | | 750–760 | 93 | 72 |

SUPERIOR DIV.

HOLE No. MB-10A
LEVEL surface
DRILL STA.
COLLAR COORD N
E
EL
DIRECTION
INCLINATION -90°
TOTAL DEPTH
STARTED
FINISHED

SCALE 1:240
NOTES BY SLM

OLE SURVEY BY:

| DEPTH | AZ MAG | AZ TRU | MEAS DIP | TRU INCL |
|---|---|---|---|---|
| | | | | |
| | | | | |
| | | | | |
| | | | | |
| | | | | |
| | | | | |

| DEPTH | COMMENTS | FORMATION | ROCK TYPE | GANGUE | SULFIDES | ALTERATION | ASSAYS INTER CEPT | INTER VAL | CU | AG | AU | ZN | PB | INTERCEPT | % RECOVERED | % R.Q.D. |
|---|---|---|---|---|---|---|---|---|---|---|---|---|---|---|---|---|
| 257' 260 850–860 | Uggy fracture coated w/ zeolites, ≤ 1 cm wide.<br>a few sealed vert. fracs but otherwise continued fairly massive<br>Fracs 30-40° | | | | | | | | | | | | | 850–860 | 92 | 63 |
| 290' 293 950–960 | Densely-welded red-brn tuff. Scattered calcite vnlts. ↑prob Si Min<br>Fracs 3-24" apart densely welded, some sealed thin fracs, no vugs 20-45° pumice less oriented<br>↕1.5" ~~calcite~~ qtz? filling (no HCl fizz) | | | | | | | | | | | | | 950–960 | 92 | 79 |
| 17 19 | | | | | | | | | | | | | | | | |
| 320 323 1050–1060 | Densely-welded tuff w/ scattered lithic frags.<br>getting into brown zone? few pumice frags, more lithic | | | | | | | | | | | | | 1050–1060 | 89 | 78 |
| 40 43 | | | | | | | | | | | | | | | | |
| 351' 354 1150–1160 | Densely-welded tuff w/ inclusions of black glass. Lithic frags. A slicked surface @ 20° to core. Subhorizontal slicks.<br>white-filled fracs (very thin) at all orientations<br>Some clear, glassy? fracture fill on high ∠ frac | | | | | | | | | | | | | 1150–1160 | 97 | 76 |
| 76-79 2 3 1160–1186 | No core saved | | | | | | | | | | | | | 1160–1186 | | |
| 1186–1196 | Densely-welded red-brn tuff | | | | | | | | | | | | | 1186–1196 | 91 | 52 |
| 364 | Abrupt transition<br>↓ 381<br>1195'-1251' - Vitrophyre. Dense, black, glassy. Partly weathered, devitrified on steep fracs. Lithic frags present. A few fracs and amygdules filled w/ opaline silica. | | | | | | | | | | | | | | | |
| 1196–1206 | | | | | | | | | | | | | | 1196–1206 | 99 | 47 |
| 1206–1216 | | | | | | | | | | | | | | 1206–1216 | 96 | 77 |
| 1216–1226 | 1224 greenish coating on fracture surfaces | | | | | | | | | | | | | 1216–1226 | 99 | 26 |
| 1226–1232 | | | | | | | | | | | | | | 1226–1232 | 100 | 40 |
| 1232–1235 | | | | | | | | | | | | | | 1232–1235 | 94 | 0 |

SUPERIOR DIV.

HOLE No. MB-10 A

LEVEL Surface

DRILL STA

OLE SURVEY BY:

COLLAR COORD N

E

EL

SCALE 1:240

NOTES BY SLM

DIRECTION

INCLINATION -90°

TOTAL DEPTH

STARTED

FINISHED

| DEPTH | AZ MAG | AZ TRU | MEAS DIP | TRU INCL |
|---|---|---|---|---|
| | | | | |
| | | | | |
| | | | | |
| | | | | |
| | | | | |
| | | | | |

| DEPTH | COLUMN | COMMENTS | FORMATION | ROCK TYPE | GANGUE | SULFIDES | ALTERATION | | | ASSAYS | | | | | | | MINERAL | % RECOVERED | % R.Q.D. |
|---|---|---|---|---|---|---|---|---|---|---|---|---|---|---|---|---|---|---|---|
| | | | | | | | | | | INTER CEPT | INTER VAL | CU | AG | AU | ZN | PB | | | |

Abrupt transition

**1251-1263'** — Moderately- to poorly-welded dacite tuff, red-brn to lt. gray in color. Quite weathered, argillic at base. Contact w/ underlying cgl is remarkably sharp and planar.

Conformable contact @ 70° to core.

1263' - Whitetail Fm.

Cobble cgl., ~1264'-1345'. Polymictic, w/ angular to subrounded clasts up to 20 cm across. Clast-rich, commonly framework-supported. Matrix is moderately indurated, sandy + calcareous. Clasts - Ls, diabase, qtzite, lesser schist + granitic rocks. Intercalated Ss lenses, tuff horizons

Cms-thick, clayey shear.

Tuffaceous Sandy lens @ 30° to core.

1260 basal tuff
Free fill

| | % RECOVERED | % R.Q.D. |
|---|---|---|
| 1232 | 94 | 0 |
| 1235 | 100 | 27 |
| 1242 | 100 | 75 |
| 1261 | 100 | 66 |
| 1271 | 75 | 72 |
| 1273 | 100 | 79 |
| 1278 | 100 | 77 |
| 1287 | 100 | 70 |
| 1297 | 94 | 84 |

# APPENDIX E
## Theory of the Bowen Ratio System

Within a few meters of the earth's surface, the water vapor flux and heat flux can be expressed as:

$$E = k_v \frac{\partial q}{\partial z} \tag{1}$$

$$H = \rho c_p k_H \frac{\partial T}{\partial z} \tag{2}$$

where $E$ = water vapor flux ($kg/m^2s$)
$H$ = heat flux ($W/m^2$)
$q$ = vapor density ($kg/m^3$)
$\rho$ = air density ($kg/m^3$)
$c_p$= specific heat of air ($kJ/kg^oC$)
$T$ = temperature ($^oC$)
$z$ = vertical height above surface (m)
$k_v$= eddy diffusivity for vapor ($m^2/s$)
$k_H$= eddy diffusivity for heat ($m^2/s$)

By applying the universal gas law to (1) and using the latent heat of vaporization, the latent heat flux is obtained in terms of vapor pressure:

$$L_e = \frac{\lambda \rho \epsilon k_v}{p} \frac{\partial e}{\partial z} \tag{3}$$

where $L_e$ = latent heat flux ($W/m^2$)
$\lambda$ = latent heat of vaporization (kJ/kg)
$\epsilon$ = ratio of molecular weight of water to the molecular weight of air
$e$ = vapor pressure (kPa)
$p$ = atmospheric pressure (kPa)

In practice, finite gradients are measured, and an effective eddy diffusivity is assumed over the vertical gradient:

$$L_e = \frac{\lambda \rho \epsilon k_v}{p} \frac{(e_1 - e_2)}{(z_1 - z_2)} \tag{4}$$

$$H = \frac{\rho c_p k_h (T_1 - T_2)}{(z_1 - z_2)} \tag{5}$$

In general, $k_v$ and $k_H$ are unknown, but can be assumed to be equal.

The Bowen ratio is the ratio of H to Le:

$$\beta = \text{Bowen ratio} = \frac{p\, c_p\, (T_1 - T_2)}{\lambda \epsilon\, (e_1 - e_2)} \tag{6}$$

where the ratio $\frac{p\, c_p}{\lambda \epsilon}$ is the psychrometric constant.

The surface energy budget is given by:

$$R_n = G + H + L_e \tag{7}$$

where $R_n$ = net radiation for the surface (W/m$^2$)
$G$ = soil heat flux (W/m$^2$)

Substituting $L_e\beta$ for H in (7) and solving for $L_e$ yields:

$$L_e = \frac{Rn - G}{1 + \beta} \tag{8}$$

The Bowen ratio system gives $\beta$ in (6) by measuring temperature and relative humidity (RH) at two heights; RH is then converted to vapor pressure. Temperature is measured with thermocouples; RH is measured with a single cooled mirror dew point hygrometer. $R_n$ is measured with a net radiometer; G is measured from soil heat flux plates, and soil and rock temperature thermocouples buried at depth in the soil or rock. $L_e$ is then used to solve for total evapotranspiration. (Theory from CSI, 1993.)

# APPENDIX F

## Campbell Scientific CR-10 datalogger program for micrometeorological station

```
Program: CR10 Bowen Ratio/Weather Program with AM416
Flag Usage:
1 High to disable averaging while mirror stabilizes
2 Active air intake:  High =  upper, low = lower
3 Battery subroutine:  High = pump & mirror off
4 Set high to output to current time and
  disable processing.  Set low to resume.
5 Used by program during user disable
6 Pulse high to turn on pump and mirror
7 Pulse high to turn off pump and mirror
8 High at end of intervals while soil T is averaged
Input Channel Usage:  see wiring diagram
Excitation Channel Usage:  see wiring diagram
Control Port Usage:  see wiring diagram
Pulse Input Channel Usage: see wiring diagram
Output Array Definitions:


*    1      Table 1 Programs
 01: 1       Sec. Execution Interval

01:  P11      Temp 107 Probe
 01: 1      Rep
 02: 1      IN Chan
 03: 3      Excite all reps w/EXchan 3
 04: 1      Loc [:panl temp]
 05: 1      Mult
 06: 0      Offset

02:  P13     Thermocouple Temp (SE)
 01: 1      Rep
 02: 1      2.5 mV slow Range
 03: 12      IN Chan
 04: 2      Type E (Chromel-Constantan)
 05: 1      Ref Temp Loc panl temp
 06: 3      Loc [:lower tc ]
 07: 1      Mult
```

```
  08: 0      Offset

03:  P14      Thermocouple Temp (DIFF)
  01: 1      Rep
  02: 1      2.5 mV slow Range
  03: 6      IN Chan
  04: 2      Type E (Chromel-Constantan)
  05: 3      Ref Temp Loc lower tc
  06: 2      Loc [:upper tc ]
  07: 1      Mult
  08: 0      Offset

04:  P6       Full Bridge
  01: 1      Rep
  02: 1      2.5 mV slow Range
  03: 2      IN Chan
  04: 1      Excite all reps w/EXchan 1
  05: 2500    mV Excitation
  06: 8      Loc [:dew pt   ]
  07: .001    Mult
  08: .00498  Offset

05:  P35      Z=X-Y
  01: 3      X Loc lower tc
  02: 2      Y Loc upper tc
  03: 4      Z Loc [:delta t  ]

06:  P59      BR Transform Rf[X/(1-X)]
  01: 1      Rep
  02: 8      Loc [:dew pt   ]
  03: 200     Multiplier (Rf)

07:  P16      Temperature RTD
  01: 1      Rep
  02: 8      R/Ro Loc dew pt
  03: 8      Loc [:dew pt   ]
  04: 1      Mult
  05: 0      Offset

08:  P56      Saturation Vapor Pressure
  01: 8      Temperature Loc dew pt
```

```
  02: 9      Loc [:vap pres ]


  OUTPUT PROCESSING

09:  P91      If Flag/Port         Bypass output if flag 5 is set
 01: 15      Do if flag 5 is high
 02: 0       Go to end of Program Table

10:  P92      If time is
 01: 0       minutes into a
 02: 60      minute interval
 03: 10      Set high Flag 0 (output)

11:  P80      Set Active Storage Area
 01: 1       Final Storage Area 1
 02: 110     Array ID or location

12:  P91      If Flag/Port
 01: 14      Do if flag 4 is high
 02: 30      Then Do

13:  P86      Do
 01: 10      Set high Flag 0 (output)  output data to current time

14:  P80      Set Active Storage Area
 01: 1       Final Storage Area 1
 02: 112     Array ID or location

15:  P86      Do
 01: 15      Set high Flag 5     disable further output

16:  P95      End

17:  P77      Real Time          DAY, HR:MIN
 01: 110     Day,Hour-Minute

18:  P70      Sample             PANEL TEMP
 01: 1       Reps
 02: 1       Loc panl temp
```

```
19: P71      Average          LOWER TC TEMP & DELTA T
 01: 2       Reps
 02: 3       Loc lower tc


20: P91      If Flag/Port     DISABLE AVERAGE IF ON UPPER INTAKE
 01: 12      Do if flag 2 is high
 02: 30      Then Do

21: P86      Do
 01: 19      Set high Flag 9

22: P94      Else

23: P91      If Flag/Port     DISABLE AVERAGE IF JUST SWITCHED
 01: 11      Do if flag 1 is high
 02: 19      Set high Flag 9

24: P95      End

25: P71      Average     DEW PT & VAP PRES FROM LOWER INTAKE
 01: 2       Reps
 02: 8       Loc dew pt

26: P86      Do     RE-ENABLE INTERMEDIATE PROCESSING
 01: 29      Set low Flag 9

27: P91      If Flag/Port     DISABLE AVERAGE IF ON LOWER INTAKE
 01: 22      Do if flag 2 is low
 02: 30      Then Do

28: P86      Do
 01: 19      Set high Flag 9

29: P94      Else

30: P91      If Flag/Port     DISABLE AVERAGE IF JUST SWITCHED
 01: 11      Do if flag 1 is high
 02: 19      Set high Flag 9

31: P95      End
```

```
32:  P71     Average      DEW PT & VAP PRES FROM UPPER INTAKE
 01: 2      Reps
 02: 8      Loc dew pt

33:  P      End Table 1


*    2     Table 2 Programs
 01: 10     Sec. Execution Interval

01:  P18     Time  TIME FOR COOLED MIRROR TO STABILIZE AFTER
            SWITCH
 01: 0      Seconds into current minute (maximum 60)
 02: 40     Mod/by     GOES TO 0 AT 40 SEC INTO MINUTE
 03: 11     Loc [:s into m ]

02:  P89     If X<=>F      CHECK IF TIME TO ENABLE AVERAGE
 01: 11     X Loc s into m
 02: 4      <
 03: 10     F
 04: 21     Set low Flag 1

03:  P91     If Flag/Port     IF OUTPUT IS DISABLED
 01: 15     Do if flag 5 is high
 02: 30     Then Do

04:  P91     If Flag/Port
 01: 24     Do if flag 4 is low      CHECK IF USER HAS RE-ENABLED
 02: 1      Call Subroutine 1

05:  P95     End

06:  P92     If time is      SOLENOID SWITCHING EVERY 2 MINUTES
 01: 0      minutes into a
 02: 2      minute interval
 03: 30     Then Do

07:  P86     Do      DISABLE AVERAGE WHEN JUST SWITCHED TO ALLOW
 01: 11     Set high Flag 1      COOLED MIRROR TO STABILIZE

08:  P92     If time is          EVERY 4 MINUTES...
```

```
 01: 0      minutes into a
 02: 4      minute interval
 03: 30      Then Do

09:  P86     Do
 01: 72     Pulse Port 2

10:  P86     Do     FLAG 2 SET HIGH WHILE ON UPPER
 01: 12     Set high Flag 2

11:  P94     Else     2 MINUTES INTO 4 MINUTE INTERVAL...

12:  P86     Do
 01: 71     Pulse Port 1

13:  P86     Do     FLAG 2 LOW WHILE ON LOWER
 01: 22     Set low Flag 2

14:  P95     End

15:  P95     End

16:  P10     Battery Voltage
 01: 10     Loc [:batt volt]

17:  P86     Do               RESET AM416
 01: 45     Set high Port 5

18:  P86     Do               CLOCK TO AM416 SET 1
 01: 76     Pulse Port 6

19:  P2      Volt (DIFF)     MEASURE NET RADIATION
 01: 1      Rep
 02: 4      250 mV slow Range
 03: 4      IN Chan
 04: 21      Loc [:uncRn w/m]
 05: 1      Mult               NR #93090
 06: 0      Offset

20:  P89     If X<=>F
 01: 21     X Loc uncRn w/m
```

```
 02: 3       >=
 03: 0       F
 04: 30      Then Do

21:  P37     Z=X*F
 01: 21      X Loc uncRn w/m
 02: 8.64    F                  CAL FOR POSITIVE RNET
 03: 15      Z Loc [:Rn W/m2  ]

22:  P95     End


23:  P89     If X<=>F
 01: 21      X Loc uncRn w/m
 02: 4       <
 03: 0       F
 04: 30      Then Do

24:  P37     Z=X*F
 01: 21      X Loc uncRn w/m
 02: 10.55   F                  CAL FOR NEGATIVE RNET
 03: 15      Z Loc [:Rn W/m2  ]

25:  P95     End

26:  P86     Do
 01: 76      Pulse Port 6     CLOCK TO AM416 SET 2

27:  P2      Volt (DIFF)
 01: 1       Rep
 02: 3       25 mV slow Range
 03: 4       IN Chan
 04: 16      Loc [:SHF #1   ] (shade)
 05: 43.6    Mult     CAL for HFT #933099
 06: 0.0000  Offset

28:  P86     Do
 01: 76      Pulse Port 6     CLOCK TO AM416 SET 3

29:  P2      Volt (DIFF)
 01: 1       Rep
```

```
 02: 3       25 mV slow Range
 03: 4       IN Chan
 04: 17      Loc [:SHf #2  ]     (open)
 05: 37.5    Mult      CAL for HFT #933102
 06: 0.0000  Offset

30: P86      Do
 01: 76      Pulse Port 6      CLOCK TO AM416 SET 4




31: P4       Excite,Delay,Volt(SE)
 01: 1       Rep
 02: 5       2500 mV slow Range
 03: 2       IN Chan
 04: 2       Excite all reps w/EXchan 2
 05: 2       Delay (units .01sec)
 06: 2500    mV Excitation
 07: 13      Loc [:Wind dir ]
 08: .142    Mult
 09: 0       Offset

32: P86      Do
 01: 76      Pulse Port 6      CLOCK TO AM416 SET 5

33: P11      Temp 107 Probe
 01: 1       Rep
 02: 2       IN Chan
 03: 2       Excite all reps w/EXchan 2
 04: 5       Loc [:T deg C  ]
 05: 1       Mult
 06: 0       Offset

34: P56      Saturation Vapor Pressure
 01: 5       Temperature Loc T deg C
 02: 12      Loc [:vpsat kPa]

35: P86      Do
```

```
  01: 76      Pulse Port 6     CLOCK TO AM416 SET 6

 36: P4       Excite,Delay,Volt(SE)     RELATIVE HUMIDITY
  01: 1       Rep
  02: 5       2500 mV slow Range
  03: 2       IN Chan
  04: 2       Excite all reps w/EXchan 2
  05: 15      Delay (units .01sec)
  06: 2500    mV Excitation
  07: 7       Loc [:RH%      ]
  08: .1      Mult
  09: 0       Offset




 37: P37      Z=X*F
  01: 7       X Loc RH%
  02: .01     F
  03: 6       Z Loc [:VP kPA   ]

 38: P36      Z=X*Y
  01: 6       X Loc VP kPA
  02: 12      Y Loc vpsat kPa
  03: 6       Z Loc [:VP kPA   ]

 39: P86      Do
  01: 76      Pulse Port 6     CLOCK TO AM416 SET 7

 40: P2       Volt (DIFF)     PYRANOMETER
  01: 1       Rep
  02: 23      25 mV 60 Hz rejection Range
  03: 4       IN Chan
  04: 18      Loc [:slr rad  ]
  05: 81.2    Mult      CALIBRATION FACTOR
  06: 0       Offset

 41: P86      Do
  01: 76      Pulse Port 6     CLOCK TO AM416 SET 8

 42: P2       Volt (DIFF)     PRESSURE TRANSDUCER
```

```
 01: 1      Rep
 02: 4      250 mV slow Range
 03: 4      IN Chan
 04: 26      Loc [:pressure ]
 05: 1      Mult
 06: 0      Offset

43:  P86     Do
 01: 55     Set low Port 5     TURN OFF AM416

44:  P3      Pulse         PRECIP
 01: 1      Rep
 02: 2      Pulse Input Chan
 03: 2      Switch closure
 04: 19      Loc [:PRECIP   ]
 05: 1      Mult
 06: 0      Offset

45:  P3      Pulse         WIND SPEED
 01: 1      Rep
 02: 1      Pulse Input Chan
 03: 11      Low level AC
 04: 14      Loc [:Wind Spd ]
 05: .075    Mult
 06: 0.2     Offset

46:  P14     Thermocouple Temp (DIFF)     MEASURE SOIL T, TC
 01: 1      Rep                      WIRED FOR SPATIAL AVG
 02: 1      2.5 mV slow Range
 03: 3      IN Chan
 04: 2      Type E (Chromel-Constantan)
 05: 1      Ref Temp Loc panl temp
 06: 20      Loc [:Tsoil oC ]
 07: 1      Mult
 08: 0      Offset

47:  P14     Thermocouple Temp (DIFF)     measure rock T--TC
 01: 1      Rep                      wired for spatial average
 02: 1      2.5 mV slow Range
 03: 5      IN Chan
 04: 2      Type E (Chromel-Constantan)
```

```
  05: 1      Ref Temp Loc panl temp
  06: 28     Loc [:Trock oC ]
  07: 1      Mult
  08: 0      Offset

48:  P92     If time is        10 MINUTES BEFORE 60 MINUTE OUTPUT
  01: 50     minutes into a      SET FLAG 8 TO ENABLE AVERAGE
  02: 60     minute interval
  03: 18     Set high Flag 8

49:  P91     If Flag/Port      WHILE FLAG 8 IS RESET...
  01: 28     Do if flag 8 is low
  02: 19     Set high Flag 9

50:  P92     If time is
  01: 0      minutes into a
  02: 60     minute interval
  03: 10     Set high Flag 0 (output)


51:  P80     Set Active Storage Area
  01: 3      Input Storage Area
  02: 24     Array ID or location

52:  P71     Average
  01: 1      Rep
  02: 20     Loc Tsoil oC

53:  P80     Set Active Storage Area
  01: 3      Input Storage Area
  02: 32     Array ID or location

54:  P71     Average
  01: 1      Rep
  02: 28     Loc Trock oC

55:  P91     If Flag/Port
  01: 10     Do if flag 0 (output) is high
  02: 30     Then Do

56:  P35     Z=X-Y      COMPUTE CHANGE IN SOIL TEMP
```

```
 01: 24      X Loc AVG Ts
 02: 23      Y Loc prev. AVG
 03: 25      Z Loc [:delta Ts ]

57:  P31      Z=X          MOVE CURRENT AVG TO PREVIOUS AVG
 01: 24      X Loc AVG Ts
 02: 23      Z Loc [:prev. AVG]

58:  P35      Z=X-Y
 01: 32      X Loc Avg Tr
 02: 31      Y Loc prev Trav
 03: 33      Z Loc [:delta Tr ]

59:  P31      Z=X
 01: 32      X Loc Avg Tr
 02: 31      Z Loc [:prev Trav]

60:  P86      Do
 01: 28      Set low Flag 8

61:  P95      End

62:  P86      Do
 01: 29      Set low Flag 9

63:  P80      Set Active Storage Area
 01: 1      Final Storage Area 1
 02: 237     Array ID or location

64:  P77      Real Time
 01: 110     Day,Hour-Minute

65:  P71      Average      AVG NET RADIATION AND HEAT FLUX
 01: 3      Reps
 02: 15      Loc Rn W/m2

66:  P70      Sample      SAMPLE CURRENT AVG Ts AND CHANGE FROM
 01: 2      Reps        PREVIOUS AVG Ts
 02: 24      Loc Avg Ts

67:  P70      Sample      SAMPLE CURRENT AVG Tr AND CHANGE FROM
```

```
 01: 2      Reps           PREVIOUS AVG Tr
 02: 32     Loc

68:  P71    Average
 01: 2      Reps
 02: 5      Loc T deg C

69:  P70    Sample
 01: 1      Reps
 02: 7      Loc RH%

70:  P69    Wind Vector
 01: 1      Rep
 02: 0      Samples per sub-interval
 03: 02     Polar Sensor/(S, U, DU, SDU)
 04: 14     Wind Speed/East Loc Wind Spd
 05: 13     Wind Direction/North Loc Wind dir

71:  P72    Totalize
 01: 1      Rep
 02: 19     Loc PRECIP



72:  P71    Average
 01: 1      Rep
 02: 18     Loc slr rad

73:  P71    Average
 01: 1      Rep
 02: 26     Loc pressure

74:  P86    Do     CALL BATTERY CHECK/PUMP&MIRROR SUBROUTINE
 01: 2      Call Subroutine 2

75:  P96    Serial Output
 01: 71     SM192/SM716/CSM1

76:  P      End Table 2
```

```
*   3      Table 3 Subroutines

01: P85     Beginning of Subroutine
 01: 1     Subroutine Number

02: P86     Do (re-enable standard output)
 01: 25     Set low Flag 5

03: P86     Do (output starting time)
 01: 10     Set high Flag 0 (output)

04: P80     Set Active Storage Area
 01: 1     Final Storage Area 1
 02: 303    Array ID or location

05: P77     Real Time
 01: 110    Day,Hour-Minute

06: P95     End
```

**SUBROUTINE 2: SWITCH PUMP AND COOLED MIRROR IN RESPONSE TO USER FLAG OR OFF IF BATTERY IS <11.5 VOLTS AND SWITCH ON AGAIN IF >12 VOLTS**

```
07: P85     Beginning of Subroutine
 01: 2     Subroutine Number

08: P91     If Flag/Port
 01: 16     Do if flag 6 is high
 02: 73     Pulse Port 3

09: P86     Do
 01: 26     Set low Flag 6

10: P91     If Flag/Port
 01: 17     Do if flag 7 is high
 02: 74     Pulse Port 4

11: P86     Do
 01: 27     Set low Flag 7
```

```
12:  P89      If X<=>F
 01: 10      X Loc batt volt
 02: 4      <
 03: 11.5    F
 04: 30      Then Do

13:  P91      If Flag/Port
 01: 23      Do if flag 3 is low
 02: 30      Then Do

14:  P86      Do
 01: 74      Pulse Port 4

15:  P86      Do
 01: 13      Set high Flag 3

16:  P86      Do
 01: 10      Set high Flag 0 (output)

17:  P80      Set Active Storage Area
 01: 1      Final Storage Area 1
 02: 317     Array ID or location

18:  P77      Real Time
 01: 110     Day,Hour-Minute

19:  P70      Sample
 01: 1      Reps
 02: 10      Loc batt volt

20:  P96      Serial Output
 01: 71      SM192/SM716

21:  P95      End

22:  P94      Else

23:  P91      If Flag/Port
 01: 13      Do if flag 3 is high
 02: 30      Then Do
```

```
24:  P89      If X<=>F
 01: 10       X Loc batt volt
 02: 3        >=
 03: 12       F
 04: 30       Then Do

25:  P86      Do
 01: 73       Pulse Port 3

26:  P86      Do
 01: 23       Set low Flag 3

27:  P86      Do
 01: 10       Set high Flag 0 (output)

28:  P80      Set Active Storage Area
 01: 1        Final Storage Area 1
 02: 328      Array ID or location

29:  P77      Real Time
 01: 110      Day,Hour-Minute

30:  P70      Sample
 01: 1        Reps
 02: 10       Loc batt volt

31:  P95      End

32:  P95      End

33:  P95      End

34:  P95      End

35:  P        End Table 3


*    A        Mode 10 Memory Allocation
 01: 33       Input Locations
 02: 64       Intermediate Locations
 03: 0.0000   Final Storage Area 2
```

```
*    C      Mode 12 Security
 01: 0000   LOCK 1
 02: 0000   LOCK 2
 03: 0000   LOCK 3
```

Input Location Assignments (with comments):

```
    Key:
    T=Table Number
    E=Entry Number
    L=Location Number

    T:  E:  L:
    1:  1:  1:  Loc [:panl temp]
    1:  3:  2:  Loc [:upper tc ]
    1:  2:  3:  Loc [:lower tc ]
    1:  5:  4:  Z Loc [:delta t  ]
    2: 33:  5:  Loc [:T deg C  ]
    2: 37:  6:  Z Loc [:VP kPA   ]
    2: 38:  6:  Z Loc [:VP kPA   ]
    2: 36:  7:  Loc [:RH%      ]
    1:  4:  8:  Loc [:dew pt   ]
    1:  6:  8:  Loc [:dew pt   ]
    1:  7:  8:  Loc [:dew pt   ]
    1:  8:  9:  Loc [:vap pres ]
    2: 16: 10:  Loc [:batt volt]
    2:  1: 11:  Loc [:s into m ]
    2: 34: 12:  Loc [:vpsat kPa]
    2: 31: 13:  Loc [:Wind dir ]
    2: 45: 14:  Loc [:Wind Spd ]
    2: 21: 15:  Z Loc [:Rn W/m2  ]
    2: 24: 15:  Z Loc [:Rn W/m2  ]
    2: 27: 16:  Loc [:SHF #1   ] (shade)
    2: 29: 17:  Loc [:SHf #2   ]     (open)
    2: 40: 18:  Loc [:slr rad  ]
    2: 44: 19:  Loc [:PRECIP   ]
    2: 46: 20:  Loc [:Tsoil oC ]
    2: 19: 21:  Loc [:uncRn w/m]
    2: 57: 23:  Z Loc [:prev. AVG]
    2: 56: 25:  Z Loc [:delta Ts ]
    2: 42: 26:  Loc [:pressure ]
```

```
2: 47: 28:  Loc [:Trock oC ]
2: 59: 31:  Z Loc [:prev Trav]
2: 58: 33:  Z Loc [:delta Tr ]
```

Input Location Labels:

1:panl temp
2:upper tc
3:lower tc
4:delta t
5:T deg C
6:VP kPA
7:RH%
8:dew pt
9:vap pres
10:batt volt
11:s into m
12:vpsat kPa
13:Wind dir
14:Wind Spd
15:Rn W/m2
16:SHF #1
17:SHf #2
18:slr rad
19:PRECIP
20:Tsoil oC
21:uncRn w/m
22:_________
23:prev. AVG
24:_________
25:delta Ts
26:pressure
27:_________
28:Trock oC
29:_________
30:_________
31:prev Trav
32:_________
33:delta Tr
34:_________
35:_________
36:_________

data for nonrecording rain gages, collected when feasible, in mm (collected by humans; not datalogger)

| date | gage 1 | gage 2 | gage 3 | gage 4 | gage 5 | gage 6 | gage 7 | gage 8 | gage 9 | gage 10 | gage 11 | gage 12 | gage 13 | average | std dev |
|---|---|---|---|---|---|---|---|---|---|---|---|---|---|---|---|
| 122193 | 9 | 9 | 2 | 9 | 3 | 5 | 6 | 9 | 7 | 6 | 4 | 7 | 4 | 6.15 | 2.35 |
| 12694 | 9 | 11 | 5 | 10 | 7 | 10 | 7 | 4 | 5 | 3 | 6 | 9 | 9 | 7.31 | 2.46 |
| 31094 | 8 | 41 | 35 | 50 | 31 | 9 | 35 | 55 | 59 |  | 29 | 34 |  | 35.09 | 15.65 |
| 32494 | 30 | 29 | 28 | 30 | 25 | 29 | 23 | 30 | 27 | 19 | 24 | 28 |  | 26.83 | 3.29 |
| 42994 | 22 | 21 | 11 | 21 | 20 | 22 | 20 | 16 |  | 19 | 18 | 18 | 18 | 18.83 | 2.94 |
| 52794 | 17 | 16 | 18 | 13 | 15 | 14 | 16 | 15 | 14 | 15 | 13 | 18 | 18 | 15.54 | 1.74 |
| 81794 | 5.8 | 4.8 | 5.9 | 4 | 4 | 4.8 | 3.9 |  | 3.9 | 4 | 3.9 | 4.1 | 5.8 | 4.58 | 0.79 |
| 82394 | 3.5 | 1 | 3 | 1 | 2 | 0 | 0.8 | 3 | 1 | 3 | 1 | 2 | 3.5 | 1.91 | 1.14 |
| 90694 | 34 | 30 | 39 | 30 | 30 | 32 | 33 | 32 | 30 | 42 | 34 | 43 | 36 | 34.23 | 4.35 |
| 91394 | 6 | 8 | 6 | 4 | 5 | 4 | 7 | 10 | 10 | 10 | 8 | 8 | 11 | 7.46 | 2.27 |
| 91494 | 8 | 8 | 8 | 3 | 5 | 5 | 3.8 | 8 | 4 | 2 | 2.5 | 8 | 7.5 | 5.60 | 2.29 |
| 102094 | 67 | 63.5 | 57 | 62 | 56 | 62 | 56 | 60 | 54 | 38 | 54 | 59 | 60 | 57.58 | 6.74 |
| 110394 | 8 | 8 | 7 | 8 | 8 | 9 | 10 | 8 | 7 | 2 | 7 | 8 | 8 | 7.54 | 1.78 |
| 111594 | 30 | 28 | 25 | 28 | 24 | 26 | 25 | 27 | 24 | 19 | 21 | 26 | 25 | 25.23 | 2.81 |
| 11295 | 14 | 14 | 14 | 14 | 12 | 14 | 14 | 16 | 12 | 11 | 14 | 12 | 13 | 13.38 | 1.27 |
| 12095 | 14.5 | 12 | 9 | 14 | 10 | 12 | 11 | 10 | 10.5 | 11 | 9 | 12.5 | 10 | 11.19 | 1.67 |
| 20195 | 24 | 22 | 18 | 22 | 17 | 19 | 19 | 26 | 18 | 15 | 16 | 24 | 18 | 19.85 | 3.28 |
| 21695 | 58 |  | 49 | 53 | 49 | 55 | 50 | 52 | 47 | 36 | 51 | 56 | 48 | 50.33 | 5.39 |
| 30295 | 11 | 52 | 9 | 10 | 7.5 | 9 | 8 | 8 | 11 | 8 | 8 | 10 | 10 | 9.13 | 1.19 |
| 31795 | 68 | 64 | 54 | 66 | 58 | 61 | 50 | 64 | 54 | 28 | 51 | 72 | 45 | 56.54 | 11.19 |
| 42595 | 24 | 22 | 18 | 19.5 | 20 | 23 | 16 | 16.5 | 19 | 11 | 20 | 25 | 20 | 19.54 | 3.57 |
| 81795 | 54 | 55 | 62 | 48 | 47 | 57 | 50 | 68 | 57 | 27 | 59 |  | 65 | 54.08 | 10.23 |
| ?82295? | 8 | 6 | 10 | 5 | 4 | 8 | 3 | 11.5 | 5 | 6 | 3 | 10 | 8 | 6.73 | 2.65 |
| 92895 | 23 | 22 | 24 | 22 | 26 | 25 | 24 | 22 | 24 | 30 | 29 | 29 | 29 | 25.31 | 2.87 |
| 110895 | 14 | 15 | 14 | 15 | 11 | 13 | 10 | 14 | 15 | 16 | 11 | 12 | 12 | 13.23 | 1.80 |
| 122195 | 8 | 9 | 2 | 9 | 1.5 | 2 | 2 | 3 | 2.5 | 2.5 | 1 | 2 | 2 | 3.58 | 2.83 |
| 20696 | 80 | 79 | 80 | 74 | 72 | 72 | 64 | 78 | 68 | 63 | 70 | 70 | 71 | 72.38 | 5.66 |
| 22796 | 29 | 28 | 26 | 25 | 18 | 26 | 18 | 14 | 18 | 10 | 14 | 20 | 20 | 20.46 | 5.71 |
| 31396 | 20 | 20 | 25 | 20 | 18 | 19 | 16 | 20 | 18 | 12 | 18 | 19 | 16 | 18.54 | 2.87 |
| TOTALS |  |  |  |  |  |  |  |  |  |  |  |  |  | YR AVG |  |
| 1994 | 248.3 | 269.3 | 247.9 | 264 | 232 | 226.8 | 240.5 | 268 | 238.9 | 176 | 221.4 | 265.1 | 201.8 | 238.46 |  |
| 1995 | 320.5 | 293 | 283 | 297.5 | 263 | 298 | 257 | 311 | 275 | 201.5 | 272 | 264.5 | 280 | 278.15 |  |

APPENDIX G Nonrecording rain gage data

## APPENDIX H

## UNIX programs used to process the BREB data

```
######################################################################
#! /usr/bin/nawk -f

#                         Program name is "jdd"

#program to convert fields 2 & 3 (day, hrmm) into decimal day, and
#   print out decimal day (field #1) and entire line

BEGIN{ FS = OFS = ","}

$1==110 || $1==237 {im=$3-int($3/100)*100
 time=(im/60.+($3-im)/100)/24.+$2}

{print time,$0}
#! /usr/bin/nawk -f
##########################################################################
#              Program is "line"
# program combines lines from same times of AWS data to make the following
# fields:

# time panT loTC dT loDP loVP upDP upVP / time Rnet SHF1 SHF2 Ts dTs Tr dTr Ta
VP RH
# 1   2   3  4  5   6  7   8  /  9   10   11   12  13  14 15  16 17 18 19
#----------array 110-------------------/-----------------------array 237---------

# wsp dwsp wdr dwdr ppt slr prs
# 20  21  22   23  24  25  26
#----------------------------

BEGIN {FS = ","
     OFS = ","
        temp=$0}

$1 == temp {print prev,$0}

$1 != temp {prev=$0
         temp=$1}
######################################################################
```

```
#! /bin/csh
#       program is "go"

# program removes maintenance data to maint. file, converts time to julian
#    decimal day, and cuts out field delimiter and day hrmm fields.
#    Then combines lines from same time.

#      output files are mwMMDDYY.dat (maint.) and nwMMDDYY.dat (data)

# EXAMPLE USAGE:  go w031094.dat
#      output files will be mw031094.dat and nw031094.dat

# The following fields of data are in nwMMDDYY.dat:
# time panT loTC dT loDP loVP upDP upVP / time Rnet SHF1 SHF2 Ts dTs Tr dTr Ta
#  1    2    3   4   5    6    7    8   / 9    10   11   12   13  14  15 16  17
#----------array 110--------------------/-------------------------array 237----

#  VP RH wsp dwsp wdr dwdr ppt slr prs
#  18 19 20  21   22   23  24  25  26
#--------------------------------------

set fn=$1        # raw data file name

egrep -v '^110|^237' ~betsy/als/data/$fn > ~betsy/als/data/m$fn          # sends maintenance
data to mwMMDDYY.dat

#        pull out nonmaintenance data and run through the nawk program jdd
#        (which converts doy and time to decimal day), remove redundant
#        fields (cut), then run through nawk program line, which combines the
#        two lines of data for each time into one, wherever two lines of the
#        same time occur.

egrep '^110|^237' ~betsy/als/data/$fn | ~betsy/als/proc/jdd | cut -d, -f1,5- | nawk -f
~betsy/als/proc/line |tr -s ',' ' ' > ~betsy/als/data/n$fn
#########################################################################

#! /usr/bin/nawk -f                                    [reg]
#  program [reg] projects the data onto a uniform time
#    series so that missing data is filled up (here they take
#        the same value as next exsisting data). This step is
```

```
#       necessary for combining BOWEN and AWS data together.


#       The data is flagged here:
#       flag=0          good data
#       flag=1          missing data


BEGIN  {#FS = "     "
        ntstep=1   # each time step is 20min  1/72 day
        nday=72
        tstart=46 #start from day tstart(first timestep AFTER 0:00am)
        tend=75  # end at 0:00am  of day tend
        flag=0
      ntime=tstart*nday
        }

      {ttime = int($1*nday+.5)          #labeled time of current line
        if(ttime==tstart*nday) ntime=ttime+1  #time of the uniform time series
}

ttime > tstart*nday && $1 <=tend    {
        nn=(ttime-ntime)/ntstep
        temp=$1
        while(nn > .5) {
           $1=ntime/nday
           flag=1
        if($1>=1.0) print $0,flag   # start at midnight, jan1 1994
#               print $0,flag      # fill the gap with next existing data
           ntime=ntime+ntstep
           nn--
           }
        flag=0
        ntime=ntime+ntstep
        $1=temp
        print $0,flag
}
##########################################################################
```

```
#! /usr/bin/nawk -f                              [intp1]
#   Linearly interpolate to replace missing/bad data according
#   to the flag. Flag itself is retained. Flag is assumed
#   to be the last field.
BEGIN        {miss=0        # of missing(bad) data
         }

         { for(i=1;i<=NF;i++)  f[i]= $i
         flag=$NF
}

flag == 0 {
         for(j=1;j<=miss;j++) {
                  for(i=1;i<=NF-1;i++) {
                           $i=f_1[i]+j*(f[i]-f_1[i])/(miss+1)
                  }
                  $NF=fg[j]
                  print
                  if(j==miss) {for(i=1;i<=NF;i++) $i= f[i] }
         }
         print
         for(i=1;i<=NF;i++)  f_1[i]= $i
         miss=0
}

flag != 0 { miss++
         fg[miss]=flag
}
##############################################################################

#! /usr/bin/nawk -f
#                  Program name is "G"
# This program calculates soil heat flux from bowen ratio data

{        flag=$NF
         $NF=""
         BD=1518               #soil bulk density, kg/m3
         CS=840                #sp heat dry soil, J/kgoC (est.)
         W =0.013       #soil H20 content, kg H20/kg soil
         CW=4190               #sp heat water, J/kgoC
         dTs=$14               #change in soil temp
```

```
        T =1200                 #output interval, seconds
        D =0.08                 #depth to soil heat flux plates, m
        SHF1=$11     #soil heat flux plate #1
        SHF2=$12     #soil heat flux plate #2

        C = BD * (CS + W * CW)              #soil heat capacity

        S = dTs / T * D * C          #soil heat storage

        F = (SHF1 + SHF2) / 2               #soil heat flux where plates are

        G = F + S     #soil heat flux= flux at depth plus heat stored above

        print $0,G,flag }
################################################################################

#! /usr/bin/nawk -f                                              [dqcor]
# [dpcor] calculates a correction term to be subtracted from the measured
# value of dq=VP2-VP1  (upper - lower arm vapor pressure, in kPa)
# this is to account for lag time between measuring humidity at
# upper and lower arm
# usage dqcor *.RnG > *.dqc

BEGIN {
        dt= 2           # switch between reading upper and lower arm every 2 min
        dT= 20          # 20 min averaging period
}
{       f1VP1= $6
        f1VP2= $8
        if (NR==2) {  dq= dqm                   # corrected dq
                      dqcor= 0          # dq correction term
                      print lastline,dqm,dqcor,dq,flagA
        }
        if (NR>=3) {
                dqcor= (f1VP1 + f1VP2 - f_1VP1 - f_1VP2)*dt/(4*dT)
                dq= dqm + dqcor
                print lastline,dqm,dqcor,dq,flagA
        }
        dqm= $8 - $6                            # measured dq
```

```
           f_1VP1= fVP1
           f_1VP2= fVP2
           fVP1= f1VP1
           fVP2= f1VP2

#          flag=$(NF-2)              # move flags to the end of line
#          flagB=$(NF-1)
         flagA=$NF
#          $(NF-2)=""
#          $(NF-1)=""
         $NF=""
           lastline= $0
 }
 END {
           dq= dqm
           dqcor= 0
           print lastline,dqm,dqcor,dq,flagA
 }
##################################################################################

#! /usr/bin/nawk -f
#        program is "energy"

# Program calculates Bowen ratio, sensible heat flux, latent heat flux
# Program sets the following flags:
#        flag    condition            result
#         -1    |dq|<.005             LE=0
#         -2     |1+B|<0.3
#         -3     LE<0 & RH > 80              keep data as is
#         -4     LE<0 & RH < 80              LE=0

# The following fields are produced from this program:
#  time panT loTC dT loDP loVP upDP upVP / time Rnet SHF1 SHF2 Ts dTs Tr dTr Ta
#   1    2    3   4   5    6    7    8   /  9   10   11   12  13 14 15 16 17
#
#   VP RH wsp dwsp wdr dwdr ppt slr prs G  dq B  LE H  VPA flag
#   18 19 20   21   22   23  24  25  26 27 28 29 30 31 32   33
BEGIN {Bcr=.3                  #Bowen ratio criterion
         dqcr=0.005    #dq criterion, kPa
         }
```

```
{ dq=$8-$6
   dT=$4
   Rn=$10
   G=$27
   RH=$19
   Ta=$17
   flag=$NF
   P=86.54                #atmospheric pressure, kPa, corr. for elevation
   CP=1.01                #spec. heat air, kJ/kgoC
   EW=2470                #latent heat vap., kJ/kg

   adq=dq
   if(adq<0.)adq=-adq
   if(adq < dqcr) {Eflag=-1;LE=0.}
    else {B=P * CP * dT / (.622 * EW * dq)
          aB1=1.+B
          if(aB1<0.)aB1=-aB1
          if(aB1 < Bcr) Eflag=-2
                 else LE=(Rn-G)/(1.+B)
   }
   if(LE < 0. && RH > 80.) Eflag=-3
   if(LE < 0. && RH <= 80.) {LE=0.
                            Eflag=-4 }

   H=Rn-G-LE
   E=LE*86400/2470000.
   esat=0.6108*exp(17.27*Ta/(237.3+Ta))
   VPA=esat*RH*0.01

   print $0,dq,B,LE,H,E,VPA,flag,Eflag}

##############################################################################
#! /usr/bin/nawk -f                          [runm]
#    3-step running mean. except flags

   {
   for(i=1;i<=NF;i++) { fl[i]= $i }

   if(NR==2) print lastline
   lastline=$0
   if(NR>=3) {
```

```
                for(i=1;i<=NF-1;i++) {
                        $i= ( f_1[i]+f[i]+f1[i] )/3.
                }
#               $(NF-2)=f[NF-2]
#               $(NF-1)=f[NF-1]
                $NF=f[NF]
                print
        }
        for(i=1;i<=NF;i++) {
                f_1[i]= f[i]
                f[i]= f1[i]
        }
}
END     { print lastline
}
################################################################################
```

```
#! /usr/bin/nawk -f                                     [hour]
#select hourly means from running mean
# labeled time is at 40min past the hour while the averaged data
#   is centered at 30min past the hour. Note: dTs is still for 20mins,
#   if you do need to use it, multiply by 3

NR%3 == 2 { print
        }
################################################################################
```

# APPENDIX I

## Calculation of Energy Fluxes from Raw Data

Soil heat flux and the latent heat flux are calculated from the Bowen ratio system measurements; net radiation is measured directly, and the sensible heat flux is determined to be the remainder of the value of net radiation after the other fluxes are subtracted.

### I.1 Soil Heat Flux

To calculate the soil heat flux, the average of the two soil heat flux plates (open and shaded) is first calculated using an arithmetic average. Next, the energy stored above the heat flux plates is calculated. Values for soil bulk density and moisture content must be input at this point. The equation used to calculate energy storage is:

$$S = dTs / T * D * BD * (CS + W * CW) \qquad (9)$$

where: S = energy stored (W/m$^2$)
dTs = change in soil temperature (°C)
T = output interval (1200 seconds)
D = depth to flux plates (0.08 m)
BD = soil bulk density (kg/m$^3$)
CS = specific heat of dry soil
(estimated to be 840 J/kg°C)
W = soil water content (kg H20/kg soil)
CW = specific heat of water (4190 J/kg°C)

Soil heat flux, Gs, is then the sum of S and the average heat flux, F (CSI, 1993).

### I.2. Latent Heat Flux

The latent heat flux is calculated from the Bowen ratio, given by:

$$\beta = (P * CP * dT) / (0.622 * EW * dq) \qquad (15)$$

where: $\beta$ = Bowen ratio
P = atmospheric pressure (kPa)
CP = specific heat of air (1.01 kJ/kg°C)
dT = temperature gradient between arms (°C)
EW = latent heat of vaporization (2470 kJ/kg)
dq = vapor pressure gradient between arms (kPa)
(note: 0.622 is the ratio of the molecular weight of water to the molecular weight of dry air)

The latent heat flux, as described in Appendix 1, is calculated from:

$$L_e = (R_n - G) / (1 + \beta) \qquad \text{(all units W/m}^2\text{)} \qquad (8)$$

### I.3. Sensible Heat Flux

The sensible heat flux is calculated once all other fluxes have been determined:

$$H = Rn - G - Le \qquad \text{(all units W/m2).}$$

### I.4 Calculation of Evapotranspiration from Latent Heat Flux

Evapotranspiration can be calculated simply by dividing the latent heat flux by the latent heat of vaporization. This depth of water is then multiplied by the area of the watershed to obtain a rate of evapotranspiration. The rate can then be used to calculate the volume of water lost to the atmosphere over a given time period, for use in the water budget.

### I.5 Filtering Of Bad Data

Bad data occur under two conditions, one relating to the operation of the Bowen ratio system, and the other relating to the ambient weather conditions. Whenever the Bowen ratio system is recalibrated and cleaned (approximately once every 2 weeks), the hygrometer must be turned off. Before this occurs, all data collected up to that point are averaged and saved, and flagged so that it is identified as an average record over less than the full 20-minute period. In the processing of data, these incomplete periods are not used, and instead, values for parameters from the time periods prior and subsequent to that time are used to interpolate values for the missing time periods.

A review of the equations for the Bowen ratio and latent heat flux shows that the Bowen ratio is undefined for $dq = 0$, and that latent heat flux is undefined when the Bowen ratio = -1. The Bowen ratio calculation could theoretically be expected to break down in the morning and evening when $R_n$ - G approaches zero. Initial plots of the unprocessed data showed poor results for some distance on either side of $dq = 0$ and $\beta = -1$, so in the data processing programs, corrections are made to account for these circumstances, and are noted with the use of flags. When $|dq|<0.005$, $L_e$ is set to 0 and one flag is set. When $|1+\beta|< 0.4$, another flag is set, and the value is interpolated according to previously calculated values. In the early plotted data, negative $L_e$ would occasionally occur, which is not usually expected in a climate as dry as this area. In some cases, however, relative humidity was high, supporting a negative $L_e$. Therefore, the processing programs leave $L_e$ as is when the relative humidity is higher than 80%, but flags it. For negative $L_e$ when relative humidity is less than 80%, $L_e$ is set to zero, and flagged differently.

# APPENDIX J
## Sample Weather Data

Note: Data for each 20-minute averaging period consists of two lines: one containing ten fields, beginning with 110, and one line containing 20 fields, beginning with 237. Data are processed using the programs contained in Appendix H.

**Key**

| line begins with | field | parameter |
|---|---|---|
| 110 | 2 | day of year |
| | 3 | time of day |
| | 4 | datalogger temperature (°C) |
| | 5 | temperature of lower thermocouple (°C) |
| | 6 | temperature difference between thermocouples (°C) |
| | 7 | dew point from lower Bowen ratio arm (°C) |
| | 8 | vapor pressure from lower Bowen ratio arm (kpa) |
| | 9 | dew point from upper Bowen ratio arm (°C) |
| | 10 | vapor pressure from upper Bowen ratio arm (kpa) |
| 237 | 2 | day of year |
| | 3 | time of day |
| | 4 | net radiation (W/m$^2$) |
| | 5 | soil heat flux, plate #1 (W/m$^2$) |
| | 6 | soil heat flux, plate #2 (W/m$^2$) |
| | 7 | soil temperature (°C) |
| | 8 | change in soil temperature (°C) |
| | 9 | rock temperature (°C) |
| | 10 | change in rock temperature (°C) |
| | 11 | air temperature (°C) |
| | 12 | vapor pressure (kpa) |
| | 13 | relative humidity (%) |
| | 14 | wind speed (m/s) |
| | 15 | change in wind speed (m/s) |
| | 16 | wind direction (degrees) |
| | 17 | change in wind direction (degrees) |
| | 18 | precipitation (.1 mm) |
| | 19 | incoming solar radiation (W/m$^2$) |
| | 20 | atmospheric pressure (not calibrated) |

## SAMPLE DATA BEGINNING AT 1420 ON JUNE 30, 1994

```
110,181,1420,36.82,33.6,.384,11.63,1.368,11.68,1.373
237,181,1420,538.4,14.67,24.82,39.45,.206,36.83,.042,33.52,1.223,23.65,3.65,2.401,21
4.5,47.39,0,646.7,16.95
110,181,1440,37,34.02,.359,11.77,1.381,11.82,1.385
237,181,1440,508.2,14.87,24.91,39.76,.315,37.16,.335,34.03,1.218,22.65,3.091,1.86,18
8.8,51.12,0,621.6,16.95
110,181,1500,37.16,34.19,.308,11.89,1.391,11.94,1.396
237,181,1500,470.2,14.71,25.3,40.07,.308,37.34,.177,34.12,1.225,22.45,2.968,1.955,21
0.4,47.32,0,580.6,16.95
110,181,1520,37.5,34.7,.389,12.12,1.413,12.16,1.416
237,181,1520,442.5,14.5,25.59,40.39,.314,37.82,.479,34.71,1.243,22.91,3.063,1.438,16
8,59,0,551.7,16.95
110,181,1540,37.69,34.74,.341,12.31,1.431,12.37,1.436
237,181,1540,403.3,14.31,25.67,40.63,.244,38.02,.197,34.82,1.26,22.24,3.138,.871,193.
6,68.84,0,436.4,16.95
110,181,1600,37.84,34.83,.301,12.26,1.426,12.39,1.438
237,181,1600,362.8,14.04,25.48,40.67,.04,38.14,.127,34.96,1.148,19.83,2.972,1.316,17
2.5,60.46,0,83.5,16.95
110,181,1620,37.89,34.87,.431,12.11,1.412,12.31,1.431
237,181,1620,314.6,13.7,24.93,40.57,-.098,38.28,.137,34.96,1.055,18.83,3.315,1.75,69.
37,55.65,0,414,16.95
110,181,1640,37.73,34.45,.28,11.81,1.384,12.03,1.405
237,181,1640,222.1,13.36,24.02,40.35,-.222,38,-.282,34.59,1.008,17.96,2.737,.308,350.
6,76.3,0,312.2,16.95
110,181,1700,37.54,34.5,.32,11.54,1.36,11.76,1.38
237,181,1700,202.3,12.94,22.62,40.03,-.315,37.78,-.219,34.54,1.002,18.49,2.459,1.589,
34.41,48.18,0,290.7,16.95
110,181,1720,37.08,34.32,.126,11.23,1.332,11.51,1.357
237,181,1720,13.93,12.5,20.84,39.65,-.382,37.03,-.748,34.5,.973,18.02,1.674,.282,183.9
,73.9,0,81,16.95
110,181,1740,36.17,33.17,.104,10.57,1.275,10.86,1.3
237,181,1740,-5.124,12,18.88,38.96,-.691,35.96,-1.077,33.56,.953,18.96,3.649,3.18,76.
2,29.04,0,57.72,16.95
110,181,1800,34.88,31.49,.11,9.63,1.197,9.94,1.222
237,181,1800,-5.369,10.93,16.16,38.1,-.861,34.51,-1.442,31.7,.912,18.96,5.057,4.817,6
9.12,17.63,0,56.51,16.95
110,181,1820,33.83,31.23,.069,8.86,1.136,9.09,1.154
237,181,1820,-14.35,9.51,13.16,37.29,-.805,33.61,-.899,31.4,.897,20.1,3.129,2.733,81.2
,28.81,0,52.01,16.95
```

# APPENDIX K

## Equations for Calculation of the Penman Evaporation ($E_p$)

$$\boxed{E_p = \frac{\Delta}{\Delta+\gamma}(R_n+A_h) + \frac{\lambda}{\Delta+\gamma}\frac{6.43(1+0.536U_2)D}{\lambda}}$$

where: Δ = vapor pressure gradient, kPa/°C:

$$\Delta = 4098\frac{e_s}{(237.3+T_a)^2}$$

$e_s$ = saturated vapor pressure, kPa:

$$e_s = 0.6108 \exp\left(\frac{17.27T_a}{237.3+T_a}\right)$$

$T_a$ = air temperature, °C
γ = psychrometric constant, kPa/°C:

$$\gamma = 0.0016286\frac{P}{\lambda}$$

P = atmospheric pressure, kPa
λ = latent heat of vaporization, MJ/kg:

$$\lambda = 2.501 - 0.002361\ T_a$$

$R_n$ = net radiation exchange for the free water surface, mm/day

$$R_n = R_N + (0.15slr)(\frac{0.0864}{\lambda})$$

$R_N$ = net radiation, W/m$^2$
slr = incoming solar radiation, W/m$^2$
$A_h$ = energy advected to the water body, mm/day, if significant
$U_2$ = wind speed measured at 2 m, m/s
D = vapor pressure deficit, $e_s$ - e, kPa
e = vapor pressure, kPa

# APPENDIX L

## Equations for Calculation of Shuttleworth's Reference Crop Evaporation ($E_{rc}$)

$$\boxed{E_{rc} = \frac{\Delta}{\Delta + \gamma *} (R_n - G) + \frac{\gamma}{\Delta + \gamma *} \frac{900}{T_a + 275} U_2 D}$$

where: Δ = vapor pressure gradient, kPa/°C:

$$\Delta = 4098 \frac{e_s}{(237.3 + T_a)^2}$$

$e_s$ = saturated vapor pressure, kPa:

$$e_s = 0.6108 \exp \left( \frac{17.27 T_a}{237.3 + T_a} \right)$$

$T_a$ = air temperature, °C

γ = psychrometric constant, kPa/°C:

$$\gamma = 0.0016286 \frac{P}{\lambda}$$

P = atmospheric pressure, kPa

λ = latent heat of vaporization, MJ/kg:

$$\lambda = 2.501 - 0.002361 \, T_a$$

$\gamma^* = \gamma \, (1.033 \, U_2)$, kPa/°C

$U_2$ = wind speed measured at 2 m, m/s

$R_n$ = net radiation for reference crop, mm/day:

$$R_n = R_N / 0.0864 \, \lambda$$

$R_N$ = measured net radiation, W/m$^2$

G = soil heat flux, MJ/m$^2$d

D = vapor pressure deficit, $e_s$ - e, kPa

e = vapor pressure, kPa

# REFERENCES

Abramowitz, M. A., and I. A. Stegun (eds.), *Handbook of Mathematical Functions with Formulas, Graphs, and Mathematical Tables*, National Bureau of Standards Applied Mathematics Series, no. 55, pp. 231 and 299, U. S. Government Printing Office, Washington, D. C., 1967.

Ahn, J. H., D. R. Peacor, and D. S. Coombs, Formation mechanisms of illite, chlorite and mixed-layer illite-chlorite in Triassic volcanogenic sediments from the Southland Syncline, New Zealand, *Contrib. Mineral. Petrol.*, v. 99, pp. 82-89, 1988.

Altaner, S. P., and R. E. Grim, Mineralogy, chemistry, and diagenesis of tuffs in the Sucker Creek Formation (Miocene), eastern Oregon, *Clays and Clay Minerals*, 38(6), pp. 561-572, 1990.

Amiro, B. D., and E. E. Wuschke, Evapotranspiration from a boreal forest drainage basin using an energy balance/eddy correlation technique, *Boundary-Layer Met.*, v. 38, pp. 125-139, 1987.

Anderson, J. E., Development of snowflake texture in a welded tuff, Davis Mountains, Texas, *Geol. Soc. Amer. Bull.*, v. 80, pp. 2075-2080, 1969.

Arizona Department of Water Resources (ADWR), 9-21-90, Well registry report, 1990.

Barenblatt, G. E., I. P. Zheltov, and I. N. Kochina, Basic concepts in the theory of seepage of homogeneous liquids in fissured rocks, *Jour. Appl. Math. and Mech.*, 24(5), pp. 1286-1303, 1960.

Bassett, R. L., S. P. Neuman, T. C. Rasmussen, A. Guzman, G. R. Davidson, and C. F. Lohrstorfer, Validation studies for assessing unsaturated flow and transport through fractured rock, NUREG/CR-6203, U. S. Nuclear Regulatory Commission, Washington, D.C., 1994.

Bingham, G. E., B. D. Tanner, J. Greene, and M. Tanner, A Bowen ratio system for long term remote measurement of evapotranspiration, *18th Conf. Agric. and For. Met. and 8th Conf. Biomet. and Aerobiol*, 15-18 Sept, Am. Met. Soc., Boston, MA, preprint volume, pp. 63-66, 1987.

Bish, D. L., *Evaluation of past and future alterations in tuff at Yucca Mountain, Nevada, based on the clay mineralogy of drill cores USW G-1, G-2, and G-3*, LA-10667-MS: Los Alamos National Laboratory, 40pp., 1989.

Bouwer, H. and R. C. Rice, A slug test for determining conductivity of unconfined aquifers with completely or partially penetrating wells, *Water Resour. Res.*, 12(3), pp. 423-428, 1976.

Brakensiek, D. L., H. B. Osborn, and W. J. Rawls, *Field Manual for Research in Agricultural Hydrology*, No. 224, U.S. Department of Agriculture, Washington, D.C., pp. 75-214, 1979.

Burger, P. A., and K. M. Scofield, Perched water at Yucca Mountain--implications on the exploratory studies facility, Nye County, Nevada: Water Resources Investigation Report, U.S. Geological Survey, Denver, CO, 1994.

Campbell Scientific, Inc. (CSI), *Bowen Ratio Instrumentation Instruction Manual*, CSI, Logan, UT, 1993.

Carr, R. G., A scanning electron microscope study of post-depositional changes in the Matahina Ignimbrite, North Island, New Zealand, *New Zealand Jour. of Geol. and Geophys.*, v. 24, pp. 429-434, 1981.

Cellier, P., and A. Olioso, A simple system for automated long-term Bowen ratio measurement, *Agric. and Forest Met.*, v. 66, pp. 81-92, 1993.

Cooper, H. H., Jr., J. D. Bredehoeft, and I. S. Papadopulos, Response of a finite diameter well to an instantaneous charge of water, *Water Resour. Res.*, 3(1), pp. 263-269, 1967.

Crosthwaite, E. G., J. J. Mundorff, and E. H. Walker, Groundwater aspects of the Lower Henry's Fork region, Eastern Idaho, U. S. Geological Survey Water-Supply Paper 1879-C, 22pp., 1970.

Culf, A. D., S. J. Allen, J. H. C. Gash, C. R. Lloyd, and J. S. Wallace, 1993. Energy and water budgets of an area of patterned woodland in the Sahel, *Agric. and Forest Met.*, v. 66, pp. 65-80, 1993.

Davidson, G. R., Geochemical and isotopic investigation of the rate and pathway of fluid flow in partially-welded fractured unsaturated tuff, Ph.D. dissertation, 208 pp., University of Arizona, Tucson, 1995.

Davis, D. A., and G. Yamanaga, Preliminary report on the water resources of the Kau District, Hawaii, Hawaii Div. Water and Land Devel. Circ. C27, Honolulu, HI, 25 pp., 1966.

de Pablo-Galan, L., Diagenesis of Oligocene-Miocene vitric tuffs to montmorillonite and K-feldspar deposits, Durango, Mexico, *Clays and Clay Minerals*, 38(4), pp. 426-436, 1990.

Dickinson, R. E., A. Henderson-Sellers, and P. J. Kennedy, *Biosphere-Atmosphere Transfer Scheme (BATS) Version 1e as Coupled to the NCAR Community Climate Model*, National Center for Atmospheric Research, Boulder, CO, 72 pp., 1993.

Driscoll, F. G., *Groundwater and Wells*, Johnson Filtration Systems, St. Paul, MN, 1089 pp., 1986.

Dugas, W. A., L. J. Fritschen, L. W. Gay, A. A. Held, A. D. Matthias, D. C. Reicosky, P. Steduto, and J. L. Steiner, Bowen ratio, eddy correlation, and portable chamber measurements of sensible and latent heat flux over irrigated spring wheat, *Agric. and Forest Met.*, v. 56, pp. 1-20, 1991.

Enlows, H. E., Welded tuffs of Chiricahua National Monument, Arizona, *Geol. Soc. Amer. Bull.* v. 66, pp. 1215-1246, 1955.

Flint, A. I., L. E. Flint, and J. A. Hevesi, Influence of long term climate change on net infiltration at Yucca Mountain, Nevada, Proceedings, 4th Annual International Conference on High Level Radioactive Waste Management, ASCE, New York, pp. 152-159, 1993.

Freeze, R. A., and J. A. Cherry, *Groundwater*, Prentice-Hall, Inc., Englewood Cliffs, NJ, 604 pp., 1979.

Gay, L. L, The Bowen ratio energy budget method and some selected applications, in Giordano, E., G. Scarascia Mugnozza, R. Valentini, and M. Agrimi, eds., *Plant- Atmosphere Relationships: Theory and Measurements of Mass and Energy Exchanges*: Proceedings of workshop, Viterbo, Italy, 1985, pp. 53-64, 1985.

Gay, L. L., Evaporation measurements for catchment scale water balances, *Proceedings, First International Seminar of Watershed Management*, Hermosillo, Sonora, Mexico, 1992, pp. 68-86, 1993.

Gringarten, A. C., Flow-test evaluation of fractured reservoirs, in *Recent Trends in Hydrogeology*, edited by T. N. Narasimhan, Geol. Soc. Amer. Special Paper 189, pp. 237-263, 1982.

Gringarten, A. C., and H. J. Ramey, Jr., The use of source and Green's functions in solving unsteady-flow problems in reservoirs, *Soc. Pet. Eng. J.*, pp. 285-296, 1973.

Gringarten, A. C., and P. A.Witherspoon, A method for analyzing pump test data from fractured aquifers, *Proc. Symp. on Percolation in Fissured Rock*, Stuttgart, Internat. Soc. of Rock Mechanics, v. 3, pp. B1-B9, 1972.

Gringarten, A. C., and H. J. Ramey, Jr., Unsteady-state pressure distributions created by a well with a single horizontal fracture, partial penetration, or restricted entry, *Soc. Pet. Eng. J.*, pp. 413-426, 1974.

Hammer, D. F. and D. W. Peterson, Geology of the Magma Mine area, in J. P. Ridge, ed., *Ore Deposits of the United States, 1933-1967*, part 9, Ch. 61, AIME Graton-Sales volume II, pp. 1282-1310, 1968.

Hardin, E. L., Uranium-324 in vadose zone and perched waters of the Apache Leap Tuff, central Arizona, Ph.D. dissertation, University of Arizona, Tucson, 1996.

Hardin, E. L., and R. L. Bassett, Summary of geophysical studies at the Apache Leap Research Site, UA Data Report 95-002, 31 pp., Department of Hydrology and Water Resources, University of Arizona, Tucson, 1995.

Harshbarger, J. W., D. D. Lewis, H. E. Skibitzke, W. L. Heckler, and L. R. Kister, revised by H. L. Baldwin, *Arizona Water*. U. S. Geological Survey Water-Supply Paper 1648. USGPO, Washington, D. C. , 85pp., 1966.

Karasaki, K., Well test analysis in fractured media, Ph.D. dissertation, 239 pp., University of California, Berkeley, 1987.

Karasaki, K., J. C. S. Long, and P. A. Witherspoon, Analytical models of slug tests, *Water Resour. Res.*, 24(1), pp. 115-126, 1988.

Kruseman, G. P., and N. A. de Ridder, *Analysis and Evaluation of Pumping Test Data*, ILRI Publication 47, 377 pp., The Netherlands, 1990.

Levy, S. S., and J. R. O'Neil, Moderate-temperature zeolitic alteration in a cooling pyroclastic deposit, in K. Gronvold, guest-editor, Water-Rock Interaction, *Chem. Geol.*, v. 76, pp. 321-326, 1989.

McNeil, D. D., and W. J. Shuttleworth, Comparative measurements of the energy fluxes over a pine forest, *Boundary-Layer Met.*, v. 9, pp. 297-313, 1975.

Milne-Home, W. A., Interpretation of pumping tests in fractured aquifers: from theory to routine field analysis, *Proceedings of the Fourth Annual Canadian/American Conference on Hydrogeology, Fluid Flow, Heat Transfer, and Mass Transport in Fractured Rocks*, pp. 177-184, Dublin, Ohio, 1988.

Moench, A. F., Double-porosity models for a fissured groundwater reservoir with fracture skin, *Water Resour. Res.*, 20, pp. 831-846, 1984.

Moncure, G. K., R. C. Surdam, and H. L. McKague, Zeolite diagenesis below Pahute Mesa, Nevada Test Site, *Clays and Clay Minerals*, 29(5), pp. 385-396, 1981.

Montgomery, E. L., and R. H. DeWitt, Water resources of the Inner Basin of San Francisco Volcano, Coconino County, Arizona, in Proc. 1974 Meeting of the Arizona Section, Amer. Water Res. Assn and the Hydrology Section, Ariz. Acadamy of Science, pp. 183-199, 1974.

Papadopulos, I. S., J. D. Bredehoeft, and H. H. Cooper, Jr., On the analysis of "Slug Test" data, Water Resour. Res., 9(4), pp. 1087-1089, 1973.

Peterson, D. W., *Dacitic ash-flow sheet near Superior and Globe, Arizona*, PhD thesis, Stanford University; U.S. Geological Survey Open-File Report 130, 1961.

Peterson, D. W., *Zoned ash-flow sheet in the region around Superior, Arizona*, in S. R. Titley (ed.), Southern Arizona Guidebook III, Geological Society of America, pp. 215-223, 1968.

Plummer, L. N., E. C. Prestemon, and D. L. Parkhurst, An interactive code (NETPATH) for modeling net geochemical reactions along a flow path, U.S. Geol. Surv. Water-Resources Investigation Rep. 91-4078, 227 pp., 1991.

Ragan, D. M., and M. F. Sheridan, Compaction of the Bishop Tuff, California, Geol. Soc. of Amer. Bull., v. 83, pp. 95-107, 1972.

Rasmussen, T. C., and D. D. Evans, Water infiltration into exposed fractured rock surfaces, *Soil Sci. Soc. Amer. Jour.*, v. 57 (2), pp. 324-329, 1993.

Ratterman, N. G., and R. C. Surdam, Zeolite mineral reactions in a tuff in the Laney member of the Green Valley Formation, Wyomin,. *Clays and Clay Minerals*, 29(5), pp. 365-377, 1981.

Roberts, R. J., and D. W. Peterson, Suggested magmatic differences between welded "ash" tuffs and welded crystal tuffs, Arizona and Nevada, *Geological Survey Research*: Short Papers in the Geologic and Hydrologic Sciences, article 320, pp. D73-D79, 1961.

Ross, C. S., and R. L.Smith, *Ash-flow tuffs: Their Origin, Geologic Relations, and Identification*, U.S. Geological Survey Professional Paper 366, 81pp., 1961.

Sageev, A., Slug test analysis, Water Resour. Res., 22(8), pp. 1323-1333, 1986.

Sample Management Facility, *Geologic summary of borehole USW UZP-4 phase 1e prototype drilling, Apache Leap, Arizona*, Draft report prepared for U.S. Department of Energy, Yucca Mountain Project, Science Applications International Corporation, 10 pp., 1990.

Sauveplane, C., Pumping test analysis in fractured aquifer formations; state of the art and some perspectives, in *Groundwater Hydraulics, Water Resour. Monogr. Ser.*, vol. 9, pp. 171-206, 1984.

Scott, R. B., R. W. Spengler, S. Diehl, A. R. Lappin, and M. P. Chornack, Geologic character of tuffs in the unsaturated zone at Yucca Mountain, southern Nevada, in *Role of the Unsaturated Zone in Radioactive and Hazardous Waste Disposal*, ed. by J. W. Mercer, P. S. Rao, and I. W. Marine, Ann Arbor, MI, pp. 289-335, 1983.

Shuttleworth, W. J., J. H. Gash, C. R. Lloyd, D. D. McNeil, C. J. Moore, and J. S. Wallace, An integrated micrometeorological system for evaporation measurement, *Agric. and Forest Met.*, 43, pp. 295-317, 1988.

Smith, R. L., Ash flows: *Geological Society of America Bulletin*, 71, pp. 795-842, 1960.

Snow, D. T., Anisotropic permeability of fractured media, *Water Resour. Res.*, v. 5 (6), pp. 1273-1289, 1969.

Souza, W. R., Exploratory drilling and aquifer testing at the Kipahulu District Haleakala National Park, Maui, Hawaii, U. S. Geological Survey Water-Resources Investigations Report 83-4066, 21 pp., 1983.

Spittlehouse, D. L., and T. A. Black, Determination of forest evapotranspiration using Bowen ratio and eddy correlation measurements, *Jour Appl Met.*, v. 18, pp. 647-653, 1979.

Spittlehouse, D. L., and T. A. Black, Evaluation of the Bowen ratio/energy balance method for determining forest evapotranspiration, *Atmos.-Ocean*, v. 18 (2), pp. 98-116, 1980.

Starkey, H. C., P. D. Blackmon, and P. L. Hauff, The routine mineralogical analysis of clay-bearing samples, U.S. Geological Survey Bulletin 1563, U. S. Government Printing Office, Washington, D. C., 323 pp., 1984.

Takasaki, K. J., Preliminary report on the water resources of southeast Maui, Hawaii, Hawaiian Division of Water and Land Development Circular C58, Honolulu, HI, 37 pp., 1971.

Tarshis, A. L., Devitrification products and textures in a rhyolitic ash flow tuff as seen by electron microscopy, *Geol. Soc. Amer. Abstracts with Programs*, pp. 114-115, 1973.

Theim, G., *Hydrologische Methoden,* Gebhardt, Leipzig, 56 pp., 1906.

Theis, C. V., The relation between the lowering of the piezometric surface and the rate and duration of discharge of a well using groundwater storage, *Trans. Amer. Geophys. Union,* 16, pp. 519-524, 1935.

Thornburg, T., Electrical resistivity of unsaturated, fractured tuff: influence of moisture content and geologic structure, Master's thesis, University of Arizona, 196 pp., 1990.

Tsolis-Katagas, P., and C. Katagos, Zeolites in pre-caldera pyroclastic rocks of the Santorini Volcano, Aegean Sea, Greece, *Clays and Clay Minerals,* 37(6), pp. 497-510, 1989.

Turner, D. R., and A. C. Bagtzoglou, Evaluation of the potential for perched water development at Yucca Mountain, in Ch. 9: *Subregional Hydrogeologic Flow and Transport Processes*, prepared by the Southwest Research Institute, 5 pp., 1995.

Unland, H. E., P. R. Houser, W. J. Shuttleworth, and Z.-L. Yang, Surface flux measurement and modeling at a semi-arid Sonoran Desert site, submitted to *Agric. and Forest Met.*

Urban, J. B., The Mahantango Creek watershed--evaluating the shallow ground-water regime, in *Watershed Research in Eastern North America: A Workshop to Compare Results*, report no. NSF/RA-770254, Smithsonian Institution, Edgewater, MD, vol 1, pp. 251-276, 1977.

U.S. Environmental Protection Agency (EPA), Environmental standards for the management and disposal of spent nuclear fuel high level and transionic radioactive wastes, *Final Rule, Code of Federal Regulations*, Title 40, Part 191, U.S. Government Printing Office, Washington, D.C., 1985.

Vogt, R., and Jaeger, L., Evaporation from a pine forest--using the aerodynamic method and Bowen ratio method, *Agric. and Forest Met.*, v. 50, pp. 39-54, 1990.

Warren, J. E., and P. J. Root, The behavior of naturally fractured reservoirs, *Soc. Pet. Eng. J.*, vol 3., pp. 245-255, 1963.

Wilson, D. H., R. J. Reginato, and K. J. Hollett, eds., *Evapotranspiration measurements of native vegetation, Owens Valley, California, June 1986*, U.S. Geological Survey Water-Resources Invest. Report 91-4159, Sacremento, CA, 83 pp., 1992.

Wise, S. W., F. M. Weaver, and N. Guven, Early silica diagenesis in volcanic and sedimentary rocks: devitrification and replacement phenomena, *Electron Micros. Soc. of Amer.*, 31st Annual Meeting, pp. 206-207, 1973.

Wu, Y.S., G. Chen, and G. S. Bodvarsson, Perched water analysis: G. S. Bodvarsson and T. M. Bandurraga, eds., *Development and Calibration of the Three-Dimensional Site-Scale Unsaturated Zone Model of Yucca Mountain, Nevada*, Lawrence Berkeley National Laboratory, Berkeley, CA, ch. 7, pp. 232-270, 1996.